RUSSIAN ACADEMY OF SCIENCE
FEDERAL AGENCY ON EDUCATION OF RUSSIAN FEDERATION
RUSSIAN NATIONAL COMMISSION FOR UNESCO
COMMITTEE ON SCIENCE AND HIGHER EDUCATION OF THE GOVERNMENT OF SAINT-PETERSBURG
COUNCIL OF RECTORS OF SAINT-PETERSBURG HIGHER EDUCATION ESTABLISHMENTS
SAINT-PETERSBURG STATE UNIVERSITY OF AEROSPACE INSTRUMENTATION (SUAI)
UNESCO CHAIR "DISTANCE EDUCATION IN ENGINEERING" OF SUAI

RUSSIAN SECTION OF THE INTERNATIONAL SOCIETY OF AUTOMATION

ИЗВЕСТИЯ КАФЕДРЫ UNESCO ГУАП «ДИСТАНЦИОННОЕ ИНЖЕНЕРНОЕ ОБРАЗОВАНИЕ»

Сборник статей

Выпуск 5

BULLETIN OF THE UNESCO DEPARTMENT "DISTANCE EDUCATION IN ENGINEERING" OF THE SUAI

Collection of the papers

Issue 5

РОССИЯ, САНКТ-ПЕТЕРБУРГ 2020 SAINT-PETERSBURG, RUSSIA

ББК 378.1
УДК 74.58
И33

И33 Bulletin of the UNESCO department "Distance education in engineering" of the SUAI: Collection of the papers. St. Petersburg, Issue 5.– SPb.:SUAI, 2020. – 137 p.

ISBN 978-5-8088-1477-6

ISA District 12 (The International Society of Automation) and SUAI (Saint-Petersburg State University of Aerospace Instrumentation) have organized the Sixteenth ISA European student paper competition (ESPC-2020) dedicated to the 75th anniversary of the ISA, 25th anniversary of the ISA St. Petersburg Russian section and 25th anniversary of the SUAI ISA student section. Papers of professors and the best students were included into this issue of the Bulletin of the UNESCO department "Distance education in engineering" of the SUAI. Papers can be interesting for students, post-graduate students, professors and specialists.

ISBN 978-5-8088-1477-6

On behalf of ISA, it is my pleasure to congratulate the ISA Russia Section and the St. Petersburg State University of Aerospace Instrumentation (SUAI) on successfully completing the ISA International Student Paper Competition.

I commend the students from around the world who contributed their time, knowledge and expertise to prepare a paper. We are proud that they selected our publication. A review committee selected the papers included in this volume. Awards have been given at gold, silver and bronze levels. Winners have been asked to prepare presentations.

Students of today are the engineers of tomorrow. Our profession sees students as future members of our profession and appreciates their interest in automation. Our society welcomes their future contributions in helping us achieve our vision of "creating a better world through automation", and our mission of "advancing technical competence by connecting the automation community to achieve operational excellence." We can accomplish these together.

Whichever career path these students choose, we hope ISA will continue to play an important role in their continuing education and professional development.

I extend my best wishes to all students and attendees in the 2020 ISA International Student Paper Competition.

Respectfully,

Eric C. Cosman
2020 ISA Society President

International Society of Automation
67 Alexander Drive
P.O. Box 12277
Research Triangle Park, NC 27709
PHONE (919) 549-8411
FAX (919) 549-8288
E-MAIL info@isa.org
www.isa.org

Setting the Standard for Automation™

The year 2020 is a year of celebrations!

ISA District 12 and SUAI have organized the Sixteenth ISA European student paper competition dedicated to the 75th anniversary of the ISA, the 25th anniversary of the ISA St. Petersburg Russian section and the 25th anniversary of the SUAI ISA student section.

Students who committed their time to prepare a paper should be very proud to be selected for this publication. The Students of today are the engineers of tomorrow. We are all excited about these talented individuals who will be instrumental in shaping our lifestyle into the future. To the lecturers and professors thank you for your development of today's students.

ISA is focusing on developing career paths for Students Internationally. I hope ISA will continue to play an important role in your and other student's education and professional development.

Congratulations to the SUAI ISA student section on their 25th anniversary. I would like to extend my best wishes to all students, lecturers and attendees at the 2020 ISA European Student Paper Competition.

Sincerely,

Brian J. Curtis
ISA Society President 2018

Standards
Certification
Education & Training
Publishing
Conferences & Exhibits

International Society of Automation
67 Alexander Drive
P.O. Box 12277
Research Triangle Park, NC 27709
PHONE (919) 549-8411
FAX (919) 549-8288
E-MAIL info@isa.org
www.isa.org

Setting the Standard for Automation™

I would like to extend congratulations to the ISA Russia Section, ISA District 12, and The Saint Petersburg State University of Aerospace Instrumentation (SUAI) for successfully organizing the Sixteenth ISA International Student Paper Competition.

As an educator and a member of ISA for over 40 years, I never tire of the opportunity to share with students the amazing challenges and personal rewards that a career in automation can bring. ISA is proud to have the opportunity to nurture the next generation of automation professionals.

We look forward to continuing the close relationship we have established between ISA, the Russia Section, District 12, and the SUAI. Through distance learning classes on project management and ongoing international online forums, we are developing new understandings in the technical, cultural, and personal arenas.

Congratulations to those who developed papers for this volume and to the advisory committee who had the difficult task of making paper selections.

Sincerely,

Gerald W. Cockrell

Gerald W. Cockrell
ISA Former President

Standards
Certification
Education & Training
Publishing
Conferences & Exhibits

ISA
67 Alexander Drive
P.O. Box 12277
Research Triangle Park, NC 27709
PHONE (919) 549-8411
FAX (919) 549-8288
E-MAIL info@isa.org
www.isa.org

DEVELOPMENT OF A SYSTEM FOR ADAPTIVE CONTROL OF ELEMENTS OF ADDITIVE PRODUCTION

Chabanenko Alexandr

Saint-Petersburg State University of Aerospace Instrumentation,
Saint-Petersburg, Russia
E-mail: Chabalexandr@gmail.com

Annotation
The use of additive technologies in the production process of case elements allows almost completely eliminating the stage of manufacturing prototypes and products manually or on traditional CNC machines, as well as the development of technological equipment, reducing the time for preparing the production of new products by 50 – 80%.

A comparison of the integral values of various technologies confirms the advantages of additive technologies in the production of additive products from the standpoint of the functioning of the installation and resource efficiency.

Identification of numerical values of indicators of production processes of additive production. The proposed private indicators consider the principles and characteristics of additive manufacturing.

To reduce the level of defectiveness, using the diagram of cause-effect relationships, corrective measures have been developed and implemented to change the physical characteristics of the case in the technological documentation and adjust the temperature regime.

Due to the incomplete coverage of the features of digital production, an organization standard has been developed that considers all the technological features of additive technologies and the requirements of modern electronic equipment.

To control the quality of the technological process, a relationship is established between quality indicators and the result of the process.

The main goal of the method of statistical control of the technological process is the identification and identification of key quality indicators figure. 1.

The initial stage is the identification, groups of quality indicators that have the greatest impact on the quality of the finished product.

This will make it possible to implement the method of monitoring and statistical control of layer-by-layer synthesis technology.

Quality levels are highlighted based on continuous values and discrete values table 1.

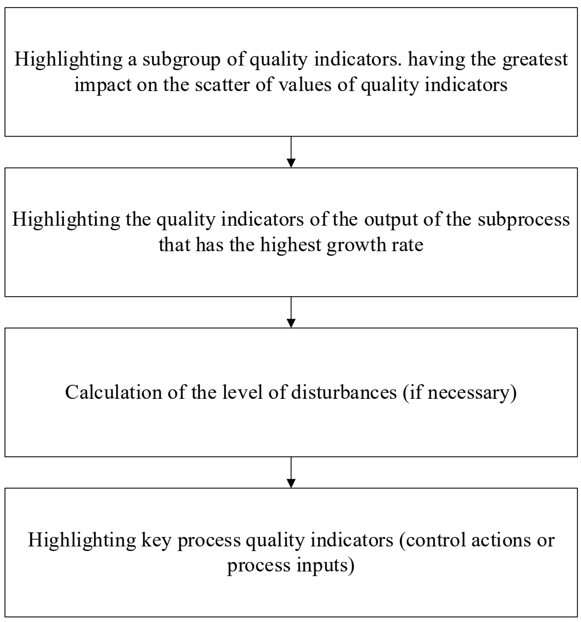

Figure 1. Scheme of establishing the relationship between quality indicators and determining a key quality indicator

Table 1 – Registration of levels of indicators of quality control actions

Symbol	The name of the control effect	Level value		
		1	2	3
ASA-plastic	Polymer temperature	160oC	200oC	240oC
ABS EG-plastic	Polymer temperature	210oC	225oC	250oC
ABS HG-plastic	Polymer temperature	220oC	212oC	260oC
ABS MP-plastic	Polymer temperature	200oC	210oC	220oC
ABS 2020-plastic	Polymer temperature	190oC	200oC	260oC

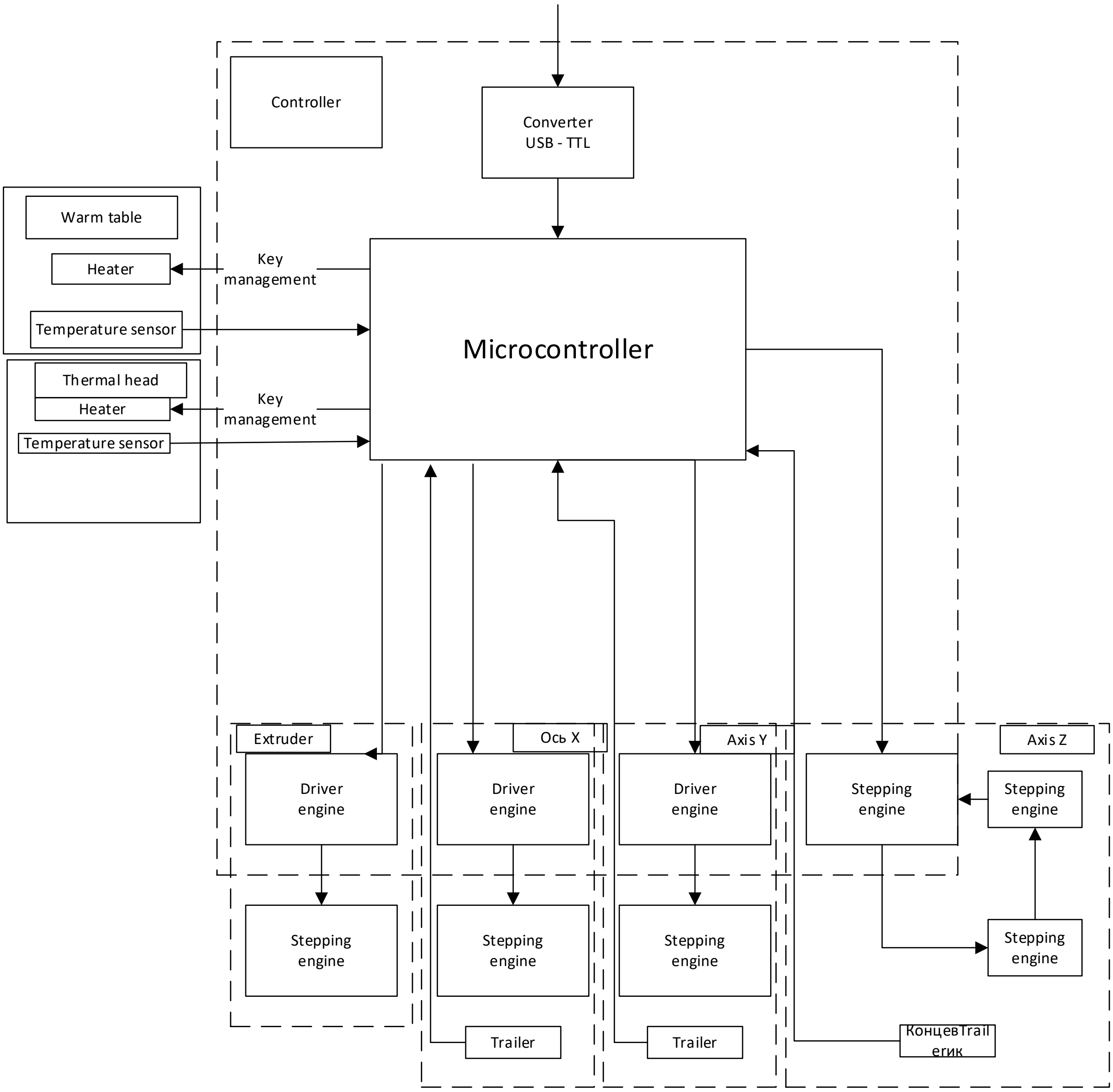

Figure 2 – Scheme of 3D printing process control

Adaptive control system

It is necessary to simulate an adaptive controller, tune and analyze its performance using Simulink to predict the operation of stepper motors and other elements of an additive installation. A direct adaptive method called Model Reference Adaptive Controller (MRAC) is used for this task. There are three main elements to this model: a reference model, a setup model, and an adaptive controller. Throughout the model it looks like this:

1.) Reference model: this part of the controller that models the desired behavior of a closed system. In other words, how do you want your system to behave as a whole,

modeled on this subsystem. In this example, the reference behavior is modeled as a transfer function. This can also come from the specifications of the feedback system described in the figure below, in the form of the desired rise time (0.413 s), settling time (0.706 s) and steady state error (0). The output of the reference model, Ut is preferably the reference path that the output plant (Yp) should follow.

2.) Installation model: in this example, the installation is a DC motor. One of the many engine parameters, Kf – Mechanical Damping, is considered variable. The initial value is assumed to be 0.2. And PID

The controller is configured to achieve the desired response with this initial Kf value. Now that the engine is aging and other environmental conditions, Kf changes, this changes the behavior of the engine. Factory exit – Yp. Therefore, the controller must adapt the parameter values to achieve the desired response (Yp – Ym = error (e) = 0) figure. 3.4.

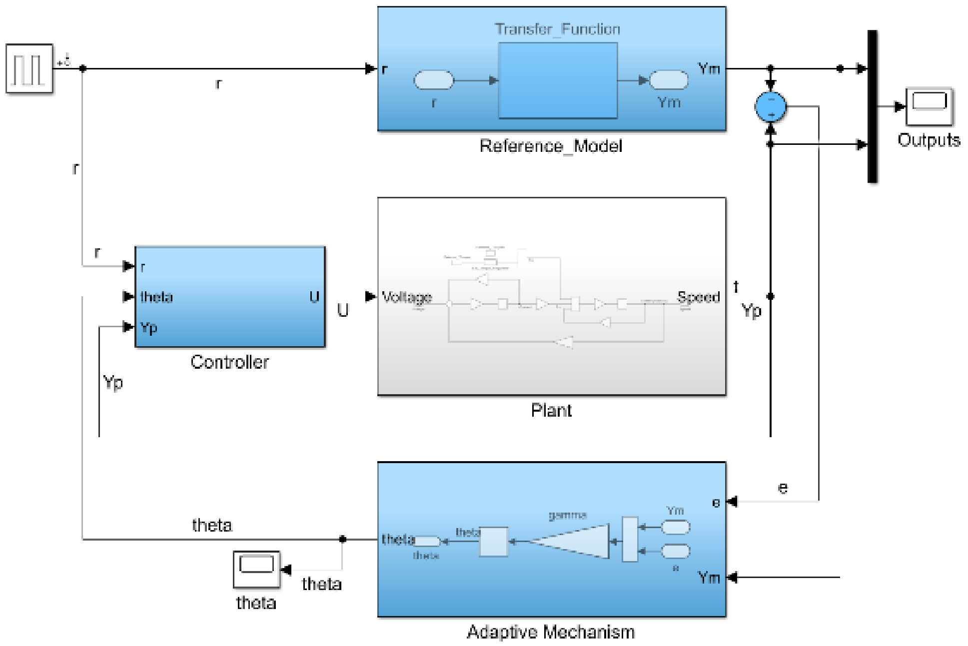

Figure 3. Adaptive control model

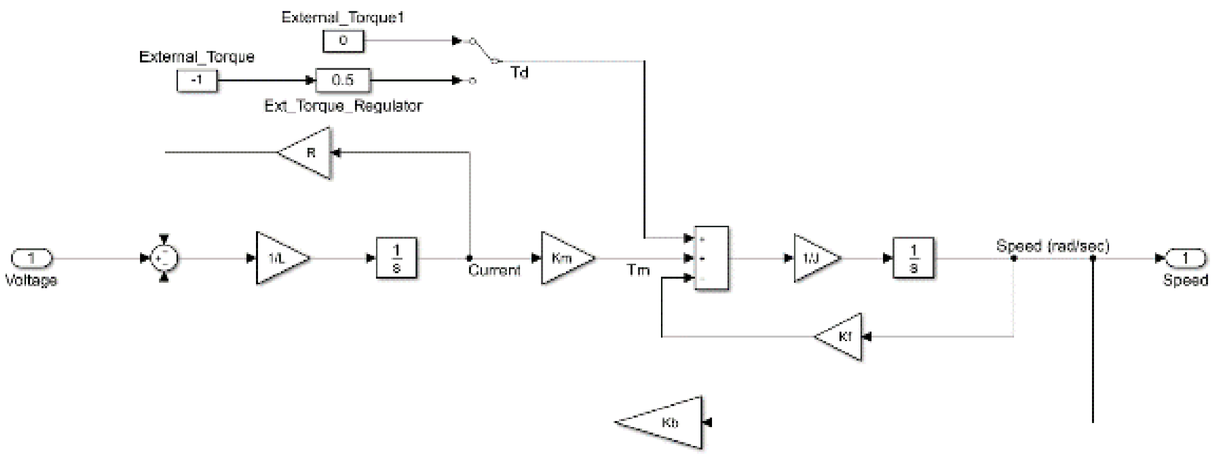

Figure 4. Enlarged engine signal fragment

3.) Adaptive controller: there are two subcomponents of this controller.

a. PID-regulator: this part of the controller isfixed, and the amplifications are configured to preserve theoriginal state and to achieve overall stability.

b. Adaptive mechanism: This is the purpose of this part of the controller to change its output signal (theta) based on error (e) between output (Yp) and the output of the reference model (Ym). The release of the controller (U) is calculated according to the formula: U q Uc q theta.

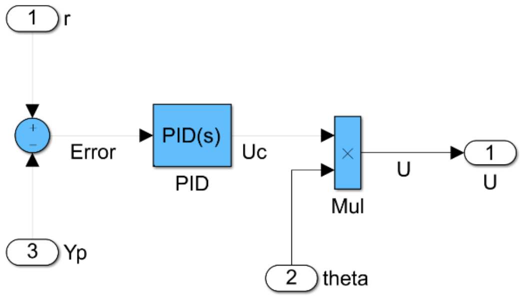

Figure 5. Management of PID regulator

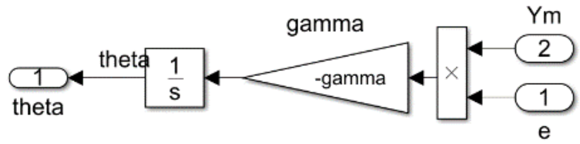

Figure 6. Adaptive mechanism

Workspace

Name	Value
B	0.2000
gamma	0.1000
J	0.0200
Kb	0.0150
Kc	1
Kf	0.2000
Km	0.0150
L	0.5000
out	1x1 SimulationO...
R	2

Figure 7. Control matrix

Launch this model with standard installation values, PID regulator and training speed. I'mnot sure that the entire closed system is generally in line with the reference model.

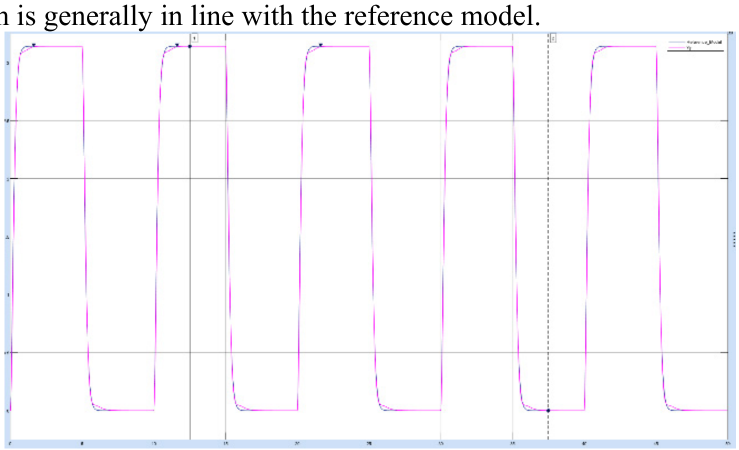

Figure 8. Output signal

How the controller adapts can be observed on the theta graph below. As you can see, theta goes from its initial value of 1 to 2.6 in 50 seconds and has not yet been exhausted. If you run the simulation log, theta will set at a slightly higher figure. 8.

The method of manufacturing additive products is characterized in that the outer casing is made based on ABS-M30, and the internal hardware fasteners are made of ABS-ESD7. The proportions vary between: 15–35% acrylonitrile, 5–30% butadiene and 40–60% styrene.

The method is characterized in that the outer casing is 80% of the mass of the structural element and 20% of the internal fasteners, which ensures electrical protection of the components.

This method involves the use of a 3D scanner to create an accurate 3D model of the product for which a housing is required.

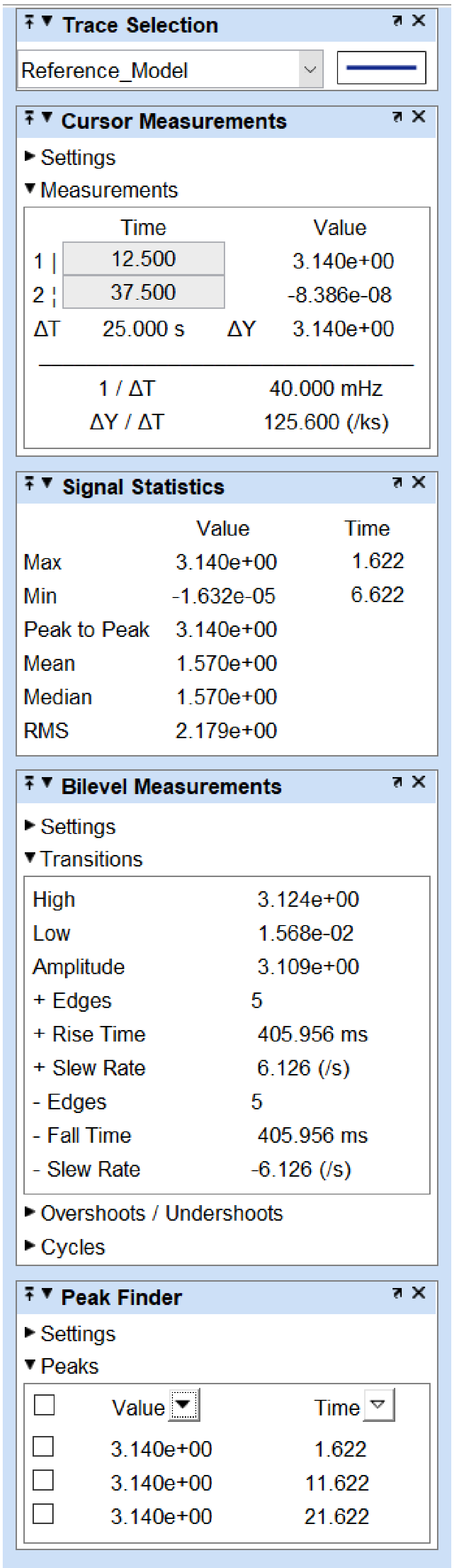

Figure 9. Control settings

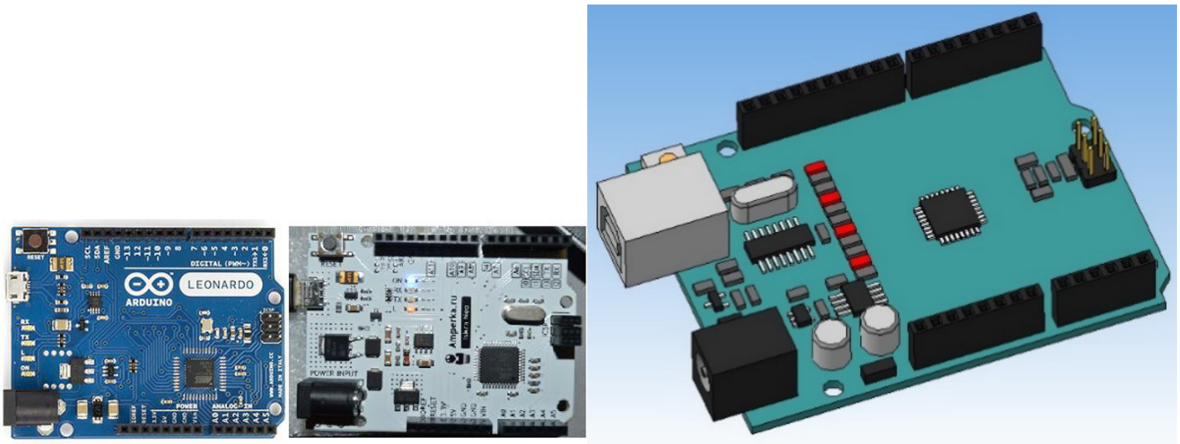

Figure 10. Designing additives

When combining ABS-M30 and ABS-ESD7 with antistatic properties, mechanical resistance and electrostatic protection of REA components are ensured. An additive product, characterized in that it is created on the basis of MPN technology using a combined printing method in a ratio of 80% and 20%, respectively. Additive product, characterized in that it is created without the use of molds and surfaces are smoothed using an acetone bath.

Stages of manufacturing a batch of housing elements for electronics:

1. The receipt of the technical specifications for the development and manufacture of additive products, which consists of four elements, the material for the body is rigid and durable.
2. Creation of technological design and design.

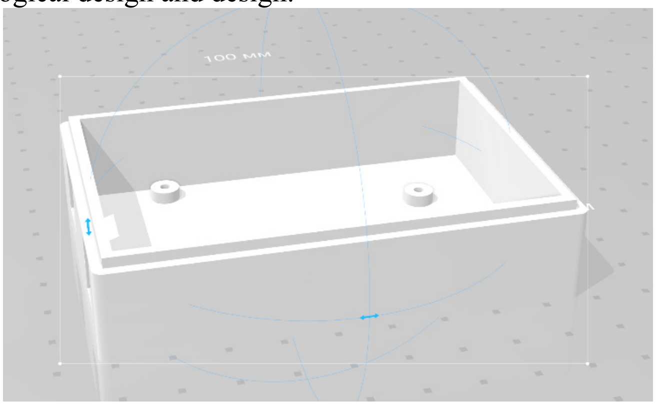

Figure 11. Design of additive products

3. Starting the process of printing products using the technology of manufacturing additive products.
4. Cleaning the product Figure 12.

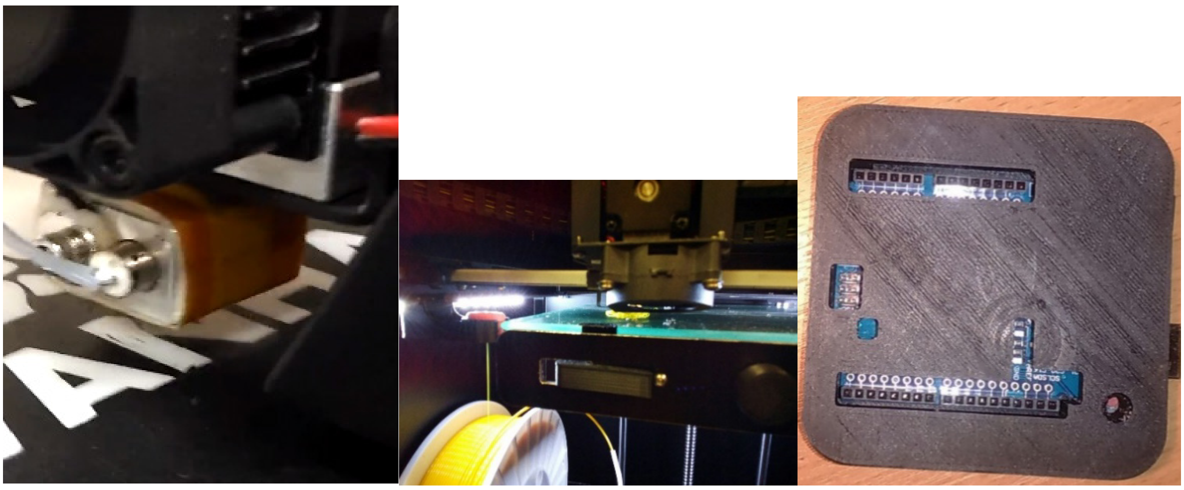

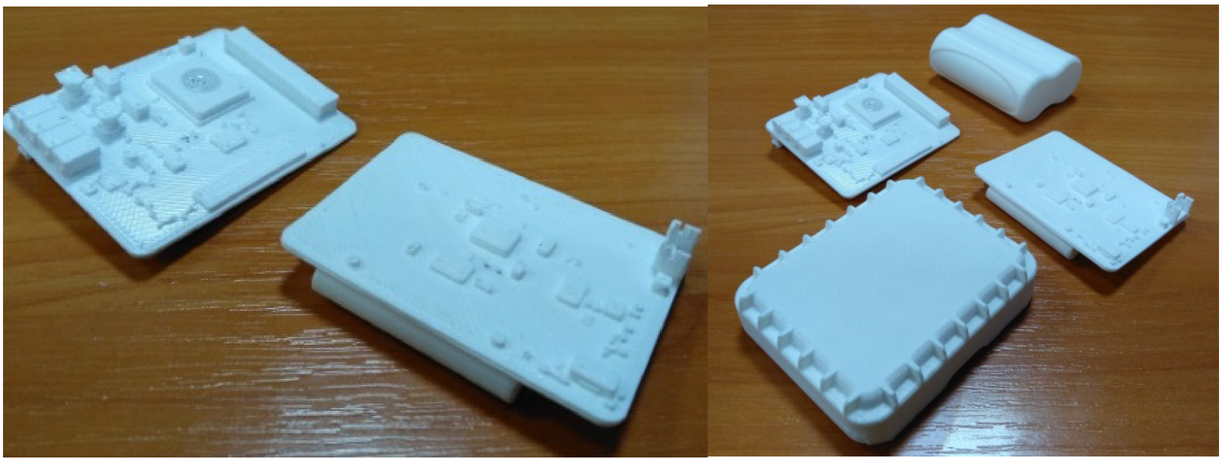

Figure 12. Ready element and prototyped component base

Conclusion

The application of this technology allows to improve the quality of products manufactured using additive technologies in small-scale production and to simulate still designed plants.

List of used literature

1. Семенова Е. Г., Чабаненко А. В., Назаревич С. А. Выявление ключевых показателей качества технологиического процесса производства корпуса РЭА на основе FDM РАДИОПРОМЫШЛЕННОСТЬ Вопросы радиоэлектроники. М. № 4. 2017. С. 53-59.
2. Quality Assurance of Hull Elements of Radio-Electronic Equipment by Means of Control System / Chabanenko, A.V., Anatoly P.Y. IEEE International Conference. 2018.
3. Electrodynamic analysis of materials for the antenna elements Chabanenko, A., Frolova, E., Balashov, V., Smirnova, M. 2018 IOP Conference Series: Materials Science and Engineering.
4. Construction of mathematical model of training and professional development of personnel support of additive production of rea Chabanenko A.V., Kurlov A.V. В сборнике: IOP Conference Series: Materials Science and Engineering International Workshop "Advanced Technologies in Material Science, Mechanical and Automation Engineering – MIP: Engineering – 2019". Krasnoyarsk Science and Technology City Hall of the Russian Union of Scientific and Engineering Associations. 2019. С. 32041.
5. Developing intelligent decision support systems in multi-criteria problems of administrative-territorial formations infrastructure projects assessment Batkovskiy, A.M., Nesterov, V.A., Semenova, E.G., Sudakov, V.A., Fomina, A.V. 2017 Journal of Applied Economic Sciences
6. Обеспечение качества аддитивного производства посредством системы контроля послойного синтеза / А.В. Чабаненко, Е.Г. Семенова, В.О. Смирнова, А.О. Смирнов, Н.Н. Рожков // Вопросы радиоэлектроники. 2018. №10. С. 75-79.
7. Управление качеством аддитивных изделий / А. В. Чабаненко // РИА: Журнал.: «Стандарты и качество». 2018. №2. С. 90-94.

ACCOUNTING FOR ELECTROMAGNETIC WAVES SCATTERING IN THE ANGULAR AREAS DURING FORMATION OF THE MULTIPATH COMMUNICATION CHANNEL FREQUENCY CHARACTERISTICS

Kryachko Alexander

Saint-Petersburg State University of Aerospace Instrumentation
67, Bolshaya Morskaya str., Saint Petersburg, 190000, RUSSIA
alex_k34.ru@mail.ru

Abstract
Intensive development of radio technical equipment for transmitting discrete messages caused a spectral resources shortage, increasing of transmitted information volume, and the quality of message transmission requirements. In this regard, solving the problem of receiving signals with a high energy spectrum decline rate while ensuring the necessary reliability of receiving messages increases is very actual. Using atomic functions to build spectral-efficient signals makes it easy to form orthogonal sequences similar to Walsh functions. Energy concentration in the band and the out-of-band emissions rate decay can be easily defined with such functions. Inter-symbol interference injection leads to the peak-factor value decrease, that is very important in radio systems with limited energy resources. Orthogonal frequency-division multiplexing (OFDM) and spatial (MIMO) diversity, that are the most important directions in the development of new generation mobile communication technologies, potentially provides an approximation of their spectral efficiency to the Shannon limit. However, further evolutionary development of cellular systems with multiple antennas and OFDM is impossible without maximum utilization of all available resources like time, frequency spatiotemporal and polarization signal processing along with error-correcting coding. These steps necessary for a transmitted power minimization and, at the same time, increase the capacity of the communication system by adapting it to the state of the radio channel.
Keywords – OFDM, WiMAX, MIMO.

Introduction

Mobile communication technologies changes are the most evident in changes of radio interfaces, where fundamental differences are clearly seen.

Orthogonal frequency-division multiplexing (OFDM) and spatial (MIMO) diversity, that are the most important directions in the development of new generation mobile communication technologies, potentially provides an approximation of their spectral efficiency to the Shannon limit.

However, further evolutionary development of cellular systems with multiple antennas and OFDM is impossible without maximum utilization of all available resources like time, frequency spatiotemporal and polarization signal processing along with error-correcting coding. These steps necessary for a transmitted power minimization and, at the same time, increase the capacity of the communication system by adapting it to the state of the radio channel.

Currently, active-passive antenna modules have appeared on the market that combine passive and active phased antenna arrays.

The passive part replaces the existing 2g and 3g operator antennas, while the active part makes it possible to solve the task of adaptive space-time and polarization processing of 4g systems, significantly improving the SINR.

Using such antenna systems can be implemented adaptive antenna arrays for base stations of new generation communication systems.

Focusing on such antenna systems, it is necessary to develop algorithms for adaptive space-time and polarization signal processing, which ensure the formation of the maximum of the DP in the direction of the useful signal, the determination of the direction to interference and its deep suppression.

Thus, an actual scientific problem is to improve a quality of mobile communication based on the new adaptive modulation methods development and signal processing in the space-frequency and space-time channels of mobile communication systems of new generations from MIMO and OFDM.

FUNDAMENTALS OF THE ATOMIC FUNCTIONS THEORY USAGE FOR THE SPECTRAL-EFFECTIVE SIGNALS CONSTRUCTION.

It is required to solve a problem of spectral-effective signals creation with a given rate of spectral decay outside the occupied band with a high concentration of energy within the occupied frequency band.

In general, it is necessary to select such time functions $\varphi_k(t)$, that with expression $\sum_{k=1}^{N} C_k \varphi_k(t)$ it was possible to provide a given rate of decay of the spectrum outside the occupied band.

Linear combinations of $\varphi_k(t)$ functions should bring the synthesized signal spectrum to the required speed with the highest possible in theory speed, i.e. have the property of approximation universality. This imposes certain requirements on the choice of functions class.

The solution to this problem can be obtained on the basis *R*-mappings theory [1], that describes construction of local class functions C^∞, possessing at the same time properties of polynomials and splines. Such functions are called atomic.

The rate of the out-of-band emission level decay for signals based on polynomials $\gamma-$degree of the final duration will decrease in proportion $C/\omega^{\gamma+1}$, if all derivatives of the signal envelope down to the derivative $(\gamma-1)$ degree has no jumps, but $\gamma-$degree derivative is finite everywhere [2].

In turn, the degree splines $\gamma-$ are functions, that are "piecewise" polynomials of degree γ, and in the nodes to pair till $(\gamma-1)-$degree derivatives.

Atomic functions are finite and represent a solution of a differential equation of the form:

$$y^{(n)}(t)+a_1 y^{(n-1)}(t)+\ldots+a_{n-1}y'(t)+a_n y(t)=\sum_{k=1}^{N} C_k y(at-b_k) \qquad (1)$$

The simplest and most important atomic functions are composed of infinite convolutions of rectangular pulses.

To research such convolutions, it is necessary to use the Fourier transform apparatus.

Using the Fourier transform, a rectangular pulse can be represented in the following form (as is well known, its spectrum has the form of $\sin x/x$)

$$\varphi(t)=\frac{1}{2\pi}\int_{-\infty}^{\infty} e^{jut}\frac{\sin(u/2)}{u/2}du .$$

$N-$ multiple convolution of $(N+1)$ identical square pulses $\varphi(t)$ is a finite spline $\theta_N(t)$.

In order to obtain a continuous finite function, the convolution of variable length pulses $\varphi_n(t)$ can be used (fig. 1).

In order to obtain even smoother functions, this process can be repeated, and to obtain an infinite smooth functions, it must be repeated an infinite number of times. The carrier of such an infinite convolution to be finite, we need to take convolutions of contractions of such functions $\varphi_1(t)*\varphi_2(t)*\ldots*\varphi_n(t)*\ldots$ so that to meet a series $\sum_{n=1}^{\infty} a_n<+\infty$. The simplest convergent series is the sum of an infinitely decreasing geometric progression with the denominator 2. Thus, the result of such an infinite convolution is a new finite function defined on the interval $[-1;1]$. It can be easy shown that it satisfies equation (0.1) in the simplest form

$$y'(t)=2y(2t+1)-2y(2t-1),$$

with conditions $\mathrm{supp}=[-1,1]$, $y(-1)=y(1)=0$, $y(0)=1$. Consider the Fourier transform of both sides of the simplest equation:

$$\int_{-\infty}^{\infty}\exp[i\lambda t]y'(t)dt=a\left[\int_{-\infty}^{\infty} y(2t+1)e^{i\lambda t}dt-\int_{-\infty}^{\infty} y(2t-1)e^{i\lambda t}dt\right].$$

$$\varphi_n(t)=\begin{cases}2^{n-1}, & |t|\le 2^{n-1}\\ 0, & |t|>2^{n-1}\end{cases}$$

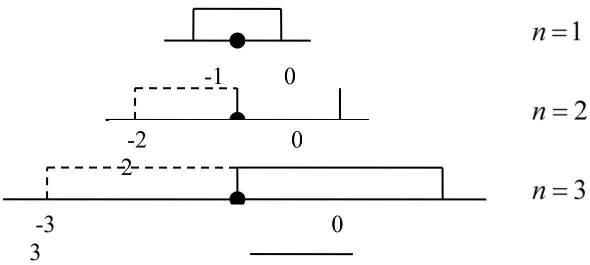

Figure 1 – Variable length pulse convolution

Then

$$-i\lambda\int_{-\infty}^{\infty}e^{i\lambda t}y(t)\,dt=\frac{a}{2}\left[\int_{-\infty}^{\infty}y(u)e^{\frac{i\lambda(u-1)}{2}}du-\int_{-\infty}^{\infty}y(u)e^{\frac{i\lambda(u+1)}{2}}du\right].$$

We can write that:

$$F_y(\lambda)=aF_y\left(\frac{\lambda}{2}\right)\frac{\sin\left[\frac{\lambda}{2}\right]}{\lambda},\tag{2}$$

where $F_y(\lambda)$ - is entire function. Formula (2) was obtained in [3] (Theorem 6). By decomposing the right and left side of this expression into a power series and equating the coefficients at the same powers λ, we get $a=2$. Then

$$F_y(0)=\int_{-1}^{1}y(t)dt=y(0)=1.$$

From here for $F_y^{(n)}(0)$ the recurrence formula is obtained

$$F_y^{(n)}(0)=\frac{n!}{2^n-1}\sum_{k=1}^{[0.5n]}(-1)^k\frac{F_{y(0)}^{(n-2k)}}{(n-2k)!(2k+1)!}.$$

There is no more than one solution of equation (1) with the specified boundary conditions. In article [3], the existence of such solution was proved and it is defined as a function $up(t)$ and using a representation based on the Fourier transform - $F(up(t))=\prod_{k=1}^{(n)}\frac{\sin\frac{u}{2^k}}{\frac{u}{2^k}}$, we have

$$up(t)=\frac{1}{2\pi}\int_{-\infty}^{\infty}e^{iut}\prod_{k=1}^{\infty}\frac{\sin\left(u2^{-k}\right)}{u2^{-k}}du\tag{3}$$

Distinctive features of atomic functions are: analyticity; the combination of the finiteness of a function with a rapid decrease (faster than any degree) of its Fourier transform; an explicit connection of the derivatives with the function itself, as well as an explicit expression for the spectrum.

NUMERICAL METHOD FOR FINDING ATOMIC FUNCTIONS

In the numerical solution of expression (3), it is necessary to determine the number n of the products that provides the specified standard deviation of the resulting function $a(t)$ from the true value obtained by the exact solution of the problem.

As an example, we consider the numerical solution of the problem to find the values of a function $up(t)$ for different values of n.

$n=3$:

$$up(t)=\frac{1}{2\pi}\int_{-\infty}^{\infty} e^{iut}\left(\begin{array}{c}\frac{\sin(0.5u)}{0.5u}\cdot\frac{\sin(0.25u)}{0.25u}\times\\ \times\frac{\sin(0.125u)}{0.125u}\end{array}\right)du=\frac{1}{2\pi}\int_{-\infty}^{\infty} e^{iut}\frac{\sin(0.5u)\cdot\sin(0.25u)\cdot\sin(0.125u)}{0.015625u^3}du$$

$n=4$:

$$up(t)=\frac{1}{2\pi}\int_{-\infty}^{\infty} e^{iut}\left(\begin{array}{c}\frac{\sin(0.5u)}{0.5u}\cdot\frac{\sin(0.25u)}{0.25u}\times\\ \times\frac{\sin(0.125u)}{0.125u}\cdot\frac{\sin(0.0625u)}{0.0625u}\end{array}\right)du=\frac{1}{2\pi}\int_{-\infty}^{\infty} e^{iut}\frac{\left(\begin{array}{c}\sin(0.5u)\cdot\sin(0.25u)\times\\ \times\sin(0.125u)\cdot\sin(0.0625u)\end{array}\right)}{0.000976562u^4}du$$

and etc.

On fig. 2 are shown the values of the standard deviation of the function $up(t)$ depending on value of n. The values of the standard deviation for different n are conventionally connected by dotted lines. Forms of function $a(t)$ for n=2, 3, 4, 5, 6, 8 are shown on fig. 3.

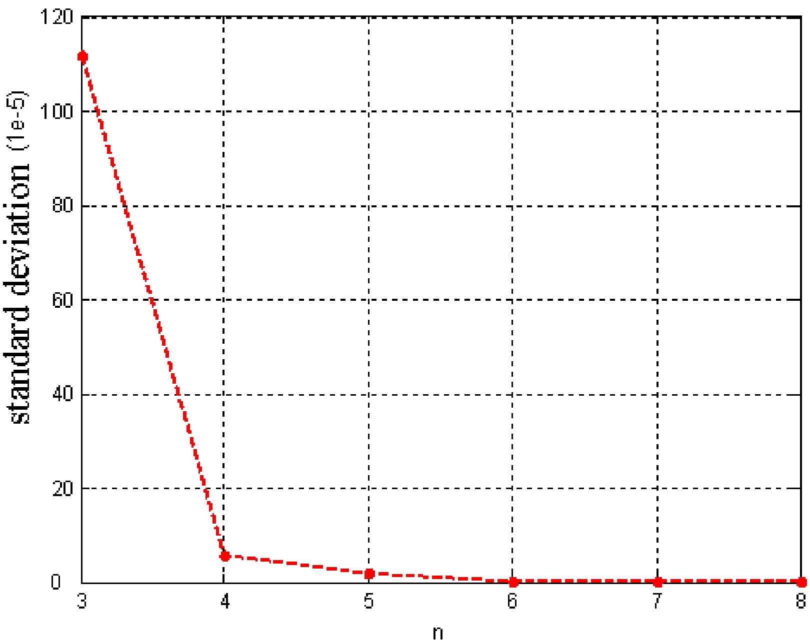

Figure 2 – The dependence of the standard deviation of the function $up(t)$, obtained by a numerical method for different values of n

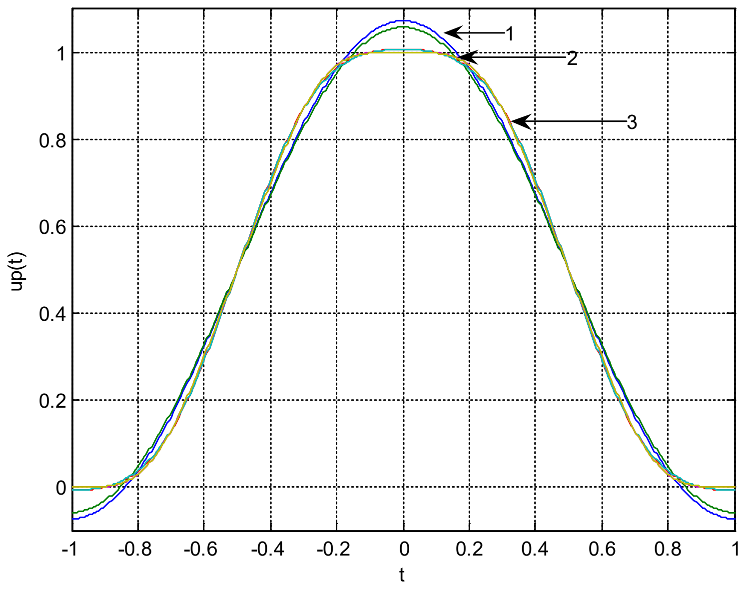

Figure 3 – View of function $up(t)$ with a numerical solution for $n = 2$ (line 1), $n = 3$ (line 2) and for $n = 4,5,6,8$ (line 3)

It is advisable to use the method of determining the number *n*, which consists in the fact that the standard deviation is determined between two calculated functions *a(t)*, have an adjacent numbers *n* and *n*+1:

$$\varepsilon(m) = \overline{\left|a_m(t) - a_{m-1}(t)\right|^2}$$

Selection of the standard deviation admissible value of the functions shape $up(t)$ defined, mainly, by the tolerance of the energy spectrum shape of a synthesized signals random sequence. Indeed, when choosing a limited number *n* of multiplication members to build optimal signals the level of out-of-band emissions increases. In this regard, it is advisable to determine the allowable number n, starting with specifying the allowable increase in the level of the energy spectrum outside the occupied frequency band. This is the essence of the proposed numerical method for solving the problem of finding the envelope shape and assessing the accuracy of its solution.

The calculation results show that for $n \geq 6$ side-lobe attenuation level is about 50 dB. Starting from $n = 10$, the accuracy of the calculation compared with the theoretical results has an 10^{-30} error.

When calculating the real characteristics and parameters of mobile communication systems, it is necessary to take into account the spectral properties of signals.

For this purpose, the energy of an electromagnetic wave per unit flat surface located at the receiving point perpendicular to the direction of wave propagation is introduced into consideration [4].

$$W_2 = \int_{t_{\text{int}1}}^{t_{\text{int}2}} \Pi_2(t)dt = \int_{t_{\text{int}1}}^{t_{\text{int}2}} E_2(t)H_2(t)dt \tag{4}$$

where $t_{\text{int}1}$ and $t_{\text{int}2}$ - are moments of time, corresponding to the appearance and disappearance of the signal at the point of reception; E_2, H_2 – are instantaneous values of the electric and magnetic field at the receive point; Z_0 – is a propagation wave impedance.

Let's suppose the signal propagates in a vacuum. Then $Z = Z_0$. In turn, the instantaneous values of the electric and magnetic fields strengths can be represented as follows:

$$E_2(t) = f_2(t)E_{02} \tag{5}$$

$$H_2(t) = f_2(t)H_{02} = f_2(t)\frac{E_{02}}{Z_0} \tag{6}$$

where $f_2(t)$ – is a function that determines the law of change in signal at the point of reception. Its maximum value is one; E_{02}, H_{02} is maximum of field strength.
Further written in the form of Fourier integrals:

$$E_2(t) = \frac{1}{2\pi}\int_{-\infty}^{+\infty} \dot{E}_2(i\omega)e^{i\omega t}d\omega \tag{7}$$

$$H_2(t) = \frac{1}{2\pi}\int_{-\infty}^{+\infty} \frac{\dot{E}_2(i\omega)}{Z_0}e^{i\omega t}d\omega \tag{8}$$

$\dot{E}_2(i\omega)$ – is spectral density of function $E_2(t)$.

Substituting the expression (7, 8) in (4) after simple transformations we obtain:

$$W_2 = \frac{1}{2\pi}\int_{-\infty}^{+\infty} \dot{E}_2(i\omega)\frac{\dot{E}_2(i\omega)}{Z_0}e^{i\omega t}d\omega = \frac{1}{2\pi Z_0}\int_{-\infty}^{+\infty} |\dot{E}_2(i\omega)|^2 d\omega \tag{9}$$

In accordance with the frequency method [5], the solution of the problem can be represented as

$$\dot{E}_2(i\omega) = \dot{E}_1(i\omega)K(i\omega) \tag{10}$$

where $\dot{E}_1(i\omega)$ is electric field spectral density at a point with the coordinates of the communication system; $K(i\omega)$ – is a frequency response of the current electrodynamic system.

Function $f_1(t)$ reflects the law of the electric field change with time (maximum value of $f_1(t)$ is 1). If the value of E_0 characterizes the amplitude of the electric field, then we can write the following equality:

$$E_1(t) = f_2(t)E_0 \tag{11}$$

Frequency response $K(i\omega)$ can be determined from the solution of diffraction problem of a flat electromagnetic wave with a complex amplitude of the electric field strength in a real communication channel in the steady-state harmonic mode. This solution is considered to be known.

Given the above expression (10) can be rewritten as follow:

$$\dot{E}_2(i\omega) = \dot{E}_1(i\omega)K(i\omega) = F_1(i\omega)E_0K(r,\theta,\varphi,i\omega) \tag{12}$$

Where

$$F_1(i\omega) = \int_{t_{\text{int}1}}^{t_{\text{int}2}} f_1(t)e^{-i\omega t}dt \tag{13}$$

$F_1(i\omega)$ – is a spectral density of function $f_1(t)$; $t_{\text{int}1}$ and $t_{\text{int}2}$ - moments of time, corresponding to the beginning and end of the emitted signal.

Substituting the expression (12) in (9) we can write:

$$W_2 = \frac{1}{2\pi Z_0}\int_{-\infty}^{+\infty} |F_1(i\omega)|^2 |K(r,\theta,\varphi,i\omega)|^2 |\dot{E}_0|^2 d\omega$$

$$\frac{1}{2\pi}\int_{-\infty}^{+\infty} \dot{E}_2(i\omega)\frac{\dot{\bar{E}}_2(i\omega)}{Z_0}e^{i\omega t}d\omega \tag{14}$$

It is easy to conclude that $\dot{E}_0$, $K(r,\theta,\varphi,i\omega)$ represents a complex amplitude at the receiving point for harmonic mode.

In this case Π_1, Π_2, can be rewritten as:

$$\Pi_1 = \frac{1}{2Z_0}\left|\dot{E}_0\right|^2 \tag{15}$$

$$\Pi_2 = \frac{1}{2Z_0}\left|\dot{E}_0\right|^2 \left|K(r,\theta,\varphi,i\omega)\right|^2 \tag{16}$$

This shows that the flux density of electromagnetic energy at the point of reception depends both on the spectrum of the signal in the actual communication channel and on the magnitude of the communication channel transfer characteristic at various frequencies within a given width of the spectrum.

Orthogonal frequency-division multiplexing (OFDM) and spatial (MIMO) diversity usage in modern and promising mobile communication systems potentially provides a significant improvement in their spectral efficiency to a value close to the Shannon limit. However, the implementation in practice of potentially high rates of communication quality in real conditions of a multipath broadband channel with variable parameters in the clock and frequency domains is not possible without adaptation to real conditions signal propagation [6]. Naturally, such an adaptation is possible only on the basis of properties and characteristics knowledge of the communication channel changes in the parameters in the clock and frequency domains, that is, its impulse and frequency characteristics, as well as their correlation properties.

In most cases, electromagnetic waves come to the receiving point as a result of multiple reflections from different scattering objects on the propagation path, which creates a complex multipath interference pattern at the receiving point. The multipath nature of radio wave propagation causes fluctuations of amplitude, initial phase and angle of signal arrival at the point of reception. In addition, the propagation paths can be non-stationary in nature, which is most often due to the mutual movement of the UE, or other objects relative to the BS (for example, people, cars, etc.). Even a small slow movement leads to a change in time of the multipath propagation conditions and, as a result, changes in signal parameters. A s a result, the impulse response *h* (τ, *t*) multipath channel will experience significant changes (fig. 4).

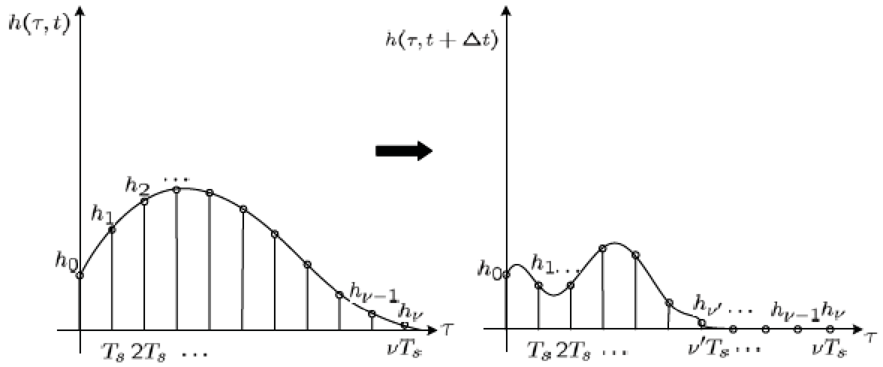

a *b*

Figure 4 – Channel impulse response change

The model that quite sufficiently describes such a channel at discrete points in time is the delay line (DL) with taps and characteristics [6]:

$$\dot{h}(t) = \sum_{r=1}^{R} \dot{h}(r,t) = \sum_{r=1}^{R} \dot{h}_r(t)\delta\left(t - \tau_r(t)\right) + n(t) \tag{17}$$

where $\dot{h}_r(t)$ – is a complex attenuation coefficient in *r* ray; $\tau_r(t)$ – is a propagation delay in *r* ray; $n(t)$ – is an additive white Gaussian noise.

For stationary multipath channels, the parameters of which slowly vary over time, we can assume $\dot{h}_r(t) = \dot{h}_r$, $\tau_r(t) = \tau_r = r/c$. In this case, the signal $y(t)$ at the output of the multipath channel can be found as the convolution of the transmitted signal $x(t)$ with channel impulse response $\dot{h}(t)$.

$$y(t) = x(t)\sum_r \dot{h}_r x(t - \tau_r) + n(t) \tag{18}$$

The frequency response of a multipath channel can be determined based on the use of the Fourier transform of the impulse response (17):

$$H_k = \sum_r h_r \exp\left(\frac{-j2\pi k\tau_r}{T_s N}\right) \tag{19}$$

where T_s – is a symbol duration.

In accordance with the frequency method [5], the solution of the determining frequency response in the communication channel in the presence of angular regions problem should be sought as the result of the inverse Fourier transform of the product of the propagating signal spectral density and the impedance wedge frequency response [7]:

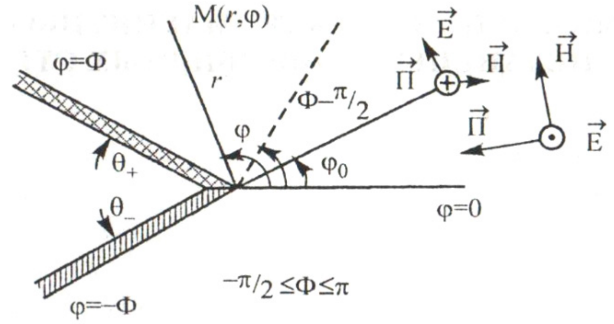

Figure 5 – Task geometry: Φ- angle of wedge opening, φ- angle of the incident wave arrival, M- observation point with polar coordinates (r, ϕ_0).

$$\dot{H}(t) = \frac{1}{2\pi}\int_{-\infty}^{+\infty} \dot{F}(i\omega)\dot{H}_z(\omega,\varphi,r)\exp[i\omega t]d\omega \tag{20}$$

Where

$$\dot{F}(i\omega) = \int_{-\infty}^{+\infty} S(t)\exp[-i\omega t]dt \tag{21}$$

— is an incident signal spectral density, and $\dot{H}_z(\omega,\varphi,r)$ - is a solution to this problem for the case of harmonic oscillations [7].

For the case of E-polarization, the solution is written similarly:

$$\dot{H}(t) = \frac{1}{2\pi}\int_{-\infty}^{+\infty} \dot{F}(i\omega)\dot{E}_z(\omega,\varphi,r)\exp[i\omega t]d\omega \tag{22}$$

where $\dot{E}_z(\omega,\varphi,r)$ - is a solution to this problem for the case of harmonic oscillations.

Considering the above, the solution for the case of diffraction of a non-harmonic pulse on an impedance wedge can be written as follows:

$$\dot{H}_z^{PL}(\varphi,r,t) \cong \frac{1}{2\pi}\int_{-\infty}^{+\infty} \dot{F}(i\omega)\left[\dot{H}_{z\ DIF}^{CYL} + \dot{H}_{z\ INC}^{PL} + \dot{H}_{z\ REF+}^{PL} + \dot{H}_{z\ REF-}^{PL} + \dot{H}_{z\ SUR\pm}^{PL}\right]\exp(i\omega t)d\omega \tag{23}$$

Based on the integration properties (23) can be rewritten as:

$$\begin{gathered}\dot{H}_z^{PL}(\varphi,r,t) \cong \frac{1}{2\pi}\int_{-\infty}^{+\infty} \dot{F}(i\omega)[\dot{H}_{z\ DIF}^{CYL}e^{i\omega t}]d\omega + \frac{1}{2\pi}\int_{-\infty}^{+\infty} \dot{F}(i\omega)[\dot{H}_{z\ INC}^{PL}e^{i\omega t}]d\omega + \\ +\frac{1}{2\pi}\int_{-\infty}^{+\infty} \dot{F}(i\omega)[\dot{H}_{z\ REF+}^{PL}e^{i\omega t}]d\omega + \frac{1}{2\pi}\int_{-\infty}^{+\infty} \dot{F}(i\omega)[\dot{H}_{z\ REF-}^{PL}e^{i\omega t}]d\omega + \frac{1}{2\pi}\int_{-\infty}^{+\infty} \dot{F}(i\omega)[\dot{H}_{z\ SUR\pm}^{PL}e^{i\omega t}]d\omega\end{gathered} \tag{24}$$

For E polarization case:

$$\dot{E}_z^{PL}(\varphi,r,t) \cong \frac{1}{2\pi}\int_{-\infty}^{+\infty}\dot{F}(i\omega)[\dot{E}_{z\ DIF}^{CYL}e^{i\omega t}]d\omega + \frac{1}{2\pi}\int_{-\infty}^{+\infty}\dot{F}(i\omega)[\dot{E}_{z\ INC}^{PL}e^{i\omega t}]d\omega + \\ +\frac{1}{2\pi}\int_{-\infty}^{+\infty}\dot{F}(i\omega)[\dot{E}_{z\ REF+}^{PL}e^{i\omega t}]d\omega + \frac{1}{2\pi}\int_{-\infty}^{+\infty}\dot{F}(i\omega)[\dot{E}_{z\ REF-}^{PL}e^{i\omega t}]d\omega + \frac{1}{2\pi}\int_{-\infty}^{+\infty}\dot{F}(i\omega)[\dot{E}_{z\ SUR\pm}^{PL}e^{i\omega t}]d\omega \tag{25}$$

If the spectral width of the signal transmitted over the channel is less than the coherence band $B_s = |f_1 - f_2| \le B_c$, then all spectral components of the signal vary approximately equally, and such fading is common.

Information on the dynamics of change in the transmission coefficient is provided by the correlation function or the nature of the change in the spectral power density fluctuations of this coefficient. This means that for analyze and synthesize of mobile communication systems adaptive signal processing, information is needed on the magnitude and nature of changes in the complex transmission coefficient $\dot{h}(\tau,t)$ or complex channel transfer function [6]:

$$\dot{H}(f,t) = \int_{-\infty}^{\infty}\dot{h}(\tau,t)\exp(-j2\pi f\tau)d\tau \tag{26}$$

and their correlation properties in the time and frequency-time domains:

$$R_h(\tau) = \lim_{T\to\infty}\frac{1}{T}\int_0^T h(t)h(t+\tau)dt \tag{27}$$

$$R_l(\Delta f,\Delta t) = \int_{-\infty}^{\infty}R_h(\tau,\Delta t)\exp(-j2\pi\Delta f\tau)d\tau \tag{28}$$

Naturally, when solving specific problems of transmitting digital information, it is necessary to use a device of discrete transformations

REFERENCES

1. Kravchenko V.F. Spectral properties of atomic functions in problems of digital signal processing. Radio engineering and electronics, 2001, v.46, #5, p.534-552.

2. S.H. Mezon. G. Cimmerman. Electronic circuits, signals and systems: Translation from English./M.: Foreign literature publisher. 1963.

3. Rvachev V.L. R-functions theory and some of its application. Kiev, 1982. – 552p.

4. Ufimtsev P.Y. Theory of diffraction edge waves in electrodynamics. M.: Binomial. Laboratory of Knowledge, 2007.

5. Zernov N.V. The solution of non-stationary boundary value problems of electrodynamics // Report Academy of Sciences of the USSR. 1951. V. 30, #1. p. 33.

6. Bestugin A.R., Kryachko A.F., Kryachko M.A. Methods to improve the spectral efficiency of telecommunication systems based on approximation of the signal envelope by atomic functions. // News of universities. Radio electronics. Vol. 59 No. 11 (629) p. 38-50, 2014

7. Kryachko A.F., Lihachev V.M., Smirnov S.N, Stashkevich A.I. The scattering of electromagnetic waves theory in angular structures. SPb.: Science, 2009.

CLIMATE CONTROL MODEL OF A GREENHOUSE

Agnello Claudia Maria
Schembari Carola

Computer Engineering and Networks Laboratory – Kore University of Enna – Italy
Email: claudiamaria.agnello@unikorestudent.it
carola.schembari@unikorestudent.it

Abstract
This paper shows a proposal for the realization of a greenhouse intended for the cultivation of roses. In particular the project is based on the realization of a management system of air conditioning and automatic ventilation of a greenhouse, in order to develop and preserve an optimal environment for the growth of the roses themselves. To simplify the operations required, smart solutions, such as the use of wireless sensors and intelligent control of internal greenhouse conditions, are used. The project consists of two networks: one wireless and one wired.

INTRODUCTION

This document shows the realization of a system that automatically regulates the ventilation of a greenhouse, according to the internal conditions of the greenhouse itself, in order to create an optimal environment for the growth of the roses. The system consists of three wireless sensors, a gateway, a controller and a regulator. In the specific case, the sensors installed inside the greenhouse will be able, periodically, to evaluate the temperature, the percentage of humidity in the air and the brightness of the environment, allowing to create the best environment for an optimal vegetation care. The system permits monitoring of environmental conditions and the possibility to adjust them. In the future, this will allow to change the required parameters, in case of change of the type of plant to grow. Similar commercial solutions are widely used. Sensors for temperature, humidity and brightness detection are easily found in companies specializing in the sale of industrial equipment. Section II shows an overview of the main technologies on the market in the field of climate sensors. In the section III specifies the architecture implemented (wired/wireless), and the control and regulation methods in more detail. Section IV shows how the scenario is simulated with appropriate software. Section V shows the measured network performance, while the VI presents the final considerations on the proposed project.

RELATED WORKS

It is very easy to find similar systems already realized, both amateur and professional, because botany enthusiasts are often interested in the creation of small greenhouses, introducing smart components for easier monitoring of the environment.

For example, temperature measurement is one of the most popular automation technologies, present both in the domestic and industrial sectors, and for this reason there are different types of sensors on the market for this purpose. Measuring the percentage of humidity is also an important factor so its monitoring and management become necessary in optimizing processes. It may need to control humidity even in situations where a high percentage of humidity is favorable to process management, for example, inside greenhouses where humidity must be precise and controlled. So, it’s easy to find instruments, such as probes, humidity regulators and hygrostats that manage to detect and regulate humidity. Brightness detectors measure the intensity of lighting in an environment and their installation allows to monitor the intensity of the light.

Our system, similarly to the home-made greenhouses construction models, in which the main physical components are the sensors, while setting of the detected parameters depends on the skill of the programmer according to his needs.

THE PROPOSED APPROACH

As you can see from the pattern, the system consists of two networks: one wired and one wireless. The wireless network consists of four blocks: three wireless sensors for temperature, humidity and brightness detection and a gateway. The wired network consists of three blocks: the gateway, which is a hybrid component, a controller and a regulator. The result is a network with star topology, where the gateway works as the star center. The sensors send the measured values to a gateway through a wireless connection.

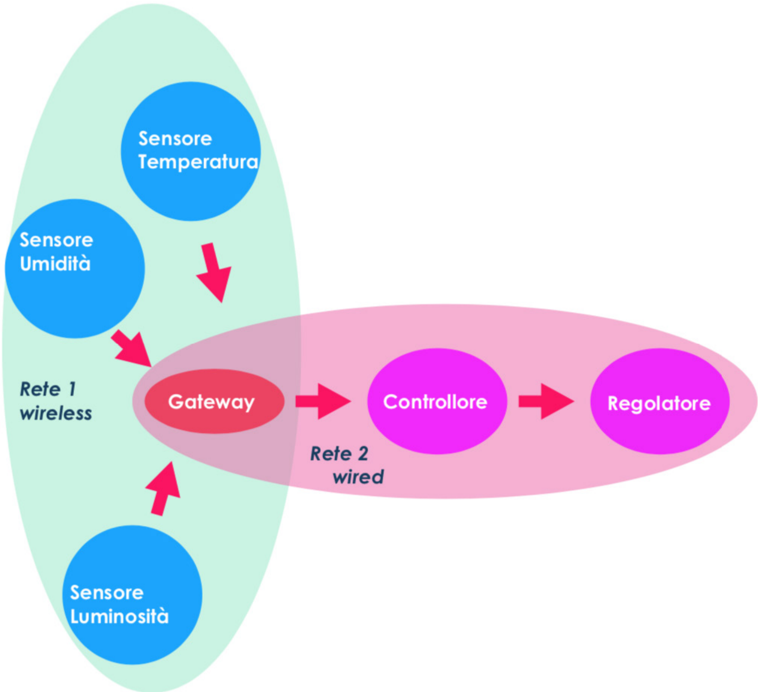

Figure 1: Network topology. Two networks: one wireless, which consists of three sensors and the gateway, and one wired, which consists of the gateway, the controller and the regulator. Nodes communicate through the gateway.

The gateway forwards the received values to a controller via wired connection (Ethernet). In the controller there is implemented a Fuzzy Logic where the inputs are the values measured by the sensors and through membership functions the ventilation of the greenhouse is measured. Finally, the controller sends the data to the controller, via wired connection. In addition to managing the air quality of the environment, in cases it is considered necessary, the controller activates the ventilation system, operated by a MBSD system.

SCENARIO

System has been simulated in Matlab/Simulink using TrueTime library.

IEEE 802.15.4 (ZigBee) is the protocol used in the wireless network, instead CSMA/CD (Ethernet) is the protocol used in wired network. In particular the ZigBee protocol is a wireless network standard that is mainly used for networks that require a low level of data flow and low power consumption. Instead, being the second network a wired network, the CSMA/CD protocol is used to avoid the collisions.

In this system soft computing techniques, such as Fuzzy Logic, are used to obtain an estimate of the greenhouse ventilation, and Model-Based Software Design (MBSD) technique for switching the ventilation system on/off.

Legend: Yellow subsystem is the gateway; Green subsystem is the controller; Red subsystem is the regulator; Shades of blue subsystems are the sensors: Blue is the temperature sensor; light blue is the humidity sensor; Violet is the brightness sensor.

As for the soft computing technique used, Fuzzy controller receives input parameters measured by sensors and generates the greenhouse's ventilation value as output, through member functions. These are generated by an appropriate combination of input parameters.

Fuzzy sets are based on characteristics of optimal environment, in our case for the cultivation of roses. The optimal ranges are:

- temperature between [15 – 25] °C
- percentage of humidity between [80 – 85] %
- intensity of lighting between [45 – 72] %.

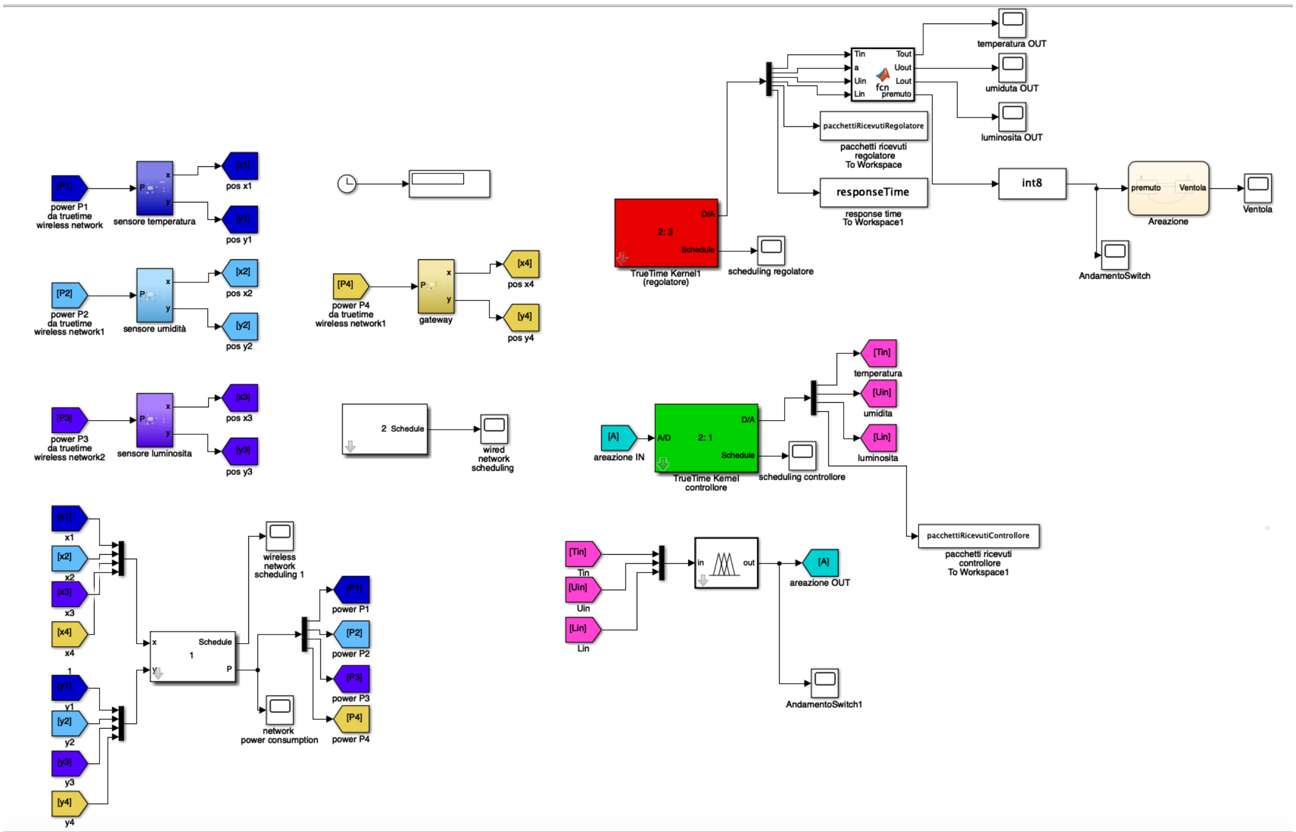

Figure 2 From up to down: sensors, TrueTime Wireless Network, clock, gateway, TrueTime Network, regulator, controller, Fuzzy Logic Controller. The gateway receives data from the sensors and send them to the controller that send data to the regulator.

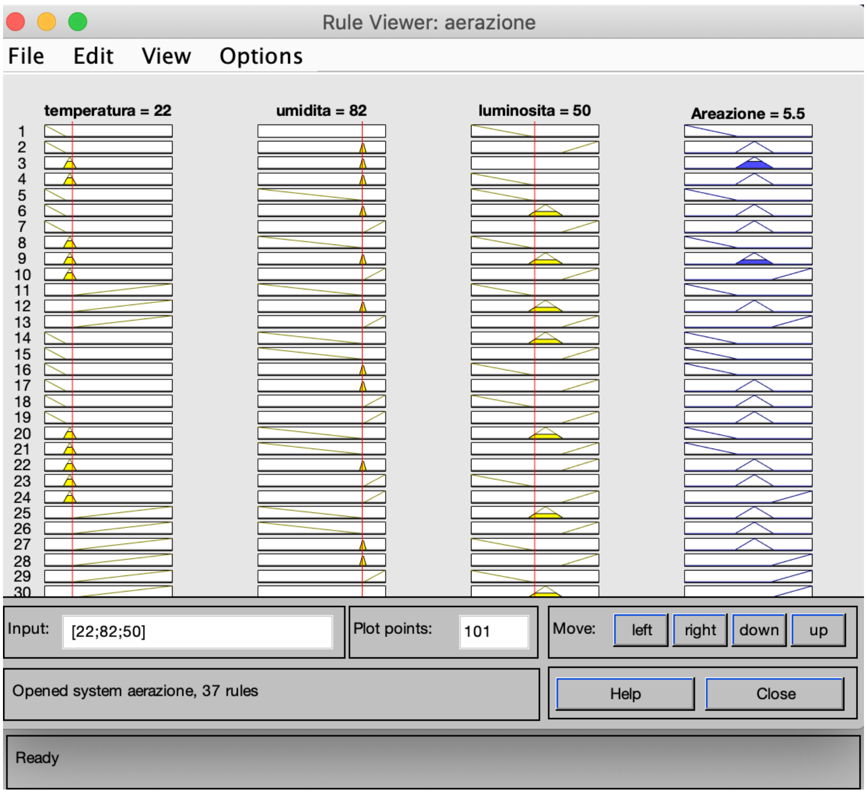

Figure 3 rule viewer of the Fuzzy logic controller

The combination of previous values generates output, whose optimal value is between [4 – 7].

MBSD system is used to manage the activation of the ventilation system: inside the state machine of the cooling fan you can control the ignition of the system:

- switching on (pressed==1)
- switching off (pressed==0)

Such states depend on parameter received at the input, that is the aeration of the system calculated by fuzzy.

Output is a signal that oscillates between 0 and 1 and that distinguishes respectively if the cooling fan is turned on or off.

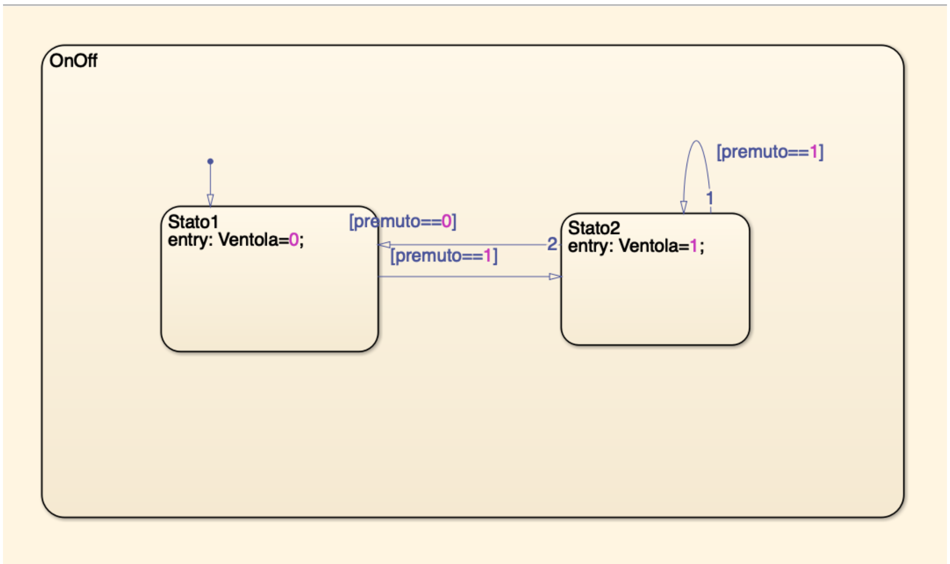

Figure 4 State model of the ventilation fan with an ON-OFF switch.

PERFORMANCE EVALUATION

Performance issues are very important in computer networks. In order to improve network performance, measurements must be carried out under different conditions.

The performance metrics measured in the system are:

- Response Time: is the interval between the user's request and the system's response
- Packet Loss.

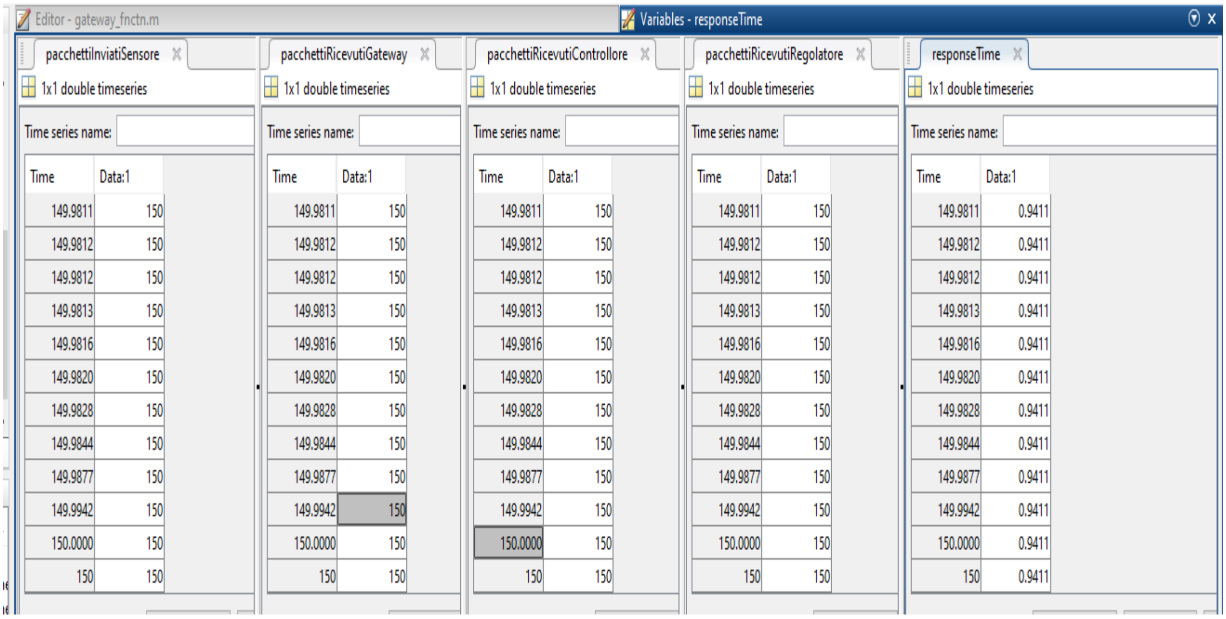

Time	pacchettiInviatiSensore Data:1	pacchettiRicevutiGateway Data:1	pacchettiRicevutiControllore Data:1	pacchettiRicevutiRegolatore Data:1	responseTime Data:1
149.9811	150	150	150	150	0.9411
149.9812	150	150	150	150	0.9411
149.9812	150	150	150	150	0.9411
149.9813	150	150	150	150	0.9411
149.9816	150	150	150	150	0.9411
149.9820	150	150	150	150	0.9411
149.9828	150	150	150	150	0.9411
149.9844	150	150	150	150	0.9411
149.9877	150	150	150	150	0.9411
149.9942	150	150	150	150	0.9411
150.0000	150	150	150	150	0.9411
150	150	150	150	150	0.9411

Figure 5 Performance metrics measured values. From left to right: packet sent to sensor, packet received by gateway, packet received by controller, packet received by regulator and Response Time

In order to better monitor the system, it has been chosen to measure these performances because it is believed that the knowledge of these values can be useful. In particular, the values of the response time for every sent package are saved in the workspace, as well as the number of packets sent by the sensor and received by each component such as, precisely, gateway, controller and regulator. In this way you can see how the response time varies in a range between [0.4 – 1.2] s.

As far as packet loss is concerned, multiple situations have been simulated and the packet loss rate is minimal in each scenario.

CONCLUSIONS

Simulations have been carried out for different periods of time.

In this case, are reported values obtained with a simulation lasting 150 seconds. In the graphs shown below it is possible to notice how the system regulates the temperature and humidity, to make them as close as possible to the desired ranges.

Our system does not modify the detected values of the brightness sensor; it is not considered necessary to include a brightness regulator, but it is useful to know these values since they affect the final temperature and humidity. It could be improved inserting brightness regulator, if it is considered necessary.

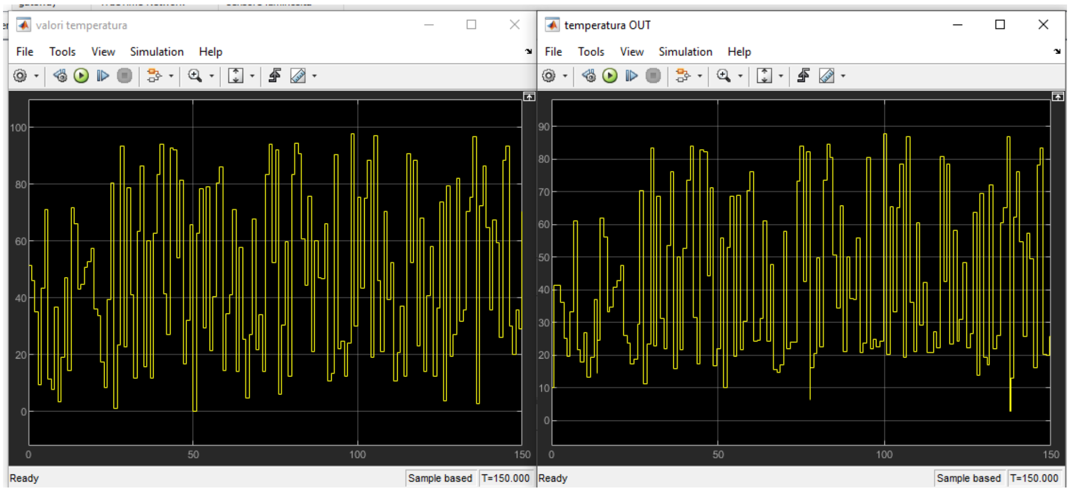

Figure 6 [a] Simulation of the temperature values measured by the sensor and [b] output temperature values, after temperature setting.

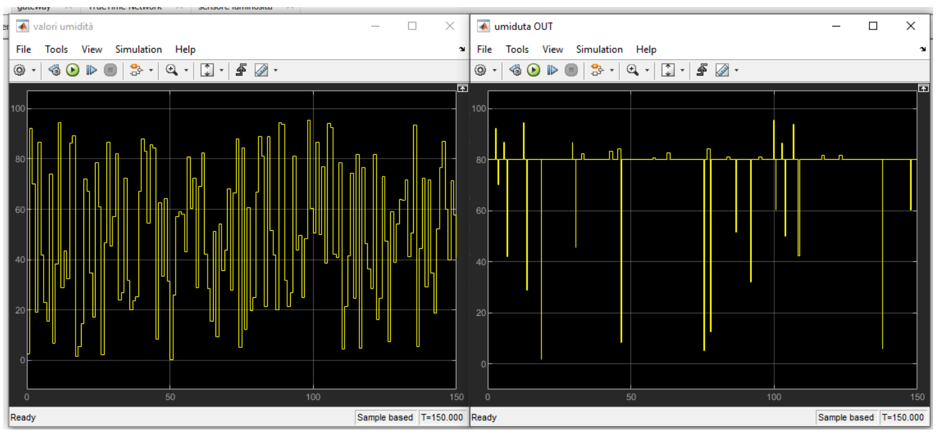

Figure 7 [a] Simulation of the humidity values measured by the sensor and [b] output humidity values, after humidity setting.

Cooling fan is only activated if the ventilation is considered high, to generate a change of air.

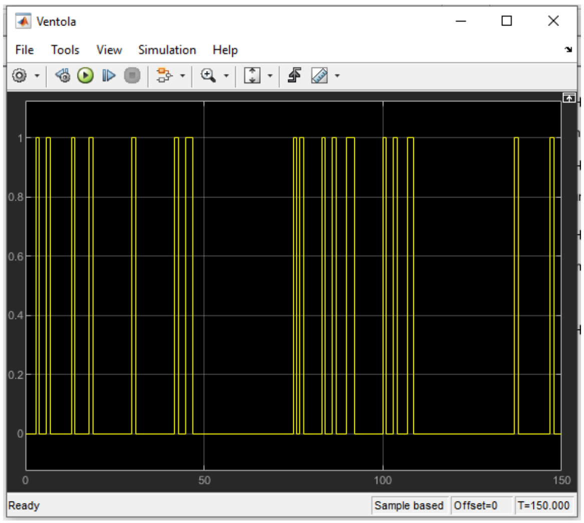

Figure 8 cooling fan binary signal. It's 0 when cooling fan is off, otherwise it is on.

REFERENCES

[1] https://www.itsensor.it/

[2] Dan Henriksson, Anton Cervin, Karl-Erik Årzén. "TrueTime: Real-time Control System Simulation with MATLAB/Simulink", Year: 2003

[3] A. Pawlowski, J.L. Guzman, F. Rodriguez, M. Berenguel, J. Sanchez, S. Dormido. "Event-based control and wireless sensor network for greenhouse diurnal temperature control: A simulated case study", Year: 2008, IEEE International Conference on Emerging Technologies and Factory Automation, 2008. ETFA 2008.

[4] K. Sohrabi, J. Gao, V. Ailawadhi, G.J. Pottie. "Protocols for self-organization of a wireless sensor network", Year: 2002, IEEE Personal Communications.

[5] Roop Pahuja; H.K. Verma; Moin Uddin. "A Wireless Sensor Network for Greenhouse Climate Control". Year: 2013, IEEE Pervasive Computing.

[6] Yiming Zhou ; Xianglong Yang ; Xishan Guo ; Mingang Zhou ; Liren Wang. "A Design of Greenhouse Monitoring & Control System Based on ZigBee Wireless Sensor Network". Year: 2017 by IEEE.

DEVELOPMENT OF A SIMULATION MODEL OF AN ELECTROCARDIOSIGNAL IN COMPUTER ALGEBRA SYSTEM

Akopyan Bella

Saint-Petersburg State University of Aerospace Instrumentation,
Saint-Petersburg, Russia
E-mail: akopyan.bella@yandex.ru

Abstract
The object of research is a computer model of an electrocardiosignal. Simulation models of realistic artificial electrocardiosignals and accompanying interference signals were developed: electromyographic interference, baseline drift, power line interference and electrode displacement artifacts. Simulated signals can be saved as a data file. The models are implemented in the MathCAD computer algebra environment and the simulation results are presented.
Keywords: electrocardiosignal, electrocardiogram, simulation model, computer model, MathCAD.

INTRODUCTION

Tests of the qualitative characteristics of electrocardiosignal processing algorithms are usually carried out both on real electrocardiograms (ECGs) and on artificially simulated ones. The advantage of the artificially simulated uncorrupted electrocardiosignals is that they have given wave amplitude and time parameters, which allows to increase the reliability of evaluating the characteristics of processing algorithms. Besides, it is also required to develop models of noise artifacts in order to obtain artificial ECG signals which are as close to real ones.

UNCORRUPTED ECG

There are many approaches to solving the problem of modeling an electrocardiogram [1], but most of them require a considerable amount of computing. The simplest mathematical models of the cardiocycle are parametric models in which individual elements of the ECG are approximated by the determinate functions of suitable forms. To simulate a single cardiocycle, the sum of asymmetric Gaussian functions described in [1] is widely used:

$$z_m\left(t, A, \mu, b\right) = \sum_{i \in \{P,Q,R,S,ST,T\}} A_i e^{-\frac{(t-\mu_i)^2}{2(b_i(t))^2}},$$

the subscript denotes the corresponding informative fragment (wave or interval) of the cardiocycle. This model can be used to simulate both the basic uncorrupted ECG signal and extraordinary cardiac contractions (extrasystoles) in any lead.

The ECG record represents the time sequence of several cardiocycles, therefore, the index m corresponding to the serial number of the simulated cardiocycle in the ECG signal is also introduced into the simulation function. For each wave of a single cardiocycle model the following parameters are set:

- wave amplitude A in mV;
- moment of time μ, in seconds, which determines when this wave of the reference cardiocycle takes the value A;
- time parameter $b(t)$ in seconds, which determines the start and end moments of each fragment.

To model the wave of an asymmetric shape, it is advisable to use two separate parameters b_1 and b_2, which define $b(t)$ as:

$$b(t) = \begin{cases} b_1, \text{ если } t \le \mu, \\ b_2 \text{ иначе.} \end{cases}$$

For the convenience of the software implementation of the developed computer model, the ECG parameters are recorded in the vector in accordance with the sequence of structural fragments of the cardiocycle. Let *par* be the generalized ECG modeling parameter, then the vector of parameter values for cardiocycle has the form of:

$$\overrightarrow{par} = \left(par_i\right), i \in \{P, Q, R, S, ST, T\}.$$

In connection with fluctuations in the heart rhythm and amplitudes of the wave of the real ECG, it is advisable to introduce the variability parameters into the model:

$$\widetilde{par}_i = par_i\left(1 + \varepsilon\_par_i\right),$$

where ε_par_i is the variability parameter, which is a random variable uniformly distributed in the interval [-ε_0, ε_0], where ε_0 is the restriction expressed as a ratio of *par*. The variability parameter has its own value for each ECG fragment.

A computer model was implemented in the MathCAD environment. The parameters of the ECG records from the MIT-BIH Normal Sinus Rhythm Database [2] were taken as parameters. Figure 1 shows the original ECG record No.1695 of the MIT-BIH Normal Sinus Rhythm Database (0.2s/0.5mV grid). Figure 2 shows the timing diagram of an ECG model based on parameters of this record (table 1). It can be seen that the shape of the model is close to the shape of the original ECG, the differences are caused by distortions of the real ECS by interfering signals, as well as the fact that the ECG is subjected to random time and amplitude fluctuations.

Table 1 – Parameters of the record No.1695 of the MIT-BIH Normal Sinus Rhythm Database

	P	*Q*	*R*	*S*	*ST*	*T*
A	0.11	-0.004	1.053	-1.053	0.63	0.52
μ	0.001	0.05	0.074	0.095	0.174	0.3
b_1	0.014	0.008	0.008	0.007	0.04	0.024
b_2	0.014	0.008	0.008	0.007	0.04	0.056

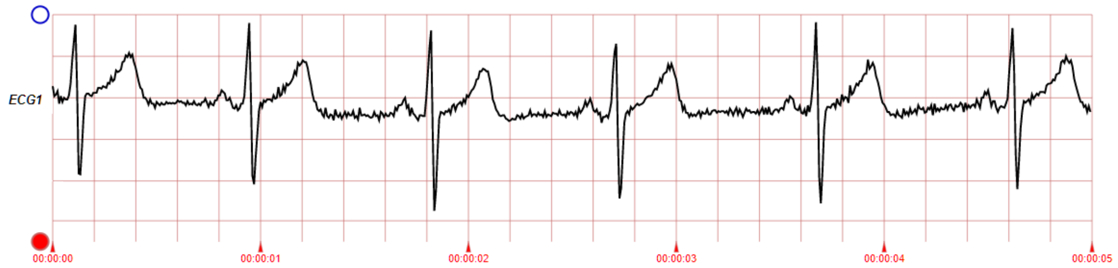

Figure 1. Timing diagram of an ECG from record No. 1695 of the MIT-BIH Normal Sinus Rhythm Database

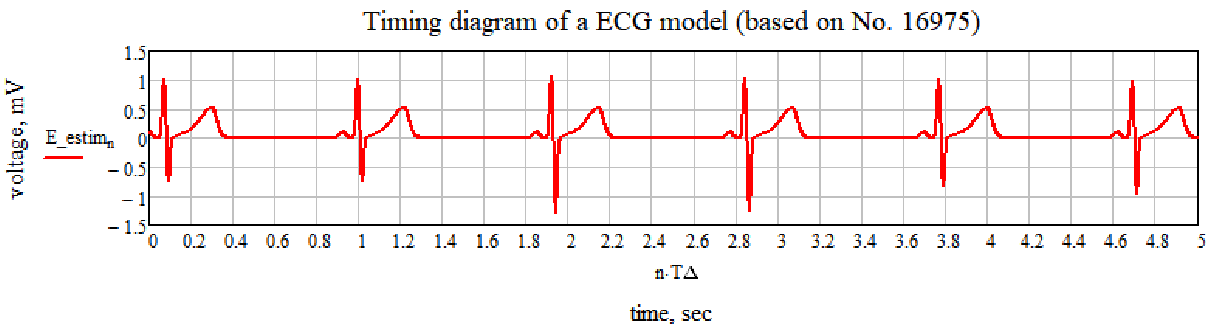

Figure 2. Timing diagram of an ECG model based on the record No. 1695 of the MIT-BIH Normal Sinus Rhythm Database

NOISE SIGNALS

As shown in [3], the following types of interference have the greatest impact on the electrocardiogram:

– electromyographic (EMG) interference caused by muscle contractions;
– baseline drift and ECG modulation with respiration;
– power line interference and electrode displacement artifacts.

All the interference signals are additive, so the real ECG model can be represented as the sum of the uncorrupted electrocardiosignal and the interference signals.

As shown in [3], EMG noise is a random signal with an amplitude of from 0.01 to 0.05 mV and could be described by a random process with normal distribution and an exponential correlation function

$$R(\tau) = \sigma^2 e^{-\mu|\tau|},$$

where σ is the standard deviation of the random process (it describes the intensity of interference), μ is the parameter of the correlation. A digital process can be modeled as:

$$v_n = e^{-\mu} v_{n-1} + \sigma\sqrt{1-e^{-\mu}} \cdot norm_n,$$

where *norm* is a sequence of mutually independent random variables distributed according to the normal distribution law with a mathematical expectation equal to zero and a standard deviation $\sigma_{norm}=1$.

Figure 3 shows a graph of an ECG model distorted by EMG interference with σ=0.5.

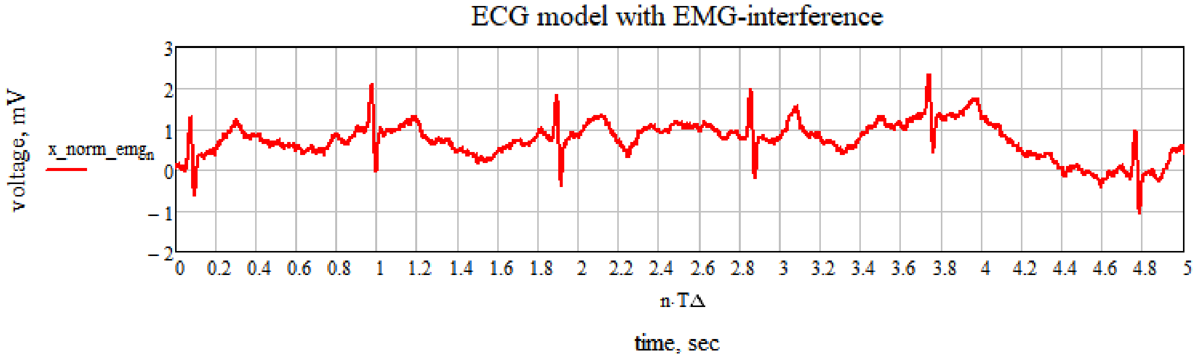

Figure 3. Timing diagram of an ECG model distorted by the EMG-interference

The baseline drift due to respiration could be implemented as the harmonic oscillations with an amplitude of 15% of the value of the R-wave of the ECG and a frequency of 0.15 to 0.5 Hz [5]:

$$v_n = 0.15 \cdot A_R \sin\left(2\pi f_д \cdot nT_\Delta\right),$$

where nT_Δ is the discrete representation of time (n is the ordinal number of the sample, T_Δ is the sampling period), f_d is the respiration rate. Figure 4 shows an ECG model with the baseline drift due to respiration drift with f_d =0.15 Hz.

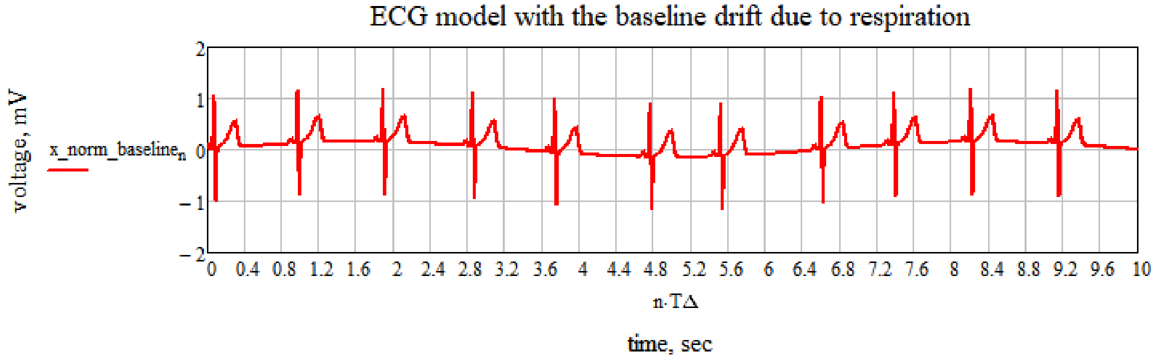

Figure 4. Timing diagram of an ECG model with the baseline drift due to respiration

As shown in [3], the power line interference is a process which contains the main harmonic with a frequency f_0 of 60 Hz and a number of odd harmonics up to 1000 Hz. The contribution of minor harmonics, however, is insignificant and they are often neglected when constructing a model. The components of the 1st, 3rd, and 5th harmonics are introduced into the model under development, so that the model of the interference signal from the power supply was implemented as:

$$v_n = \left|0.15 \cdot A_R \cdot \sin\left(2\pi f_д \cdot nT_\Delta\right)\right| \cdot$$
$$\left(\sin\left(2\pi f_0 \cdot nT_\Delta\right) + 0.05\sin\left(2\pi \cdot 3 f_0 \cdot nT_\Delta\right) + \right.$$
$$\left. +0.01\sin\left(2\pi \cdot 5 f_0 \cdot nT_\Delta\right)\right).$$

Figure 5 shows an ECG model with the power line interference.

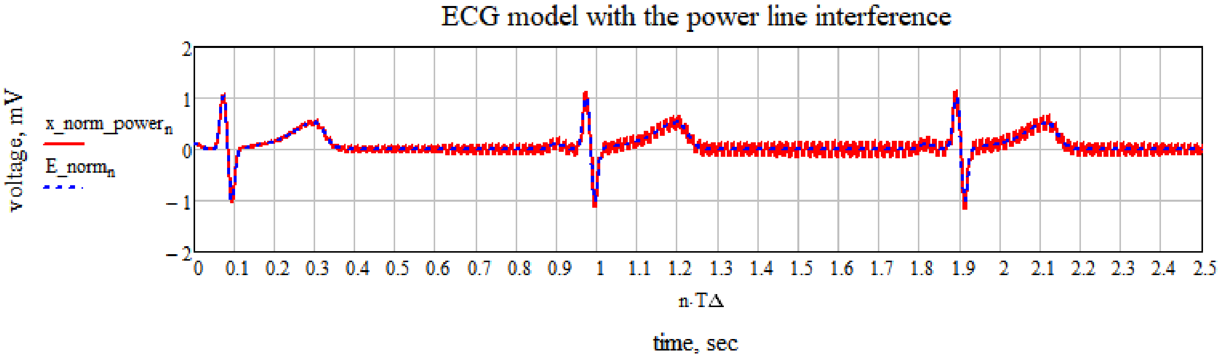

Figure 5. Timing diagram of an ECG model with the power line interference

The electrode displacement artifacts are emissions of random amplitude and duration, forming the structural interference in ECG recordings; in many cases, they are the causes of gross errors in the recognition of cardiocycles in the automatic processing of electrocardiograms. The simplest option for implementation of the electrode displacement artifacts is a random change in the level of a zero signal at a random moment in time; the amplitude level is a uniformly distributed random variable lying in the interval from $-A_R$ to A_R. Figure 6 shows a timing diagram of an ECG model with an abrupt drift caused by displacement of the electrodes.

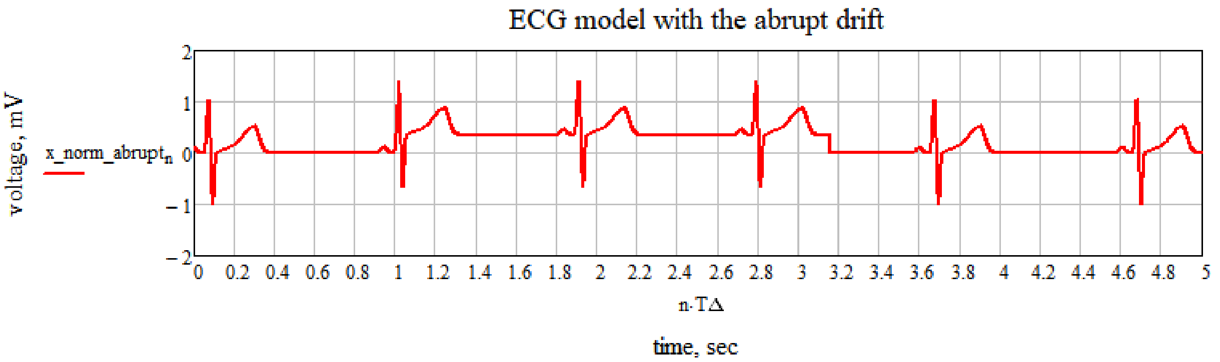

Figure 6. Timing diagram of an ECG model with the abrupt drift caused by displacement of the electrodes

All the marked interference components affect the ECGs simultaneously in different proportions, which can be mathematically represented as the weighted sum of all simulated interferences v with the electrocardiogram s_{ECG}:

$$x_{ECG} = s_{ECG} + w_{EMG} \cdot v_{EMG} + w_R \cdot v_R +$$
$$+ w_{abr} \cdot v_{abr} + w_{\sup} \cdot v_{\sup},$$

where v_{EMG} is the signal of EMG interference, v_R is the baseline drift due to respiration, v_{abr} is the abrupt drift caused by the displacement of the electrodes, v_{sup} is the interference signal from the power supply, and w with the corresponding index is the weight coefficient for this interference signal.

The advantage of this model is that the level of each interference component in the simulation can be set by researcher so the model can be used to study the qualitative characteristics of ECG processing algorithms (for example, detection of arrhythmias) under various conditions of an interference environment. Figure 7 shows a graph of an ECG model distorted by all types of interference with weight coefficients $w_{EMG} = 0.2$, $w_R = w_{abr} = 1$, $w_{sup} = 0.3$.

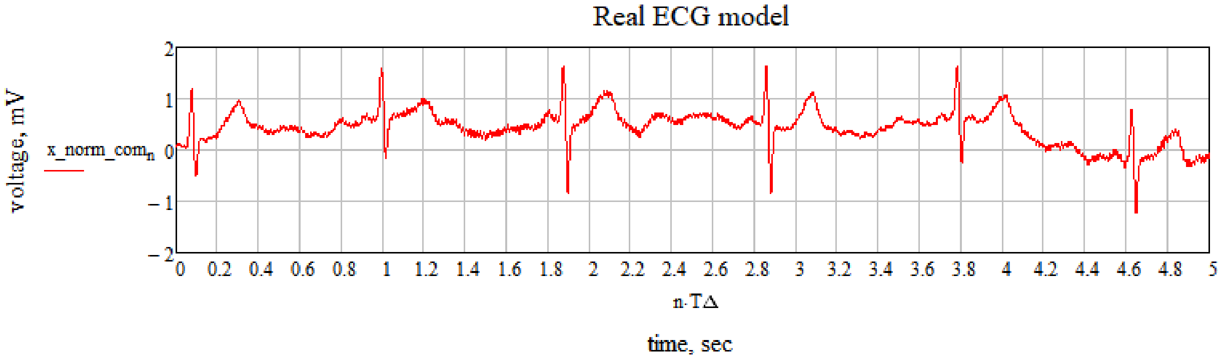

Figure 7. Timing diagram of an ECG model with the abrupt drift caused by displacement of the electrodes

CONCLUSION

The application of the described ECG model allows the formation of realistic ECG records for research – just enter the parameters of uncorrupted ECG and noise signals. Simulated signals can be saved as a data file. In addition to various forms of cardiocycles, the developed model allows you to simulate various types of cardiac arrhythmias.

REFERENCES

[1] Bekler, T.YU. Modelirovaniye iskusstvennykh elektrokardiogramm normal'noy i patologicheskoy formy/ Kibernetika i vychislitel'naya tekhnika. Kiyev: Mezhdunarodnyy nauchno-uchebnyy tsentr inf. tekhnologiy i sistem NAN i MON Ukrainy, 2012. Vyp. 169. S.19-33. [Beckler, T.Yu. Modeling of artificial electrocardiograms of normal and pathological forms / Cybernetics and computer engineering. Kiev: International Research and Training Center inf. technologies and systems of NAS and MES of Ukraine, 2012. Vol. 169. S. 19-33.] (in Russian)

[2] MIT-BIH Normal Sinus Rhythm Database URL: https://physionet.org/content/nsrdb/1.0.0/

[3] Friesen, G.M. A comparison of the noise sensitivity of nine QRS-detection algorithms/ G.M. Friesen, T.C Jannett, M.A. Jadallah et al.// IEEE Transactions on biomedical engineering, vol. 37. №1. 1990. P. 85-97.

SMART AQUARIUM

Cammalleri Giuseppe,
Crinò Francesco Giuseppe

Computer Engineering and Networks Laboratory – Kore University of Enna – Italy
Email: giuseppe.cammalleri@unikorestudent.it
francescogiuseppe.crino@unikorestudent.it

Abstract
The proposed project aims to manage a brackish aquarium in a functional and smart way.
In particular, the goal of the proposed system is to detect and keep the parameters of pH, temperature, and salinity of the water within their ideal ranges in order to ensure optimal living conditions at all times.
The aquarium management system consists of two networks: a wireless one (ZigBee) and a wired one (Ethernet) connected by a gateway. A controller combined with a fuzzy block expresses the environment degree of "livability". In the end, a regulator manages the parameters' values to improve livability if it is not optimal. Depending on the temperature, the power applied to a resistor for heating the water is also controlled.

INTRODUCTION

Managing an aquarium daily can be difficult, especially if you are away from home for a long time. An automated system that manages the internal environment can be fundamental. Clearly, more sensors and functions has the aquarium, more autonomous the system is. In this project we focused mainly on some basic aspects of livability.

The proposed project consists of a system for the management of a brackish water aquarium.

In order to ensure a perfect condition of the environment inside the aquarium, the water values of pH, salinity, and temperature are monitored. To monitor these parameters, sensors are used that are able to transfer the collected data through ZigBee wireless technology.

The ZigBee wireless technology is one of the most widely used in the sector of telecommunications and there are numerous applications in smart sensor networks applied to the industrial field, especially in smart house projects. In general, we can say that ZigBee is widely used in WPAN (Wireless Personal Area Network) projects.

ZigBee is based on the standard IEEE 802.15.4

and operates on frequencies such 868 MHz, 915 MHz and 2.4 MHz, which is the most used.

The wireless network is connected to a wired network consisting of three nodes: the gateway, the controller, and the regulator.

To connect the wireless network to the wired network, we have to use a gateway, which is a device that connects heterogeneous networks operating at network or application level.

The medium access control, or MAC protocol, used in the wired network is the CSMA/CD.

The data collected by the sensors are sent to the gateway which transmits them to the controller node.

The controller node sends the data received from the gateway to a specially programmed fuzzy block which processes the data collected by the sensors and provides a livability value.

This livability value is sent, together with the values detected by the sensors, to the regulator block that regulates the values of interest in order to ensure a good livability of the environment inside the aquarium.

In the end, the system's performance metrics will be measured, in particular a count of lost packages will be made and the system response time will be calculated.

In section II of this report, existing smart aquariums is presented.

Section III illustrates the network architecture of the proposed control system.

Section IV shows the simulated network scenario, the use and operation of soft techniques computing (fuzzy logic), and MBSD.

Section V of this paper presents the results obtained regarding the assessments of the

network performance.

Section VI summarizes the conclusions on the success of the project and its possible future development.

RELATED WORKS

Nowadays there are not many aquarium management smart systems that are produced on a large scale; however, there are some interesting startups such as 'Bluenero' and 'Felix' that propose a smart management which allows you to control different parameters of the aquarium even remotely.

One of the few products of this kind is a smart aquarium produced by Xiaomi that allows you to manage all the parameters useful for the management of an aquarium.

It is clear that the development of smart aquariums is of interest for many companies that invest in startups and attempt to market such products.

The proposed project does not aim to deal with finished and ready-to-trade products such as Xiaomi's one or the above mentioned startups; however, it seeks to present itself as a solid basis to allow functional developments of an aquarium management smart system.

THE PROPOSED APPROACH

The proposed aquarium management system consists of two networks: a wireless network and a wired network connected by a gateway.

The wireless network consists of the three sensors that detect the values of temperature, pH, and salinity of the water, plus the gateway that connects the wireless network to the wired network.

The wireless network is a WPAN network and it has been decided to use the ZigbBee technology, identified as IEEE 802.15.4, as a communication protocol.

The data collected by the sensors are sent to the gateway which plays the role of central connection point of the proposed network, which forms a star topology.

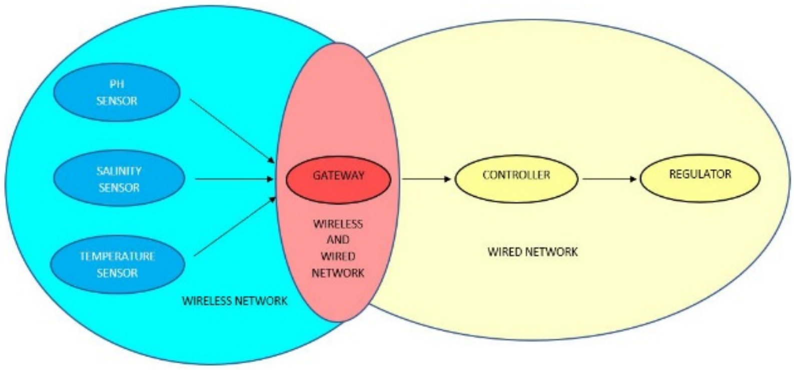

Figure 1. Network topology

In particular, the gateway performs all the necessary operations in order to connect the wireless network to the wired network and to allow the transmission of the data between the two networks.

For the wired network, it was decided to use a CSMA/CD as a MAC protocol.

This protocol requires that all nodes of the network listen to the channel before transmitting the frame.

If the channel is free, the node transmits the frame; otherwise, it waits for the channel availability.

After sending the frame, the node verifies that no collisions have occurred.

If a collision is detected, the emitter node notifies the other nodes of the network by transmitting a jam signal.

After a collision, the transmission is interrupted and the emitter node will wait a certain time before carrying out the retransmission that will be regulated by a back-off algorithm.

The data are sent from the gateway to the controller which forwards them to a 'fuzzy logic controller' Simulink block.

In order to allow the analysis of all possible combinations of the three parameters detected, all the necessary rules have been inserted into the 'fuzzy logic controller'.

The fuzzy logic controller then performs an analysis of the received data of pH, temperature, and salinity and calculates the level of livability in the aquarium.

Afterwards, the controller forwards the values received from the gateway and the livability value which have been calculated by the fuzzy logic controller to the controller.

The regulator acts on the parameters of interest according to the input values received by the controller in order to ensure a livable environment inside the aquarium at all times and it sets the parameter 'power' according to the analysis of the temperature value.

This parameter is sent to the MBSD block that manages a resistor which is used to heat water.

SCENARIO

The project was implemented using the Simulink of Matlab.

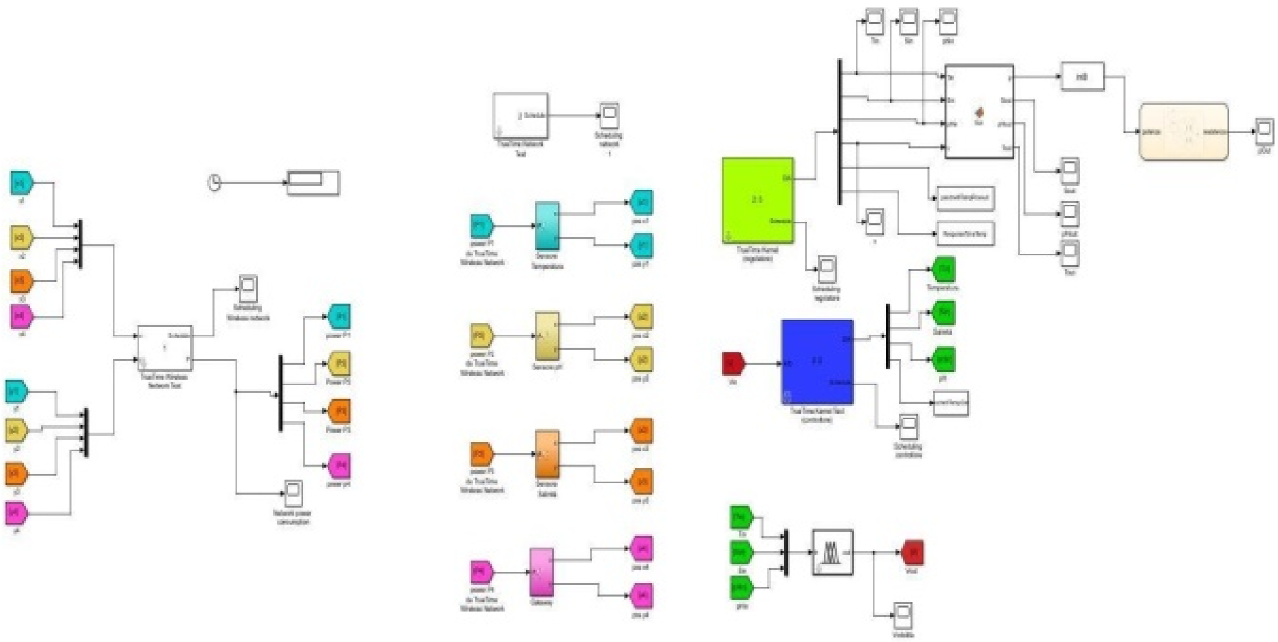

Figure 2. Simulink project structure

In particular, to create the wireless network, the Simulink block 'True Time Wireless Network' was used and for the wired network a block 'True Time Network' was used.

In order to set the wireless network properties, a date rate of 0.8 mbits/s and a loss probability of 0.3 – that is packets loss probability pairs to 30% – have been set into the block 'True Time Wireless Network'.

This value of packets loss probability was chosen in order to account for a possible disturbance on the wireless data transmission due to the environment of the aquarium.

It is also necessary to set 802.15.4 (ZigBee) as a network type.

To create the wired network, a date rate of 10Mbits/s has been set into the Simulink block 'True Time Network' and the CSMA/CD was set as a MAC protocol.

All sensors have a Matlab block 'uniform random number', a random number generator that simulate sensor readings.

The gateway receives the pH, salinity, and temperature values from the sensors which exist in the wireless network, and forwards them to the controller, which is part of the wired network.

Thus, the gateway interacts with both networks and it is necessary to set up two network interfaces in its 'true time kernel'; one for the wireless network and one for the wired network.

The controller forwards the values received from the gateway to a block 'Fuzzy Logic Controller' which is responsible for processing the data collected by the sensors and estimate, according to the rules inserted inside, a degree of livability of the water that can be poor, medium or high.

The rules inserted into the 'fuzzy logic controller' have been designed to make the system able to react to every situation and to prevent any cases of indecision.

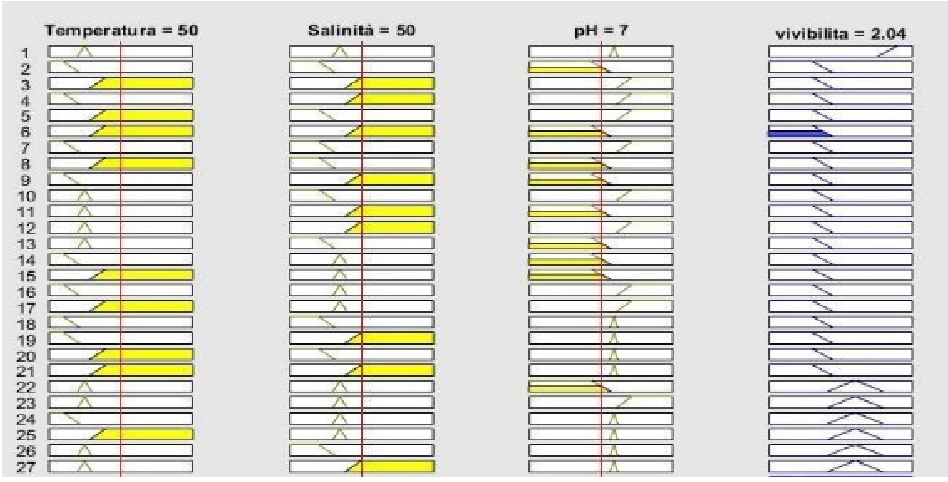

Figure 3. Fuzzy rules 2D graphics

The regulator, which receives the pH, temperature, salinity, and livability values from the controller, has an algorithm specially created to regulate the parameters of interest.

This algorithm contained in the block ‘Matlab function’ is able to perform an analysis of the data received and understands which data to act upon and whether or not it is necessary to act.

Based on the water temperature value the algorithm provides an output parameter ‘power’ which is used by a block MBSD (model based software design) to manage the power applied to a resistor which serves to heat the water.

The MBSD block is programmed using a state chart language.

This language involves the representation of a system through the use of states and transitions.

In this case, the states are related to the condition of the resistor that can be turned off or turned on at level one, two, or three.

The transitions are managed by the power parameter managed by the regulator block algorithm.

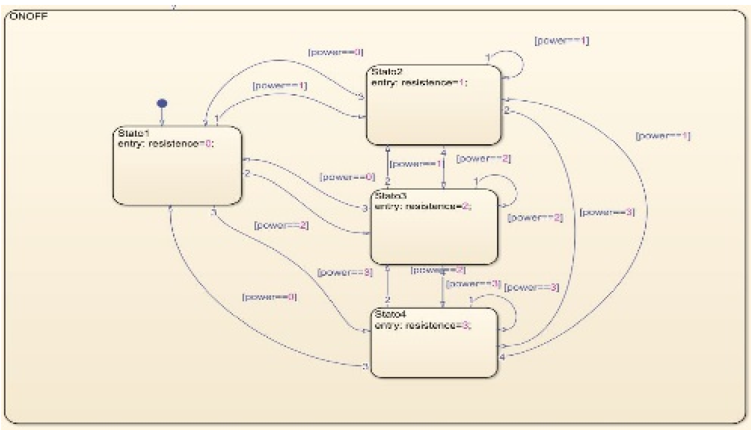

Figure 4. MBSD structure

PERFORMANCE EVALUATION

To verify the proper functioning of the planned network, network performance metrics such as response time and the number of packages missed are estimated.

Response time refers to the time interval between the user’s request and the system’s response.

To measure this network performance, it was necessary to transmit the timestamp in which the packet was sent along with the packet. To do this it was decided to treat the sending time as a property of the single package.

When the regulator receives the packet, the response time is calculated by subtracting the receiving time from the sending time.

To calculate the amount of packets lost, it was thought to count the amount of packets sent by the sensor and the amount of packets received by the regulator.

In particular, for each packet sent by the sensor, a counter is updated to track the number of packets sent. For each packet received by the regulator, another counter is updated to track the packets received.

CONCLUSIONS

The purpose of the regulation system is to ensure a constant optimal livability in the aquarium via the control of the parameters of water temperature, salinity, and pH.

To ensure this, the three measured parameters are constantly adjusted to their optimum value.

After a simulation of 500 seconds we obtained output values that fluctuate around the optimal values.

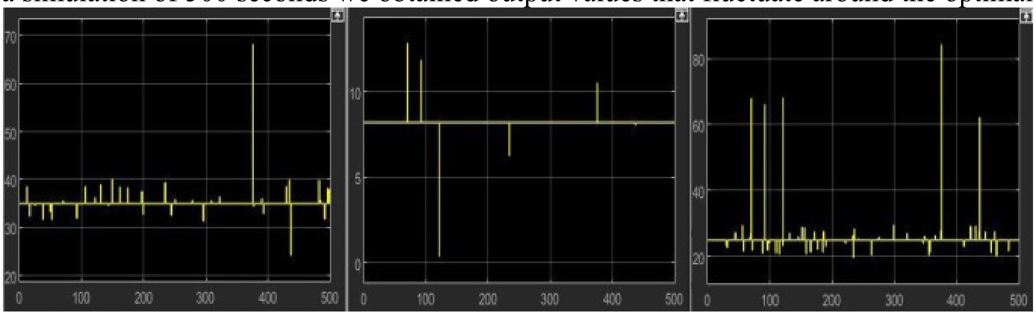

Figure 5. Output trend of power parameter

In particular, the following trends in salinity, pH and temperature parameters were observed.

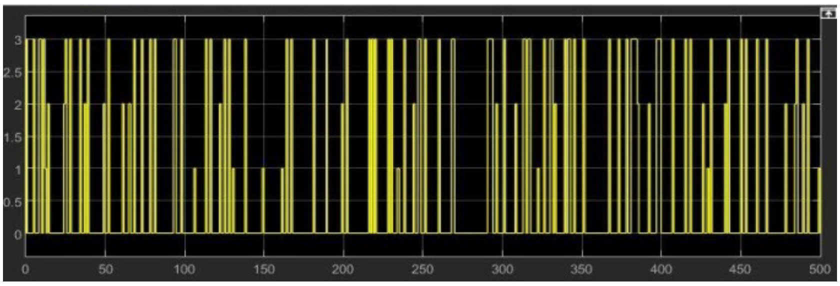

Figure 6. Output trend of salinity, pH and temperature

It is interesting to see the output values from the MBSD of the p parameter.

Regarding the performance metrics calculated, the results are excellent.

In particular, no package was lost and regarding the response time the obtained values are between 0.6 and 0.9 seconds with an average value of 0.71 seconds.

In accordance with the output values obtained, it can be said that the proposed system has been able to handle all the situations that have occurred and has managed to regulate the values of pH, salinity, and temperature in an optimal way.

The two networks that make up the system interact with each other without problems and the response time and the number of lost packages highlight the optimal functioning of the entire network.

In conclusion, the proposed project could be considered an excellent basis for possible future developments, notably by increasing the parameters on which it can act and the functions it can perform.

REFERENCES

[1] Dan Henricksson, Anton Cervin and Martin Ohlin “TrueTime 2.0 – Reference Manual ”, Departement of Automatic Control, Lund Institute of Technology, February 2016.

[2] https://www.acquaportal.it/acquario-smart-bluenero/

[3] https://bluenero.org/

[4] https://www.fastweb.it/smartphone-e-gadget/felix-smart-aquarium-un-nuovo-modo-smart-per-gestire-il-proprio-acquario/

[5] https://www.xiaomitoday.it/xiaomi-smart-fish-tank-acquario-smart-xiaomi.html

[6] https://www.xiaomitoday.it/xiaomi-smart-fish-tank-acquario-smart-xiaomi.html

SMART WATER PURIFIER

Diquattro Giuseppe, Rizzo Luca

Università degli Studi di Enna "Kore"
giuseppe.diquattro@unikorestudent.it
luca.rizzo@unikorestudent.it

Abstract.
Nowadays the "Internet of Things" is going to diffuse particularly in a smart city, for this reason it was decided to introduce a "Smart water Purifier". It is a city purifier used to purify dirty water and able to notice every parameters in a little mount of time to notice if water is "good" or "poor".
Obviously using dirty water it's odd to have good water immediately, in fact few times water is "good" only with an initial analysis.

INTRODUCTION

This system is implemented in two different networks where, one network is used to manage four sensors that detect four parameters: color of the water, amount of minerals, pH and bacterial load and the second one is used to determine the quality of the water (for a deepening read section II).

PROPOSED APPROACH

Sensor, used to detect the aforementioned parameters, are part of first network (Network 1), instead controller, where are transmitted data, is part of second network (Network 2).

Both networks are wired and is present a gateway that interfaces with them to allow the communication between sensors and controller, in particular the various detection are sent through the network to the gateway that forward all the received messages from the sensors to a controller linked to the second network using fuzzy controllers. They will be able to notice the water quality and switch on a green led if the water is "good" or a red led if the water is "poor". Led are controlled by a MBSD to which pass a signal suitably filtered to make the correct led light up.

SCENARIO

To simulate the reality under consideration have been used four "TrueTime Kernel" which are four sensors used to detect the parameter of the water. Every sensor is connected to a "Uniform Random Number" that generate random value inside an established range (see Figure 1a):

- 0 – 14 for pH sensor;
- 0 – 400 for mineral sensor;
- 0 – 2 for bacterial load sensor;
- 0 – 2 for color sensor.

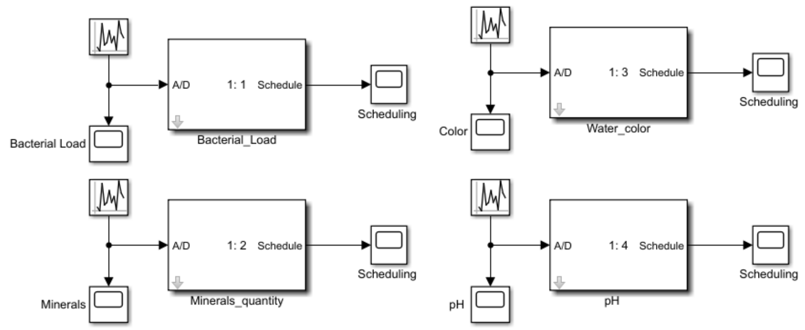

Figure 1a: four sensors, each one notice a parameter.

Sensor, as mentioned above, are associated to the first network that is linked to the second through the gateway. Both networks being wired and it was preferred to implement two "TrueTime Network", both with the same parameters:

- Protocol used: CSMA/CD;
- Bitrate: 1 Mbps;
- Frame size: 512 bit;
- Maximum number of nodes: 10.

All data detected from sensors are sent to the controller (through second network) that receive data (see Figure 1b), route them to the correct output and sand all scheduled data to the fuzzy controller.

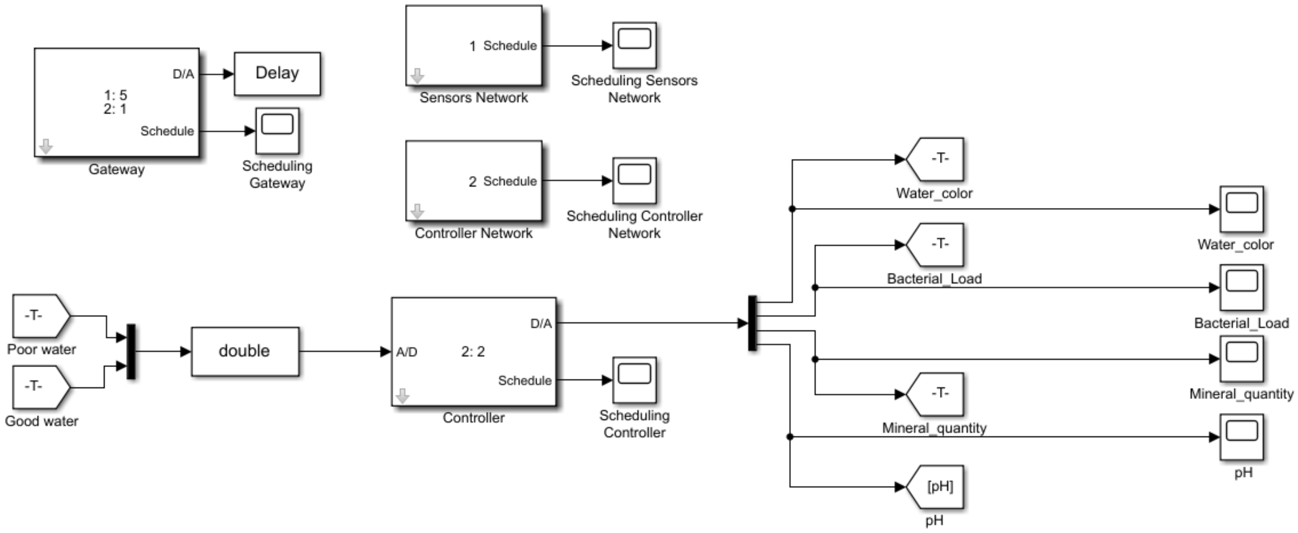

Figure 7b: Two networks and Controller that schedule data to the fuzzy.

All data received by fuzzy, specifically color of the water and bacterial load, need to have a preliminary check and according to how are processed data, you may have a first feedback about quality of the water. It will be analysed in the most appropriate manner by the second fuzzy that have in input the output of the first fuzzy, amount of mineral and pH of the water sample (see Figure 1c).

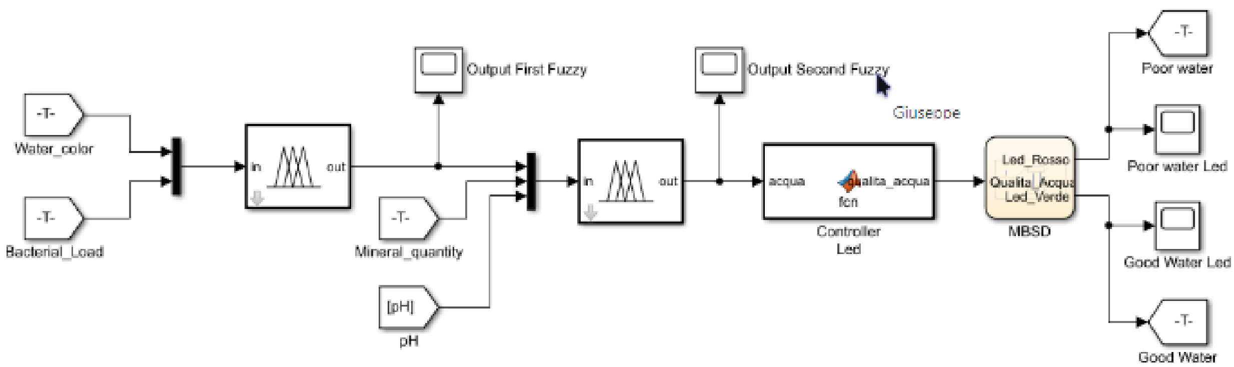

Figure 8c: Two fuzzy connected to each other and the fuzzy output is sent to an MBSD controller.

This output is filtered in such a way that is being manipulated to utilize the MBSD (see Figure 1d) used to turn on the leds:

- Green if water is "good";
- Red if water is "poor".

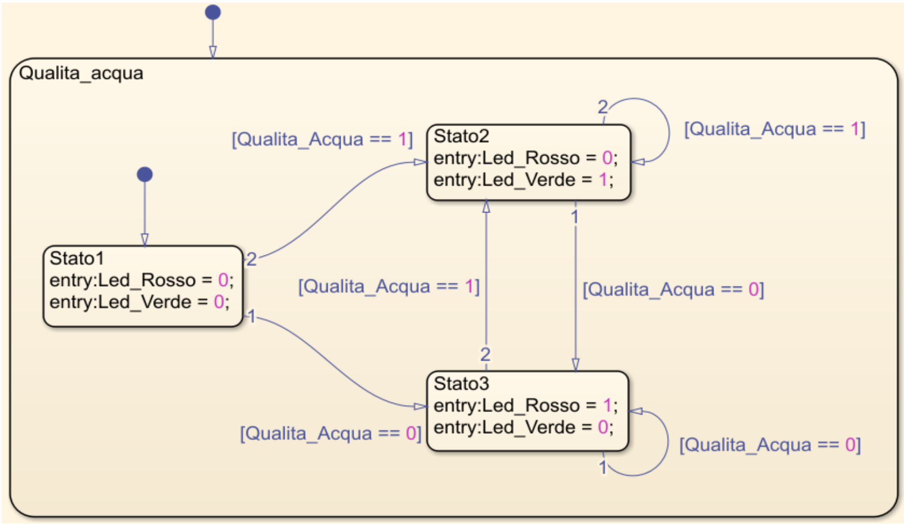

Figure 1d: Structure of MBSD system.

PERFORMANCE EVALUATION

The measured performance metrics are:

- Delay: used to check if there are important delay when data are received from the gateway. All data must be received as quickly as possible for an immediate response (graph at Figure 3);
- Elaboration time: used to check how quickly is fuzzy to elaborate all data received: if data are received quickly, the elaboration and the response (about quality of water) are coming up fast (graph at Figure 4);
- Response time: used to verify if the response of controller is quick: more slowly is the response and all data will receive later to fuzzy used to analyse the water (graph at Figure 5).
- Reaction time: used to verify if controller (in the second network) is active as soon as it gets data and therefore to receive an immediate response (graph at Figure 6).

Every performance metrics is opportunely calculated, the graphs, plotted in a limited range of time (about twenty seconds to improve the readability), are shown below.

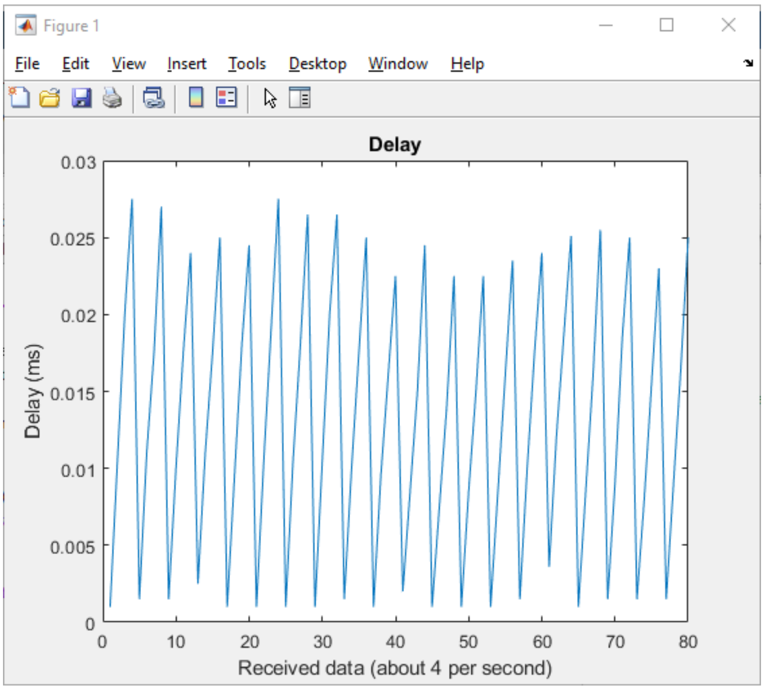

Figure 3: Plot that describe Delay trend

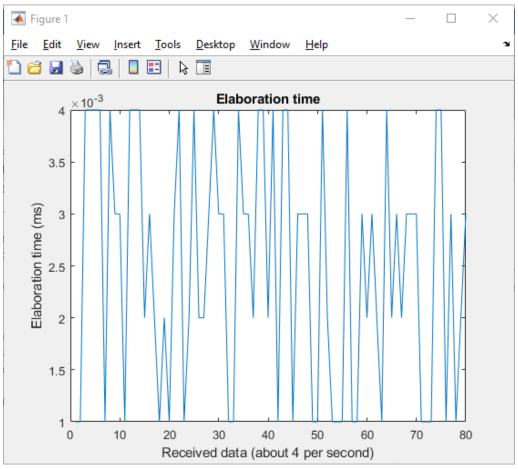

Figure 4: Plot that describe Elaboration time trend

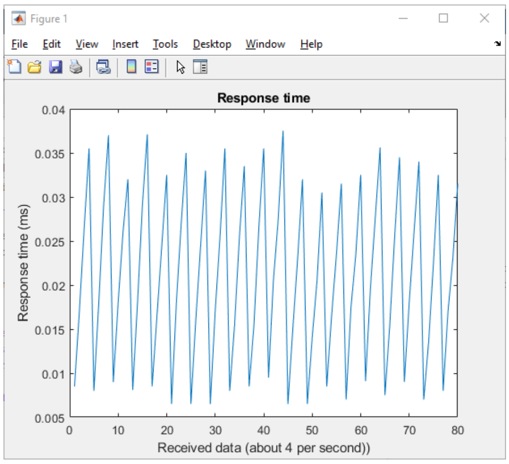

Figure 5: Plot that describe Response time trend.

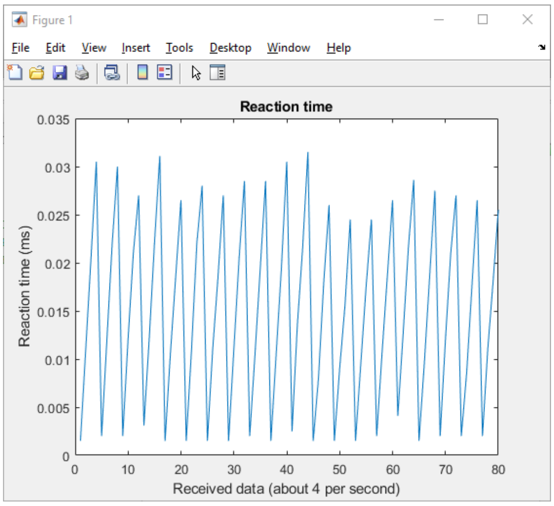

Figure 6: Plot that describe Reaction time trend.

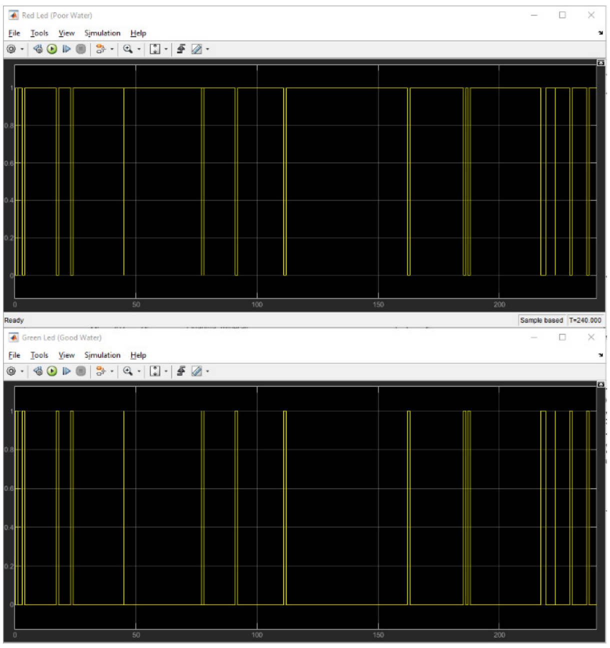

Figure 7: The upper graph describe how many times is present "poor" water, and the lower graph describe how many times is present "good" water. The simulation time is about 240 seconds and these signals represented in these graphs show when leds light are on

CONCLUSIONS

The water immediately “good”, as supposed in the abstract, is lesser then “poor” and red led turn on frequently then green led (see Figure 7).

An idea to improve the efficiency of this project is to purifier another time this water to have more frequently “good” water, an other idea is to add more sensors to notice if the water may be fine also for alimentary purposes.

This is a city purifier for dirty water and it can be used in smart cities in a way that could get also an optimal use and development about “Internet of things”.

ANALYSIS OF RADIO-FREQUENCY IDENTIFICATION SYSTEMS WITH APPLICATION OF SAW TAGS

Fedorov Ilia

Saint-Petersburg State University of Aerospace Instrumentation,
Saint-Petersburg,Russia
E-mail: iliagus2@gmail.com

Abstract
The technology of a radio-frequency identification system with using tags on surface acoustic waves is considered. This article analyzes the possibility of using LFM and FSK signals in identification systems as an interrogation signals.
Keywords: linear frequency modulation signals (LFM), autocorrelation function (ACF), cross correlation function (CCF), frequency shift keying signals (FSK), impulse response, code sequence.

The principle of FSK system.

The designing RFID systems, needs a large numbers of passive identification tags and the simple operation of the interrogate device (reader). At present surface acoustic waves (SAW) tags are promising. They are passive radiation-resistant elements, the production technology of which is quite well developed. Various schemes of identification systems are possible with used of this SAW tags.

In work [1] an identification method was considered in which the reader emits a sequence of FSK radio pulses, with intra-pulse encoding of symbol frequencies according to a certain rule. The impulse response (IR) of SAW tags are FSK radio pulses which are complex conjugate with the signals emitted by the reader. The correlation principle of tags classification was used. It was considered that the tags are located at the same (or close) distance from the reader. The structural diagram of such system is shown in Figure 1.

According to this scheme, a certain number of coherent FSK radio pulses are generated in the reader control and processing device, which are sequentially emitted through the transceiver to the tag location area.

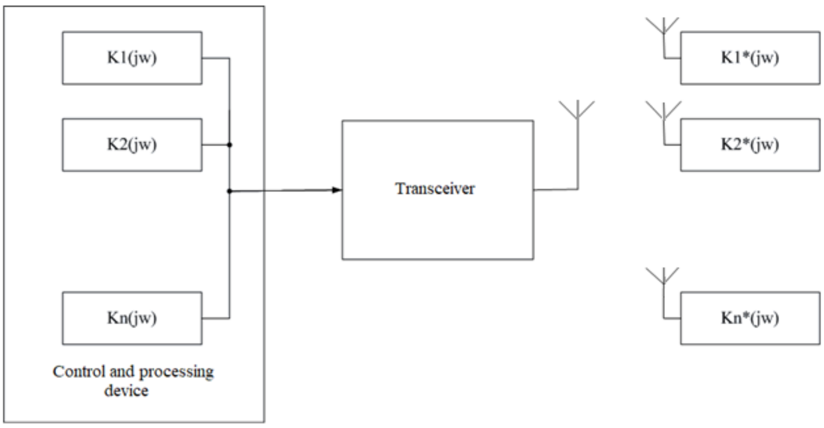

Figure 1. Structural diagram of an identification system with FSK interrogation pulses

In Figure 1, the following notation is accepted.

$Kn(j\omega)$ – spectral characteristics of the emitted signals.

$Kn^*(j\omega)$ – spectral characteristics of the IR of tags on SAW.

Every emitted by the reader signal is received by the tag and re-emitted by it with a certain delay- t_d, determined by the topology of the tag. t_d are the same for all tags. The tag topology is shown in Figure 2. The frequency characteristics of the tags are complex conjugate to the spectral characteristics of the signals.

Following the correlation processing method, radio signal with a spectral function $Kn(j\omega)$ interacting with a tag which have a frequency characteristics $Kn^*(j\omega)$, forms the ACF $\psi 11(\tau)$ of the emitted radio signal. It can be written as

$$S_{out}(t) = F^{-1}\left[Kn(j\omega) \times Kn^*(j\omega)\right],$$

(1)

where F^{-1} – symbol of the Fourier inversion

At some time, signal will have a maximum value of – $U1_{max}$. With all other tags, this signal will form CCF – $\psi12(\tau)$ of this signal with the IR of the tag. In this case maximum of the value of the signals $\psi12(\tau)$ – $U2_{max}$ will be significantly less than $U1_{max}$.

The difference between $U1_{max}$ and $U2_{max}$ will depend on the length of the code sequence in the FSK signal and the frequency coding rule in this code sequence [2].

When a radio signal is emitted, the reader receiver is locked for a time equal to the duration of this interrogation signal. Reflected electromagnetic signals from nearby objects that arrived at the receiver input at this time will be filtered out. After time – t_d the input of the broadband receiver of the reader will be open and all received signals reflected by tags will go to the input of the control and processing module. The memory module of reader contains all the codes which were sequent emitted. If a radio signal n-th code sequence in a FSK signal was emitted at the n-th period of radiation, then the tag "match" with this signal will form the maximum reflected signal $U1_{max}$. At the output of the receiver, when $U1_{max}$ exceeds a certain threshold, the fact of detection of this tag will be recorded in the processing device.

All other tags (for which the codes of the emitted signal and the marks "do not match") will form the reflected signal $U2_{max}$ and will not be identified. The signal processing algorithms in the reader can be either analog or digital.

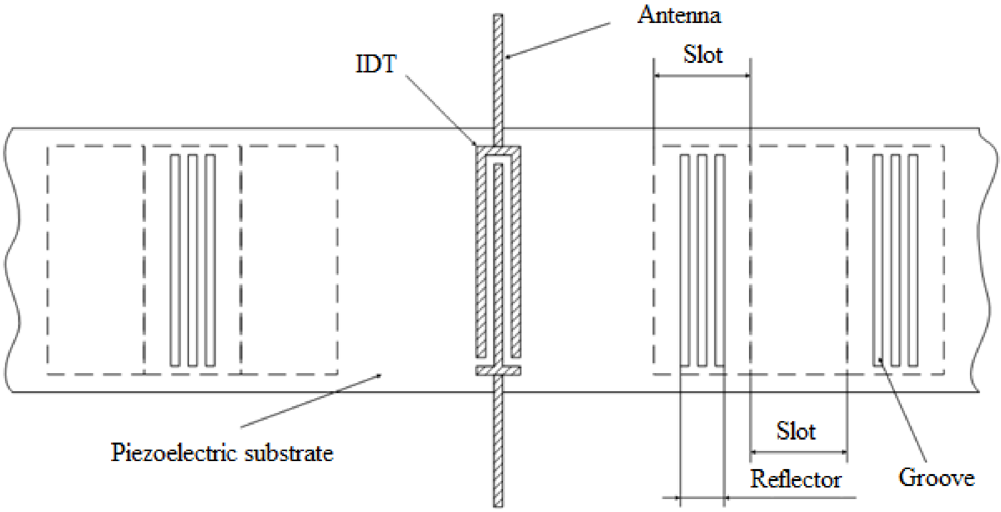

Figure 2. SAW tags' topology

The disadvantage of such an identification system is the need for sequential radiation of a large number of FSK signals, which greatly complicates the reader's transmitter. One of the requirements for the signal emitted by the reader is the constancy of its modulus of the spectral function $|S(j\omega)|$ in active spectrum width. At the same time, the active spectrum width $|S(j\omega)|$ must be greater or equal to the active width of the spectrum of IR tags – $Kn^*(j\omega)$.

The active spectrum width of the impulse response of the labels is determined by the number of characters in the tag and the magnitude of the frequency jump from symbol to symbol. The number of frequencies and the number of characters in the impulse response of the tag are equal. These parameters are set during system design. The active width of the spectrum of the tag does not depend on the places of frequencies in its code sequence. Therefore, the impulse response of the tags will have the same active spectrum width.

The system work principle with using LFM signals

As an interrogation signal, a LFM radio pulse with a carrier frequency of – f_o, equal to the operating frequency of IR of the tags can be used. The modulus of the spectral function of the LFM radio pulse $|S(j\omega)|$ can theoretically be considered constant in the required active width of the spectrum of IR tags (Figure 3). In this case, the transceiver of the system will contain a transmitter periodically emitting one radio signal. The block diagram of the system is shown in Figure 4.

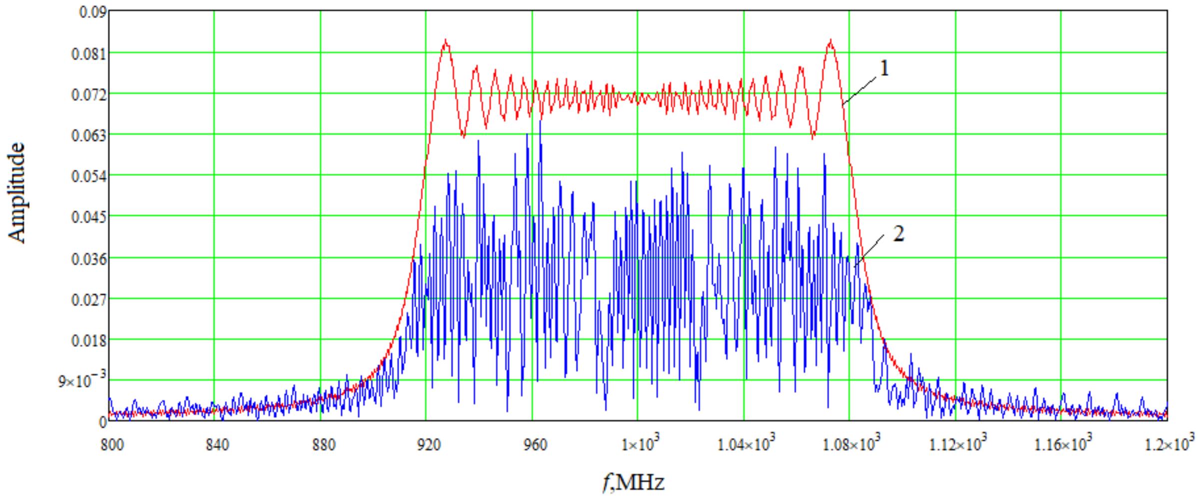

Figure 3. Amplitude spectra of the LFM signal (1) and IR tags (2)

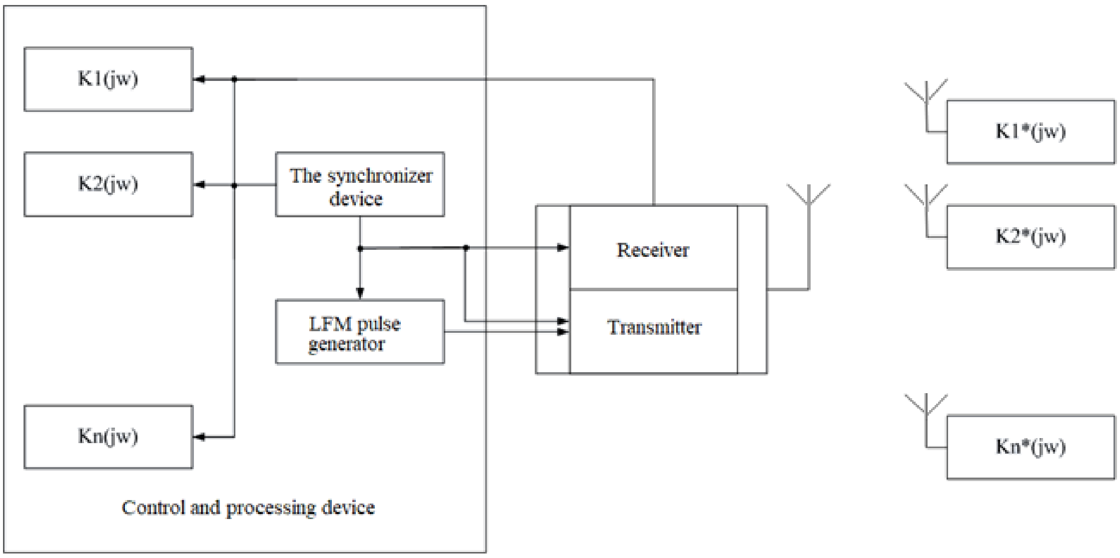

Figure 4. Structural diagram of the identification system with LFM interrogation pulses

The operation of the system can be simply described. The control and processing unit generates a LFM radio pulse at the operating frequency of the tags and the reader's transmitter emits it. Signals re-emitted by the tags are received by the reader's receiver, which is optimal for the emitted LFM signal.

The frequency response of the receiver can be determined as follows

$$K_{opt}(j\omega) = S^*(j\omega)\,, \tag{2}$$

where $S^*(j\omega)$ – complex conjugate spectrum of the LFM signal.

The spectral characteristic of the signal (reflected by the tag) at the output of the reader's receiver can be written as follows

$$S_{ref}(j\omega) = S(j\omega) \times Kn^*(j\omega) \times S^*(j\omega)\,, \tag{3}$$

where $S(j\omega)$ – spectrum of the emitted LFM signal, $Kn^*(j\omega)$ – spectrum of the IR of tags.

In the memory of the control and processing module the spectra of complex – conjugated IR tags code sequences – $Kn(j\omega)$ are stored. In the time domain, they are FSK signals, complexly conjugated IR tags – $S_{FSK}(t)$. The signals reflected from the tags and received by the reader's receiver are recorded in the device memory. During one period of the reader's operation they are sequentially processed in N channels (matched the number of tags in the system).

The spectral function of the signal at the output of the n-th channel can be written as follows

$$Sn_{out}(j\omega) = S(j\omega)\times Kn^*(j\omega)\times K_{opt}(j\omega)\times Kn(j\omega) \tag{4}$$

Since the system of transmission, receive and processing can be conventionally considered linear, it is possible to write down

$$Sn_{out}(j\omega) = S(j\omega)\times S^*(j\omega)\times Kn(j\omega)\times Kn^*(j\omega) = \left|S(j\omega)\right|^2 \times \left|Kn(j\omega)\right|^2 \tag{5}$$

For the channel, for which $Kn(j\omega)\times Kn^*(j\omega) = |Kn(j\omega)|^2$, (using the Wiener-Khintchine theorem) it is followed that the inverse Fourier transform of formula (5) is a convolution ACF of LFM signal and ACF of FSK signal in this channel.

$$Sn_{out}(t) = \psi_{11}(\tau) * \psi_{FSK}(\tau)\,, \tag{6}$$

where $\psi_{11}(\tau)$ – ACF of LFM signal, $\psi_{FSK}(\tau)$ – correlation function of FSK signal, * – convolution sign.

The envelope of the ACF of the LFM signal is a function of $sinc(t)$. $Lim(\sin c)_{npu\Delta F\to\infty} = \delta(t)$. And the convolution $\delta(t)$ with any other function – $s(t)$ defines this function $s(t)$ itself [3].

Since ΔF_{LFM} – frequency deviation in the LFM signal, is a certain value, the envelope of signal at the output of the channel processing $S_{out}(t)$ is an estimate of the envelope ACF of the FSK signal. For the channel, for which $Kn(j\omega)\times Kn^*(j\omega) \neq |Kn(j\omega)|^2$, the envelope of the signal at the channel output will be an evaluation of the envelope CCF of the FSK signal in that processing channel and the IR ($n+1$) tag. With a certain processing algorithm in the control and processing module, the task of tag identification in a certain time period of emission can be solved.

Comparison of system work

A program for calculating the output signal of the system channel on the computer has been developed. Formulas (5) and (6) were used for calculation. If the IR of the tag was "matched" with the processing filter IR (FSK signal) in the reader's n-th channel, the signal at the channel output corresponded to the ACF code of the tag. Otherwise, the signal at the channel output corresponded to the CCF code of the tag and the code of IR of the channel. After the calculations, the envelope of the received radio signals was analyzed. During the calculations, the values of envelope ACF and CCF were normalized. For both systems the correlation method of signal classification was used, where the decision about the recognition of the mark is taken if the signal at the output of the processing system exceeds a certain threshold, forwards determined. Since the CCF signal is always much smaller than the ACF signal, then the smaller the maximum CCF signal value, the smaller the recognition threshold in the system can be determined. This value is particularly important if a certain number of labels are polled at the same time. For this reason, the criterion for system comparison was the CCF value normalized to the maximum ACF value resulting from the signal processing in each system.

The operating (carrier) frequency of LFM, FSK signals and IR tags – f_0 is 1GHz. The active spectrum width of the LFM signals is limited by the value ΔF, equal to 170MHz. The symbol frequencies are arranged in the FSK signal according to the code relative to f_0 frequency. The frequency difference from symbol to symbol in the FSK signal is Δf. Symbol frequencies in IR tags were picked of the code sequences described in [2]. The change in frequencies from symbol to symbol is the same as in the FSK signal. In this paper, 17 – symbol code sequences were selected for the study. The number of frequencies in the signal – q is equal to the number of symbols in the code sequence M, $M=q=17$. Δf was determined by the ratio $\Delta f=\Delta F/q=170/17=10$MHz. The symbol duration was chosen from the $t_{symb}=1/(2\Delta f)=1/(2*10\text{MHz}) = 50$ns [1].

The duration of the signal is – t_s, $t_{signal} = M * t_{symb} = 850$ns.

Frequency deviation in the LFM signal – ΔF_{LFM} is selected equal to the active spectrum width of the FSK signal, because in the spectral area the signals must be matched.

For example, Table 1 shows the calculation results of normalized envelope CCF_{max} for 10 pairs of codes. The values of the obtained maximum CCF are normalized to the maximum ACF.

Table 1 – Values of normalized envelope CCF_{max} calculated for systems with different interrogation signals.

CCF_{max}	FSK	0.161	0.167	0.185	0.157	0.159	0.175	0.179	0.134	0.183	0.206
	LFM	0.172	0.186	0.216	0.17	0.18	0.183	0.201	0.149	0.213	0.211

To evaluate the results obtained, an average value of CCF_{max} for each system was found.

The average value of the normalized envelope of the CCF_{max}, in a system where the FSK radio pulse was used as an interrogation signal, was 0.1706. In the system where the interrogation signal was the LFM signal – 0.188.

On the basis of averaging calculations on a large number of pairs of code sequences [2], we can say that the average values of normalized envelope CCF_{max} for both systems are approximately the same.

Figures 5,6 show examples of normalized envelope ACF and CCF calculated on computer for 17 symbol code pairs.

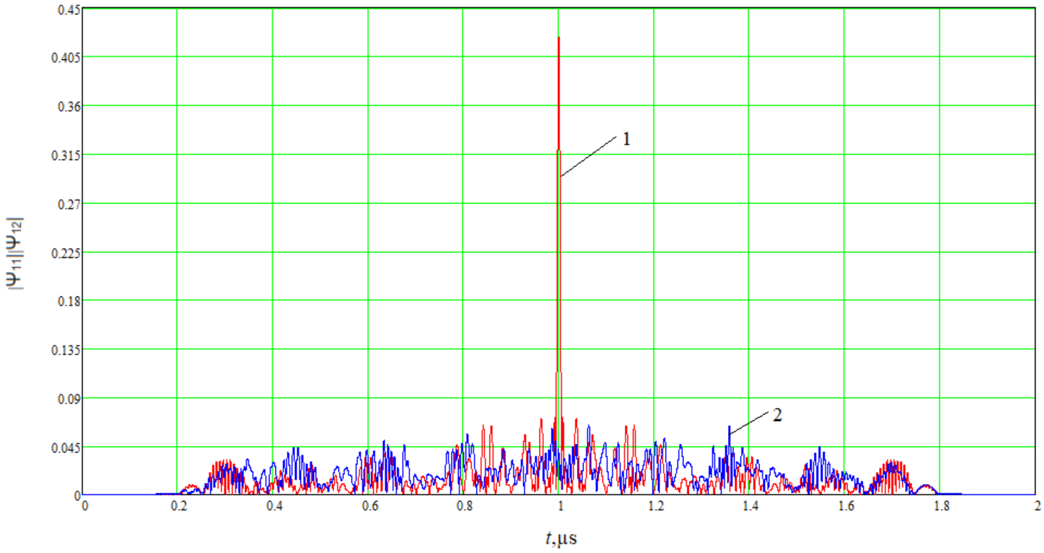

Figure 5. Plots of envelopes of ACF (1) and CCF (2) for17-symbol pair of codes, in the system where the interrogation signal are FSK signal

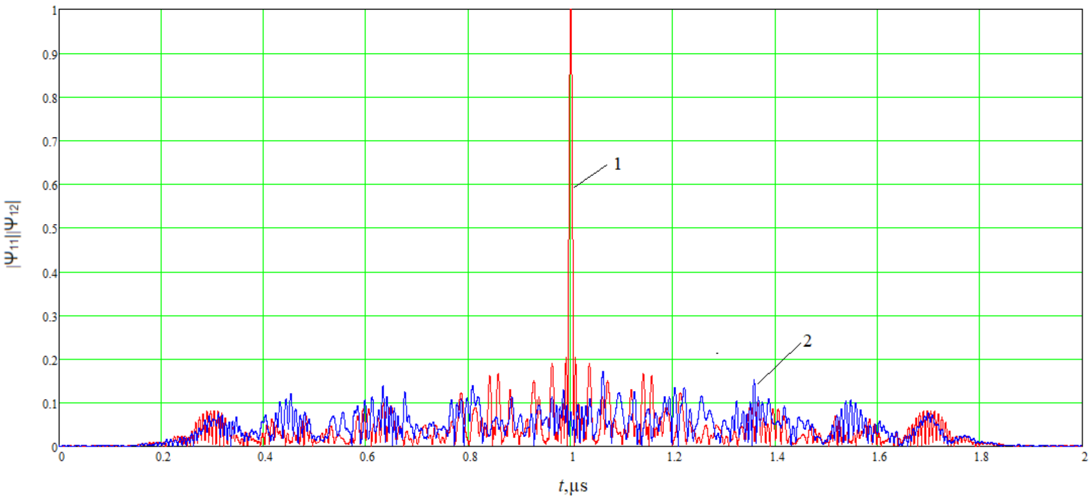

Figure 6. Plots of envelopes of ACF(1) and CCF(2) for17-symbol pair of codes, in the system where the interrogation signal are LFM signal

Conclusions

Accordingly research it is possible to assert that the system with the LFM signal allows to solve problems of tag identification. The results of statistical processing show that the level of average normalized value of envelope CCF_{max} in the system with the use of LFM signal is slightly higher (approximately – 0.02) in comparison with the system in which the FSK signal is used. The advantage of the system with the LFM signal is the simplification of the reader transmitter. At the same time the structure of the processing module of the signal received by the reader becomes more complex. The use of the identification system with the LFM signal allows keep in mind of the reader more information about codes of tags without complicating the work of the transmitter.

REFERENCES

1. Fedorov I., Research of methods formation SAW tags for identification systems / The fifteenth ISA European students paper competition (ESPC-2019). Bulletin of the Department «Distance education in engineering» of the SUAI. SPb.: SUAI, 2019. p. 37-41.

2. Жежерин А.Р., Чугунов А.А. Разработка и исследование кодовых последовательностей большого объема для идентификационных меток на ПАВ / Волновая электроника и ее применения в информационных и телекоммуникационных системах. XXI международная конференция ГУАП. Сб. статей. СПб.: ГУАП, 2018. С. 112-118.

3. Баскаков С.И. Радиотехнические цепи и сигналы. Учебник. 3-изд. перераб. дополн. М.: Высшая школа 2000 год. 462 стр.

OUTPUT QUANTIZATION OF BINARY INPUT AWGN CHANNEL FOR DECODING OF 5G LPDC CODES

Fominykh Anna

Student
Saint-Petersburg State University of Aerospace Instrumentation,
190000, St. Petersburg, st. B. Morskaya, 67
E-mail: aawat@ya.ru

Abstract
We study the effects of quantization at the output of a binary-input additive white Gaussian noise channel on the performance of 5G NR low-density parity-check (LDPC) codes under belief propagation decoding.
Keywords: LDPC, 5G, quantization.

INTRODUCTION

Low-density parity-check codes (LDPC codes) were firstly proposed by Robert G. Gallager in 1962 [1], but due to the limitation in computational effort in implementing the coder and decoder for such codes, LDPC codes were ignored for almost 30 years. LDPC codes were rediscovered by David Mackay in the 1990s and subsequent development of computers arose a new wave of interest to LDPC codes, which deserve attention due to the near-Shannon-Limit error-correcting capability, low error-floor [2], and easy design with parallel decoding.

Most recently, quasi cyclic LDPC (QC-LDPC) codes have been recommended by 3GPP as the channel coding scheme for the enhanced mobile broadband data channel of 5G communication [3], since QC-LDPC codes are able to reach the same decoding performance as previously used turbo codes, but at the same time allowing rate-compatible property [4], and can support multiple lifting sizes. These properties make such codes easily adapt various information lengths and rate matching. The reinvention of LDPC codes with performance superior to that of turbo codes led to similar work on quantization for LDPC codes for following implementation in hardware according to its restrictions. Furthermore, since these codes are used as a main coding scheme, it is of a great interest to investigate the channel quantization that will lead to the best decoding performance.

The following quantizers will be considered: uniform and non-uniform such as optimizing the equivalent channel capacity, cutoff-rate [5], [6]. We focus on the case of the binary input additive white Gaussian noise (BI-AWGN) channel with quantized output values.

LDPC codes

A binary (n,k) linear code is a k -dimensional subspace of an n-dimensional vector space over $\mathbb{F}_2$. If a parity-check matrix of a code is sparse, then the corresponding code is called a low-density parity-check (LDPC) code. The sparse nature of LDPC codes means that decoding processes have a fast run-time, as there are fewer operations to compute when compared to a non-sparse parity-check matrix. It can be specified by a matrix $\mathbf{H}$. The parity check matrix is usually visualized as a bipartite graph (Tanner graph) between check nodes and variable nodes, as shown in Fig. 1.

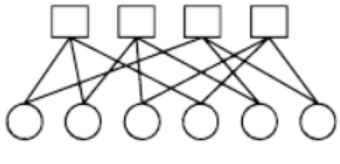

Figure 1 – Tanner graph

Every variable node of the graph corresponds to a column of $\mathbf{H}$, while every check node corresponds to a row. The example of parity-check matrix

$$\mathbf{H} = \begin{bmatrix} \mathbf{1} & \mathbf{1} & \mathbf{0} & \mathbf{1} & \mathbf{0} & \mathbf{0} \\ \mathbf{0} & \mathbf{1} & \mathbf{1} & \mathbf{0} & \mathbf{1} & \mathbf{0} \\ \mathbf{1} & \mathbf{0} & \mathbf{0} & \mathbf{0} & \mathbf{1} & \mathbf{1} \\ \mathbf{0} & \mathbf{0} & \mathbf{1} & \mathbf{1} & \mathbf{0} & \mathbf{1} \end{bmatrix}$$

and its corresponding Tanner graph

5G QC-LDPC codes

The main requirements for codes of a new standard were low complexity encoding and decoding procedures and support of multiple lifting sizes and rates. Choice of QC-LPDC codes fulfilled the first requirement, because its structure allows efficient encoding and decoding. A binary QC-LDPC code is defined by the null space of sparse parity-check matrix over $\mathbb{F}_2$, which consists of an array of circulants

$$\mathbf{H}_{\mathbf{QC}} = \begin{bmatrix} \mathbf{H}_{\mathbf{1,1}} & \mathbf{H}_{\mathbf{1,2}} & \cdots & \mathbf{H}_{\mathbf{1,\rho}} \\ \mathbf{H}_{\mathbf{2,1}} & \mathbf{H}_{\mathbf{2,2}} & \cdots & \mathbf{H}_{\mathbf{2,\rho}} \\ \cdots & \cdots & \cdots & \cdots \\ \mathbf{H}_{\boldsymbol{\gamma},\mathbf{1}} & \mathbf{H}_{\boldsymbol{\gamma},\mathbf{2}} & \cdots & \mathbf{H}_{\boldsymbol{\gamma},\boldsymbol{\rho}} \end{bmatrix}.$$

Also, one must mention that the parity-check matrix of QC-LDPC codes can be equivalently represented in a compact manner through their exponent matrix, whose entries are the integer values that are shifts of corresponding circulants. Besides QC structure, these standard codes simultaneously must possess rate-compatible property and support multiple lifting sizes. These properties make such codes easily adapt various information lengths and rate matching. In order to implement various information lengths and rate adaptation, shortening and puncturing methods are used. Puncturing is applied to both the information and parity bits in the codeword, while shortening is just designed by zero padding for the information bits [3].

Quantization

Quantization, in mathematics and digital signal processing, is the process of mapping input values from a large set to output values in a smaller set, often with a finite number of elements. We focus on the case of the binary input additive white Gaussian noise channel with quantized output values to K levels, usually K is a power of two since it represents the number of bits that is used for a received value in the decoder. The additive white Gaussian noise channel maps the input vector $\mathbf{c}$, to the vector $\mathbf{x} \in \{+1,-1\}$ and then adds the result with Gaussian white noise to give an output vector $\mathbf{y} = \mathbf{x} + \mathbf{n}$, where $\mathbf{n} \sim \mathcal{N}(0,\sigma^2)$.

Uniform and non-uniform quantization

In the uniform quantization after the announcing the bounds [6], area between these bounds is uniformly quantized into intervals, symmetric with respect to the origin. It is supposed by non-uniform quantization that the quantization intervals are not of the same size, intervals became narrower closer to zero. Uniform quantization method is applied widely because of its simple realization and low complexity in application. In order to reach similar performance of non-uniform quantization for uniform quantization, a larger maximum limit, smaller minimum limit and narrower quantization interval are required.

Capacity-maximizing quantization

Channel capacity C is the maximization of mutual information over all input distributions $P(X)$, so a reasonable metric for designing channel quantizers is to similarly maximize mutual information between the channel input X and the quantizer output Z:

$$C = \max I(X;Z) = \max \sum_{x\in X, z\in Z} P_{X,Z}(x,z) \log \frac{P_{X,Z}(x,z)}{P_X(x)P_Z(z)}.$$

The algorithm of calculating the channel capacity that is used in this paper is described in [7], [8] and has cubic complexity in the number discrete channel outputs M, so it must be mentioned that before applying the algorithm, we suppose that the AWGN channel is first uniformly quantizing to a DMC with M outputs.

Cutoff-rate maximizing quantization

From [5] the cutoff-rate for the equivalent equiprobable binary input discrete memoryless channel is

$$R_0 = \max_{P_X}\left[-\log_2 \sum_{z\in Z}\left(\sum_{x\in X} P_X(x)P_{Z|X}^{1/2}(z\mid x)\right)^2\right].$$

Using cutoff-rate as a metric for designing channel quantizers is reasonable because its an upper bound on bit-error probability. Namely, R_0 restricts bit-error probability $P_b < \sum_{w=d}^{N} A(w)D_0^w$, where $D_0 = e^{-RE_b/N_0}$ is a function of the channel transition probabilities called Bhattacharyya parameter, $A(w)$ – is the number of codewords of weight w, $R_0 = 1 - log_2(1 + D_0)$. Therefore, minimizing D_0 and thus maximizing R_0 over all possible choices of quantization levels or decision boundaries achieves minimization of bit-error probability [9].

Simulation results

In this Section we simulate the LDPC codes considered previously (simulation is applied to base graph 1 with information lengths 100 and 1000 and rate 8/9) with quantized channel measurements using uniform and non-uniform quantization such as capacity-maximizing, cutoff-rate-maximizing quantizers and compare their performance.

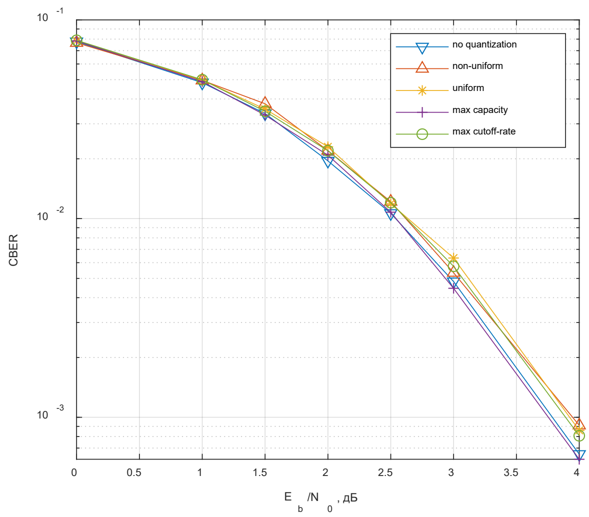

Figure 2 – Performance of 5G LDPC code with K = 100

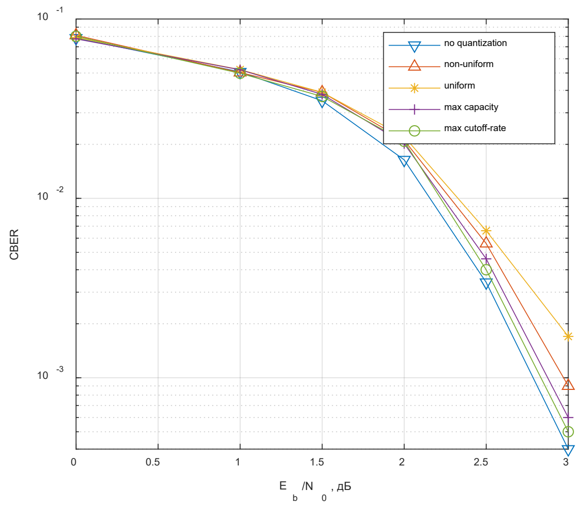

Figure 2 – Performance of 5G LDPC code with K = 1000

CONCLUSION

The paper examined different quantizers of BI-AWGN channel for 5G LDPC codes under belief propagation decoding. From a simulation results it may be concluded that with increasing the code length cutoff-rate maximization yields better performance than capacity maximization.

REFERENCES

[1] R. Gallager, "Low-density parity-check codes," in *IRE Transactions on Information Theory*, vol. 8, no. 1, pp. 21-28, January 1962.

[2] T. Richardson, Error-floors of LDPC codes Proceedings of the 41st Annual Conference on Communication, Control and Computing, 2003.

[3] H. Li, B. Bai, X. Mu, J. Zhang and H. Xu, "Algebra-Assisted Construction of Quasi-Cyclic LDPC Codes for 5G New Radio," in *IEEE Access*, vol. 6, pp. 50229-50244, 2018.

[4] T. Richardson and S. Kudekar, "Design of Low-Density Parity Check Codes for 5G New Radio," in *IEEE Communications Magazine*, vol. 56, no. 3, pp. 28-34, March 2018.

[5] G. Jeong and D. Hsia, "Optimal quantization for soft-decision turbo decoder," *Gateway to 21st Century Communications Village. VTC 1999-Fall. IEEE VTS 50th Vehicular Technology Conference (Cat. No.99CH36324)*.

[6] J. Cho, J. Kim and W. Sung, "Optimal Output Quantization of Binary Input AWGN Channel for Belief-Propagation Decoding of LDPC Codes," *2012 IEEE Workshop on Signal Processing Systems*, Quebec City, QC, 2012, pp. 282-287.

[7] B. M. Kurkoski and H. Yagi, "Quantization of Binary-Input Discrete Memoryless Channels," in *IEEE Transactions on Information Theory*, vol. 60, no. 8, pp. 4544-4552, Aug. 2014.

[8] B. M. Kurkoski and H. Yagi, "Finding the capacity of a quantized binary-input DMC," *2012 IEEE International Symposium on Information Theory Proceedings*, Cambridge, MA, 2012, pp. 686-690.

[9] F. J. MacWilliams and N. J. A. Sloane. The theory of error correcting codes / F.J. MacWilliams, N.J.A. Sloane North-Holland Pub. Co.; sole distributors for the U.S.A. and Canada, Elsevier/North-Holland Amsterdam; New York: New York, 1977.

RESEARCH OF METHODS OF ANALYSIS OF SPEECH SIGNALS

Gerasimov Serafim

Saint-Petersburg State University of Aerospace Instrumentation
Saint-Petersburg, Russia
E-mail: gerasimov310796@gmail.com

Abstract

The article presents a study of the most common methods for analyzing speech signals. In this paper, one-word speech signals are examined. The methods of constructing spectrograms, the use of cepstral mel frequecy coefficients, and the algorithm for the dynamic transformation of the time scale are considered.
The object of study is a set of 4 pre-recorded commands:

- two commands «on» with slight differences in pronunciation;
- command «off»;
- command «close».

INTRODUCTION

There are various methods for analyzing speech signals in both the time and frequency domains. When it is necessary to process sequences of words and sentences, complex methods are usually used that combine hidden Markov models [1] or neural networks to predict the most likely sounds in sequences. When processing a single word, simpler methods based on spectral analysis or time series comparison can be used.

The purpose of this work is to study various methods of analysis of speech signals consisting of one word. The following methods will be considered:

- construction and analysis of spectrograms;
- application of mel cepstral coefficients;
- dynamic time warping algorithm.

CONSTRUCTION AND ANALYSIS OF SPECTROGRAMS

The spectrogram is a graph of the dependence of the spectral power density of the signal on time. To build such a dependence, the window Fourier transform is used. As a result, gaps with certain frequency and time ranges are obtained that are characterized by the amplitude of the signal in this region. On the graph, the amplitude-yes is visualized using brightness or color (usually the brighter the area, the greater the amplitude-yes) [2].

Spectrogram simulation results are presented in Figure 1.

As can be seen from Figure 1, the spectrograms (a – b) almost completely coincide in their frequency composition, although they have different time intervals. Despite the fact that the word “off” consists of almost the same sounds, its spectrogram is significantly different from the spectrograms of the “on” commands. The “close” command has a high-frequency component, which is not peculiar to all other audio samples presented. This can be explained by the presence of voiced sound in the composition of the word.

APPLICATION OF MEL FREQUENCY CEPSTRAL COEFFICIENTS

Mel-frequency cepstral coefficients (MFCC) are a relatively small set of values that characterize the frequency properties of the signal.

This method is based on the fact that the frequency bands are distributed evenly on a logarithmic scale, which is characteristic for a person’s sound perception [3]. The value obtained during the conversion is usually called mel, and its dependence on frequency is shown in Figure 2.

As in the construction of the spectrogram, this method also uses the window Fourier transform, but for the voice command represented by one word, the transformation can be taken over the entire sample size. The obtained spectral values pass through triangular window filters, and then a discrete cosine transform is applied to the obtained values in each window. The amplitudes of the resulting spectrum represent the final result — the cepstral melofrequency coefficients.

The simulation results of the MFC coefficients are shown in Figure 3.

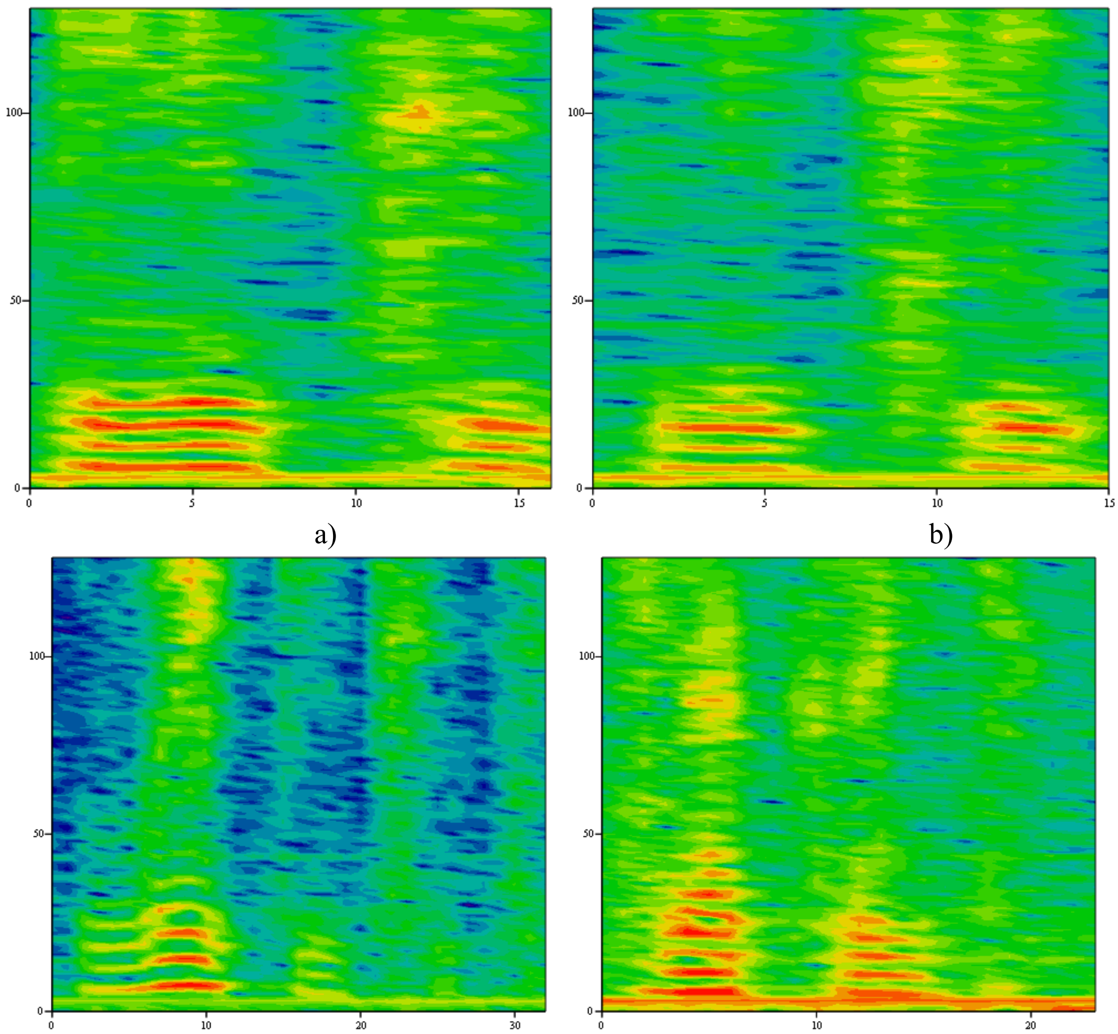

b) *d)*

Figure 1 – Spectrograms of various voice commands:
a – b) the «on» command pronounced with different intonation; c) the «off» command; d) the «close» command

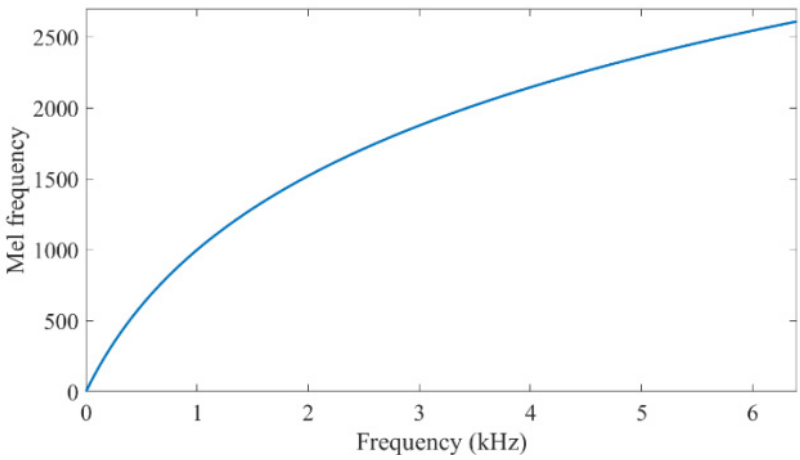

Figure 2 – Mel scale

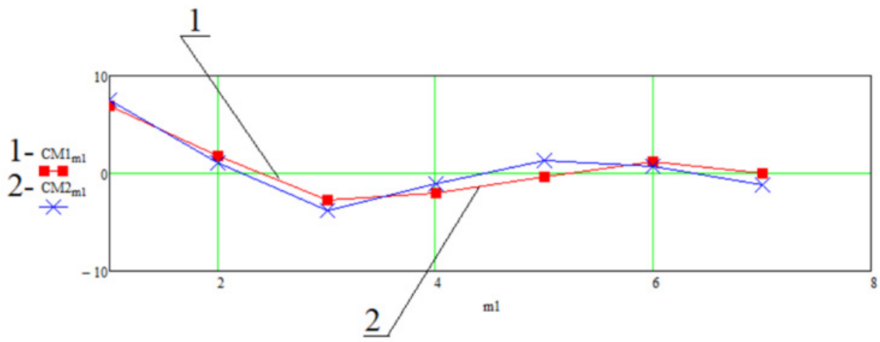

1 – command «on», 2 – command «on»

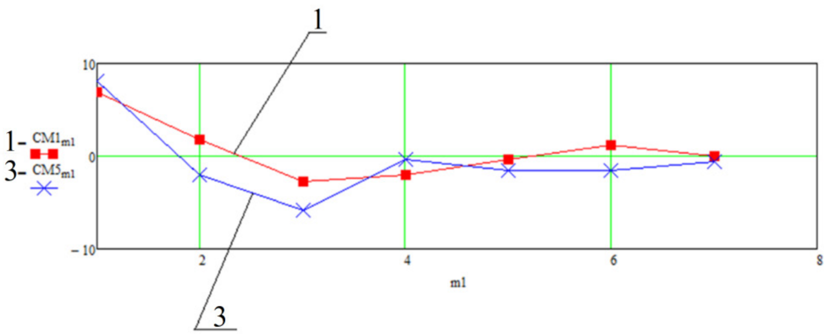

1 – command «on», 3 – command «off»

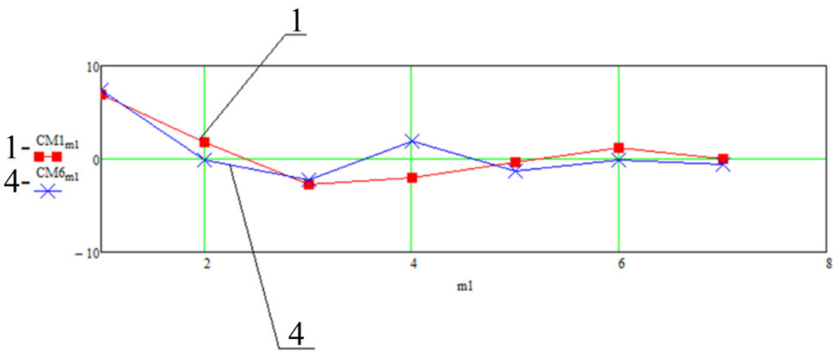

1 – command «off», 4 – command «close»

Figure 3 – Comparison of MFCC sequences of voice commands

As can be seen from Figure 3, the MFCC “on” voice commands (1 and 2) are very close in value. The rest of the voice commands vary greatly in terms of coefficients.

DYNAMIC TIME WARPING ALGORITHM

One of the simple measures for calculating the distances between sequences is the Euclidean metric. The distance in such a space is determined by the formula (1):

$$d(p,q)=\sqrt{\sum_{k=1}^{n}(p_k-q_k)^2}\ , \tag{1}$$

where p and q are sequences in Euclidean space.

This measure cannot be used when processing speech signals. One and the same word cannot be pronounced the same way – all the same, some kind of bias will occur on the time and frequency scale, even without taking into account the interference. The Dynamic Time Warping (DTW) algorithm was developed with the aim of establishing the consistency of sequences on a time scale [4]. A comparison of time series with the Euclidean metric and the DTW algorithm is presented in Figure 4.

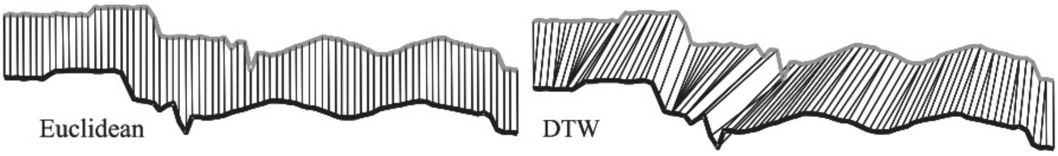

Figure 4 – Comparison of time series with the Euclidean metric and DTW algorithm

The obtained simulation results of the DTW algorithm are presented in Figure 5. One of the sequences obtained by processing the word "on" is used as a reference for comparison.

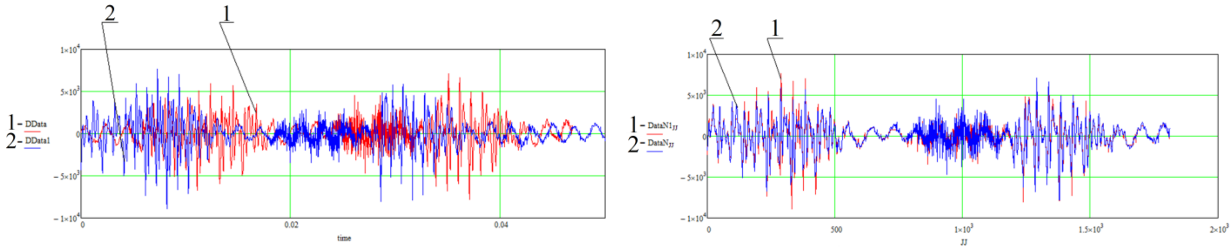

Before using DTW After using DTW

1 – command «on», 2 – command «on»

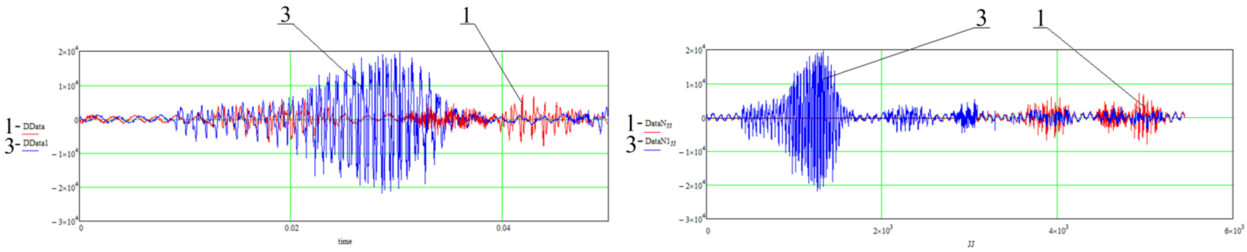

Before using DTW After using DTW

1 – command «on», 3 – command «off»

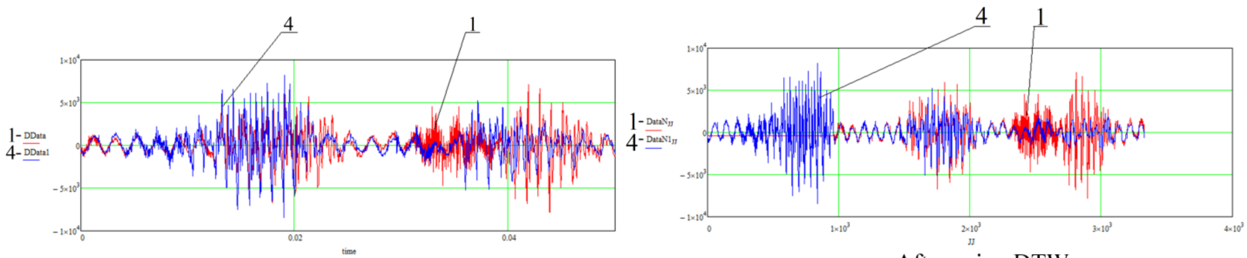

Before using DTW After using DTW

1 – command «off», 4 – command «close»

Figure 5 – Comparison of speech signals before and after using the DTW algorithm

If speech signals correspond to the same word, then after applying the dynamic transformation algorithm of the time scale, the sequence data practically coincide, having some differences in signal level and time (commands 1 and 2). When comparing different words, the algorithm can find similar fragments, but in general, the sequences do not coincide in signal level and have direct degenerate parts (commands 3 and 4).

CONCLUSION

All the methods presented in this article have, to one degree or another, coped with the task of comparing various speech signals.

The method of constructing spectrograms is the fastest in terms of performing computational operations and, if the time and frequency boundaries are set correctly, visualizes the obtained results well.

The MFCC calculation method requires a bit more processing time, in comparison with the spectrogram, because it implements a fast Fourier transform, as well as a discrete cosine transform. This method allows to identify the main frequency properties of the word for comparison using a small set of coefficients, which makes it possible to effectively compare voice commands represented by speech signals.

The DTW algorithm allows signal processing in a time rather than a frequency scale. A significant drawback is that of the presented methods, this one is processed the longest. With this method of comparing sequences, the differences in the signals are clearly noticeable, because when they do not match, they do not coincide in level and possess straight-line degenerate segments.

REFERENCES

1. Lawrence R. Rabiner. A Tutorial on Hidden Markov Models and Selected Applications in Speech Recognition // Proceedings of the IEEE. Feb. 1989 vol. 77, No.2.

2. Trakhtman A.M., Trakhtman V.A. Fundamentals of the theory of discrete signals on finite intervals. – M.: Soviet Radio, 1975 208s.

3. V. Tyagi On desensitizing the Mel-cepstrum to spurious spectral components for robust speech recognition / V. Tyagi, C. Wellekens // Proceedings. (ICASSP '05). IEEE International Conference on Acoustics, Speech, and Signal Processing, 2005 .-- P. 1-21.

4. Lawrence Rabiner Conferences in Dynamic Time Warping for Discrete Word Recognition / Lawrence Rabiner, Aaron G Rosenberg, Stephen E. Levinson // IEEE Transitions on Acoustics Speech and Signal Processing, January 1979. – P. 575 – 582.

DETERMINING THE MEASURE OF SIMILARITY OF TEXTS

Glushkova Ekaterina

Saint-Petersburg State University of Aerospace Instrumentation,
Saint-Petersburg, Russia

E-mail: cate.glushkova@yandex.ru

Abstract
This article provides two distinct approaches to solving a problem of measuring text similarity. The first approach is based on widely used term frequency–inverse document frequency metric (TF-IDF). The second approach utilizes a generative statistical model – latent Dirichlet allocation (LDA).
Keywords: term frequency–inverse document frequency, latent Dirichlet allocation, text comparison.

Introduction

There are thousands of new texts published on the Internet every hour such as news articles, blog posts, wiki pages, etc. It is impossible for a single human to keep track of even a small part of them so natural language processing technics must be applied. A significant number of texts published worldwide cover the same or similar stories and news, so they can be grouped together in order to make their analysis easier. Here comes the problem of measuring text similarity.

TF-IDF algorithm

Different methods are used to implement text comparison algorithms, one of which is TF-IDF, which states for term frequency–inverse document frequency.

The metric that this method is based on calculates the significance score for each word contained in the text.

The parameter that is calculated using the metric, also called TF-IDF, is calculated as the product of two internal parameters [1,2]:

$$\text{tf-idf}(t,d,D) = \text{tf}(t,d) * \text{idf}(t,D). \quad tf - idf(t,d,D) = tf(t,d) * idf(t,D)$$

The first multiplier TF (term frequency) is the ratio of the number of repetitions of a word in a document to the total number of words in it:

$$\text{tf}(t,D) = \frac{n_t}{\sum_k n_k},$$

where n_t – the number of occurrences of a word t in the document. The denominator of a fraction is the total number of words.

Using the second IDF multiplier (inverse document frequency), the weight (i.e. the value for calculations) of common words (pronouns, prepositions, introductory words, etc.), which obviously do not affect the similarity/difference of texts, is decreased:

$$\text{idf}(t,D) = \log \frac{D}{\{d_i \in D \mid t \in d_i\}}$$

where D — number of documents in the collection; $\{d_i \in D \mid t \in d_i\}$ – the number of documents from the collection D, that contain t.

Obviously, the weight of a word contained in all documents in the collection will be zero – *log1=0.* The base of the logarithm is not specified in the formula – it can be anything, since it causes the weight of each word to change by a constant value, which does not affect the ratio of weights in any way.

The size of the collection shown in the formula is important to consider, because the larger it is, the less likely it is that random matches will affect the calculation. Thus, words that are frequently used within a particular document and rarely used in other documents in the collection get the most weight.

To study the quality of the algorithm using the TF-IDF metric, three texts were used, two of which are articles on the same topic from different news sources («Israeli election: Netanyahu and Gantz both claim victory» [3] and «Benjamin Netanyahu's re-election plans in limbo as Israeli election too close to call» [4]), and the third is an article on another topic («Coca-Cola reveals how much plastic it uses» [5]). The data collected after running the algorithm is shown in table 1.

Table 1. Results of comparing texts using the tf-idf metric

	Text 1	Text 2	Text 3
Text 1	1	0.806	0.369
Text 2	0.806	1	0.334
Text 3	0.369	0.334	1

The unit coefficients in the table indicate that the document is identical to itself, the other results are symmetrical relative to the main diagonal, since the results of comparing a pair of texts do not depend on the order in which they are inserted into the formula.

Further, to increase the accuracy of the algorithm results, we used libraries of «stop words», which are words that do not carry a semantic (and, including, thematic) load, for example, 'somewhere', 'and', 'mine', 'too', 'also', and the like. After the realization of the comparison with the use of these libraries provided data:

Table 2. Results of comparing texts using the tf-idf metric, refined using the «stop-words» libraries

	Text 1	Text 2	Text 3
Text 1	1	0.554	0.020
Text 2	0.554	1	0.022
Text 3	0.020	0.022	1

After removing the «stop words», the results significantly decreased: the similarity coefficient for texts on the same topic (texts №№ 1 and 2) changed by several tenths, and for texts on different topics (texts №№ 1 and 3 and also №№ 2 and 3) by almost an order of magnitude.

Using stemming also improved the quality of results. Stemming is an algorithm that allows to normalize words, i.e. highlight their basis. This type of text processing allows to identify words that have a similar meaning as identical, even if they may differ significantly in their spelling.

The study was conducted using the Porter stemmer [6], which does not use libraries of word bases, but only cuts off endings and suffixes, applying a number of rules based on the features of the language. Because of this, it works with a certain margin of error, although faster than the others. The results of comparison with the normalization of this stemmer are presented in table 3.

Table 3. Results of comparing texts using the tf-idf metric, refined with the help of «stop-words» libraries and normalization

	Text 1	Text 2	Text 3
Text 1	1	0.585	0.035
Text 2	0.585	1	0.026
Text 3	0.035	0.026	1

All the coefficients in the table have increased because words that differ from each other only by their endings and suffixes were brought to the same word basis and counted as similar.

Thus, using the TF-IDF method, one can clearly tell whether the presented texts are similar, or have a different thematic focus.

LDA method

There is also another method for determining the measure of similarity of texts, called LDA (Latent Dirichlet allocation), that defines the results of calculations using implicit groups and thematic modeling [7].

To apply the method to a collection of texts, one must convert it to a term-document matrix with dimensions N *x* W, where N – number of documents in the collection, and W – the number of unique words contained in the texts. For this matrix and the previously set number of topics T (in this case, the word topic defines some abstract entity, and rarely coincides with the topics that exist in the text collection), two distributions are created: N *x* T – distribution of topics by text, and T *x* W – distribution of words by topic.

The results of realization the LDA method depend on the collection of texts and the number of topics, so having a collection of the selected texts, it remains to determine the number of topics.

To select the optimal number of topics, we used a collection consisting of two texts on a similar topic, which allowed us to track the ratio of the number of topics and the similarity coefficient.

Next, a set of the number of topics from 10 to 100 in increments of 10 was used. For each number of topics, so many LDA models were created that the average similarity coefficient of the two texts could be approximately determined.

The obtained data, taking into account the LDA parameter (random_state) that is responsible for creating different models for each realization of the algorithm, are shown in figure 1.

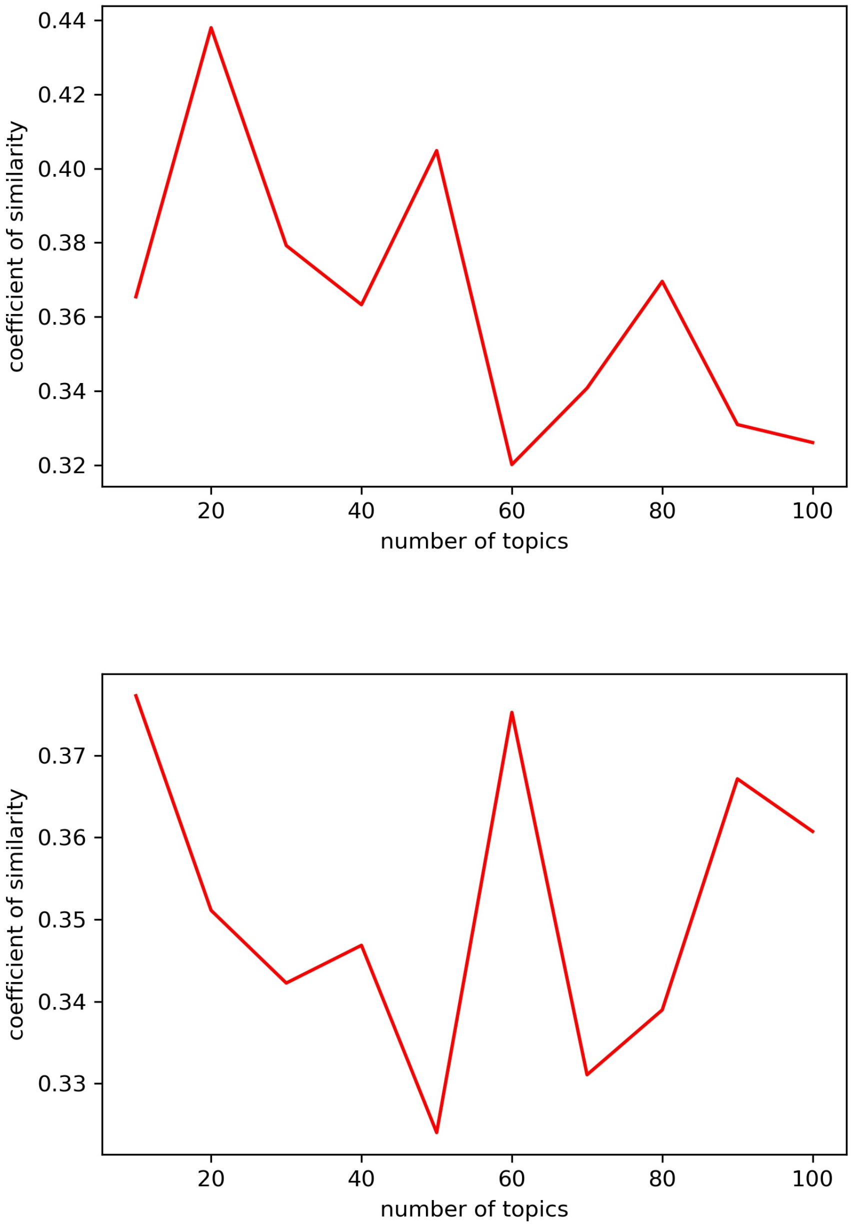

Figure 1. Results of realization the lda metric with the random_state parameter

Because of the parameter responsible for updating the model after each realization, getting data about the optimal number of topics required further calculations.

Two collections consisting of two texts each were used to study changes in the number of topics. The first includes texts with similar themes, and the second – with different. This is necessary in order to know that the data did not overlap, otherwise, it will not be possible to say unequivocally whether the texts presented are similar, or have different thematic focus.

To increase accuracy, the number of LDA models created has been increased for each number of themes, and the average standard deviation of the similarity coefficient is found to check the data spread. The result of calculations is shown in figure 2:

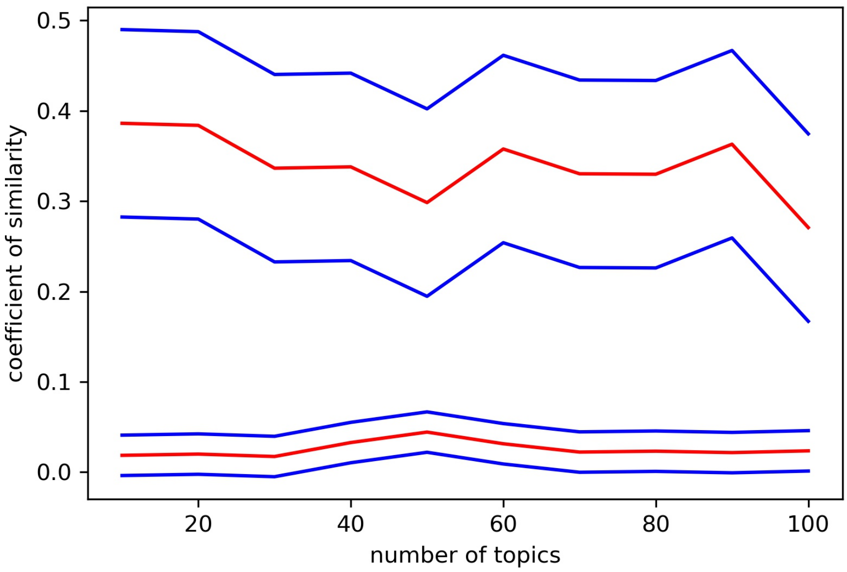

Figure 2. Results of calculations using the lda metric for pairs of texts with similar and different themes.

The graph shows that 95% confidence intervals for similarity coefficients of identical texts and texts on different topics do not overlap, which allows to uniquely determine the relationship between the texts. It also shows that an increase in the number of topics has a negligible effect on the average value, from which it can be concluded that an increase in the number of topics affects only the accuracy, but not the definition of similarity of texts. It should be noted that increasing the number of topics increases the number of created LDA models, and therefore increases the running time of the program that implements the comparison algorithm.

To improve the accuracy of realization of the LDA method (using the data of the conducted research) on a collection of three texts, the «stop-words» libraries and the normalization method were used in the same way as when working with the TF-IDF method [8]. The results of realization of this algorithm are shown in table 4.

Table 4. Results of comparing texts using the lda metric, refined using the «stop-words» libraries and normalization

	Text 1	Text 2	Text 3
Text 1	1	0.701	0.021
Text 2	0.701	1	0
Text 3	0.021	0	1

Conclusion

Using the LDA method, it is possible to clearly distinguish similar texts from different ones. Moreover, because of the gap between this method and method TF-IDF, it is noticeable that the LDA metric more accurately determines the similarity of texts, but because of the parameter of the number of topics, which is set separately, the time of working with this algorithm increases, unlike the realization of TF-IDF.

REFERENCES

1. Breitinger C., Gipp B., Langer S. Research-paper recommender systems: a literature survey // International Journal on Digital Libraries. 2015. N 17 (4). P. 305–338.

2. Jones K. A Statistical Interpretation of Term Specificity and Its Application in Retrieval // Journal of Documentation. 1972. N 28. P. 11–21.

3. BBC News. Israeli election: Netanyahu and Gantz both claim victory. URL: https://www.bbc.com/news/world-middle-east-47874948 (date of request: 19.03.2020).

4. CNN World. Benjamin Netanyahu's re-election plans in limbo as Israeli election too close to call. URL:https://edition.cnn.com/2019/04/09/middleeast/benjamin-netanyahu-israel-election-exit-poll-intl/index.html (date of request: 19.03.2020).

5. BBC News. Coca-Cola reveals how much plastic it uses.

URL: https://www.bbc.com/news/newsbeat-47569233 (date of request: 19.03.2020).

6. Porter M. An algorithm for suffix stripping // Program. 1980. N 14 (3). P. 130−137.

7. Blei, David M.; Ng, Andrew Y., Jordan, Michael I. Latent Dirichlet allocation // Journal of Machine Learning Research. 2003. N 3. P. 993—1022.

8. Seventy-second international student scientific conference of SUAI: collection of reports in 4 p. P. 2. Technical science. SUAI., 2019. P. 203 – 205.

MATHEMATICAL MODEL OF A LINK WITH DISTRIBUTED PARAMETERS

Goncharova Viktoria

St. Petersburg State University of Aerospace Instrumentation
Saint – Petersburg, Russia
goncarovav344@yandex.ru

Abstract
The article considers a mathematical model of a link with distributed parameters. Results are obtained for a long electric line, which can be fully used in the synthesis of automatic control systems containing hydraulic pipeline lines (PL).
Keywords: parametric synthesis, linearization, ACS with distributed parameters, nonlinear systems.

As a link with distributed parameters, we consider a long line with no losses open at the end, that is, we assume that the load of the ACS under consideration is a device with an infinitely large output resistance. This makes it possible to take into account the wave phenomena of hydraulic shock in pipelines, and to take into account the wave processes in long electric lines when transmitting effects from one link of the automatic control system to another, or when regulating processes in the pipelines themselves or long lines.

The equation of an electric line without losses has the form [1]:

$$\begin{cases} -\dfrac{\partial u}{\partial x} = L\dfrac{\partial i}{\partial t}, \\ -\dfrac{\partial i}{\partial x} = c\dfrac{\partial u}{\partial t}, \end{cases} \tag{1}$$

where u – direction, i– current at arbitrary points defined by the coordinate x along the line; $L u C$ – inductance and capacitance of the line length unit.

The equation of the pipeline without taking into account losses has the form:

$$\begin{cases} -\dfrac{\partial P}{\partial x} = \rho_* \cdot \dfrac{\partial \vartheta}{\partial t}, \\ -\dfrac{\partial \vartheta}{\partial x} = \dfrac{1}{\rho_* \cdot \vartheta_0^2} \cdot \dfrac{\partial P}{\partial t}, \end{cases} \tag{2}$$

where P – pressure in the cross section of the PL at a time t; ϑ – the velocity of the liquid in the cross section PL at a time t; ρ_* – liquid density; ϑ_0 – the speed of sound in a liquid is PL.

The form of equations (1) and (2) shows that the processes in the hydraulic TL can be studied using an analog model of a four-pole electric line.

It is necessary to consider the following analogy: the character of change of pressure P and fluid velocity (equation (2)) corresponds to a change in voltage and current in the quadrupole. Additionally, the inductance of the electric circuit model is proportional to the density of the fluid , because of both the increased inductance slows down the transition process current and increasing the density of the liquid slows the speed of fluid flow in the PL. The capacity of a long electrical line C is inversely proportional to the value $\rho\vartheta_0^2$, since the increase in capacitance slows down the rise of voltage on the output line, which has the effect of slowing the transfer of pressure from entering the output of PL with decreasing speed of propagation of sound in the liquid PL.

Thus, based on the above analogy, the results obtained below for a long electric line can be fully used in the construction of a mathematical model for solving the problem of synthesis of hydraulic PL.

For a long electrical line without losses, the following equations are valid:

$$\begin{cases} u(x,s) = u_{вх}(s)\dfrac{ch\vartheta(l-x)}{ch\vartheta l}, \\ i(x,s) = u_{вх}(s)\dfrac{sh\vartheta(l-x)}{\rho ch\vartheta l}, \end{cases} \tag{3}$$

where $u_{вх}(s)$ - Laplace image of the line input voltage;

$$\rho = \sqrt{\frac{L}{C}};\ \nu = s\sqrt{LC}. \tag{4}$$

To solve the problem of parametric synthesis of nonlinear ACS containing links with distributed parameters, it is necessary to consider the following questions:

- defining boundary conditions for long-line averages;
- the definition of original $u_{вых}(t)$ and $i_{вых}(t)$, to use the latter in state equations describing the dynamics of ACS with distributed parameters;
- determining the boundary values of switching moments t_ρ nonlinear element.

Identify the originals $u_{вых}(t)$ and $i_{вых}(t)$ average length of the line in the case of an arbitrary type of impact $u_{вых}(t)$ at the exit of the line.

For an input action of an arbitrary type $u_{вых}(t)$, applied at the moment $t = 0$, the transition process at the output of the link under zero initial conditions can be determined based on the Duhamel-Carson integral for the transition function.

$$u_{вых}(t) = u_{вх}(0)h(t) + \int_0^t u_{вх}(\lambda)h(t-\lambda)d\lambda \tag{5}$$

where λ – auxiliary integration time, varying from zero to the current moment under consideration t, $h(t)$ – transition characteristic of a link.

In the case of a link with distributed parameters, the expression (5) will look like:

$$u_{вых}(t,x) = u_{вх}(0)h(t,x) + \int_0^t u_{вх}(\lambda)h(t-\lambda,x)d\lambda \tag{6}$$

Using the ratio (6), we determine the average length of the coordinates of the output of the link with distributed parameters, which coincides with the output of the system. As a result, we have:

$$\begin{aligned}\theta_{cp}(t) &= \frac{1}{l}\int_0^l \theta(t,x)dx = \\ &= \frac{1}{l}\int_0^l dx\left[u_{вх}(0)h(t,x) + \int_0^t u_{вх}(\lambda)h(t-\lambda,x)d\lambda\right]\end{aligned} \tag{7}$$

or after simple transformations we get:

$$\begin{aligned}\theta_{cp}(t) &= \frac{1}{l}u_{вх}(0)\int_0^l h(t,x)dx + \\ &+ \frac{1}{l}\int_0^l dx\int_0^t u_{вх}(\lambda)h(t-\lambda,x)d\lambda,\end{aligned} \tag{8}$$

Let's change the order of integration in the second integral of the relation (8):

$$\begin{aligned}\theta_{cp}(t) &= \frac{1}{l}u_{вх}(0)\int_0^l h(t,x)dx + \\ &+ \frac{1}{l}\int_0^t u_{вх}(\lambda)d\lambda\int_0^l h(t-\lambda,x)dx\end{aligned} \tag{9}$$

Denote

$$h_{cp}(t-\lambda)=\frac{1}{l}\int_0^l h(t-\lambda,x)\,dx, \tag{10}$$

Or when $\lambda=0$

$$h_{cp}(t)=\frac{1}{l}\int_0^l h(t,x)\,dx \tag{11}$$

Taking into account the accepted designations (10), (11), we finally have:

$$\begin{gathered}\theta_{cp}(t)=u_{вх}(0)h_{cp}(t)+\\ +\int_0^t u_{вх}h_{cp}(t)+\int_0^t u_{вх}(\lambda)h_{cp}(t-\lambda)\,d\lambda\end{gathered} \tag{12}$$

Using the relations (10), (11), it is possible to determine the originals of the average values of the transmission functions of the link along the line length with distributed parameters in the direction and current.

Figure $u(x,s)$ и $i(x,s)$ when the line is switched to a constant signal, the following originals correspond:

$$\begin{gathered}u(t,x)=1-\frac{4}{\pi}\sum_{K=0}^{\infty}(-1)^K\cdot\\ \cdot\frac{\cos\left(\frac{2K+1}{2}\cdot\frac{l-x}{l}\pi\right)cos\left(\frac{2\pi+1}{2}\cdot\pi\cdot\frac{t}{l\sqrt{LC}}\right)}{2K+1},\end{gathered} \tag{13}$$

$$\begin{gathered}i(t,x)=\frac{4}{\pi\rho}\sum_{K=0}^{\infty}(-1)^K\cdot\\ \cdot\frac{\sin\left(\frac{2K+1}{2}\cdot\frac{l-x}{l}\pi\right)sin\left(\frac{2\pi+1}{2}\pi\frac{t}{l\sqrt{LC}}\right)}{2K+1},\end{gathered} \tag{14}$$

Using equations (11), (10), and (13), we find the average length of the original value of the long line transfer function in terms of voltage at $\lambda=0$ and $\lambda\neq 0$.

$$h_{ucp}(t)=\frac{1}{l}\int_0^l u(t,x)\,dx \tag{15}$$

If $\lambda=0$ we get the following:

$$h_{ucp}(t)=\frac{1}{l}\int_0^l dx-\frac{4}{\pi}\sum_{K=0}^{\infty}(-1)^K\frac{\cos\left(\frac{2K+1}{2}\right)}{K+1}\cdot\frac{1}{l}\int_0^l\cos\left(\frac{2K+1}{2}\cdot\frac{l-x}{l}\pi\right)dx, \tag{16}$$

where

$$\tau=\frac{t}{l\sqrt{LC}}, \tag{17}$$

After integrating equation (16), we get the following:

$$h_{ucp}(t)=1-\frac{8}{\pi^2}\sum_{K=0}^{\infty}(-1)^K\times$$
$$\times\frac{\sin\left[(2K+1)\frac{\pi}{2}\right]\cos\left[(2K+1)\frac{\pi}{2}\tau\right]}{(2K+1)^2}; \qquad (18)$$

Then, after simple transformations, we bring the expression (18) to the form:

$$h_{ucp}(t)=1-\frac{4}{\pi^2}\left[\sum_{K=0}^{\infty}(-1)^K\frac{\sin\left[(2K+1)\frac{\pi}{2}(1-\tau)\right]}{(2K+1)^2}+\right.$$
$$\left.+\sum_{K=0}^{\infty}(-1)^K\frac{\sin\left[(2K+1)\frac{\pi}{2}(1+\tau)\right]}{(2K+1)^2}\right] \qquad (19)$$

where

$$\sum_{K=1}^{\infty}(-1)^K\frac{\sin\left[(2K+1)z\right]}{(2K+1)^2}=\frac{\pi}{4}(\pi-z),$$
$$npu-\frac{\pi}{2}\le z\le\frac{\pi}{2}$$
$$=\frac{\pi}{4}(\pi-z),\ npu\frac{\pi}{2}\le z\le\frac{3\pi}{2} \qquad (20)$$

Taking into account (20), the equation (19) takes the form:

$$h_{ucp}(t)=1-\frac{4}{\pi^2}\left[\sin\left(\frac{\pi}{2}-\frac{\pi}{2}\tau\right)+\right.$$
$$\left.+\frac{\pi^2}{8}(1-\tau)+\sin\left(\frac{\pi}{2}+\frac{\pi}{2}\tau\right)+\frac{\pi^2}{8}(1+\tau)\right]$$

Or after simple transformations taking into account (19) we finally get:

$$h_{ucp}(t)=\frac{8}{\pi^2}\cos\left(\frac{\pi}{2}\cdot\frac{t}{l\sqrt{LC}}\right) \qquad (21)$$

Similarly, (21) we find the average length of the original value of the transfer function of the long current line at $\lambda=0$

$$h_{icp}(t)=\frac{1}{l}\int_0^l i(t,x)\,dx \qquad (22)$$

Taking into account (14) we get:

$$h_{icp}(t)=\frac{4}{\pi\rho}\sum_{K=0}^{\infty}(-1)^K\frac{\sin\left[(2K+1)\frac{\pi}{2}\tau\right]}{2K+1}\times$$
$$\times\frac{1}{l}\int_0^l\sin\left(\frac{2K+1}{2}\cdot\frac{l-x}{l}\pi\right)dx \qquad (23)$$

Integrating the expression (23) we get:

$$h_{icp}(t)=\frac{8}{\pi^2\rho}\left[\sum_{K=0}^{\infty}(-1)^K\frac{\sin(2K+1)\frac{\pi}{2}\tau}{(2K+1)^2}-\right.$$
$$\left.-\sum_{K=0}^{\infty}(-1)^K\frac{\sin\left[(2K+1)\frac{\pi}{2}\tau\right]\cos\left[(2K+1)\frac{\pi}{2}\right]}{(2K+1)^2}\right] \tag{24}$$

After simple transformations, we bring the expression (24) to the form:

$$h_{icp}(t)=\frac{8}{\pi^2\rho}\left[\sum_{K=0}^{\infty}(-1)^K\frac{\sin\left[(2K+1)\frac{\pi}{2}\tau\right]}{(2K+1)^2}+\right.$$
$$+\frac{1}{2}\sum_{K=0}^{\infty}(-1)^K\frac{\sin\left[(2K+1)\frac{\pi}{2}(\tau-1)\right]}{(2K+1)^2}- \tag{25}$$
$$\left.-\frac{1}{2}\sum_{K=0}^{\infty}(-1)^K\frac{\sin\left[(2K+1)\frac{\pi}{2}(1+\tau)\right]}{(2K+1)^2}\right]$$

Then using the equation (20), we give the ratio (25) to the form:

$$h_{icp}(t)=\frac{8}{\pi^2\rho}\left\{\sin\left(\frac{\pi}{2}\tau\right)+\frac{\pi^2}{8}\tau+\right.$$
$$\left.+\frac{1}{2}\left[\cos\left(\frac{\pi}{2}\tau\right)+\frac{\pi^2}{2}(1-\tau)-\cos\left(\frac{\pi}{2}\tau\right)-\frac{\pi^2}{8}(1+\tau)\right]\right\},$$

Or after simple transformations taking into account (18) we finally get:

$$h_{icp}(t)=\frac{8}{\pi^2\rho}\sin\left(\frac{\pi}{2}\cdot\frac{t}{l\sqrt{LC}}\right) \tag{26}$$

Similarly, (21) and (26) can be obtained ratios $h_{ucp}(t-\lambda)$ b $h_{icp}(t-\lambda)$ (so $\lambda\neq 0$)

$$h_{ucp}(t-\lambda)=-\frac{8}{\pi^2}\cos\left(\frac{\pi}{2}\cdot\frac{t-\lambda}{l\sqrt{LC}}\right) \tag{27}$$

$$h_{icp}(t-\lambda)=\frac{8}{\pi^2}\sin\left(\frac{\pi}{2}\cdot\frac{t-\lambda}{l\sqrt{LC}}\right) \tag{28}$$

Thus, using ratios (14), (21), (26) ÷ (28) you can determine the average length value of the output coordinate of a link with distributed parameters at a time when the input signal is of an arbitrary type.

In [2] it is shown that the period of natural oscillations of T is defined as:

$$T=4l\sqrt{LC} \tag{29}$$

and if the inductance and capacitance of a long line were concentrated, then the period of natural oscillations of such a circuit from a coil with inductance Ll and capacity Cl would be:

$$T_0 = 4l\sqrt{LC} \tag{30}$$

Then the expressions (21), (26) can be represented as:

$$h_{ucp}(t) = -\frac{8}{\pi^2}\cos\left(\frac{2\pi t}{T}\right), \tag{31}$$

$$h_{icp}(t) = \frac{8}{\pi^2}\sin\left(\frac{2\pi t}{T}\right), \tag{32}$$

or

$$h_{ucp}(t) = -\frac{8}{\pi^2}\cos\left(\frac{\pi^2 t}{T_0}\right), \tag{33}$$

$$h_{icp}(t) = \frac{8}{\pi^2}\sin\left(\frac{\pi^2 t}{T_0}\right), \tag{34}$$

It should be noted that the equations $h_{ucp}(t)$ and $h_{icp}(t)$ were obtained based on the fact that the argument of the series (20) changes from $\frac{\pi}{2}$ before $\frac{3\pi}{2}$. Therefore, it is necessary to determine the limits of the change in the value t, in which the resulting ratios $h_{ucp}(t)$ and $h_{icp}(t)$ will fair.

If $-\frac{\pi}{2} \le z \le \frac{3\pi}{2}$, then we can write:

$$-\frac{\pi}{2} \le \frac{\pi}{2}\left(1 - \frac{t}{l\sqrt{LC}}\right) \le \frac{3\pi}{2},$$

$$-\frac{\pi}{2} \le \frac{\pi}{2}\left(1 + \frac{t}{l\sqrt{LC}}\right) \le \frac{3\pi}{2}.$$

How do we get that

$$-2l\sqrt{LC} \le t \le 2l\sqrt{LC},$$

It is obvious that only positive values of the time coordinate have a physical meaning. Therefore, the formulas that define $h_{ucp}(t)$ и $h_{icp}(t)$ will be valid only if *t* changes within the limits of:

$$0 \le t \le 2l\sqrt{LC} \tag{35}$$

Using equation (36) you can estimate the value t_{max} for various electric long lines and hydraulic pipeline lines.

As for lines of communication is important to create conditions under which there would be no distortion of the transmitted signal (current and voltage), it is necessary to impedance, attenuation coefficient and phase velocity is not draped on the frequency, which is achieved when the ratio of phase proportional to frequency [3-6].

In this case, the phase speed takes the maximum value:

$$\vartheta_{max} = \frac{1}{\sqrt{LC}} \tag{36}$$

and is equal to the speed of propagation of electromagnetic waves in the dielectrics surrounding the line wires.

Taking into account (36) we get

$$t \le \frac{2l}{\vartheta_{max}} \tag{37}$$

For overhead lines $\vartheta_{max} \approx 3 \cdot 10^8 \frac{m}{s}$, and for cable lines $\vartheta_{max} < 3 \cdot 10^8 \frac{m}{s}$, because the dielectric constant of the insulation in the cable is greater than the dielectric constant of the air. Taking into account that usually the length of communication lines is hundreds or thousands of kilometers, we get $t_{max} \approx 0,01 \div 0,11 s$.

For pipeline lines t_{max} it depends on the speed of sound propagation in the liquid PL:

$$t_{max} \leq \frac{2l}{\vartheta_0}, \tag{38}$$

It follows from equation (38) that when $\vartheta_0 \approx 1000 \frac{m}{s}$ and a length equal to tens of meters – $t_{max} \approx 0,02 \div 0,2 s$.

References

1. Theoretical foundations of electrical engineering: In 3 volumes. Textbook for universities.. – 5th ed. / K. S. Demirchyan, L. R. Neiman, N. V. Korovkin, V. L. Chechurin. – SPb.: Peter, 2009. – 512 p.: Il.
2. A. A. Bazarov, Synthesis of an automatic control system for objects with distributed parameters containing delay links, (2011)
3. Moore C. F., Smith C. L., Murrill P. W. Instruments and Control Systems, 43(1), 70(1970).
4. N. D. Demidenko, Yu. a. Tereshchenko, I. N. Melnik, Mathematical modeling and optimization of systems with distributed parameters: article / Bulletin of the Siberian state aerospace University named after academician M. F. Reshetnev, pp. 29-34
5. Egorov, A. I. Introduction to the theory of control of systems with distributed parameters: textbook / A. I. Egorov, L. N. Znamenskaya. – Saint Petersburg: LAN, 2017. — 292 p.
6. Besekersky V. A., Popov E. P., Theory of automatic control: Ed. 4-e pererab. and additional-SPb, publishing house "Profession", 2003-752 p. – (Series: Specialist)

METHODS OF GENERATION AND ANALYSIS OF STRATEGIES FOR CALCULATING CYCLIC QUASI ORTHOGONAL MATRICES

Grigoriev Evgeniy

Saint-Petersburg State University of Aerospace Instrumentation,
Saint-Petersburg,Russia
E-mail: ev.grig95@gmail.com

Abstact
The paper considers quasi-orthogonal matrices generalizing orthogonal matrices. Possible applications of these matrices are considered, as well as a circulant, as a basis for constructing cyclic matrices most convenient for implementation in computer technology. Strategies for computing cyclic quasi-orthogonal matrices are considered, and the characteristics of their software implementation are given.
Keyworlds: Quasi-orthogonal matrices, circulant, calculation strategies, cyclic structure.

INTRODUCTION

Currently, matrix computing is widely used in many fields of scientific and engineering activities. The structure of matrices and operations with them suggest a further expansion of their application.

Separately, it is worth highlighting the orthogonal and quasi-orthogonal matrices that are used in communication systems, digital image processing systems, cryptography, etc.

Definition 1. A square matrix **A** of order n is orthogonal if the condition $\mathbf{A}^{-1}\mathbf{A}= \mathbf{A}^{T}\mathbf{A}= \mathbf{I}$ [1].

The most famous orthogonal matrices are the Haar, discrete cosine transform (DCT), Hadamard, Belevich, and jacket matrices. Over a long period of time, the Hadamard matrices have been most widely used, since they are represented by elements 1 and -1, which greatly simplify the procedure of summing paired products and not introducing rounding errors into it.

Definition 2. A quasi-orthogonal matrix is a square matrix **B** of order n such that $\mathbf{B}^{T}\mathbf{B} = \omega(n)\mathbf{I}$, where **I** is the identity matrix, $\omega(n)$ is the weight function [2].

Obviously, in this form, quasi-orthogonal matrices generalize orthogonal matrices. In the further discussion, we will use the term “quasi-orthogonal” matrices both as indicated by the generalization and by the designation of a new class of matrices [2].

Recently, there has been an intensification of research related to the search for new orthogonal and quasi-orthogonal matrices [2-5], which manifest themselves in the direction of searching for optimal and universal matrices that are independent of the statistical characteristics processed with their data. The initiative is aimed at obtaining a pragmatic effect by the developers of a wide class of systems in terms of increasing their speed, reducing the amount of memory needed, and improving the quality of transformations. In connection with the foregoing, the urgent task is to formulate a strategy for their calculation.

Various structures of quasi-orthogonal matrices are described in detail in [2-5], and prospects for their practical application are discussed. This paper is devoted to the consideration of strategies for computing cyclic quasi-orthogonal matrices and the features of their computer implementation.

APPLICATIONS OF QUASI ORTOGONAL MATRICES

Most of the applied problems solved in distributed transceiver automated systems use data conversion procedures to compress, mask, and encode information [6]. In the process of transmitting information in communication channels, there is a need to increase the noise immunity of the transmitted information, as well as the subsequent separation of the transmitted data against various noise and interference.

As a result of the development of modern digital signal processors and programmable logic integrated circuits (FPGAs), floating-point calculations can be performed as effectively as using integers without increasing implementation complexity. This allows us to consider quasi-orthogonal matrices as an alternative to orthogonal ones and to improve existing information processing algorithms.

There are known applications of quasi-orthogonal matrices in error-correcting coding — the strip transform [7], which attenuates the effect of pulsed noise on the data transmitted in the channel.

To compress images of more than 2K or their sequences in frame-by-frame compression algorithms [8], quasi-orthogonal Mersenne-Walsh matrices are used as an alternative to DCT [9]. Similar experiments were described in [10–12].

Using quasi-orthogonal matrices, image masking / unmasking procedures are implemented to protect data from unauthorized viewing [13,14].

Quasi-orthogonal matrices are also used for error-correcting coding during correlation reception of signals, for example, in radar and communications. The results of studies of Mersenne codes obtained from rows of quasi-orthogonal Mersenne matrices that demonstrate the prospects for their use are presented in [15, 16].

STRUCTURE AND METHODS FOR CALCULATING CYCLIC QUASI ORTHOGONAL MATRICES

For application in applied problems, it follows, firstly, that the quasi-orthogonal matrix is as possible two-level, since an increase in the number of levels leads both to an increase in the computational cost of matrix generation, if provided for in this system, and to an increase in the computational cost of processing all information in whole.

There are several options for organizing quasi-orthogonal matrices. Within the framework of this article, we consider a cyclic structure as having the most promising applications in digital technology. The advantage of this structure is that only the first row of this matrix can be stored in the memory of the computing device — a circulant of length N. The remaining rows can be obtained sequentially by shifting the elements of the previous row by one position to the right, placing the shifted last element from the left – at the beginning of a new row [1], as shown in the matrix **M**.

$$\mathbf{M} = \begin{pmatrix} a_1 & a_2 & \cdots & a_n \\ a_n & a_1 & \cdots & a_{n-1} \\ \vdots & \vdots & \ddots & \vdots \\ a_2 & a_3 & \ldots & a_1 \end{pmatrix}$$

As an example, we give Figure 1, which shows a cyclic Mersenne matrix of order 15, obtained in [17]. Black elements correspond to the negative element –b, other than -1, white elements correspond to unity.

Figure 1 – Mersenne cyclic matrix of order 15

In the course of work on this topic, three calculation strategies were identified as the most convenient for practical implementation:

1) Based on the calculation of Legendre symbols
2) Based on the computation of Jacobi symbols
3) Based on the calculation of the modified m-sequence and its modified forms.

We present the results of the calculation using these methods in the form of portraits of quasi-orthogonal cyclic matrices of the order of 15 formed on the basis of the above methods, where the white field corresponds to 1 and the black field –b is different from -1 to show that, although the calculation methods are similar, the results are different. Figure 2 shows a quasi-orthogonal matrix based on Legendre symbols, figure 3 shows a matrix based on Jacobi symbols, and Figure 4 shows a matrix formed on the basis of a modified m-sequence.

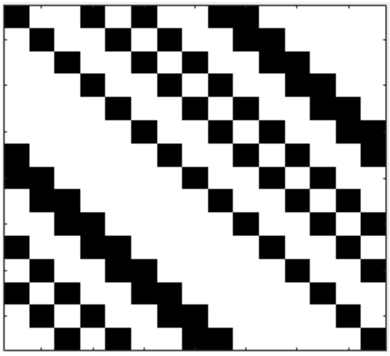

Figure 2 – Cyclic matrix based on Legendre symbols

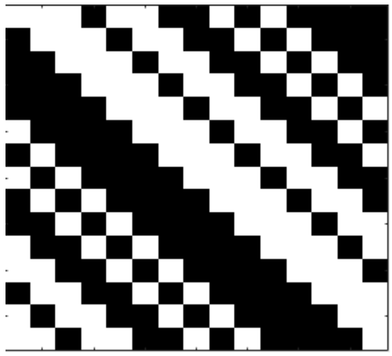

Figure 3 – The cyclic matrix based on Jacobi symbols

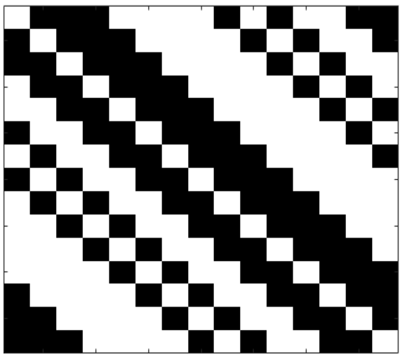

Figure 4 – The cyclic matrix based on a modified m-sequence

DEVELOPMENT OF SOFTWARE FOR COMPUTING CYCLIC MATRICES

During the development of software products for calculating the above cyclic quasi-orthogonal matrices [18–20], the following numerical characteristics of the program volume, the amount of RAM used, and the calculation speed were presented, which are presented in Table 1. These numerical values were given for close orders of quasi-orthogonal matrices, namely 15 order. The software products are implemented in the MATLAB environment, and allow you to evaluate the approximate performance for subsequent application implementation. All calculations were performed on the Intel core i5 7600k processor, at standard frequencies. The choice of MATLAB is justified by the fact that with built-in MATLAB tools you can get an implementation in C ++ that is more suitable for commercial development.

Table 1 – Calculation results

Strategy	Memory size	RAM size	Calculation speed
1	60 kb	2048kb	0.110 s
2	64 kb	13352kb	1.284 s
3	30 kb	2048kb	0.111 s

CONCLUSIONS

The article describes the possible areas of application of the theory of quasi-orthogonal matrices, as applied to applied problems arising for developers of communication systems and automated information processing systems.

A description of the cyclic matrix structure is given, as well as practical recommendations for choosing a circulant for the subsequent implementation of the quasi-orthogonal cyclic matrix structure.

The numerical characteristics of the amount of programs spent during the execution of RAM, as well as the time to execute the program for software products developed in the MATLAB environment are given. These software products can be useful as elements of the generation of quasi-orthogonal matrix structures to accelerate the design of applied commercial software tools using new algorithms using the theory of quasi-orthogonal matrices.

REFERENCES

[1] Voevodin V. V., Kuznecov YU. A. Matrices and calculations. M.:Nauka, 1984. 320 p.

[2] Balonin N.A., Sergeev M.B. Matrices of the local maximum of the determinant. Information and Control Systems. 2014. № 1. p. 2 – 15. DOI 10.31799

[3] Sergeev A. M. On the relationship of one kind of quasi-orthogonal matrices constructed on the orders of sequences 4k and 4k – 1. Izvestiya SPbGETU "LETI". 2017. № 7. p. 12–17.

[4] Sergeev A.M., Blaunshtejn N.SH. Orthogonal matrices of symmetric structures for digital image processing tasks. Information and Control Systems . 2017. № 6. p. 2 – 8. DOI 10.31799

[5] Yu. N. Balonin, A. A. Vostrikov, A. M. Sergeev, I. S. Egorova, “On relationships among quasi-orthogonal matrices constructed on the known sequences of prime numbers”, Tr. SPIIRAN, 50 (2017), 209–223

[6] Chernyshev S. A. Razrabotka i issledovanie metoda matrichnogo maskirovaniya videoinformacii v global'no raspredelennyh sistemah: Ph.D. thesis.Saint-Petersburg, 2018, 120 p.

[7] Mironovskij L. A., Slaev V. A. Strip method for converting images and signals. SPb.: Politekhnika, 2006. 163 p. (in Russian)

[8] Vatolin D., Ratushnyak A., Smirnov M., YUkin V. Data compression methods. The device archivers, image and video compression. M.:Dialog-MIFI. 2002. 384 p.(in Russian)

[9] Ahmed N., Rao K. R. Ortogonal'nye preobrazovaniya pri obrabotke cifrovyh signalov: Per. s angl./Pod red. I. B. Fomenko. — M.: Svyaz', 1980. — 248 p. (in Russian)

[10] Nenashev V.A., Sergeev A.M., Kapranova E.A., Ryzhov K.YU. Experiments on the replacement of DCT by quasi-ortogonal transformation algorithms and image compression. Nauchnaya sessiya SUAI: sb. dokl.: V 3 ch. CH. II. Tekhnicheskie nauki / SPb.: GUAP. SPb., 2018. 475 p. (in Russian)

[11] Vostrikov A.A., Sergeev M.B., Litvinov M.YU. Masking digital visual information: the term and basic definitions Information and Control Systems, 2015. №5. p. 116-123. DOI 10.31799

[12] Erosh I.L., Filatov G.P., Sergeev A.M. On the protection of images during transmission over communication channels // Information and Control Systems. 2007. № 5(30). p. 20 – 22. DOI 10.31799

[13] E. Fienberg S., Jin J. (2009) Matrix Masking. In: LIU L., ÖZSU M.T. (eds) Encyclopedia of Database Systems. Springer, Boston, MA

[14] Vostrikov A.A., Sergeev M.B., Balonin Yu. N. Chernyshev S.A. Digital masking using Mersenne matrices and their special images. Procedia Computer Science 112(2017). 1151-1159.

[15] Nenashev V. A., Sergeev A. M., Kapranova E. A Issledovanie i analiz avtokorrelyacionnyh funkcij kodovyh posledovatel'nostej, sformirovannyh na osnove monociklicheskih kvaziortogonal'nyh matric // Informacionno-upravlyayushchie sistemy. 2018. №3. p. 9 – 14. https://doi.org/10.31799/1684-8853-2018-4-9-14 (in Russian)

[16] Sergeev A., Nenashev V., Vostrikov A., Shepeta A., Kurtyanik D. Discovering and Analyzing Binary Codes Based on Monocyclic Quasi-Orthogonal Matrices // Smart Innovation, Systems and Technologies Volume 143. Springer, 2019. P.113 – 123. https://doi.org/10.1007/978-981-13-8303-8.

[17] The program for calculating structured quasi-orthogonal Mersenne matrices / Vostrikov A.A., Sergeev A.M., Kurtyanik D.V., Nenashev S.A., Grigoryev E.K. / Certificate of state registration of computer programs No. 20169612775 of the Russian Federation, publ. 02/27/2019. ROSPATENT

[18] The program for generating quasi-orthogonal cyclic matrices formed on the basis of the calculation of quadratic residues Nenashev V.A., Shepeta A.P., Sergeev M.B., Chernyshev S.A., Grigoriev E.K. Certificate of state registration of a computer program No. 2019611539 of the Russian Federation, publ. 03/04/2019. ROSPATENT

[19] The program for generating special quasi-orthogonal cyclic matrices formed on the basis of the calculation of Jacobi symbols / Vostirkov A.A., Sergeev A.M., Kurtyanik D.V., Nenashev V.A., Grigoriev E.K., Shepeta A.P., Skuratov V.V. / Certificate of state registration of a computer program No. 20169660821 of the Russian Federation, publ. 08/13/2019. ROSPATENT

[20] The program for generating special quasi-orthogonal matrices formed on the basis of modified m-sequences. / Grigoriev E.K., Nenashev V.A., Sergeev M.B., Sergeev A.M., Ivanova M.S., Nenashev S.A. / Certificate of state registration of a computer program No. 2019663534 of the Russian Federation, publ. 11/13/2019. ROSPATENT

SYNTHESIS OF ALGORITHMS FOR STATISTICAL EQUIVALENTS OF INPUT SIGNALS OF INFORMATION PROCESSING SYSTEMS BASED ON EMPIRICAL DATA

Ivanova Maria

Saint-Petersburg State University of Aerospace Instrumentation,
Saint-Petersburg, Russia
E-mail: ivanovamariya_94@mail.ru

Abstract
An algorithm for generating input signals of information processing and automation systems is presented, synthesized from empirical data of the input stream, presented in the form of histograms. The algorithm is the statistical equivalent of the input signals of complex systems so far, which allows you to study the characteristics of automation and information processing methods of mathematical modeling on a computer with a significantly larger volume of statistical tests. The characteristics of the synthesized algorithm that simulates the flows of input signals that are statistically equivalent to the actually observed flows are analyzed.
Keywords: complex system, automation, input stream, statistical equivalent, histogram, empirical distribution density, modeling algorithm, uniform distribution.

When designing complex systems, in particular information processing systems, the performance of the systems is checked by methods of mathematical modeling of the algorithm of functioning of the designed systems on a computer. In addition to the implementation of the functioning algorithm, it is necessary to synthesize and implement algorithms that simulate the input information flows – the input signals of the designed and studied systems [1]. When the statistical characteristics of the input signals are known exactly, the synthesis is reduced to the synthesis of algorithms for generating sequences, in particular random variables, with specified statistical distributions. However, the statistical characteristics of input signals can only be known accurately in the simplest cases, or with a fairly significant simplification of the mathematical models of input flows.

Therefore, in practice, the statistical characteristics of the input signals are determined from the actual observed experimental data. At the same time, in the vast majority of cases, consent criteria are used to determine the distribution laws, which allow you to "choose" a distribution law that does not contradict experimental data. Further, this law is actually postulated as the law of distribution, according to which fluctuations of input signal parameters (amplitudes, powers, phases, etc.) occur. It should be noted that any criterion of consent can reject a correct hypothesis of the distribution law with probability α – level of the test (error of first kind) or accepting the hypothesis when it is true, with probability β, in accordance with the power of the criterion (error of the second kind in a simple alternative). As a result, in a "single" experiment that involves testing a hypothesis on a single, even a large enough sample, errors are always possible – rejecting the correct hypothesis or accepting a false one. The desire to "guess" the true distribution leads to small values of α equal, depending on the available sample size, 0.1, 0.05 or even 0.01, which corresponds to the probabilities to accept the correct hypothesis and "guess" the distribution with probabilities of 0.9, 0.95 and 0.99, respectively. However, at the same time, the probability of a second-type error β is also growing – to accept the hypothesis when it is not true.

Further, using the postulated distribution law, the system is studied by methods of mathematical (most often imitation) modeling. In this case, the adopted law and the corresponding input signal sequences of the designed system are the statistical equivalent of the actually observed signals, according to which mathematical models are constructed and modeling algorithms are synthesized. However, it should be recalled that this statistical equivalent may not be the actual statistical equivalent of the sequence of input signals due to errors of the first and second kind, inevitable when testing the hypothesis. Therefore, such a "tough" approach to determining and postulating a statistical equivalent is not always acceptable. This approach is convenient to use in theoretical studies, since with the well-known distribution law (which, in fact, is postulated), it is possible to synthesize the system, determine its potentially achievable quality characteristics, etc.

When checking the system's performance in practice, it is quite common to use experimentally obtained data as input streams, which in this case are test input streams. Here the system is checked for operability in almost real operating conditions. This approach is already used for developed systems, which, due to their life cycle during their design, are modified in accordance with the results of testing on real records of input signals. The algorithm of functioning, in this case, can be implemented on a computer, and the synthesis of input signals is not required, since there are records of implementations of input streams. The advantages of this approach, in comparison with the" hard " statistical equivalent, are indicated above, but the disadvantages are obvious – the records allow you to test the system only in a limited number of situations for which these records are obtained (for radar, these are units of records). Using such an “empirical” approach, it was found that some systems synthesized by “hard” statistical equivalents are generally inoperative under real operating conditions. In particular, such situations are typical for those cases when a relatively small sample (of the order of 200-300 samples, with a larger size, it is difficult to obtain a homogeneous sample due to changes in the operating conditions of the system, namely, due to unsteadiness), a theoretical distribution law is selected that “Well” agrees with experiment near the distribution maxima, but in practice the real distribution has long “tails”, that is, it refers to distributions with heavier “tails”.

A compromise between these two approaches – theoretical and experimental, can be considered an approach that uses the composite Huber distribution, which allows one to take into account the experimental data, according to which a mathematical model of signals is adopted in accordance with the used criterion of agreement and takes into account the fact of a possible error when accepting the hypothesis about the functional form of the law. In this approach, the signal model uses a distribution $f(x)$ of the form

$$f(x) = (1-\gamma)\cdot f_{\mathrm{T}}(x) + \gamma \cdot f_{\mathrm{H}}(x) \ , \tag{1}$$

where $f_{\mathrm{T}}(x)$ and $f_{\mathrm{H}}(x)$ is the theoretical distribution that is accepted using the consent criterion, and an unknown distribution that allows us to take into account the error of accepting the hypothesis, and $\gamma \in [0,1]$ -γ a certain coefficient, which, in this context of the use of expression (1), reflects the degree of confidence of the researcher in the correct choice $f_{\mathrm{T}}(x)$. When γ=1, the researcher fully trusts the results of the consent criterion, and when – completely distrusts. In particular, we can choose α as *γ=0* because (1-*α*) and there is a probability to accept the correct hypothesis. After selecting the coefficient γ, the question arises – how to choose $f_{\mathrm{H}}(x)$? There are two approaches used here.

The first is to try to find the distribution $f_{\mathrm{H}}(x)$, in which the system has the "worst" quality characteristics, using a known algorithm for the functioning of the system under study. In this case, under real operating conditions, the quality characteristics of the system under study will be better than the characteristics determined by mathematical modeling. This approach, in fact, allows you to "guarantee" the characteristics of the system not lower than those obtained in mathematical modeling. The difficulty of practical use of this approach is mainly in the complexity of determining the "worst" distribution, and if it can be found, this distribution can be so complex that it is difficult to synthesize and implement an algorithm for its exact reproduction on a computer, and the approximate implementation of the algorithm may contain difficult to account for methodological errors.

The second approach consists of selecting the $f_{\mathrm{H}}(x)$ distribution of one of the distributions with "weighted tails", for example, a two- way exponential distribution. In this case, as a rule, the algorithm for modeling the selected distribution is also known, and there are no methodological errors in reproducing this distribution on a computer.

In an approach based on a composite distribution of the form (1), as the sample size increases, the density of the distribution of the modeled sequence of input signals will converge not to the distribution $f_{\mathrm{T}}(x)$ that does not contradict the experimental data (the histogram of experimental data), but to the $f(x)$ distribution defined by the Huber model, whose histogram at *γ=0* will differ from the experimental histogram. Therefore, this approach, as well as those discussed above, actually postulates the type of density distribution of input signal parameters of the system under study.

The paper considers a new approach to the synthesis of input signal modeling algorithms for the complex systems under study, based on the idea of a statistical equivalent of the input signal stream that does not contradict the experimental data. With this approach, it is necessary to synthesize an input data stream generation algorithm that would generate sequences whose statistical characteristics would be equivalent to the statistical characteristics of the input signal stream. The term equivalence of statistical characteristics can be understood as different concepts: average values, variances, densities and distribution functions, correlation spectral characteristics, etc. It should be borne in mind that these characteristics should be determined from empirical data, therefore, we may not have the characteristics themselves, but only their estimates from the samples of the observed signals. When it comes to the fact that the adopted mathematical model of the input signal stream does not contradict empirical data, it is always implicitly implied that the characteristics of the adopted mathematical model do not contradict the estimates obtained from samples of input signals. Therefore, hereafter, by statistical equivalent we mean the statistical equivalent for evaluating the characteristics of signals, and we restrict ourselves to considering the case when the characteristics are the estimation of the distribution density, which is often used as a histogram. This case is considered below.

So, let the empirical data at our disposal be presented in the form of a histogram. The histogram can be displayed in different forms. In our case, the histogram shown in Fig. 1 and normalized accordingly is actually the empirical distribution density $f_{\text{э}}(x)$ of the numerical stream of input data of the systems under study.

The range of fluctuations of the input data is limited by the set $[a_0, a_m]$ divided by m subsets $[a_{i-1}, a_i)$, i=1,2,…m], while the last subset $[a_{m-1}, a_m]$ is closed, but in the general expression for $i=m$, for simplicity of notation, it is denoted as open $[a_{m-1}, a_m)$, which is insignificant, since for continuous random variables the sets $[a_{m-1}, a_m]$ and $[a_{m-1}, a_m)$ are equivalent, therefore so that the probability of "falling out" of the value of a_m is zero (in Fig. 1, m=9).

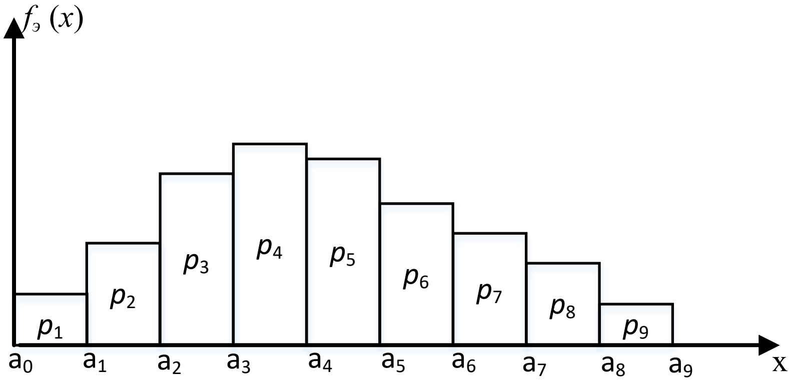

Figure 1. Empirical distribution density

The area of the rectangles in Fig. 1 is equal to the empirical frequencies p_i — estimates of the probability of the input sample entering the corresponding sets $[a_{i-1}, a_i)$, i=1,2,…m, $p_1+ p_2+… p_m=1$.

Integrating $f_{\text{э}}(x)$, we obtain an analog of the empirical distribution function $F_{\text{э}}(x)$, constructed not from the variational series of the observed sample, but from the empirical distribution density $f_{\text{э}}(x)$. The empirical distribution function $F_{\text{э}}(x)$ shown in Fig. 2 is a piecewise linear function, which directly follows from the corresponding representation of the normalized histogram $f_{\text{э}}(x)$. This function is actually a piecewise linear approximation of the actual distribution function of the parameters of the input data stream.

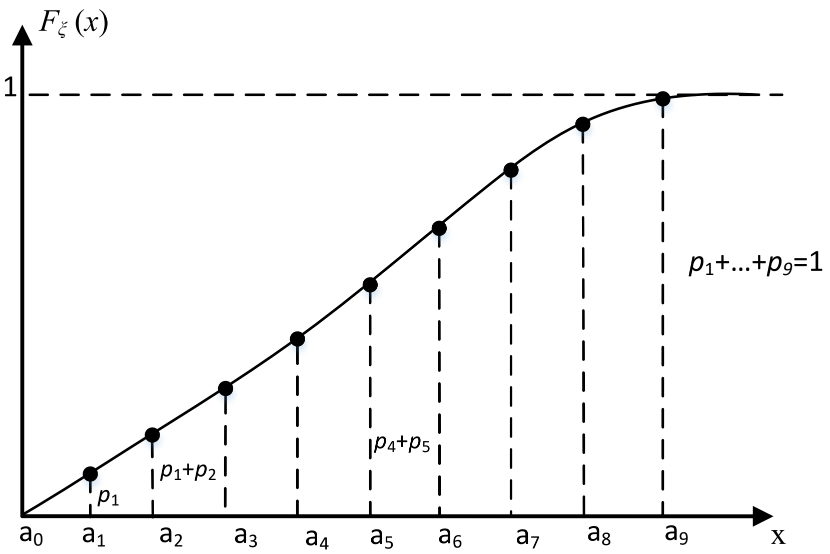

Figure 2. Empirical distribution function

With an increase in the volume of the observed sample, an increase in m, and, correspondingly, a decrease in the sizes of the sets $[a_{i-1}, a_i)$, i=1,2,…m, the empirical density $f_э(x)$ and the distribution function $F_э(x)$ converge to the actual density and input stream distribution functions.

In our case, $f_э(x)$ and $F_э(x)$ are the functions from which it is required to construct the statistical equivalent of the input data stream. It can be seen from Fig. 1 and Fig. 2 that in each interval $[a_{i-1}, a_i)$ the distribution is uniform, and the probability of a "random" sample value falling into the set $[a_{i-1}, a_i)$ is equal to the probability p_i. This directly implies an input flow modeling algorithm, which can be summarized as a two-step algorithm: at the first step, the number i of the set is played with probability p_i; at the second step, a number is modeled, evenly distributed in the interval $[a_{i-1}, a_i)$, i=1,2,…m. Thus, the input data stream is simulated. It should be noted that the histogram of this flow with a fixed m and an increase in the size of the simulated sample converges to the empirical density $f_э(x)$, that is, such a flow is the statistical equivalent of the real flow and, accordingly, does not contradict empirical data.

In the particular, most common case, the size of the intervals is the same a_i-a_{i-1}=Δ, i=1,2,…m, and a_0=0, which corresponds to non-negatively defined sequences, the algorithm for modeling the numerical sequence R_j, j=1,2,…, has the simplest form

$$R_j = \Delta \cdot \left(E\left(r_j \cdot m \right) + r_j^* \right), \tag{2}$$

where r_j and r_j^* are random variables uniformly distributed over the interval (0, 1), $E(.)$ is the Antje function (the integer part of the number in brackets). It is clear from the construction of the algorithm that the distribution density of the sequence R_j is $f_э(x)$, and the distribution function is $F_э(x)$. The algorithm for modeling the sequence R_j can be synthesized in another way, namely, using the inverse function method [2]. When using the inverse function method for modeling the next value of the sequence, only one number r_j was needed, distributed over the interval (0,1), but the algorithm itself would be a little more complicated, although its properties would be the same as the algorithm defined by expression (2) .

To confirm the operability of the above algorithm, simulation was carried out for two cases of using the algorithm as a generator of statistical equivalents of random sequences under the synthesis conditions described above. As the basic distributions, two distributions were chosen, the parameters of which were selected so that the distributions had equal mathematical expectations and variances [3].

In the first case, the Rayleigh distribution was taken as the base distribution for generating the histogram $f_э(x)$

$$f_R(x) = \frac{1}{\sigma_R} \cdot \exp\left(-\frac{x^2}{2\sigma_R^2} \right), \quad x \geq 0, \tag{3}$$

where σ_R is the distribution parameter. In the second case, the lognormal distribution

$$f_{LN}(x) = \frac{1}{\sqrt{2\pi} \cdot x \cdot \sigma_{LN}} \cdot \\ \cdot \exp\left(-\frac{\left(\ln x - \ln \bar{x}\right)^2}{2\sigma_{LN}^2} \right), \quad x \geq 0, \tag{4}$$

where $\bar{x}$ and σ_{LN} are distribution parameters.

In the first case, using the Rayleigh distribution, a histogram $f_э(x)$ was obtained, based on which a generation algorithm of the form (2) was implemented. For the sequences obtained using algorithm (2), for two different sample sizes, the number of intervals m, and different levels of α, two hypotheses were tested: the first – the distribution of the sequence has a Rayleigh distribution, and the second – the distribution of the sequence obeys a log-normal distribution. Hypothesis testing by the criterion of consent χ^2 confirmed the correct hypothesis and rejected the false one.

Such a check is actually testing the proposed algorithm for some special cases of non-negative definite numerical sequences. These two distributions were chosen as test ones for the reason that they are close enough near the maxima, but differ in their “tails” – the log-normal refers to distributions with heavier “tails”. The test confirms, at least for these situations, the efficiency and effectiveness of the proposed algorithm.

CONCLUSION

The paper presents a simple and fairly effective algorithm for modeling the input signals of information processing and automation systems, using empirical data on the statistical characteristics of the input flows. The algorithm allows you to generate input streams, which are statistical equivalents of the input signals of these complex systems, which allows you to study the characteristics of computer systems by simulation methods using sequences of input signals, the statistical characteristics of which practically coincide with the characteristics of real signals available to system developers.

REFERENCES

[1] Maurits V.G. A mathematical model of the echoes of the sea surface observed by airborne aircraft locators. / V.G. Maurits, M.A. Klimova, M.S. Ivanova // In the collection: Scientific session of SUAI. Collection of reports. In 3 parts. 2018. P.351-357.

[2] Shakhov, V.V. Review and comparative analysis of pseudorandom number generator libraries / V.V. Shakhov // Problems of Informatics. –2010. – №2. – P. 66-74.

[3] Isakov V.I., Modeling location signals. reflected from the edge of the land-sea/ D.A. Shepeta., V.I. Isakov // Information management systems. 2017. No5 (90). P. 89-94.

METHOD TO COMBINE MULTI-ANGLE IMAGES IN HIGH-RESOLUTION ON-BOARD OPTICAL LOCATING SYSTEMS

Kapranova Ekaterina, Burylev Dmitry

Saint-Petersburg State University of Aerospace Instrumentation,
Saint-Petersburg,Russia
E-mail: kapranovakk@gmail.com, arahnik121@gmail.com

Abstract
The task of combining multi-angle images into one and linking the obtained actual data with real-time cartographic information is applied in many spheres. For example, for mapping the Earth and sea surfaces in the course of environmental monitoring from small aircraft (UAV), in traffic control systems, in search during emergencies and natural disasters associated with tsunamis, floods, hurricanes, etc., as well as in preventive safety systems.
To solve the problem of combining images and allocating useful information on it in the work were considered ways of correlation-extreme combination of images, methods of distributed combination of information, as well as new ways of representation, compression, storage, masking and noise-resistant coding of high-resolution images with a common mathematical basis.
For realization of the system of operative display of the local information received from various boards of small aircraft, it is required to perform coding of the generated multi-angle images, to carry out their combination in a single information field. For this purpose, it is necessary to find the corresponding functional transformation in order to superimpose actual data generated in real time mode.
The results obtained in this work are important for structures that carry out operational search and rescue operations in areas of emergency situations and disasters of natural and man-made nature.
Keywords: multi-angle images, image fusion, high-resolution images, key points, information fusion, small aircraft, location information, real-time mode.

INTRODUCTION

Today in many fields of science and technology the task of combining (stitching) images obtained from different angles, as well as their combination, if they are obtained in different spectral ranges or from different sources is relevant. Such areas are: mapping of land and sea surfaces, technical vision of aircraft (AC) and robotic systems, automatic robotic control.

To obtain a stitched image, spatial transformation procedures are used. It is applied in case of merging images of one scene obtained from different sources of local information or sequentially formed by one source, for example, a high resolution video camera. In this case, the task of combining images is set as the task of finding some transformation at which the greatest coincidence is achieved based on correlation-extreme methods. The paper considers the solution of the problem of image fusion by the method of key points search and the method of data fusion, image georeferencing to geographical coordinates of the area (two or more images). The considered methods allow to achieve high accuracy of georeferencing and eliminate errors of combining between cross-linked frames.

IMAGE FUSION REVIEW

Combining and stitching images is not an easy task. The main stage of merging is selection of corresponding points or contours in images. In other words, it is necessary to find such a transformation of one image relative to another, which will provide a match of pairs of points or its contours, where each such pair will be a representation of the other same pair in the study area.

SIFT and SURF are one of the well-known and effective key point search algorithms. The points found using the SIFT method [1] are resistant to stretching, image rotation, and partially to changes in the observation point. These factors are a great advantage of the method under consideration, which is implemented in four stages.

Stage 1. Finding extrema across all image points using Gaussian functions – detection of special points that are invariant to stretching and rotation.

Stage 2. Localization of the key points found in the first step – drawing a detailed model to specify the position of the key point and its size.

Stage 3. Adding orientation – adding to each point one or more orientations based on the gradient directions. All operations are made over the obtained position, size and orientations of the point. This allows you to get resistance to image rotation and stretching.

Stage 4. Getting key point descriptors – measurement of local image gradients on a selected scale in the area of each key point. The data are converted to a view that allows a significant degree of change in shape and light. For each key point a 64 or 128 real numbers descriptor is constructed.

Analysis of the experimental results showed that SIFT processing is complex and the speed of detection and alignment of image features is low.

The SURF algorithm allows you to define specific points using the Hessian matrix [2]. First, using Hessian values, we find the key points in the image. This is done by working with the brightness of the image and overlaying a special mask. The Hesse Matrix determinant reaches the extremum at the points of maximum change of the brightness gradient. It precisely determines spots, angles and boundaries of objects. Hessian is invariant to rotation. For each key point, the direction of maximum brightness change (gradient) and the scale taken from the scale coefficient of the Hesse Matrix are considered.

After finding key points, the SURF algorithm forms their descriptors in the same way as the SIFT algorithm. These numbers show the gradient fluctuations around the key point. Since the key point represents the Hessian maximum, this ensures that there should be areas with different gradients in the vicinity of the point. Thus, the dispersion (difference) of descriptors for different key points is ensured [3].

The main task of image stitching based on the SURF algorithm is to select a method for detecting the main feature points. The SURF feature vector is a three-dimensional space and corresponds to the algorithm for determining the closest adjacent distance. The stitching process is equivalent to the adjacent search task for a large dimensional space, which requires complex calculations. In the process of merging two images and forming a single output image, a problem arises in determining characteristic (key) points, perspective and adjusting color rendering. The significant disadvantages of the considered algorithm are: the inability to perceive blurred images, problems of combining multiscale images or images taken at different angles.

The use of SURF when flying an aircraft with any curves can lead to significant problems that negatively affect stitching quality.

Researches have shown that in general the use of SIFT is more reliable. But in the case of special data sets or time-critical applications, SURF is a good solution.

The SURF algorithm is an improvement of SIFT, which is mainly reflected in speed and higher efficiency. The main difference between SURF and SIFT is the method of building a multi-scale space. SURF can simultaneously process multi-scale images formed on board of small aircraft, which increases the productivity of image fusion.

Image matching is a way to significantly improve the accuracy of the object coordinates determination, as well as the aircraft navigation parameters, due to overlaying of images received from sensors of different spectral ranges [4]. Such sensors are often video cameras of visible and infrared (IR) bands. In this case, the main task is to combine images of different spectral ranges and combine them with cartographic information. Such combination is intended, first of all, to improve image quality [5] and provide more complete information.

Stitching has several advantages:

- detection of visually comprehensible image at different times of the day, regardless of meteorological conditions;
- possibility of geometric transformations of the image, such as zooming, rotating, etc., received from different sensors;
- identification of the total field of view from different sensors;
- possibility of bright image transformations, such as noise filtering, sharpening or contrast enhancement;
- combining two multi-angle images into one, with improved quality and information characteristics.

The advantages of such an aggregation are increased informativeness of the resulting image when combined with cartographic information. However, even known methods of combining have a number of disadvantages and do not always allow to identify the correct matches. This is due to the fact that often the images received from the aircraft, there are areas with little information. For example, fields or smooth reliefs. The resolution of images in the visible and IR ranges varies both in resolution and in the size of images determined by the parameters of their lenses.

The problem of image fusion is also a computer vision task that requires recognition of changes in a series of images, analysis of aircraft movement, recognition of objects in the images.

IMAGE FUSION EXPERIMENTS

Fig. 1 shows two images recovered after compression [6, 7], received from different angles and received by wireless high-speed interference-proof channel [7, 8] to the data processing and integration center from small aircraft$_1$ (left image) and aircraft$_2$ (right image).

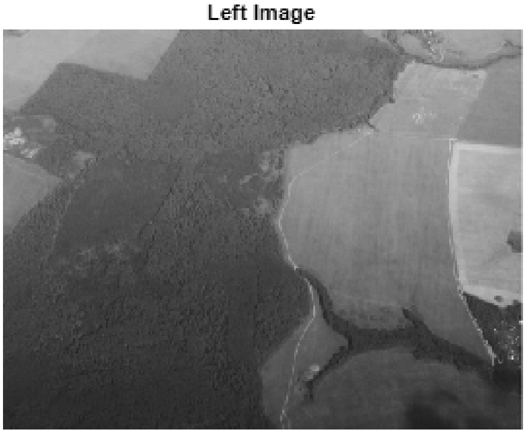

Figure 1(a) – Image from first aircraft.

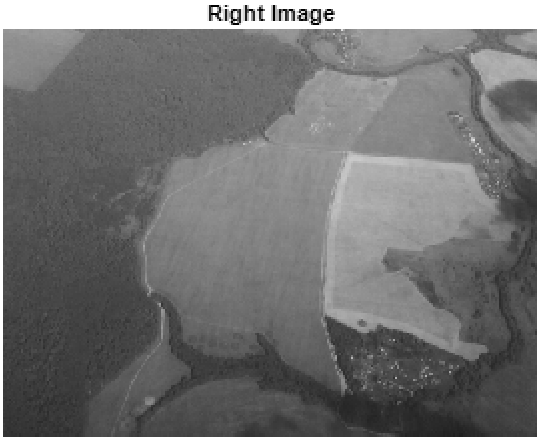

Figure 1(b) – Image from first aircraft.

To obtain a combined image developed software search and select on of key points on images (Fig. 2). Further on these points through their comparison (Fig. 3) on both images are made their cross-linking.

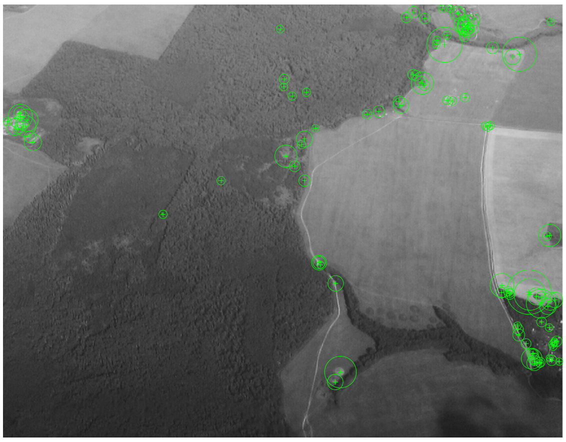

Figure 2(a) – Displaying key points on first imag

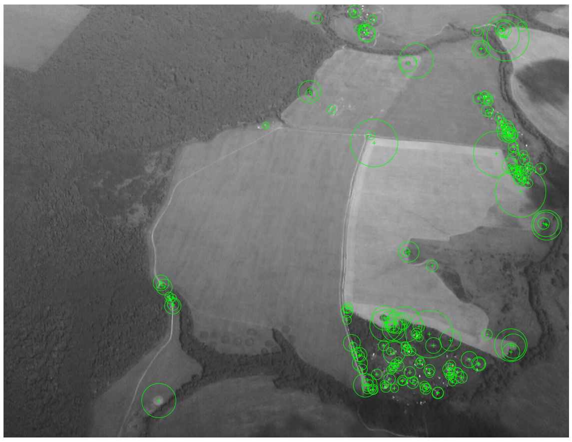

Figure 2(b) – Displaying key points on second image

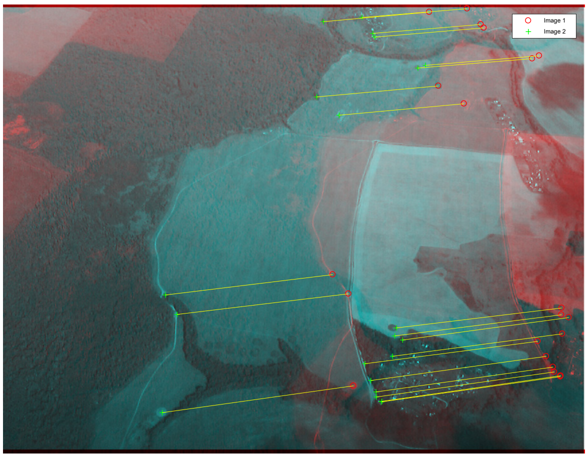

Figure 3 – Key point mapping process

As a result, the final image, shown in Fig. 4, is formed, ready for further implementation of algorithms of location and classification of objects in order to perform specific tasks: environmental monitoring, search and rescue work, etc.

Figure 4 – Result image

This combined image serves as a source material for further implementation of algorithms of location and classification of objects in order to perform specific tasks: environmental monitoring, search and rescue work, etc. [9, 10].

CONCLUSIONS

The results of the experiments confirmed the possibility of combining images obtained from different angles by high-resolution video cameras placed on two aircrafts included in the system.

The analysis of the experimental results made it possible to formulate a number of recommendations on software adjustment and selection of technical means for processing high-resolution images in real time.

The developed software complex including the procedures of key point selection and image stitching is applicable for implementation of information fusion in small UA onboard systems.

The results of the work are simply enough adapted for processing of images received in different spectral ranges and their combining in order to increase informativeness during the accumulation during field tests.

ACKNOWLEDGMENTS

The research was carried out with the financial support of a grant ISA 2019 Educational Foundation Scholarships.

LIST OF SOURCES USED

1. Efimov A.V. "Development and research of the algorithms of the image alignment from the onboard video sensors with the virtual terrain model", Ryazan, 2016, p.40.
2. Jianxia Wang, Yawei Wang. Modified SURF applied in Remote Sensing Image Stitching. School of Information Science and Engineering, Hebei University of Science and Technology, Shijiazhuang, 2015
3. T. Sledevič, A. Serackis. SURF Algorithm Implementation on FPGA Department of Electronic Systems, Vilnius Gediminas Technical University, Naugarduko str. 41, LT-03227 Vilnius, Lithuania, 2015.
4. Erosh I. L., Solovyev N. V., Sergeev M. B., Kozlov A. A., Litvinov M. Yu., Filatov G. P. Way of combining images obtained with the help of various photo sensors and the device for its implementation. Patent for invention RU 2435221 C2, 27.11.2011.
5. Osipov LA, Sergeev M. B., Solovyov N. V.; Shepeta, A.P. Spectral characteristics application for the remote sensing image recognition // Fundamental investigations. 2004. № 6. p. 83-85.
6. Ekaterina A. Kapranova, Vadim A. Nenashev, Mikhail B. Sergeev. Compression and coding of images for satellite systems of Earth remote sensing based on quasi-orthogonal matrices // Proc. of SPIE, Image and Signal Processing for Remote Sensing XXIV. Berlin, Germany. 2018. Vol. 10789. PP. 1078923-1 – 1078923-6.
7. Kapranova E.A., Nenashev V.A., Sergeev A.M., Burylev D.A., Nenashev S.A. Distributed matrix methods of compression, masking and noise-resistant image encoding in a high-speed network of information exchange, information processing and aggregation, SPIE Future Sensing Technologies, Tokyo, Japan, 2019, pp. 111970T-1-111970T-7.

8. Nenashev, V.A.; Vasil'ev, I.A.; Sergeev, A.M. Simulation of the complex code-modulated signals for the modern systems of information detection and transmission // SUAI Scientific Session: Collection of reports: 3 p. P.II. Technical sciences. – SPb.: SUAI, 8-17 April 2019. – P. 413-417.

9. M. G. Wattimena, V. A. Nenashev, A. A. Sentsov and A. P. Shepeta, "On-Board Unlimited Aircraft Complex of Environmental Monitoring," 2018 Wave Electronics and its Application in Information and Telecommunication Systems (WECONF), St. Petersburg, 2018, pp. 1-5.

10. Zhou J., Bai X., Caelli T. Computer Vision and Pattern Recognition in Environmental Informatics. IGI Global, 2016. – 437 p.

THE RESEARCH OF OUTPUT WAVEFORM ON THE CHANGE OF FILTER PARAMETERS IN THE TELEPHONE LINE DATA TRANSMISSION SYSTEM

Kolegov Andrey

Saint-Petersburg State University of Aerospace Instrumentation,
Saint-Petersburg, Russia
E-mail: kolegov03.10.99@gmail.com

Abstract
Nowadays the majority of objects are provided with a telephone. The telephone line can be used as a data transmission line. This article introduces the data-transmission system working on busy voice-frequency telephone lines. The author describes the development of the method.
Keywords: data-transmission system, phase-modulation signal, phase modulation, telephone channel, filter.

Nowadays data transmission devices that work on busy voice-frequency telephone lines are widely used by security systems. These devices are economically efficient in small cities and urban-type settlements with automatic dial-telephone service. Guard service companies successfully organize centralized surveillance offices using current telephone lines. In this case, both telephone messages on standard frequency range (0.3-3.4 kHz) and security company data can be passed through the telephone channel simultaneously. Usually, data transmission of security systems is realized by radiofrequency signals with a carrier frequency 18 kHz that is standard for Russia. Resistance against interference is provided by phase modulation of signals. Active bandwidth of that signals can reach tens of kHz. However, the telephone message signal spectrum and spectrum of security system messages do not cross in the frequency domain. That data can be transmitted in one open-wire telephone feeder.

Amplitude spectrum graphs of telephone signal and security system signals are represented in figure 1.

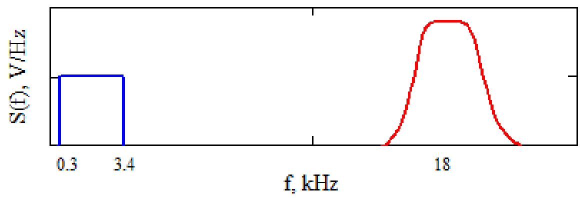

Figure 1 – The signal spectrum of the telephone line and the data transmission active bandwidth

It is sufficient to transmit over a communication channel status data of two sources in the security system. Each provider (alarm circuit or relay output of control panel, for example) can accept two values: “norm” and “alarm”. Message transferring is accomplished through harmonic vibration with phase modulation. In such a case, a signal can be written like this:

$$S(t) = U_0 \cdot \exp[j(\omega_0 t + \varphi(t) + \theta_{нач})] \tag{1}$$

where $\varphi(t) = \begin{cases} \pi, 0 \le t \le T/2 \\ 0, T/2 \le t \le T \end{cases}$ – phase control function; T – period of phase change on π;ω_o – carrier signal frequency; $\theta_{нач}$ – input phase angle.

Transmitted data about information source status is enclosed in the period duration of the control signal. The definite period duration corresponds to specified source status. Two data resources can be in four conditions (“norm” or “alarm”). Three different control signal periods are in accord with three statuses. There is no modulation when two information sources report “alarm”.

Radiofrequency signal formed on the object is transmitted on the telephone line to the automatic telephone radio relay station that demodulates signal that means selection of period change $\varphi(t)$. Correct rectification shows the quality of the data transmission system. Precision is related to the random input phase angle $\theta_{нач}$. So, it is necessary to minimize the impact of different factors on an input phase angle $\theta_{нач}$ to achieve the desired quality.

Random nature of $\theta_{нач}$ is defined as:

1. Non-coherence of the signal with carrier frequency and control signal. It means that an input phase of the first control signal harmonic component is a random value concerning the input phase of the carrier signal.

2. A random input phase drifts in the channel (noise).

The first reason always exists in the work of phase modulator when harmonic signal generator and carrier signal generator work independently of each other. It is possible to make generators coherent in the data transmission system [4]. It is required to apply the radio signal shaping circuit in which a carrier signal and control signal will be formed from one meander signal with a stabilized tracking period. To reach this condition engineers use digital instrumentation elements that have high stability and accuracy of parameters. The N-bit binary counter can form control signals and reference meander that has a frequency of first harmony (carrier signal frequency) from meander signal of the driving generator. The signal structure is shown in figure 2.

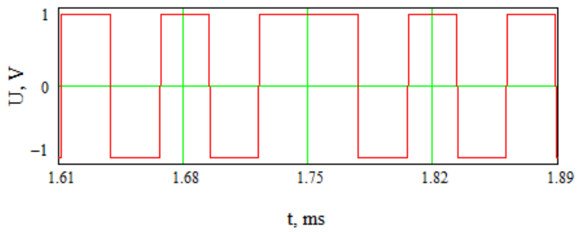

Figure 2 – The form of the meandering signal in the output of phase modulator

After signal filtering phase-modulated signal is formed at the device output. Such system construction maintains carrier and control signals coherence.

The second reason can be eliminated by applying a phase detector scheme at the far end.

Industrial electronic devices form security system radio signals on the objects. Figure 3 shows its system architecture.

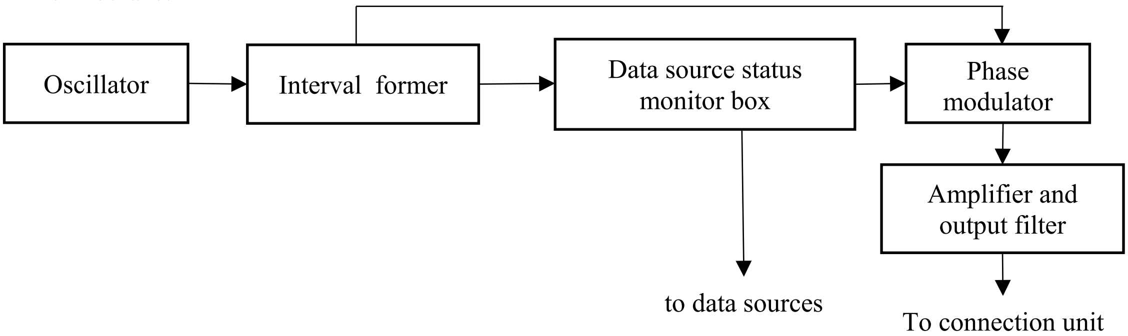

Figure 3 – Structural scheme of the industrial electronic device

The crystal-controlled oscillator generates a meandering signal with first harmonic frequency equal to 36 kHz. An interval former develops it to the carrier meander signal with first harmonic frequency equal to 18 kHz. This signal is routed to one of the phase modulator outputs through the monitor box of loopback high impedance state. The control signal is fed to another output from the interval former. The signal on the phase modulator output is shown in figure 2. At this rate, the modulator changes the polarity of the reference signal instantaneous value every half-period of the control signal.

The generated signal has complex spectral content. The signal amplitude spectrum computer-aided calculated is shown in figure 4.

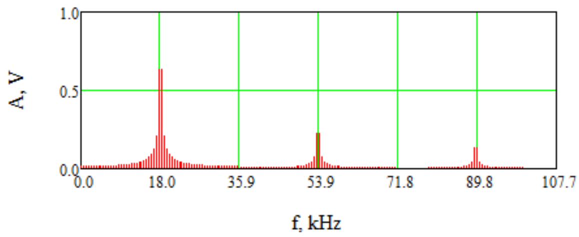

Figure 4 – Amplitude spectrum of the signal in the output of phase modulator

As is clear from figure 4 spectral components are located in spectral bands equal to 18, 54, 72 kHz in relation to frequencies of ungerate carrier meander spectrum harmonics. The spectral band structure is identical in the neighborhood of each carrier meandering spectrum frequency. It is determined by the control signal period *T* and phase modulation index π. All information about source status (phase transfer period) is contained in the spectral band in relation to the first carrier meandering spectrum harmonic. Thus, it is appropriate to transmit this frequency content to the channel. In addition to this, it is possible to interfere frequency components while sending all wavebands. It can lead to the expansion of interfering with signals in telecommunications and the degradation of information transmission fidelity. Consequently, the process of the radio signal forming has the following sequence. It is necessary to send the signal from the phase modulator output to the bandpass filter that extracts the required frequency spectrum. In figure 5 is shown a spectral component band in the neighborhood of the first carrier spectrum harmonic which includes communication channel status data of the security system.

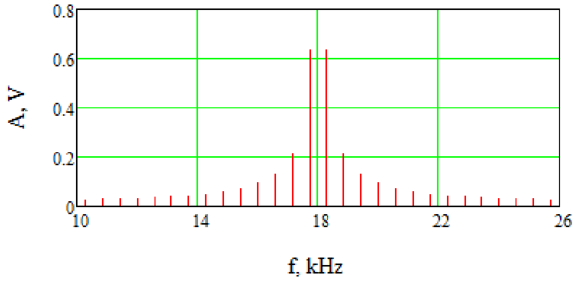

Figure 5 – Amplitude spectrum in the band near 18 kHz

The phase-modulated radio signal transmission through the bandpass filter leads to the change of the envelope while phase change. The signal in the output of the filter can be written like this:

$$a(t) = U(t)\cos(\omega_0 t + \theta_{нач} + \varphi(t)) \qquad (2)$$

U(t) – an instantaneous value of the radio signal envelope in the industrial electronic devices output.

Figure 6 shows a gain frequency characteristic of a parallel-oscillatory circuit. Figure 7 shows the radio signal in the filter output. Figure 8 shows the moment of phase transfer in the radio signal.

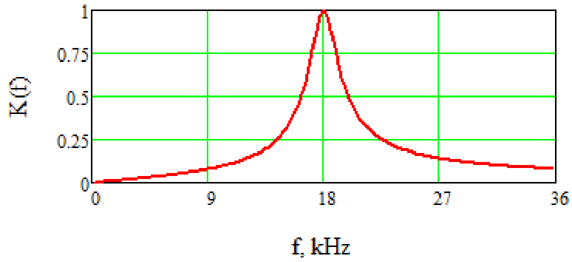

Figure 6 – Amplitude-frequency characteristic of the filter (parallel-oscillatory circuit)

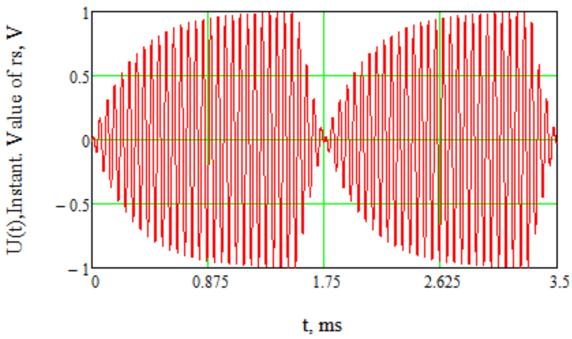

Figure 7 – The form of the radio signal in the output of the industrial electronic device

The operation frequency of a parallel-oscillatory circuit is 18 kHz; the filter transmission band is Δf = 1.714 KHz; the period of π phase change is T =3.5 ms.

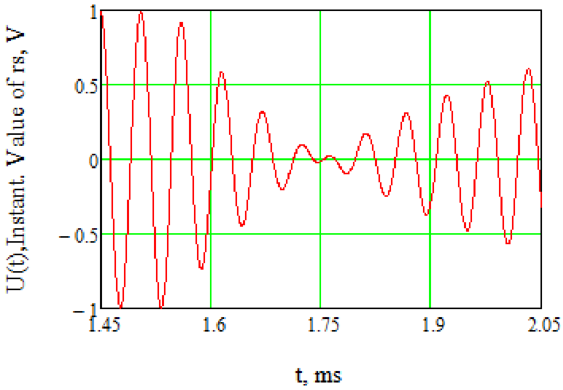

Figure 8 – The radio signal in the filter output at the moment of the phase change

Figure 7 shows that the radio signal envelope *U(t)* is not constant in the filter output. The signal (2) is transmitted to the phase detector input in the channel. Phase detector clears $\theta_{нач}$ in the received signal. The signal in the output of the phase detector can be written like this [4]:

$$U_{вых}(t) = \frac{1}{2} K \cdot U(t) \cdot U_{Г} \cdot \cos[\varphi(t)] \tag{3}$$

where K – coefficient of proportionality; $U_{Г}$ – heterodyne amplitude in the phase detector scheme; $\varphi(t)$ – phase modulation function.

From (3) it is obvious that the form of $U_{вых}(t)$ varies depending on $\varphi(t)$ and $U(t)$. The determination accuracy of the period (information parameter) is related to front edge steepness.

So, it is suitable to assess the impact of filters parameters on the envelope shape of the formed radio signal.

The circuit parameter that was analyzed in the article has a steel of squareness. That is why the author has been observing filters with a different form of a amplitude-frequency curve.

The author has conducted the computation of radio signals envelopes in the output of different filters in the research. The parallel-oscillatory circuit, Chebyshev filter and Butterworth filter were observed as filters. Conducted calculations have verified that it is worthwhile to choose tertiary Chebyshev and Butterworth filters. Further degree increase cannot improve the speed of the front envelope steepness of the radio signal in the filter output. Degree decrease causes impairment in the quality of filtration.

The tertiary Butterworth filter has been considered as the first filter. The filter transmission band is Δf =5.143 KHz.

A transfer function can be written like this:

$$H(\omega) = \frac{1}{1 + p(\omega) + p^2(\omega)} \cdot \frac{1}{1 + p(\omega)} \tag{4}$$

where $p(\omega) = \left(\frac{(-\omega^2 + \omega_н \omega_в)\omega_н \omega_в}{j\omega} \right)$ $\omega_н$ и $\omega_в$ – lower and upper cutoff frequency.

Figure 9 shows the Butterworth filter (1) amplitude-frequency curve.

Figure 10 shows the part of a radio signal (2) envelope while using the Butterworth filter.

It is possible to reach definite determination accuracy in finding the phase change period while rectification with using the Butterworth filter in industrial electronic devices. The speed of the front envelope steepness is estimated as a buildup time of growth from 0 to the maximum of instantaneous envelope radio signal value. For the Butterworth filter, the value is equal to 0,18 ms.

Also, the tertiary Chebyshev filter with the filter transmission band is Δf =5.143 KHz has been considered as another filter. The pulsation coefficient is equal to 0,5. A transfer function can be written like this:

$$H(\omega) = \frac{1}{1 + 0{,}5 \cdot p(\omega) + p^2(\omega)} \cdot \frac{0{,}5}{0{,}5 + p(\omega)} \quad (5)$$

Figure 9 shows the Chebyshev filter amplitude-frequency curve.

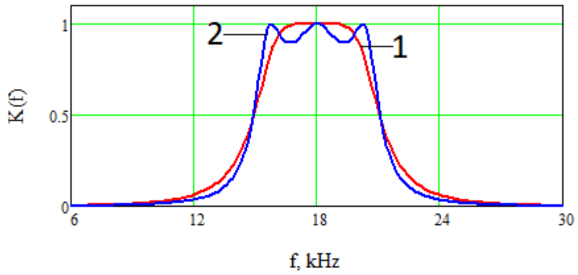

Figure 9 – Amplitude-frequency characteristics of the Butterworth (1) and Chebyshev (2) filters

Figure 10 shows the part of a radio signal envelope while using the Chebyshev filter. The speed of the front envelope steepness for that filter is 0,145 ms.

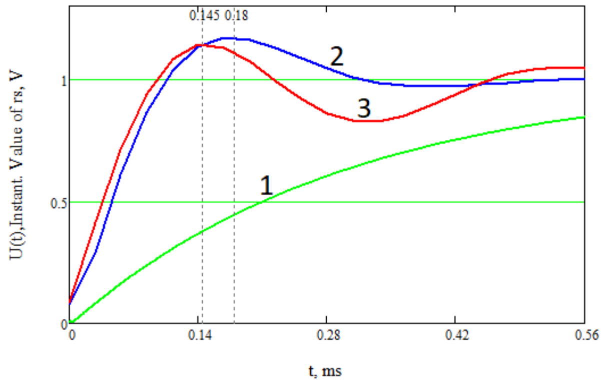

Figure 10 – The part of a radio signal envelope while using the parallel-oscillatory circuit (1), the Butterworth (2) and Chebyshev (3) filters

As may be inferred from figure 10 the front envelope steepness of the Butterworth and the Chebyshev filters is better in comparison with the use of the parallel-oscillatory circuit. Amplitude-frequency characteristic unevenness of the Chebyshev filter causes fluctuation of the envelope's shape. Nevertheless, the front envelope steepness grows faster than the Butterworth filter.

Conclusion

Filters in industrial electronic devices form the radio signal with incidental amplitude modulation in the output. Information transmission fidelity will be related to the radio signal envelope shape in the filter output. The faster the front envelope steepness grows the more exact would be data on the receiver end. The Chebyshev filter presents the top speed of the front envelope steepness growth in industrial electronic devices output. However, it is complicated to implement the Chebyshev filter.

REFERENCES

[1] Baskakov S.I. Radio-engineering circuits and signals: Textbook. – M.: High school 2000. – 462 p

[2] Zernov N.V. and Karpov V.G. Radio-engineering circuits theory, publishing house “Energia” », 1965 y. – 888 p

[3] Volhonskii V.V. Security alarm systems, Ecopolis and culture, 2005 y. – 202 p

[4] Alarm device “Atlas – 6” ЯЛБИ. 425612.001 ПС (Дв2. 403.038 ПС).

THE USAGE OF DC-MICROGRID IN INTELLIGENT BUILDINGS

Kuzmenko Vladimir

Saint-Petersburg State University of Aerospace Instrumentation,
Saint-Petersburg, Russia
E-mail: mr.konny@gmail.com

Abstract
Currently, everybody uses a variety of hi-tech things like tablets, laptops, mobile batteries, solar panels – all that work with direct electrical current, but the supply electrical power system and infrastructure is based on alternating current. Powerful IT systems, LED lighting systems, photovoltaic systems with batteries and charging stations for electric vehicles are operate on direct current are increasingly being used. Therefore, an obvious step in the modern engineering environment is the equipping of smart buildings with DC-networks. This article discusses a number of unresolved issues and suggests possible solutions in this direction.

1 INTRODUCTION

The conditions for current production and its usage in the context of modern requirements have undergone major changes in recent years. An important role in this is played by photovoltaic systems and batteries, LED lighting systems and other elements, that operate on direct current (DC). Therefore, the demand for the use of DC-grids is constantly growing.

Obviously, in the wake of the demand for consumption, there is a need to equip modern buildings with DC networks, which avoids losses when converting alternating current (AC) to direct, or vice versa.

In modern wind generators, in view of the variable speed of their rotation, it is necessary to double-convert the energy they generate (AC-DC-AC) in special converters to match the AC voltage. To work on a constant voltage network, the converter can be simplified by reducing its weight and dimensions. The management of solar-powered generators and various backup drives is also simplified, since their output voltage is not required to be converted to a voltage synchronous with the mains.

Almost all current household appliances are powered by AC voltage. However, if you carefully analyze the circuit of each household appliance, it turns out that for none of them such a power supply is natural. In almost every (!) Modern electrical appliance, the alternating input voltage is converted to constant with its further diversified use of various electronic circuits to create the necessary consumer qualities.

The usage of DC networks shows a real reduction in reactive power and losses in the conversion of electric energy, as well as its more efficient transmission and allows to achieve savings of 5 to 20% [1, 2]. In addition, DC networks may help improve the quality of electricity (reduce backlash due to harmonics) and ensure uninterrupted operation when switching to uninterruptible power systems (UPS).

2 DC-MICROGRIDS

In the context of the time-varying demand intensity, when using renewable energy sources, it is necessary to improve coordination of the transmission of electric energy and its use by the end user. This is achieved with the help of so-called intelligent microgrids, in which a high IT system takes charge control, as well as data storage.

Such infrastructure can be used in all directions for an intelligent building. Using sensors and actuators, an intelligent building is able to respond to changing environmental conditions and user needs.

For example, electric cars are gaining more and more popularity, which can also soon become mass consumers of electric energy. Batteries in electric vehicles are charged with direct current, so their use will largely depend on the infrastructure of the charging stations and charging time.

Therefore, it is necessary to take into account the flow of current in both directions and the corresponding bi-directional connection, which will allow the batteries in the connected electric vehicles to help compensate for load fluctuations (in the case of a combined charging system, this extended connection is mandatory in accordance with ISO15118).

Different loads can be connected directly to a 380 V DC distribution network or via a step-down DC converter. For example, through a reduced voltage of 12, 24 or 48 V DC. Such voltage are common in various industries.

However, in the course of resolving these issues a number of unsolved problems arise, in particular with regard to safety and protection against electric shock. These problems arise also because the experience with AC networks is much bigger, than the usage of networks.

Since 48 V DC is still in the range of safety extra-low voltage and, compared to 12 or 24 V, enables smaller line cross-sections and lower line losses, this standard is not only establishing itself in the lighting sector and has been defined by IEC/SEG 4 as the preferred voltage level for low power ranges.

The proposed topology of a DC microgrid (DC microgrid) is shown in Figure 1.

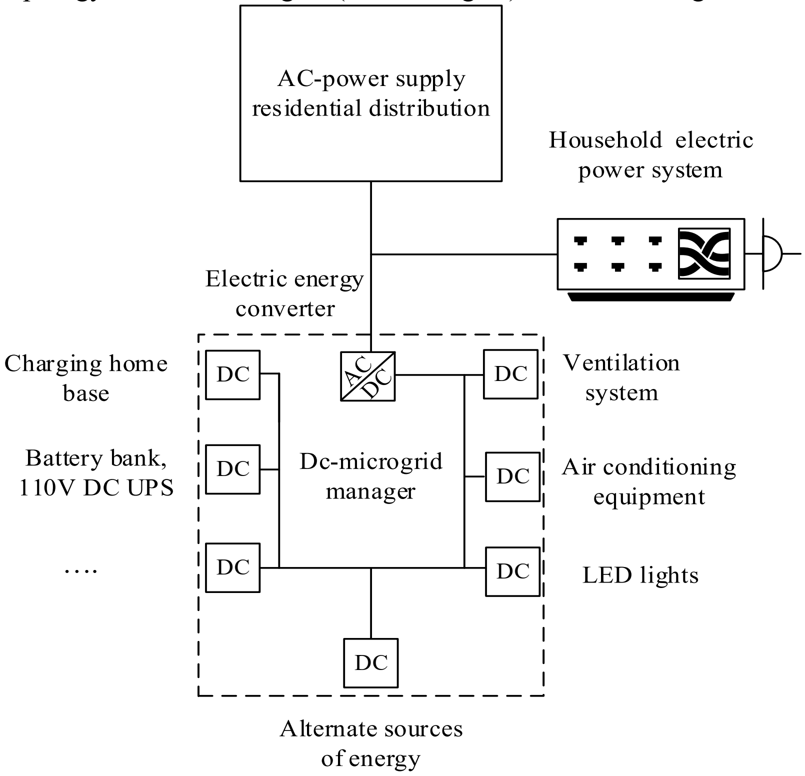

Fig. 1. An example of DC-microgrid topology

To operate such a DC microgrid in an intelligent building, you can use one "central" rectifier, instead of equipping many devices with separate rectifiers, as is currently done. The photovoltaic system, LED lighting systems, battery system (UPS) and fast charging system for electric vehicles are also connected to the DC-microgrid.

3 DIRECT CURRENT IN LED LIGHT SYSTEMS

As the required nominal power of LED (LED) lighting systems are getting lower, it becomes possible to use a reference voltage of 48 V DC.

One of the possible approaches to direct current transmission in LED lighting systems is the Power over Ethernet (PoE) method, based on the Western standard IEEE 802.3. Here, a data cable designed for Ethernet communication is used to simultaneously supply loads (the so-called Power Devices PD) with direct current through free pairs of lines that do not carry a constant signal.

The appeal of PoE lies in its ability to correlate data transmission with direct IP addressing and power supply in one infrastructure. [3] The disadvantage of this approach is its low power, which is limited due to the small cable cross-sections. But in recent years, it has been possible to increase the power from 15.4 W to 40 W, on two pairs of lines (class 5 according to the IEEE 802.3bt-2018 standard).

On the other hand, the power supply in PoE systems is limited by the resistance of the wires inside the Ethernet cable. This resistance generates heat and causes a voltage drop in proportion to the length of the cable. High-quality cabling and dedicated Ethernet switches should be used to maximize the power supply in lighting systems.

The advent of a 48 V DC distribution system requires some standardization of connectors and devices. One of these connectors can be a COB-matrix (chip-on-board) – one of the most common LED technologies used in directional light systems.

The essence of COB technology is to place crystals on the circuit board without cases and ceramic substrates, as well as coating these crystals with a common phosphor layer. Thanks to this, the cost of the LED matrix is really significantly reduced.

LED crystals with COB technology are much closer to each other than with SMD LEDs. The density can be up to 70 crystals per 1 square. see. However, each technology has its pros and cons. The first thing that should be noted here is the appearance of the holder, which is shown in Figure 2.

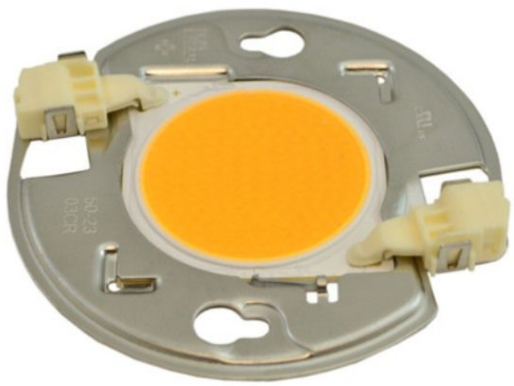

Fig. 2 The COD matrix and docking port

Often, it is the appearance that is decisive when a customer selects an LED light source. However, these are not all the advantages of this technology.

Luminous efficiency of COB-matrix, and superbright diode: 100 lm / W, and power factor of the used lamp power supply:> 0.95.

In addition, they have a common phosphor coating. Therefore, the COB matrix glows uniformly; individual points are almost indistinguishable in it.

With equal power, the size of the COB matrix is smaller than the size of the matrix of SMD LEDs. This allows you to create a semiconductor light source with the size of a luminous body, as in traditional sources.

The power of the COB matrix can reach 100 watts. The use of modern technological processes in the production of COB matrices and good heat dissipation make it possible to achieve a real light output of the matrix of 100-150 lm / W.

The luminous surface of a typical COB matrix is a square with a side of 1-3 cm or a circle with a diameter of 1-3 cm. Matrices with a luminous surface of large sizes, for example, 12x3 cm, are also found. Such matrices are used in outdoor lighting and allow, thanks to the large size of the luminous body, do without additional measures to reduce the blinding effect.

Radio standards for lighting management systems (LMS) and the Internet of things (IoT) are becoming increasingly popular. In addition to the IEEE 802.11 standard for WiFi networks, there are low-power standards such as Thread, ZigBee or ZigBee Green (IEEE 802.15.4 standard), Bluetooth (IEEE 802.15.1 standard) and EnOcean (IEC 14543-3-10 standard)) This type of wireless solution involves basic power supply up to 48 V DC and allows for control of lighting and sensors.

During operation, as a result of current surges in the network, disturbances in the operation of the luminaire driver, drying of the capacitor, the appearance of starting (pulse currents), the crystal lattice is damaged and the LED matrix luminous power decreases. An effect similar to the hole conduction effect occurs, and the electric current ceases to pass through portions of crystals that emit light, and because of the decrease in the voltage in current across the crystal, its power decreases. The DC current will downgrade these problems.

Since solutions based on radio communications have already found their application in intelligent buildings, they can be used for complex building automation. So, for example, you can combine different systems at the field level, and then combine them through the IP trunk, for example via BACnet-IP. At the automation level, you can use the ZigBee protocol as the communication level. The control level can be displayed via BACnet (DIN EN ISO 16484-5), via oBIX, or through the OPC-UA general automation standard (IEC 62541).

4 CONCLUSION

Despite its many advantages, DC systems also pose problems that should not be left without mention. These include technical solutions related to problems of electric energy transmission, problems of electromagnetic compatibility, losses when converting one type of current to another, and also the still insufficiently developed standardization of this equipment and the industry as a whole.

All these problems are closely related, since at this stage the solution of such technical issues as the transmission and conversion of electrical energy without losses is possible only after the elimination of certain gaps in standardization, as well as the safety and compatibility of equipment.

However, in addition to integrating renewable energy sources, charging systems for electric vehicles, LED lighting systems, as well as data storage and transmission systems, an approach using DC microgrids can help improve network stability. This aspect should not be underestimated, given the growing problems with pollution of AC networks. [4]

In this regard, in the coming years there should be a wider use of hybrid solutions for converting one type of current to another, together with solutions for LED lighting systems and other consumers of electric energy. The development of this direction should probably be promoted by both current achievements in the economic efficiency of domestic electricity consumption, for example from new photovoltaic systems, as well as domestic promotion and a policy of intelligent, balanced energy consumption.

REFERENCES

[1] B. Wunder, 380 V DC in commercial buildings and offices, Fraunhofer, 2013

[2] W. Buchs, M. Wendt, DC Power Supplies for Buildings, IEEE, 2015

[3] S.V. Solonyy, V.F. Shishlakov, i soavtory. Problemy integratsii sistem osveshcheniya i komponentov IoT / Metrologicheskoye obespecheniye innovatsionnykh tekhnologiy: tezisy // Mezhdunarodnyy forum. SPb.: GUAP, 2019. p. 224-227.

[4] S.V. Solonyy, V.F. Shishlakov, i soavtory. Izmereniye kachestva elektroenergii v sisteme elektrosnabzheniya so svetodiodnymi osvetitel'nymi ustroystvami / Nauchnyy vestnik NGTU, tom 74, № 1, 2019, p. 197-212.

METHOD FOR LOCATING MOVABLE OBJECTS IN HIGH-RESOLUTION OPTO-ELECTRONIC SYSTEMS

Nenashev Sergey

Saint-Petersburg State University of Aerospace Instrumentation,
Saint-Petersburg,Russia
E-mail: nenashev_sergey178@mail.ru

Annotation
Modern methods of object detection and tracking are considered in this paper. Based on the optical system, an algorithm for calculating the coordinates and velocities of small physical objects on the generated image of the frame stream is presented. A simulation model and a semi-natural optical-location system for estimating the trajectory coordinates of mobile objects and tracking their object trajectories have been implemented. The results were made taking into account the scale and the specified camera extension. Recommendations for installing an optical system for correct calculation of parameters are given

INTRODUCTION

Optoelectronic location systems are currently used in many areas of modern life, for example, in medical equipment, traffic control systems, satellite systems, environmental monitoring systems, security systems of municipal institutions, etc.also, every year there is an increase in modern requirements for such systems with a high resolution of about 8K, 12K and their processing becomes more difficult to implement performance with a frame reading frequency of about 50. This imposes a number of requirements for the implementation of such systems in the first place these are the requirements for GPU performance and other characteristics. In addition, such systems work in real time, for example, tracking cars in the video stream, tracking road signs, people at pedestrian crossings from the side of a vehicle, etc.in this regard, the task of developing and improving models and algorithms for processing video information for solving location problems is urgent [1, 2].

In this paper, we consider a video surveillance system for tracking a moving object and determining its trajectory coordinates in the video data stream.

When developing such systems, special attention should be paid to the following main processing steps:

- detecting objects of interest in the video data stream;
- measurement of the position coordinates of the detected object in the frame;
- measurement of object coordinates in the next frame;
- determining the speed of an object in the video data stream;
- support in the video frame stream;
- classification of the object.

When processing frames of a video stream in order to solve the problem of detecting and evaluating trajectory coordinates for the movement of objects, a number of features arise. For example, such as the movement of an object relative to the camera, changing their scale, and changing background conditions. Traditional tracking methods allow you to accompany an object in a video stream, but their performance does not allow you to implement real-time mode of the required quality.

DETECTION OF OBJECTS IN THE GENERATED IMAGE FRAME STREAM

In recent years, the scientific literature has seen rapid development of methods for recognizing and classifying objects [1-4]. The main idea of these methods is to select the object of interest against the background of the current frame, and then update the classifier in accordance with the dynamics of changes in the frame stream [5, 6]. The corresponding flowchart is shown in Fig. 1.

There are many ways to detect and track an object in a video stream, among which the most common method of processing is the method of "classification without a teacher" based on cluster analysis, by which the space of spectral features is divided into distinguishable groups, and the classification of image elements allows you to simultaneously segment the scene into spectrally homogeneous regions.

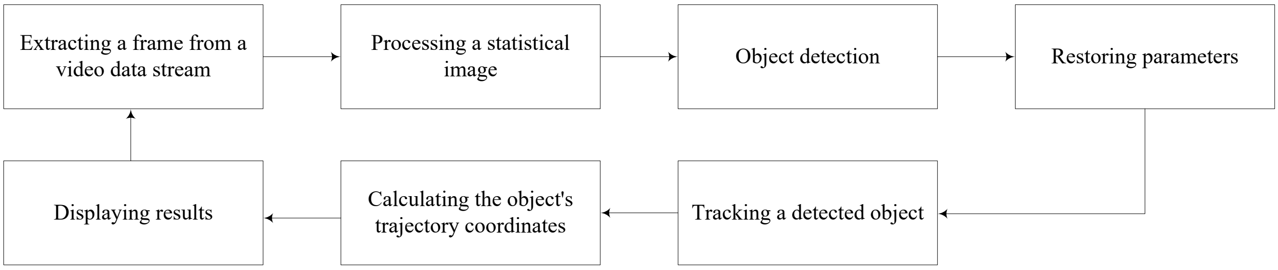

Fig.1 Scheme for calculating the object's trajectory coordinates

1. The Lucas-Canada method [4] – the essence of this method is to track a specific pixel (a set of pixels). The assumption is that the values of the pixels move from one frame to another without changes.

2. Method "median flow" – this algorithm tracks the movement of an object not only from frame t-1 to frame t, but also Vice versa. To do this, the image is divided into small regions and an optical stream search algorithm is used for them. The median offset of all points of an object is taken as the offset of its center. This algorithm is good at detecting tracking failures and works well in cases of smooth object movement. Poorly handles cases of overlapping and partial disappearance of an object [5].

3. TLD (tracking learning detection) method-the algorithm consists of three parts: detection, tracking, and training. The recognition process starts on each frame and the tracking process is adjusted based on the result. The essence of training is to evaluate the detector readings and recognize its errors. It works well in cases of partial overlap of the object [6].

However, if the object is completely hidden from the surveillance system of video cameras for a long time, any "tracker" that uses an adaptive model will give an error message, after which the object is lost.

In [8] and [9] describe an object detection model based on a multiscale and deformable part that uses a discriminant learning method. The proposed algorithm is almost insensitive to changes in the angle, scale, and rotation of the object in the frame. however, the detection speed is relatively slow, and does not meet the requirements of real-time processing.

In work [10], an algorithm for tracking a moving object based on models of the appearance of the object of interest is proposed. The maintenance process is mainly divided into two categories: the "generating" algorithm [11, 12] and the "refining" algorithm [13]. The "generating" algorithm is used to define objects based on a typical learning model. This model is then used to find the desired object in the image with the least error. In the "clarifying" algorithm, the task of tracking and detection is solved using binary classification, which is able to determine the boundaries between a moving object and the background, and then separate the object from the background. Thus, these algorithms have limitations and therefore models are required for their development and evaluation of their accuracy.

Let's consider a simulation model of optical location, when data is received from an optoelectronic device to the processing unit, then a decision is made whether there is a moving object in this video stream or not, and then the problem is solved: evaluating its trajectory coordinates, tracking, recognition, as well as the problem of resolving two large nearby objects. Next, we will limit ourselves to the case when a single object is located in the video stream. In figures 2a and 2b, a white dot shows a moving object in various frames of the video stream.

Simulation of object movement scenarios in the video data stream and implementation of detection algorithms, estimation of trajectory coordinates, etc.was carried out in the MATLAB computer simulation package. At the same time, the developed software package is implemented with the following requirements and restrictions.

First of all, in the developed model, the position of the location sensor should be set so that the object is located for a long time in its field of view and does not go over obstacles [15]. The speed of the object is limited by the following range V from 5 km/h to 250 km/h (set values for the minimum and maximum speed of the vehicle). The distance from the camera to the object is from 5 to 50 meters. The number of frames per second to read is 5, 12, 25, 50. The model assumes that the video data source and other internal parameters of the video surveillance system have already been focused.

In the model, it is possible to add random white Gaussian noise, like background noise, when working with grayscale frames – Fig. 2. It is possible to set the number of frames per second, the number of objects, their initial position, speed and size, as well as the trajectory of their movement.the equations of motion are nonlinear, which complicates processing and can lead to additional methodological errors [9].

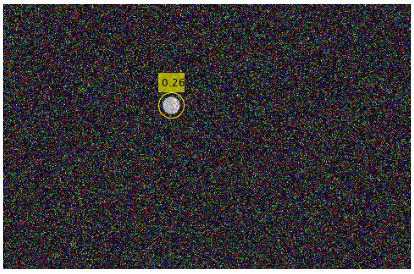

Fig.2(a). Indicator at time t-1

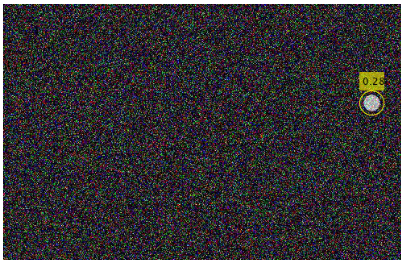

Fig.2(b). Indicator at time t

For fig.2a and 2b show how the software module detects a moving object against the background of noise, as well as determines its current position, distance traveled and speed in real time.

So, optical location systems without special algorithms for processing video data can successfully solve the problems of detection, tracking, and determining trajectory coordinates, but to solve the problems of recognizing and resolving objects in groups, provided that the signal/noise indicators are satisfactory, specialized processing algorithms are required [14].

Testing of the speed estimation module program is structured as follows:

1) selecting a frame at time t_1 and t_2;

2) calculating the coordinates of the center point of the tracking object at time t_1 and t_2;

3) calculating the tracking point offset;

4) determine the average V_m speed and compare it with the specified V value.

We fix the moment of time t_1 = 5.32 sec (Fig.3a). The tracking point P is marked in red (the same for t_2). The value of the p coordinate on the abscissus axis P_{X1} = 179 pixels. Then output the second frame at time t_2 (Fig. 3b). We note the time t_2 = 6.47 s. the value of the coordinate P on the axis of the abscissus P_{x2} = 248 pixels. Then we calculate the offset and time:

$$\Delta P = P_{x2} - P_{x1} = 69\ px$$

$$\Delta t = t_2 - t_1 = 1{,}15\ \text{sec}$$

where ΔP – the offset for the time Δt. After calculating the offset and the time it took for this shift to occur, we determine the average speed:

$$V_{cp} = \frac{\Delta P}{\Delta t} = 60\ px/\text{sec}$$

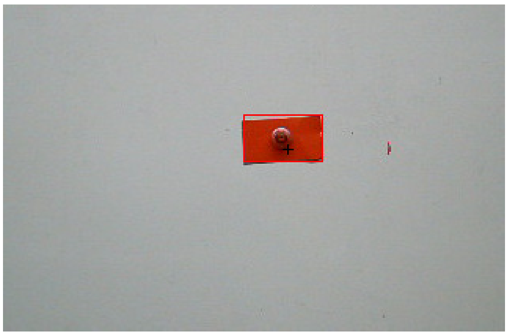

Fig.3a. Fixing an object at time t-1

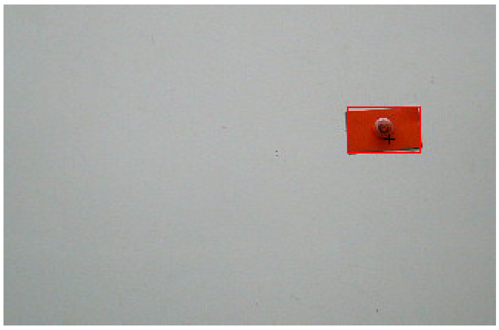

Fig.3b. Fixing an object at time t-1

Taking into account the parameters for converting pixels to centimeters, we calculate the V_m in cm/sec. according to the calibration data, C = 10.67 px/cm, where C is the number of pixels per centimeter, therefore

$$C = \frac{P_x}{l_x} = 320/30 = 10{,}67\ px/\text{sec}$$

$$V_m = \frac{60\ px/\text{sec}}{C} \approx 5{,}62\ cm/\text{sec}$$

The value of the set speed of movement of the observed object is in the range 5 < V < 6, which coincides with The V_m value calculated experimentally. Thus, we can say that the program for detecting and evaluating the object's speed is working correctly. The accuracy of speed measurement is affected by the method that will be used for calibration and scaling in the software before starting the program [9].

CONCLUSIONS

As a result, an optical-location system for detecting and evaluating the speed of moving physical objects on the generated image of the frame stream was implemented. Speed measurement is possible both in real time and on a pre-recorded video stream. All the developed algorithms are implemented in the MATLAB package, using the "Image Acquisition Toolbox" functions.

LIST OF SOURCES USED

11. Object Detection Using Deep Learning. URL: https://ww2.mathworks.cn/examples/computer vision/mw/deeplearning_shared-ex69834039-object-detection-using-deep-learning (Date of request: 11.03.20)
12. .Television measuring systems for road speed control.URL: https://kite.ru/articles/sensor/2007_4_34.php (Date of request: 13.03.20)
13. V.E. Gau, V.A. Unrobin, E.N. Vikulova, N.A. Nikiforov, N.N. Makarov, D.A.Lakhmanov. " Method for detecting objects in an image from the perspective of the theory of active perception " Proceedings of NSTU. R. E. Alekseeva, no. 1 (120), 2018, pp. 9-15.
14. Calculation of the optical flow by the Lucas-Canada method. https://habr.com/ru/post/169055/ (accessed: 25.02.20)
15. L. Beinenson. Methods for tracking objects. URL: **Ошибка! Недопустимый объект гиперссылки.** (Date of request: 11.03.20)
16. Zd. Kalal, Kr. Mikolajczyk, and J. Matas. Tracking-Learning-Detection. IEEE TRANSACTIONS ON PATTERN ANALYSIS AND INTELLIGENCE, VOL. 6, NO. 1, JANUARY 2010.
17. Gutsev R. A., Solonar A. S., and Tsupriks.V.."Laboratory-modeling complex for the study of quality indicators of the optical-location system of television type" Reports of the Belarusian state University of Informatics and Radioelectronics, no. 6 (100), 2016, pp. 55-61.
18. Daniel A. Forsyth Computer vision. Modern approach: a textbook / David A. Forsyth. Jean Pons-Mer. with English. Moscow: Williams Publishing house, 2004. – Pp. 66-67.
19. Code Generation for Depth Estimation From Stereo Video URL: https://ww2.mathworks.cn/examples/computer-vision/mw/vision-ex25603429-code-generation-for-depth-estimation-from-stereo-video (Date of request: 11.03.20)
20. N.N.Vasin, V. Y. Kura "measurement of the speed of motion of extended objects video surveillance systems". News of higher educational institutions. Instrumentation, vol. 56, no. 10, 2013, pp. 77-80.
21. Vakhitov L. T. Review of stereo vision algorithms / A. T. Vakhitov. L. S. Gurevich, D. V. Pavlenko. Stochastic optimization in computer science. Vol. 4 / Under the editorship of O. N. Granichina – SPb.: Saint Petersburg University press 2008. – 299c.
22. How to Detect and Track Red, Green and Blue Colored Object in LIVE Video.URL: https://www.mathworks.com/matlabcentral/fileexchange/40154-how-to-detect-and-track-red-green-and-blue-colored-object-in-live-video. (Date of request: 16.02.20)
23. R. Cipolla, S. Battiato,and G. M. Farinella (Eds.). Computer Vision Detection, Recognition and Reconstruction. Studies in Computational Intelligence 2010. – 362 p.
24. Chernyshev S.A., Nenashev V.A., Kurtyanik D.V. Environment modeling stages of processing photos and video. Binarization plugin // Certificate of state registration of computer programs № 2018664970 of the Russian Federation, publ. 11/27/2018. ROSPATENT.
25. A. P. Chupakhin, M. L. Savin. "Assessment of the flight speed of small aircraft using video equipment" Izvestiya Tula state University. Technical Sciences, no. 9-1, 2014, pp. 126-130.
26. A. T. Levinsky N. M. Salute I. D. Rodionov. Tracking the movement and evaluating the speed of an object in the video stream.// MSTU im. N. E. Bauman, 2017. 12 p.

INELASTIC SYNCHROTRON RADIATION SCATTERING IN $PbZr_{0.985}Ti_{0.015}O_3$ IN THE VICINITY OF M-POINT

Petroukhno Konstantin

Postgraduate student
Peter the Great St.Petersburg Polytechnic University,
Saint-Petersburg, Russia
E-mail: k.a.petroukhno@gmail.com

Abstract

The paper presents a preliminary analysis of the data provided by inelastic X-ray scattering method in $PbZr_{0.985}Ti_{0.015}O_3$ in the vicinities of two Brillouin zone M- points: symmetric (h=k) and asymmetric (h≠k). The observed results have been adequately described in approximation of two non-coupled phonon resonances and one central peak. We have demonstrated that high-frequency phonon resonances are not directly related to the rotation of oxygen octahedra A dramatic increase in intensity of the low-frequency phonon resonance was found at Q =(3.45 0.55 0) T = 700K. Tentative conclusion is made about the nature of this phenomenon.

INTRODUCTION

Antiferroelectric materials have a long study history. First researches were carried out in the early 50s of the last century [1]. The very first material investigated was $PbZrO_3$ (PZ) – one of variety of widely used solid solutions $PbZr_{1-x}Ti_xO_3$ (PZT) [2,3]. Both PZ and PZT belong to the perovskite family and have the cubic Pm3m structure above the Curie temperature and show paraelectric properties. Figure 1 shows the primitive unit cell of a cubic perovskite. The cell consists of cation A, located in the origin of the coordinates, cation B in the center, and three oxygen atoms X located on the faces of a cube.

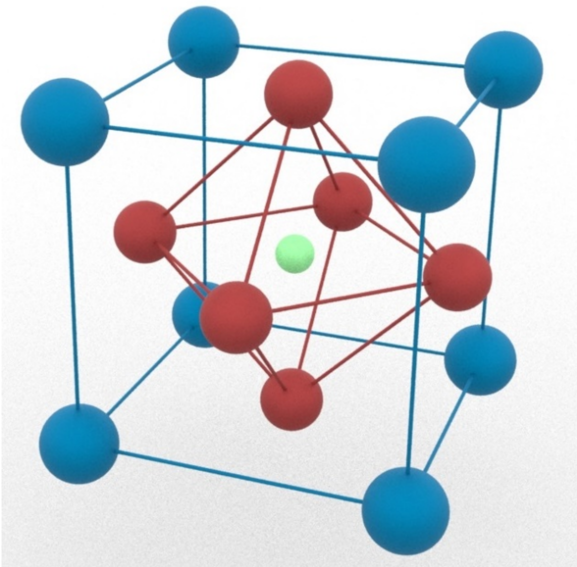

Fig. 1. 3D representation of a perovskite structure

Perovskite structure can be represented as a network of connected BO_6 octahedra while the perovskite structure disordering can be described in terms of oxygen octahedra rotations, cations displacements and distortions of oxygen octahedra. Oxygen octahedra rotations may result in primitive cell doubling (because the next one has to rotate in the opposite direction) and are described by their "pitch, yaw and roll" and also by relevant rotation of octahedra in adjacent layers [4]. M-type superstructural reflexes on diffuse scattering images occur when oxygen octahedra rotate in phase $Q_M = \left(h+\frac{1}{2} \;\; k+\frac{1}{2} \;\; l \right)$.(Fig. 2.)

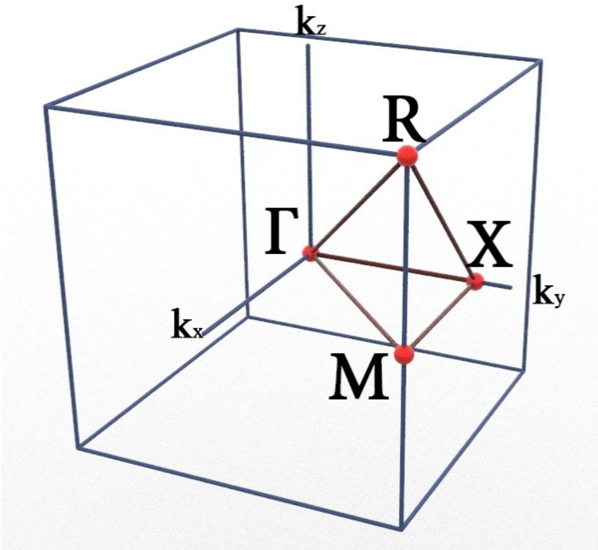

Fig.2. Brillouin zone for the space group Pm $\overline{3}$*m [5]*

Even though compositions with Ti concentration close to morphotropic phase boundary already have a wide practical application in sonars, hydrophones, ultrasound generators, high-voltage generators, micropositioners [6], the microscopic nature of phase transition mechanisms remains incompletely explained. The region with Ti concentration below 6% demonstrates complicated phase diagram, and raises one of the most contradictory questions, which is related to the intermediate ferroelectric phase origin of the $\left(h+\frac{1}{2}\ \ k+\frac{1}{2}\ \ \ l\right)$ superstructure and a set of satellites around this M-type peaks.

The difference between diffuse scattering around symmetric (h=k) and asymmetric (h≠k) M-points was observed experimentally and reported in ([3], [7]). The excess of diffuse scattering was observed only on one side of asymmetric M-point. Such asymmetric peak of diffuse scattering was interpreted in terms of combination of lead and oxygen displacements. However, the direct summation of contributions of such two modes cannot explain the effect because of huge difference in squares of atomic form factors of Pb and O.

Theoretical papers predict the existence of the soft mode related to the oxygen octahedra rotation. However, the condensation of such mode should result in the h=k extinction rules which is not observed in the experiment. Full information about the phonon frequencies and eigenvectors for the all low-frequency phonon modes at and around the M-point is needed to design a more complicated model of coupled modes interaction and provide it with realistic parameters. Single crystals of PZT in the antiferroelectric region are very small and could not be studied by neutron inelastic scattering technique. To address the problem above we used inelastic X-ray scattering method.

EXPERIMENTAL SECTION

The paper presents the results of preliminary analysis of data obtained in the European ESRF synchrotron radiation center on small single crystals of $\mathrm{PbZr_{1-x}Ti_xO_3}$ at Ti concentration of 1.5% (PZT1.5). The samples were properly polished and etched. The experiment covered a temperature range of 450K < T < 700K. Experiment started with the high-resolution measurements of the diffuse scattering at the side station of the ID28 (Fig. 3.) to determine the exact position of the critical scattering in the reciprocal space (on the Σ-line or slightly aside of it similar to the Bragg satellites). All measurements were concentrated in the vicinities of the 2 M-points $(2.5\ 2.5\ 0)$ (h=k) and $(3.5\ 0.5\ 0)$ (h≠k). In order to determine phonon dispersion parameters more precisely the measurements were done within $\mathrm{Q_{M1Start}} = (2\ 3\ 0)$ and $\mathrm{Q_{M1End}} = (3\ 2\ 0)$, and between $\mathrm{Q_{M2Start}} = (3\ 1\ 0)$ and $\mathrm{Q_{M2End}} = (4\ 0\ 0)$ respectively. All measurements were redone at several temperatures so one may trace a temperature dependence. Within a specified temperature range, a set of spectra was obtained for a number of reciprocal points. The obtained IXS spectra shared a same structure: presence of at least two easily distinguishable symmetric phonon resonances, and a so called "central peak" at zero transmitted energies. Preliminary data analysis was performed under the assumption of non-coupled modes and both phonon resonance energy and phonon resonance width were described as if they were damped harmonic oscillators.

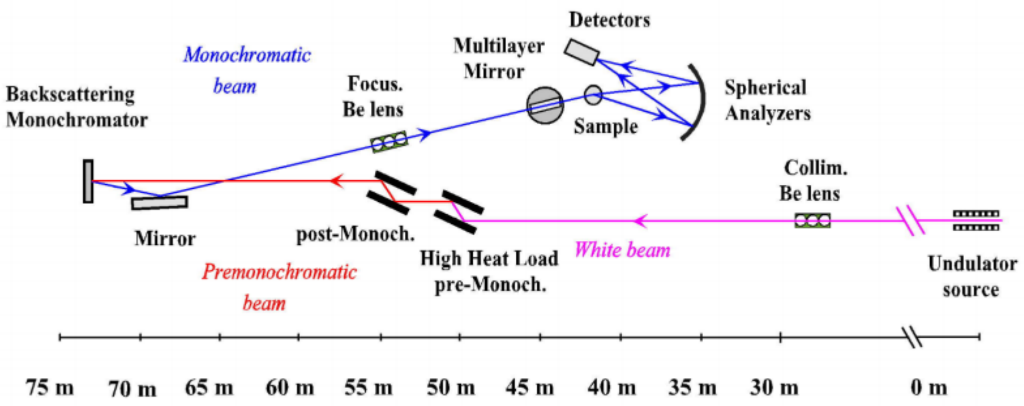

Fig. 3. Schematic representation of an ID28 backscatter spectrometer [8]

Bose-Einstein occupation factor was also taken into the consideration. Thus, formula for each of phonon resonances was:

$$I(\omega)=\frac{\omega}{1-e^{\frac{h\omega}{kT}}}\frac{F_{ph}\gamma}{\left(\omega_{ph}-\omega\right)^2+\omega^2\gamma^2} \tag{1}$$

where ω_{ph} is the phonon energy, γ is the phonon attenuation constant, and F_{ph} is the structural factor. The shape of the central peak was described by the Lorentz function:

$$I_{cp}(\omega)=\frac{1}{\pi}\frac{F_{cp}{}^2\gamma^2{}_{cp}}{\omega^2+\gamma^2{}_{cp}} \tag{2}$$

where γ_{cp} is the damping constant of the central peak and F_{cp} is the structural factor. The approximation formula on this step had a total of 8 parameters and looked like:

$$I(\omega)=\frac{\omega}{1-e^{\frac{h\omega}{kT}}}\frac{F_{ph_1}\gamma_1}{\left(\omega_{ph1}-\omega\right)^2+\omega^2\gamma_1{}^2}+\frac{\omega}{1-e^{\frac{h\omega}{kT}}}\frac{F_{ph2}\gamma_2}{\left(\omega_{ph2}-\omega\right)^2+\omega^2\gamma_2{}^2}+\frac{1}{\pi}\frac{F_{cp}{}^2\gamma^2{}_{cp}}{\omega^2+\gamma^2{}_{cp}} \tag{3}$$

Each spectrum was approximated by a function (3) using variable metric method (MIGRAD) [9] from the MINUIT C++ package via the iminuit Python interface.

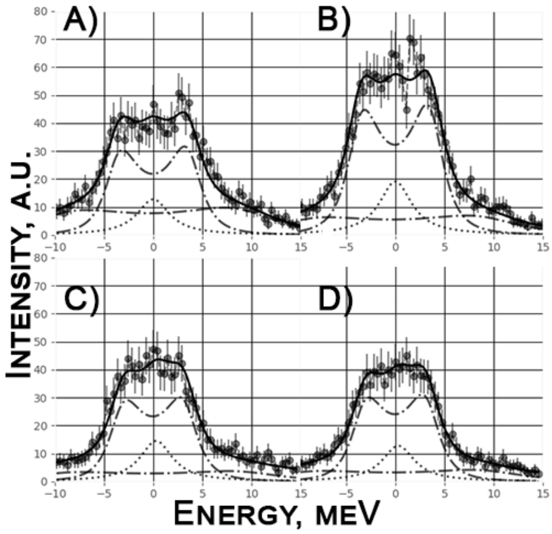

Fig. 4. Positions of studied points in reciprocal space

The difference in locations of two sets of points in reciprocal space is shown on the figure 4.

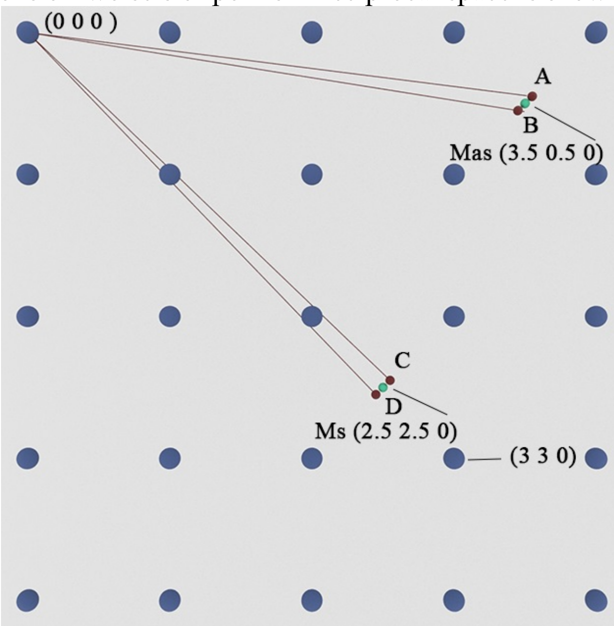

Fig.5. A) and B) spectra near asymmetric M-point(3.55 0.45 0) *and* (3.45 0.55 0)*respectively C) and D) near symmetric M-point* (2.55 2.45 0) *and* (2.45 0.55 0) *T = 700K*

Figure 5 presents spectra near asymmetric M-point with coordinates (3.5 0.5 0) and symmetric M-point coordinates (2.5 2.5 0). Dotted lines on figure 5 demonstrate a contribution of the central peak. Dash-dotted lines are used to show phonon resonances. Points and error bars display experimentally obtained data, while the solid lines present the approximation results. It can be clearly seen from all the subplots, that there are 2 major phonon resonances. Contributions from low-frequency phonon resonance (LFPR) have energies about 4.4-4.5 meV while the ones from high-frequency phonon resonances (HFPR) are located within the range of 10.5-11 meV. The intensity and location of HFPR are almost the same on all four plots. LFPRs in the vicinity of symmetric reciprocal lattice point looks exactly the same from both sides. The situation around asymmetric point differs dramatically. The intensities of low-frequency phonon resonances turn out to be nonidentical to each other (Fig.5 A and B). Moreover, a stronger central peak component emerges from one side.

CONCLUSION

We performed the systematic study of the shapes of phonon resonances in PZT1.5 in the vicinities of symmetric and asymmetric M-points. We found that observed results are adequately described by contribution from two phonon resonances and one central peak. On the one hand performed analysis clearly demonstrates that high-frequency phonon resonance cannot be attributed to the rotation of oxygen octahedra due to very weak oxygen atomic factor as compared to the lead one. On the other hand, the difference between two equivalent low-frequency phonon resonances is clearly seen near asymmetric M-point. This difference can be tentatively attributed to the existence of a contribution from the interference of the low frequency acoustic mode (probably related to a lead displacements) with the oxygen octahedra rotation mode. For a more detailed analysis, a simultaneous data processing of sets of points under different temperature conditions in the vicinities of symmetric and asymmetric M-points should be done. Such an analysis will be carried out in the future.

REFERENCES

[1] Shirane G., Sawaguchi E, Takagi Y. Dielectric properties of lead zirconate // Journal of the Physical Society of Japan. 1951. V. 6, No 3, pp. 208–209.

[2] Jaffe Bernard, Cook WR, Jaffe Hans. Piezoelectric Ceramics // Academic, New York. — 1971.—P. 135.

[3] Zhang, N., Pasciak, M., Glazer, A. M., Hlinka, J., Gutmann, M., Sparkes, H. A., Welberry, T. R., Majchrowski, A., Roleder, K., Xie, Y. & Ye, Z.-G. (2015). J. Appl. Cryst. 48, 1637-1644.

[4] Glazer AM. Simple ways of determining perovskite structures // Acta Crystallographica Section A: Crystal Physics, Diffraction, Theoretical and General Crystallography. — 1975. — Vol. 31, no. 6. — P. 756–762.

[5] Setyawan, Wahyu, and Stefano Curtarolo. "High-Throughput Electronic Band Structure Calculations: Challenges and Tools." Computational Materials Science 49.2 (2010): 299–312. Crossref. Web.

[6] Noheda B. Structure and high-piezoelectricity in lead oxide solid solutions. // Current Opinion in Solid State and Materials Science. 2002. V. 6, P. 27 -34.

[7] M. Pasciak et al., Atomistic modeling of diffuse scattering in cubic PbZrO3. Phase Transit. 88 (3), 273 (2014).

[8] ID28 – inelastic scattering. — https://www.esrf.eu/UsersAndScience/Experiments/DynExtrCond/ID28/BeamlineLayout

[9] James, F., & Roos, M. (1975). Minuit – a system for function minimization and analysis of the parameter errors and correlations. Computer Physics Communications, 10(6), 343–367.

DIFFRACTION SPECTRAL DEVICE IN THE MULTI-ALTERNATIVE AUTOMATIC CONTROL SYSTEM

Serdiuk Ksenia

Saint-Petersburg State University of Aerospace Instrumentation
Saint-Petersburg, Russia
E-mail: kserdiuk@yandex.ru

Abstract
On the basis of multi-channel automatic control, the possibility of multi-alternative automatic control of physical and physico-chemical processes accompanied by the optical emission is considered. The output vector is formed by means of spectral measurements with a diffraction prism spectral device, the action of which is considered in the framework of an alternative approach based on the signaling theory and the linear systems theory.
Keywords: multi-alternative automatic control system; output vector; spectral measurements; spectroscopic information; diffraction prism spectral device; instrument function.

INTRODUCTION

In physics and engineering, spectral analysis methods and devices are among the most common, and harmonic spectrum analysis refers to the number of the most important physical measurements. The role of harmonic analysis is particularly important in spectroscopy, where the information obtained is contained in the function of electromagnetic radiation energy distribution through frequencies. This information is being extracted using spectral devices that perform harmonic analysis. Spectroscopic methods of obtaining information are the only ones possible when studying very remote or hard-to-access objects. The distinguishing feature of these methods consists in the fact that the study of an object by the emission or absorption spectra does not violate the physical conditions existing in this object.

In spectroscopic measurements, spectral devices study electromagnetic radiation as a signal sent by matter and carrying information about the chemical composition of a substance, about the physical and physico-chemical processes occurring, along with the physical properties of the medium through which the radiation propagates. Thus, the spectral devices largely represent the tools for the microcosm study. These spectral measurements are characterized by obtaining spectroscopic information in the form of a continuous frequency function (wavelength).

In the paper [1], a fundamentally new direction of optical spectroscopy methods application is defined. We are talking about multi-alternative automatic control [2] of physical or physico-chemical processes accompanied by electromagnetic radiation in the optical range, while the error signal is formed by spectroscopic measurements. If a spectral device is used as a measuring device in multi-alternative automatic control systems, spectroscopic information must be provided in the form of reference values of the measured spectrum, i.e. in matrix form. For this purpose, a multi-channel optical spectral device that implements the resonant multi-channel principle of spectrum measurement and belongs to the new ones [3] is quite suitable. This device is characterized by obtaining spectroscopic information in the form of reference values of the measured spectrum, which constitute the output vector $\{y_k'\}$ of a multi-channel automatic control system. The vector values $\{y_k'\}$ are determined by the controlled spectroscopic variables that are defined by the results of the spectrum measurement.

The use of well-established diffraction, spectral devices, in this case – prism one, for the formation of the output vector $\{y_k'\}$ is possible if the CCD is used for reading spectroscopic information.

During the automatic control system operation, the information, the carriers of which are dynamic signals, is processed. Here such signals are being optical radiation, their description and processing must be performed in terms of signaling theory and the linear systems theory. The traditional theory of diffraction optical spectral devices, for example [4, 5, 6], relies on the principles of geometric optics, and it is not possible to apply its results to solve the set task. In this regard, an alternative theory of the diffraction prism spectral device (DPSD) used in this work is proposed. Its prerequisites are proposed in the paper [7], within which the properties of the output vector are obtained .Within this theory the properties of the output vector $\{y'_k\}$ are obtained.

MULTI-ALTERNATIVE AUTOMATIC CONTROL SYSTEM

The functional scheme of a multi-channel automatic control system (ACS) [8], which is shown in Fig.1., is adopted as the basis of the functional scheme of a multi-alternative automatic control system, where the error signal is proposed to be formed based on the spectroscopic measurements results.

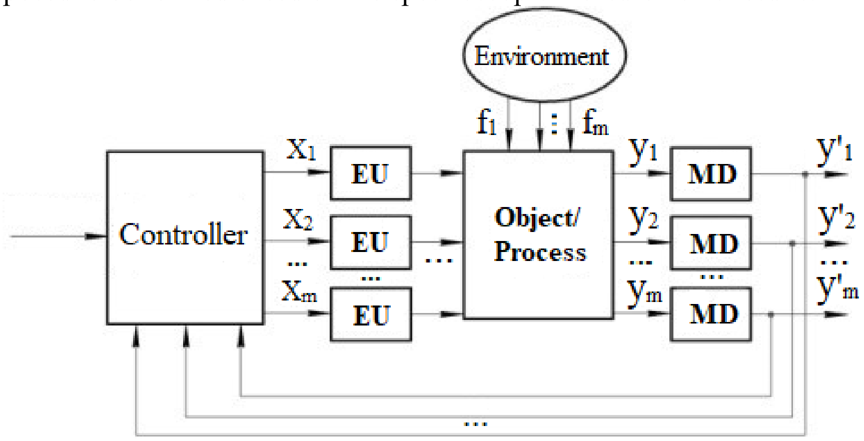

Fig.1. Functional scheme of the ACS

In this scheme, the following signs are introduced: Controller – control system; x_k - input variables; EU-execution units; Environment – external environment; f_k – disturbing influences; Object/Process – object/process; y_k – regulated devices; MD – measuring devices; y'_k – output variables that are combined in the output vector $\{ y'_k \}$.

Transition from the diagram shown in Fig.1, to the scheme of multi-alternative ACS is as follows:

1) measuring device system {EU} is replaced by a single measuring device DPSD, on the input of which falls the optical radiation. The radiation, generated by a controlled physical or physico-chemical process, carries information about the development of the latest and replaces the system of vectors $\{y_j\}$; the formation of the output vector $\{y'_k\}$ is performed by reading out spectroscopic information using a CCD, this information is extracted using pixels corresponding to those narrow-band spectrum sections, which are controlled;

2) the control device is supplemented with a device for prioritizing control by a particular output vector component $\{y'\}$.

The corresponding functional diagram of a multi-alternative automatic control system is represented in Fig.2.

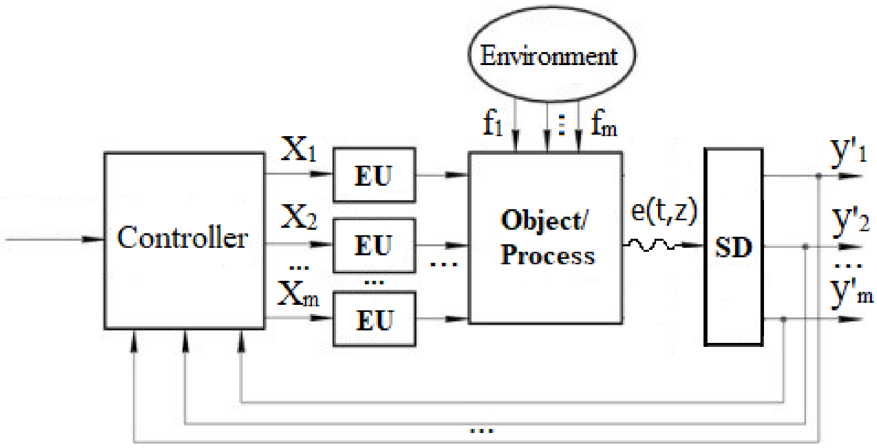

Fig.2. Functional scheme of the multi-alternative ACS

In contrast to Fig.1, in Fig.2 the following designations are introduced: $e(t,z)$ – optical radiation that carries spectroscopic information about the object/control process; SD- optical spectral device.

OPTICAL DIFFRACTION PRISM SPECTRAL DEVICE

The optical scheme of the diffraction prism spectral device is shown in Fig.3, it consists of two parts: the collimating system (A) and the analyzing (resolving) system (B), where a prism is used as a dispersing element (DE).

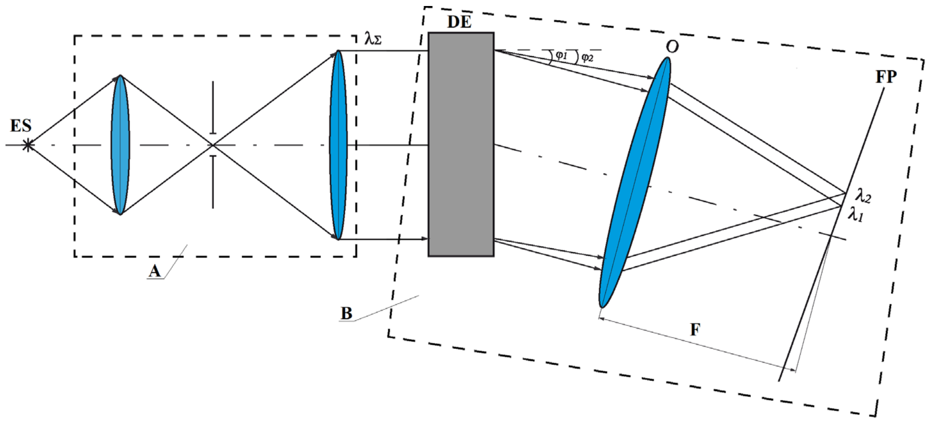

Fig.3. Optical scheme of a diffraction spectral prism device

Fig.4 shows the optical scheme of the analyzing part of the diffraction prism spectral device, it consists of a prism (1), a lens (3) with a focal length F that is assumed to be ideal, and two layers of free space (2) two planes – input one $z = 0$ and output one (4) $z = 2\mathrm{F}$.

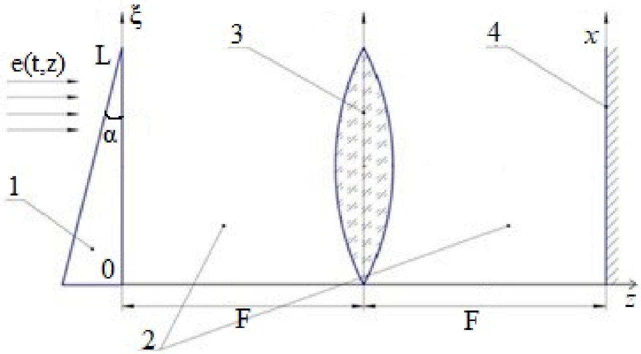

Fig.4. Optical scheme of the analyzing part of a diffraction prism spectral device

The diffraction prism spectral device analyzing system under illumination by a flat homogeneous monochromatic light wave is considered as an optical coherent Fourier processor [9], where the input device for the processed signal is a prism.

The main prism parameters are: the size of its input aperture L, the angle of the prism α, and the refractive index of the prism material $n(\cdot)$, attenuation in the prism material is not taken into account. Through these parameters, the transmission function of the prism as a phase transparency, takes the form of [7]:

$$\dot{\mathrm{T}}(\xi,\nu) = \exp[(i\nu n(\nu)\xi tg\alpha / c_0],, \tag{1}$$

where $\nu -$ is the time circular frequency of a monochromatic light wave; c_0 – the speed of light.

The action of an optical coherent Fourier processor is described by the ratio [9]:

$$S_x(\omega_x) = \alpha \int_L f(\xi) \exp(-i\omega_x \xi) d\xi\,, \tag{2}$$

where $S_x(\omega_x)$ – is the spatial frequency spectrum; $\omega_x = \nu x / c_0 F$- is the spatial frequency; $\alpha = \sqrt{2\pi c_0 F / \nu}$; $f(\xi)-$ spatial signal in the input plane.

The most important relation of the linear systems theory is the «input $x(\cdot)$ - output $y(\cdot)$» ratio of a linear system [10]

$$y(\lambda) = \hat{\mathrm{L}}\, x(\lambda) = y(\lambda) = \int\limits_{\Lambda} H(\lambda,\lambda')x d\lambda' , \tag{3}$$

where $\hat{\mathrm{L}}-$ is a linear bounded operator; $H(\lambda,\lambda')-$ is the instrument function; the meaning of variables λ,λ' and the interval of integration Λ are determined by the current tusk.

The relation (3) is a von Neumann problem, representing a linear operator in the form of an integral [11]; in relation to the linear systems theory, its solution is proposed in [12], where the meaning of the integral transform of the linear integral operator (3) is defined in the form:

$$H(\lambda,\lambda') = \hat{\mathrm{L}}\,\delta(\lambda-\lambda') . \tag{4}$$

When performing spectral measurements, this $\delta-$effect is represented by a spectral function $\delta(\omega-\nu)$ that has no physical interpretation, however, the following expression has a clear physical meaning:

When performing spectral measurements, such an effect is represented by the spectral function that does not have a physical interpretation, however, a clear physical meaning is reflected by a harmonic vibration, under the influence of which the instrument function of a spectral device that performs measurements of the spectrum of oscillatory processes is determined:

$$\hat{\mathrm{F}}^{-1}\,\delta(\omega-\nu) = \exp(i\nu t), \tag{5}$$

where $\hat{\mathrm{F}}^{-1}-$ is the inverse Fourier transform operator; $\omega-$ is the circular time spectral frequency.

The complex spectrum spread function of the diffraction prism spectral device, as a wave analyzer, is determined when its analyzing system is exposed to a homogeneous plane monochromatic light wave, which can be represented in a scalar form characteristic of optical spectrometry:

$$e(z,t) = \exp(i(\nu t - kz)) = \hat{\mathrm{V}}\hat{\mathrm{F}}^{-1}\exp(i\nu t) , \tag{6}$$

where $k = \nu / c_o -$ is the wave number;

$$\hat{\mathrm{V}} = \int\limits_{-\infty}^{\infty} e(t')\delta((z/c_0) - t - t')dt' . \tag{7}$$

If the analyzing system action is described by a linear bounded operator $\hat{\mathrm{A}}$, then the result of complex spectrum measurement, according to (3), has the form:

$$S_a(\omega) = \int\limits_{-\infty}^{\infty} H(\omega,\nu)S_0(\nu)d\nu\, , S_0(\nu) = \hat{\mathrm{F}}\,e(t) , \tag{8}$$

where $\hat{\mathrm{F}}-$ is the direct Fourier transform operator; the complex instrument function

$$H(\omega,\nu) = \hat{\mathrm{A}}\hat{\mathrm{V}}\hat{\mathrm{F}}^{-1}\,\delta(\omega-\nu) = \hat{\mathrm{L}}\,\delta(\omega-\nu) \tag{9}$$

satisfies the definition (4).

When a homogeneous plane monochromatic light wave falls on a prism, a spatial-temporal signal acts on the output face of the prism, i.e., on the input of an optical coherent Fourier processor

$$s(t,\xi,z=0) = \exp(i\nu t)\cdot \dot{\mathrm{T}}(\xi,\nu) , \tag{8}$$

which, according to the ratio (2) is converted by an optical coherent Fourier processor to the form:

$$\mathrm{S}(\omega_x,t) = \exp(i\nu t)\int\limits_{0}^{L} \dot{\mathrm{T}}(\xi,\nu)\exp(-i\omega_x\xi)d\xi , \tag{9}$$

where $S(\omega_x, t)$ - is the spatial-temporal signal in the output plane of an optical coherent Fourier processor.

Substituting expression (1) in the relation (9) gives a spatial-temporal signal, i.e. electric component vibrations of the light field in the output plane of an optical coherent Fourier processor:

$$e(\omega_x, t, z = 2F) = \exp(i\nu t + \phi) \cdot \frac{\sin[n(\nu)tg\alpha - x/F]\nu L/2c_0}{[n(\nu)tg\alpha - x/F]\nu/2c_0}, \tag{10}$$

where $\varphi = (n(\nu)\,\mathrm{tg}\,\alpha - x/\mathrm{F})L\nu/2c_0)$.

Further transformation of the ratio (10) is based on the refractive index expansion of the prism material into a Taylor series in the point vicinity ν_j:

$$n(\nu_j + \Delta\nu) = n(\nu_j) + n'(\nu_j)\Delta\nu + ... \tag{11}$$

Substituting the expansion (11) into the ratio (10) gives an expression of the complex spectrum spread function of the diffraction prism spectral device:

$$H(\omega, \mu) = \exp(i\mu t) \cdot \frac{\sin(\omega - \mu)T_a/2}{(\omega - \mu)}, \tag{12}$$

which is a necessary and sufficient condition for calculating the instantaneous spectrum [13], the definition of which is proposed in [14], where $\omega = \omega(x) = ((x/\mathrm{F}n'(\nu_j) - n(\nu_j)/n(\nu_j)) -$ circular time spectral frequency; $T_a = L(\nu_j + \Delta\nu)n'(\nu')/c_0$; $\mu = \nu_j + \Delta\nu$.

Based on the formula (12), the result of measuring the complex spectrum of the diffraction prism spectral device is given in the form:

$$S_a(\omega, t) = \int_\Omega H(\omega, \mu, t) \cdot S_0(\mu)d\mu, \tag{13}$$

where $\Omega -$ is the analyzed frequencies band.

In the paper [13] it is demonstrated that the complex spectrum spread function (12) is a necessary and sufficient condition for calculating the complex instantaneous spectrum, the definition of which is proposed in the paper [14], i.e., a complex instantaneous spectrum of optical vibration $e(t)$ is formed in the output plane of a diffraction prism spectral device.

In the output plane of the diffraction prism spectral device acts a spatial-temporal optical signal

$$e(t, z = 2\mathrm{F}) = \exp(i\omega t) \cdot S_a(\omega, t), \tag{14}$$

which is subject to photodetection, which results in a characteristic for optical spectral measurements' energy spectrum. The energy spectrum measurement $\overline{G}(\omega)$ includes [13] the operation of the function calculating $|S_a(\omega, t)|^2$ and the operation of its time-averaging over the interval $[-T_R, T_R]$, i.e.

$$\overline{G}(\omega) = \frac{1}{2T_R}\int_{-T_R}^{T_R} S_a(\omega, t)S_a^*(\omega, t)dt. \tag{15}$$

Integration of the expression (15) demonstrated [15] that there is an energy spectrum estimation with the Bartlett spectral window.

As noted previously, to form the output vector, it is necessary to read out the spectrometric information using the CCD, the conditional scheme f which is shown in Fig.5.

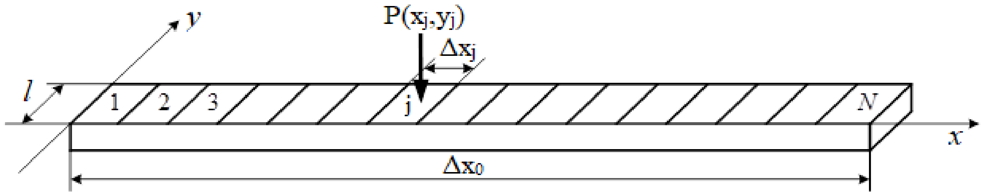

Fig.5. CCD (j-th element)

Since the frequency interval associated with the j-th pixel, $\Delta\omega_j << \Delta\nu$, we assume zero approximations in the series involved in the calculations of functions [13], which are not given here.

Electric current in the $j-$ th pixel

$$i_j = \gamma \frac{q_e p}{\hbar \nu_j}, \tag{16}$$

where $\gamma -$ is the quantum efficiency; $p-$ the optical radiation power incident on the sensitive surface of the $j-$th pixel ; $\hbar -$ Planck's constant.

The power p is given by the ratio:

$$p = \iint_{\Delta S_j} \mathrm{P} ds, \tag{16}$$

where P – the Poynting vector; $\Delta S_j = \Delta x_j l$ – the sensitive surface area of the CCD $j-$th pixel.

The Poynting vector

$$\mathrm{P} = \mathrm{E} \times \mathrm{H} = |\mathrm{E} \times \mathrm{H}| s = \sqrt{\varepsilon / \mu} \cdot |\mathrm{E}|^2 s = \sqrt{\mu / \varepsilon} \cdot |\mathrm{H}|^2 s, \tag{17}$$

where E, H - are the electric and magnetic vectors, respectively, s - is the unit vector; ε, μ - are the permittivity and permeability, respectively.

Comparison of expressions (14), (15), (16), (17) and (18) demonstrates that the values of the energy spectrum $\overline{G}(\omega)$ are proportional to the power p. Therefore, the current from the CCD j-th pixel is given by the ratio:

$$i_j = \beta l \int_{\Delta\omega_j} \overline{G}(\omega) d\omega, \tag{18}$$

where β - is the coefficient of proportionality; $\Delta\omega_j = \Delta x_j / \mathrm{F} n'(\nu_j)$.

The currents i_j allow to form output vectors $\{y'_k\}$ and thus to realize the possibility of multi-alternative automatic control of physical and physico-chemical processes accompanied by optical radiation.

I. CONCLUSION

The possibility of multi-alternative automatic control of physical and physicochemical processes accompanied by optical radiation by forming output vectors based on spectroscopic measurements with a diffraction prism spectral device is demonstrated. These measurements provide spectroscopic information about the various sides of the above-mentioned processes' development, which can be used for multi-alternative automatic control.

Such processes include combustion, which is a complex physical and chemical process, and, in turn, is an information process. The information reflecting the combustion process has as its carrier a dynamic signal in the form of optical radiation. The outstanding role of optical spectroscopy methods within the study of combustion processes is well known, and it encourages the further development of these methods and technical means of optical spectroscopy in studying the combustion processes as well as for the purpose of multi-alternative management of these processes.

The combustion in the furnaces of powerful plants, primarily powerful thermal plants, leads to the environmental tension. It seems that multi-alternative automatic management of this process will improve the environmental situation. It seems that multi-alternative automatic control of this process by various output variables will reduce the environmental burden.

The use of a diffraction prism spectral device as an integral part of a multi-alternative automatic control system required the development of an alternative description of the operation of such a device, seeing that it is necessary to describe the process of output vectors forming and their properties. In the framework of a new approach to the DPSD action description, it is demonstrated that a complex instantaneous spectrum of optical radiation vibrations is formed in the input plane of this device. Further transformations of this spectrum allowed us to establish that the output vectors are being formed on the basis of an estimate of the energy spectrum with a Bartlett spectral window.

ACKNOWLEDGMENT

The work was supported by the Russian Science Foundation (RSF, Grant № 19-79-10110).

REFERENCES

[1] M.A. Vaganov, O.D.Moskaletz. Application of contactless optical spectroscopy in problems of multi-alternative automatic control of physical and physico-chemical processes // Sensors and systems. 2019. №11. C. 5 – 10.

[2] S.L.Podvalniy, E.M.Vasiliev Intelligent systems of multi-alternative management: principles of construction and ways of implementation. // All-Russian meeting on management problems. AMMI 2014. Moscow, 16 – 19 Juli 2014. p.996 – 1007.

[3] Patent 86734 RF, IPC8 G 01 J 3/26. The parallel spectrum analyzer of optical signals range / I. N. Archipov, M. A. Vaganov, S. V. Kulakov, O. D. Moskaletz, L. N. Preslenev, V. N. Prokashev (RF). № 2009116195/22 // Inventions and utility models. 2009. № 25. 2 p.

[4] K. I. Tarasov Spectral devices/ 2nd ed. L.: Mechanical engineering, 1977. 367 p.

[5] V. V. Lebedev The technique of optical spectroscopy / 2nd ed., Moscow University, 1992. 352 p.

[6] U. M. Belyakov, N. K. Paliychev Spectral devices: textbook / Kazan: State Technical University, 2007. 203 p.

[7] Moskaletz .O.D., Serdiuk K.V Complex spectra in a prizm optical spectrum device. // XX International Conference for Young Researches. Wave Electronics and Its Applications in the Information and Telecommunication Systems. Saint – Petersburg, 26 – 30 June 2017. P. 175 – 179.

[8] I.V. Miroshnik Automatic control theory. Linear systems / St.-P.: Piter. 2005. 336 p.

[9] Papoulis A. Systems and transforms with applications in optics. McGraw – HILL BOOK COMPANY New York St. Louis Sun Francisco Toronto London Sydney

[10] Khurgin Yu.I., Yakovlev V.P., Finite functions in physics and engineering. Ed. 2nd, ext. M .: Book House "LIBROKOM", 2010.

[11] B. V. Korotkov Integral operators. Novosibirsk: Nauka. Siberian branch. 1983. 224 p.

[12] Moskaletz .O.D. Classical and quantum approach to power spectrum measurement by diffractional methods, Proceedings of SPIE, 1999, Vol. 3900, P. 297-308.

[13] Kazakov V.I., Kuryleva, A.S., Moskaletz D.O., Moskaletz O.D. Instantaneous spectra in spectral and correlation processing of dynamic signal devices of radio and optical ranges and their linear and nonlinear transformations / // Proc. SPIE 10680, Optical Sensing and Detection V. 2018. P. 1068025

[14] Moskaletz .O.D. Dynamic signals and spectral measurements // Progress in modern radio-electronics. 2013. №2. C. 152-158.

[15] Moskaletz D O., Moskaletz O.D. Complex and Energy Spectra in Optical Diffraction Spectral Devices // Electronic ISBN: 978-1-7281-2288-5 Print on Demand(PoD) ISBN: 978-1-7281-2289-2 INSPEC Accession Number: 19058550

THE MATHEMATICAL MODEL OF THE BIOLOGICAL SYSTEM "PREDATOR-PREY WITH FOOD"

Shchegoleva Aleksandra

Saint-Petersburg State University of Aerospace Instrumentation,
Saint-Petersburg, Russia
E-mail: aleksandrasheg@yandex.ru

Abstract
This article describes the mathematical model of the biological system "predator-prey with food". The model allows to consider the impact of food on the change in the population of predators and preys. Core steps are: description of the model, inclusion of food, solution of the system with food.
Keywords: Lotka-Volterra equations, predator-prey model, non-linear differential equations.

INTRODUCTION

In the surrounding world there are many processes that various models describe. Consider the Lotka-Volterra model, which describes the population change of two competing species. This model can be used to describe changes in the population of two species, isolated from the outside world. However, it is not sufficiently indicative, since it does not consider the change in the amount of food, which depends on the number of victims and predators. Food in the process of coexistence of predators and prey varies in time and is a function.

LOTKA-VOLTERRA MODEL

Created at the beginning of the 20th century, the Lotka-Volterra model [1] describes the change in the population of two species: predators and preys. It has the form of a system of two differential equations described in formula (1), where x_1 и x_2 – are the population of prey and predators, respectively, $\alpha_1, \alpha_2, \beta_1, \beta_2$ – are the coefficients that affect the change in populations [2]:

$$\begin{cases} \dfrac{dx_1}{dt} = \alpha_1 x_1 - \beta_1 x_1 x_2 \\ \dfrac{dx_2}{dt} = -\alpha_2 + \beta_2 x_1 x_2 \end{cases} \tag{1}$$

The solution to this system is shown in the graph (Fig. 1) with $\alpha_1 = \dfrac{2}{3}, \alpha_2 = \dfrac{4}{3}, \beta_1 = 1, \beta_2 = 1$.

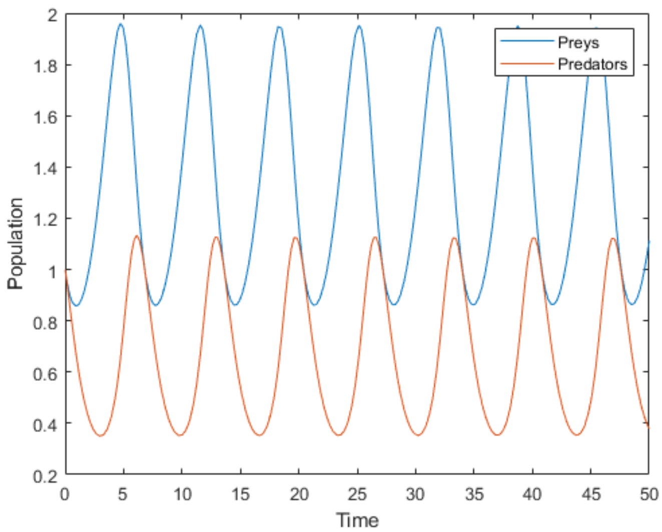

Figure 1.

System (1) cannot be solved analytically; therefore, numerical methods are used to solve it. Let us compare two methods for solving this system: the Runge-Kutta method and the Euler method, see Fig. 2. We obtain the following data on the differences between the solutions calculated by different numerical methods: $M(x_1) = -0.3189$ (expected value of differences in prey solutions), $M(x_2) = 0.2731$ (expected value of differences in solutions for a predator), $\sigma(x_1) = 0.3818$ (standard deviation of differences in prey decisions), $\sigma(x_2) = 0.2709$ (standard deviation of differences in predator decisions). Analyzing this data, we can conclude that both methods have approximately the same solutions, and the averaged difference between them ("error") is not significant. In the future, when solving systems, the Euler method will be used.

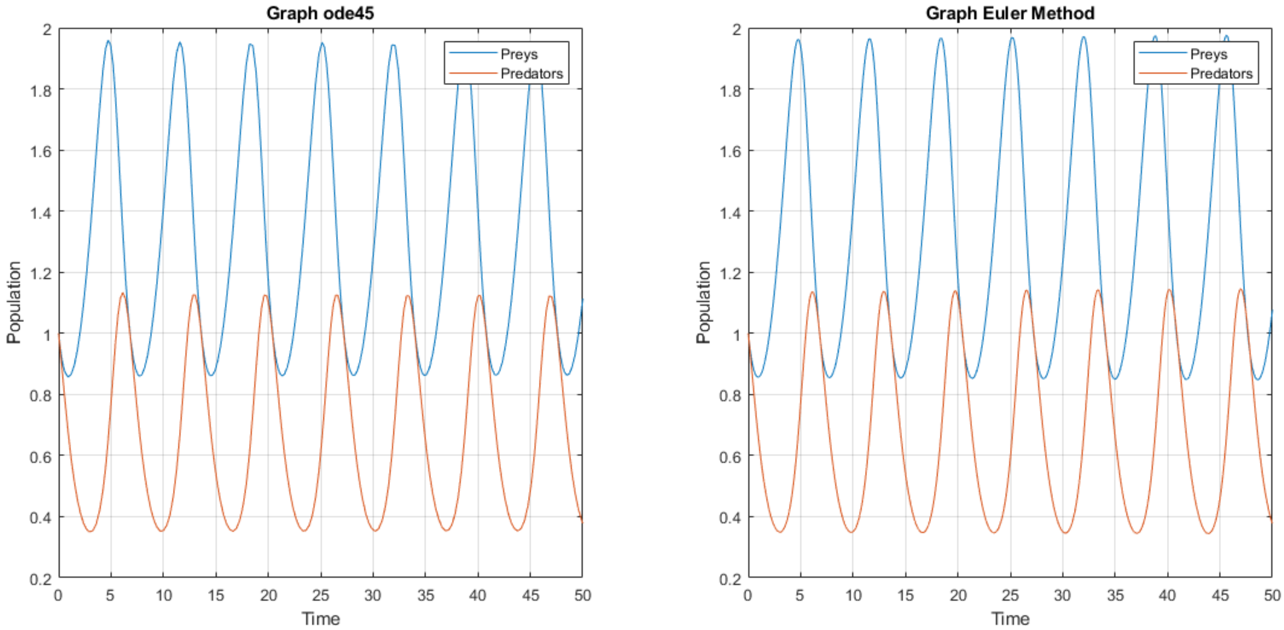

Figure 2.

LOTKA-VOLTERRA MODEL WITH FOOD

To allow the system to account for changes in power, must enter the corresponding function, which changes over time. To do this, add the function $x_3(t)$ that affects the change in the number of preys. Then the system will take the following form:

$$\begin{cases} \dfrac{dx_1}{dt} = f_1(x_1(t), x_2(t), x_3(t)) \\ \dfrac{dx_2}{dt} = f_2(x_1(t), x_2(t), x_3(t)) \\ \dfrac{dx_3}{dt} = f_3(x_1(t), x_2(t), x_3(t)) + U(t) \end{cases} \tag{2}$$

Suppose

$$\begin{aligned} &x_3(t) = \alpha_1(t) \\ &f_1(x_1(t), x_2(t), x_3(t)) = \alpha_1(t)x_1 - \beta_1 x_1 x_2 \\ &f_2(x_1(t), x_2(t), x_3(t)) = -\alpha_2 x_2 + \beta_2 x_1 x_2 \\ &f_3(x_1(t), x_2(t), x_3(t)) = 0 \end{aligned}$$

Then the system will take the following form

$$\begin{cases} \dfrac{dx_1}{dt} = \alpha_1(t)x_1 - \beta_1 x_1 x_2 \\ \dfrac{dx_2}{dt} = -\alpha_2 x_2 + \beta_2 x_1 x_2 \\ \dfrac{d\alpha_1(t)}{dt} = U(t) \end{cases}$$

where $U(t)$ some function depending on the time, which will be the power function. At different time periods, the population of preys will vary depending on the function $U(t)$ and constant coefficient β_1.

CONTROL OF THE FOOD IN THE SYSTEM

Statement of the control problem

To control the change in the value of the function $U(t)$ we introduce the function

$$\psi(t) = x_1 - x_1^* \underset{t\to\infty}{\to} 0$$

Where x_1^* is some variable that is the goal of x_1. In the meantime x_1 is a function in which a global minimum is achieved for the functional

$$\Phi = \int_0^\infty F(t,\psi,\dot\psi)dt = \int_0^\infty ((\psi(t))^2 + \omega^2\dot\psi^2)dt \to \min$$

The basis of the AKAR method is the statement [3] [4]:
The equation $\omega\dot\psi + \phi = 0$ is the Euler-Lagrange equation for the functional.

$$\Phi = \int_0^\infty F(t,\psi,\dot\psi)dt = \int_0^\infty (\phi^2(\psi(t)) + \omega^2\dot\psi^2)dt \to \min$$

Under the following conditions:
1) $\phi(\psi)$ - single-valued, continuous, and differential function for all ψ
2) $\phi(0) = 0$
3) $\phi(\psi)\psi > 0, \forall\psi \neq 0$

In order for the relation $\psi(x(t)) = 0$ to be an invariant manifold of the system, it is necessary and sufficient that the following statement is fulfilled (it follows from the results of theoretical mechanics):

$$\frac{d\psi}{dt} = \sum_{i=1}^{n} \frac{\partial\psi(x_1,....,x_n)}{\partial x_i} R_i(x_1,....,x_n) = \phi(\psi, x_1,....,x_n)$$

where $R_i(x_1,....,x_n)$- the right parts of the i-th equations for an n-dimensional system description $\phi(\psi, x_1,....,x_n) = 0$

Further, we can verify that the Euler-Lagrange equation $F(t,\psi,\dot\psi)dt$ is a solution to the equation $\omega\dot\psi + \phi = 0$ and vice versa.

$$\frac{F(t,\psi,\dot\psi)}{dt} = \frac{\partial F}{\partial\psi} - \frac{d}{dt}\frac{\partial F}{\partial\dot\psi} = 2\phi\frac{\partial\psi}{\partial t} - 2\omega\ddot\psi = 0$$

Definition of the structure of AKAR control

We introduce the intermediate macro variable:

$$\psi^{(I)}(t) = \alpha_1(t) - \varphi(x_1(t), x_2(t)) \tag{3}$$

The point of creating an intermediate variable is that need to control x_1 when the control variable is in the 3rd equation. This technique allows to transfer control from the 3rd variable $\alpha_1(t)$ to the auxiliary variable $\varphi(t) = \varphi(x_1(t), x_2(t))$.

At this stage, the task is as follows (we omit t in subsequent calculations)

$$\Phi_1 = \int_0^\infty F(\psi^{(1)}, \dot\psi^{(1)})dt = \int_0^\infty ((\psi^{(1)})^2 + T_1^2(\dot\psi^{(1)})^2)dt \to \min, T_1 > 0$$

Knowing from section "Statement of the control problem" that $\omega\dot\psi + \phi = 0$ is a solution for the Euler-Lagrange equation, we solve the problem (in the simplest case $\phi = \psi$)

$T_1 \dfrac{d\psi^{(1)}}{dt} + \psi^{(1)} = 0$ (4)

Where from (3) $\psi^{(1)}(t) = \alpha_1(t) - \varphi(x_1(t), x_2(t)) = x_3(t) - \varphi(x_1(t), x_2(t))$

Considering (3) and (4), we obtain $T_1(\dfrac{dx_3}{dt} - \dfrac{d\varphi}{dt}) + \psi^{(1)} = 0$

Knowing from section "Lotka-Volterra model with food" that $\dfrac{dx_3}{dt} = f_3(x_1(t), x_2(t), x_3(t)) + U(t)$

We obtain $T_1(f_3 + U - \dfrac{d\varphi}{dt}) + \psi^{(1)} = 0$

Then $U(t) = -\dfrac{\psi^{(1)}}{T_1} - f_3 + \dfrac{d\varphi}{dt}$

The problem statement was of the form $\Phi_1 \to \min, \psi^{(1)} \to 0$, then

$$0 = x_3(t) - \varphi(x_1(t), x_2(t)) \Rightarrow x_3(t) = \varphi(x_1(t), x_2(t)) \tag{5}$$

Next task: find $\varphi(x_1, x_2)$ and $\dfrac{d\varphi}{dt}$

$$T_2 \frac{d\psi}{dt} + \psi = 0$$

$$\frac{d\psi}{dt} = \frac{d(x_1(t) - x_1^*)}{dt} = \frac{dx_1}{dt}, \psi \neq x_1$$

$$T_2 \frac{dx_1}{dt} + \psi = 0$$

$$T_2 f_1 + \psi = 0$$

Considering the results (5) and (1)

$$f_1 = \alpha_1 x_1 - \beta_1 x_1 x_2 = x_3 x_1 - \beta_1 x_1 x_2 = \varphi(x_1, x_2)x_1 - \beta_1 x_1 x_2$$

$$T_2(\varphi(x_1, x_2)x_1 - \beta_1 x_1 x_2) + \psi = 0$$

$$\varphi(x_1, x_2) = \beta_1 x_2 - \frac{1}{T_2} + \frac{x_1^*}{T_2 x_1} \tag{6}$$

We find $\dfrac{d\varphi}{dt}$

$$\frac{d\varphi(x_1, x_2)}{dt} = \frac{\partial\varphi}{\partial x_1}\frac{dx_1}{dt} + \frac{\partial\varphi}{\partial x_2}\frac{dx_2}{dt}$$

$$\frac{\partial\varphi}{\partial x_1} = 0 - 0 + \left(-\frac{x_1^*}{T_2 x_1^2}\right)$$

$$\frac{\partial\varphi}{\partial x_2} = \beta_1$$

$$\frac{d\varphi(x_1, x_2)}{dt} = -\frac{x_1^*}{T_2 x_1^2} f_1 + \beta_1 f_2 \tag{7}$$

Then the system with the power on will take the following form

$$\begin{cases} \dfrac{dx_1}{dt} = f_1 = \alpha_1(t)x_1 - \beta_1 x_1 x_2 \\ \dfrac{dx_2}{dt} = f_2 = -\alpha_2 x_2 + \beta_2 x_1 x_2 \\ \dfrac{d\alpha_1}{dt} = f_3 + U(t) \\ f_3 = 0 \\ U(t) = -\dfrac{\psi^{(1)}}{T_1} - f_3 + \dfrac{d\varphi}{dt} \\ \psi^{(1)}(t) = \alpha_1(t) - \varphi(x_1(t), x_2(t)) \\ \varphi(x_1, x_2) = \beta_1 x_2 - \dfrac{1}{T_2} + \dfrac{x_1^*}{T_2 x_1} \\ \dfrac{d\varphi(x_1, x_2)}{dt} = -\dfrac{x_1^*}{T_2 x_1^2} f_1 + \beta_1 f_2 \end{cases}$$

SOLUTION OF THE LOTKA-VOLTERRA MODEL WITH FOOD

To solve the system, we apply the Euler method (in section “Lotka-Volterra model”, the possible deviations of this method from the more accurate Runge-Kutta method are described). To solve the system, we introduce some restrictions under which the system will be stable: $x_1^* = 10$ (target variable for preys), $\varepsilon_1 = 25$ (criterion for stability of the system), $\varepsilon_2 = 0.2 * x_1^*$ (criterion for achieving the goal). The lifetime of the system $t = 0 \ldots 50$, the initial data: $U(0) = 0, x_1(0) = 1, x_2(0) = 1, \alpha_1(0) = 1$

The next task was to determine the coefficients $\alpha_2, \beta_1, \beta_2, T_1, T_2$ and step h to solve the equations. During calculations and tests, it was found out that the value of step $h = 0.3$ is optimal. At higher pitch values, the system becomes less stable. Subsequent charts will be drawn with this step.

It was further determined that the system is stable at $T_1 < 1, T_2 > 50$ (subject to sustainability criteria). The following graphs prove this:

When checking all the values, it was found that the most stable system is at $T_1 = 0.3$. At higher values, as can be seen from figure 3.b, the system shows exponential growth, which is unacceptable for bio-communities.

In section “Statement of the control problem”, we introduced the target variable x_1^* (when calculating $x_1^* = 10$), the prey population should strive for this number. But now, no coefficient values were found at which this goal is achieved. The graph in figure 4 shows the time variation of the difference between the target variable and the prey population. One can see a vibrational change in this value with a constant decrease in the interval from 0 to 30. However, at $t > 30$ the difference goes up again, reaching the initial difference and again rapidly decreasing at $t \geq 45$, reaches almost zero value (i.e. the goal is almost reached). An explanation of this system behavior has not yet been found.

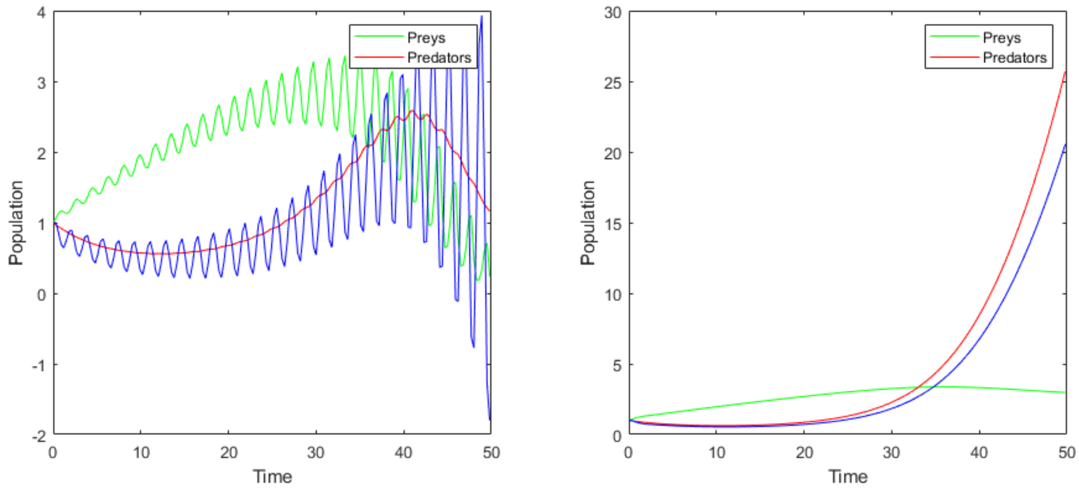

Figure 3. a) $\alpha_2 = 0.2, \beta_1 = 0.8, \beta_2 = 0.1, T_1 = 0.3, T_2 = 100$ *,б)* $\alpha_2 = 0.2, \beta_1 = 0.8, \beta_2 = 0.1, T_1 = 1.0, T_2 = 100$

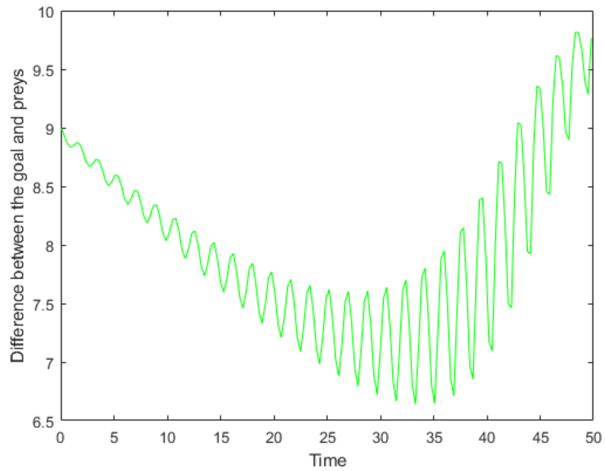

Figure 4. $\alpha_2 = 0.2, \beta_1 = 0.8, \beta_2 = 0.1, T_1 = 0.3, T_2 = 80$

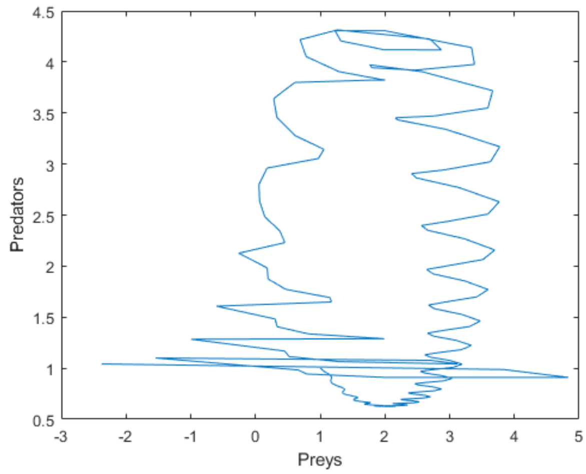

Figure 5. Phase portrait of the solution of the system of equations "predator-prey with food"

The graph of figure 5 shows the dependence of the predator population on prey. As you can see between them there is no direct relationship or any specific law. However, there is some vibrational dependence.

CONCLUSION

The formulation of the control problem for the predator-prey model with food is formulated in the work. The calculations are carried out and a new system of differential equations is obtained. However, significant difficulties arose in solving the system (they are described in section "Solution of the Lotka-Volterra model with food"). During the study, a lot of new data was obtained on the behavior of the system at various values of the coefficients; these data must be correctly interpreted, and a mathematical explanation is given. Work on this topic will be continued.

REFERENCES

[1] A. J. Lotka, "Contribution to the Theory of Periodic Reaction", The Journal of Physical Chemistry A, vol. 14, No. 3, pp. 271-274, 1910

[2] Y. Takeuchi, Global Dynamical Properties of Lotka-Volterra Systems. Singapore, World Scientific Pub Co Inc, 1996. ISBN 978-9810224714

[3] A. A. Kolesnikov, Al. A. Kolesnikov, A. A. Kuz'menko, "The ADAR Method and Theory of Optimal Control in the Problems of Synthesis of Nonlinear Control Systems", Mekhatronika, Avtomatizatsiya, Upravlenie, vol. 17, No. 10, pp. 657-669, 2016 (in Russian)

[4] С.И. Колесникова, "Синтез управления нелинейным объектом второго порядка с неполным описанием", Автоматика и телемеханика, № 9, стр. 18-30, 2018 (in Russian)

УДК 62-527.7

DEVELOPMENT OF AN AUTOMATED SYSTEM OF LAYERED SYNTHESIS WITH APPLICATION OF ROBOTICS.

Shchukina Daria

student of the Department of Innovation and Integrated Quality Systems
Federal State Autonomous Educational Institution of Higher Education
St. Petersburg State University of Aerospace Instrumentation
+7-921-857-29-57
E-mail: shchukinad@icloud.com

Abstract
A new automated layer-by-layer synthesis system was developed using continuous monitoring of the printing process and the ability to correct inconsistencies in the printing process, or with the ability to restart the printing process with the exception of the human factor.
Keywords: Layer-by-layer synthesis, additive technologies, mechanical arm, robotic arm, 3D printing, video monitoring.

Relevance

Currently, the use of layered synthesis in production is undergoing serious development. However, the control of these processes is not fully implemented, in connection with this there is an increase in the number of discrepancies, deterioration in the quality of products and the costs of additive manufacturing. In this regard, the development of a system for continuous monitoring of the printing process to fix inconsistencies is required.

In additive technologies, such inconsistencies are often present:

- At the beginning of the printing process there is no 3D plastic feed;
- 3D-model does not stick to the platform, there is not enough adhesion;
- Not enough plastic for 3D printing;
- Plastic is extruded too much;
- Holes and crevices are visible in the upper layer of the model;
- The presence of hairs, cobwebs and other foreign materials;
- Overheating is observed during 3D printing;
- Displacement of layers or lack of their alignment;
- Separation and splitting of layers;
- Sewing plastic and stopping the feed;
- clogged extruder;
- Termination of extrusion by a 3D printer;
- Poor filling quality, friability;
- Stains on the surface of the 3D product.

These discrepancies entail large financial and time costs.

To solve this problem, it would be most appropriate to establish continuous monitoring of this process and to eliminate the human factor as much as possible using robotics. To do this, it is possible to apply a system consisting of (Fig. 1).

Camera Specifications:

- the ability to outline the image (increase the clarity of the image in low light conditions);
- the ability to produce high-quality images with minimal illumination, at least 0.05 lux for poorly lit areas;
- synchronization from the AC power supply with phase adjustment;
- automatic adjustment of the video signal gain is not worse than 18 decibels (hereinafter – dB);
- control of scaling (not less than 25 times);
- automatic imputation of sensitivity using the electronic aperture of the camera;
- dynamic range of at least 48dB.

Technical requirements for the robot manipulator (mechanical arm):

- Management through the Arduino programming environment, via Bluetooth;

- Functional capabilities- capture and movement of various small items;
- Development Environment Arduino IDE;
- Power adapter 5 V, 2 A – Dimensions 35 cm × 10 cm × 8.8 cm;
- Weight 500 gr.

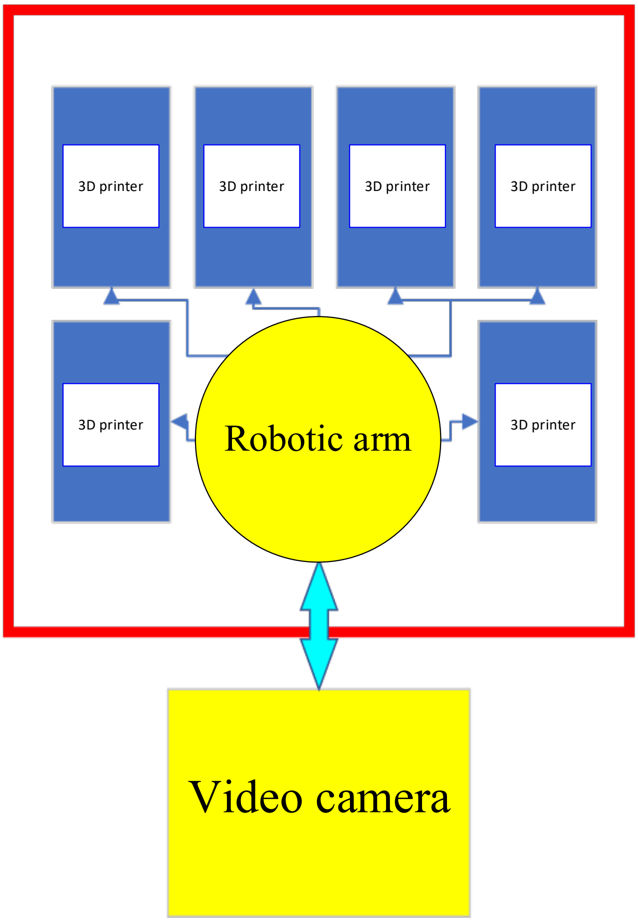

Figure 1 – the principle of the system

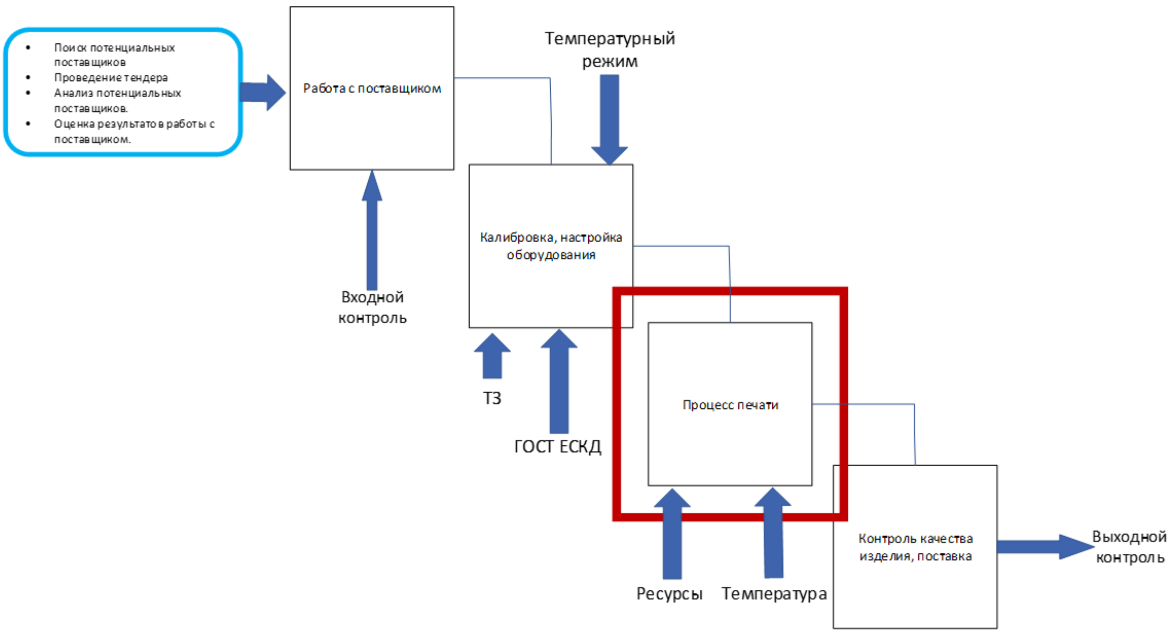

Figure 2 – decomposition of the process

The purpose of the creation of this project is to ensure control of 3d printing in production using video recording of the process and control in an automatic way, i.e. during the printing process, each stage is monitored, if a deviation from the norm established in advance is possible, a signal is sent to the robotic arm, which stops the process and corrects or restarts it.

This system is applicable to any 3D printers and there is a possibility of application at the production level.

The quality level of the system is determined by the formula:

$$У_к = \frac{N_{без.д.}}{N_{общ.}},$$

where $У_к$ – product quality factor; $N_{без.д.}$ – the number of products made without inconsistencies; $N_{общ.}$ is the total number of products.

This system provides a new approach to using the camera to monitor the 3D printing process and eliminate defects in the printing process. The use of robotics (namely, a robotic arm of a mechanical arm) to readjust equipment and restart the printing process eliminates the human factor, which is also a positive quality.

Conclusion

This system allows constant monitoring of the printing process, eliminates the human factor and minimizes the financial and time costs of ensuring the operation of a 3D printer.

References

1. ГОСТ Р ИСО 12100-1-2007 Безопасность машин. Основные понятия, общие принципы конструирования. Часть 1. Основные термины, методология
2. ГОСТ 12.0.003-74 Система стандартов безопасности труда. Опасные и вредные производственные факторы. Классификация
3. ГОСТ 12.0.230-2007 Система стандартов безопасности труда. Системы управления охраной труда. Общие требования
4. Чабаненко А.В., Семенова Е.Г, Назаревич С.А., Диагностические методики для повышения качества технической системы. Избранные научные 8 труды Шестнадцатая Международная научно-практическая конференция «Управление качеством» М.,2018 Вып. 1 (444) С. 280-288
5. Чабаненко, А.В. Стандартизация наукоемкой продукции / А.В. Чабаненко // // РИА: Журнал.: «Стандарты и качество». 2015.. №1. С. 169-176.
6. Чабаненко, А.В. Технология аддитивного производства, моделирование и управление качеством процесса послойного синтеза (учебное пособие) / А.В. Чабаненко, С.А. Назаревич, А.Ю. Гулевитский, Я.А. Щенников // СПб.: Изд-во: ГУАП, 2018. С. 206.

MODELLING AND OPTIMIZATION OF DIFFRACTION GRATING TOPOLOGY FOR OPERATING IN HIGH ORDERS

Vasilyeva Olga

Undergraduate student
Saint Petersburg State University of Aerospace Instrumentation
(SUAI),
Saint Petersburg, Russia
olgaevgenevna15@gmail.com

Annotation
The paper considers the issue of increasing the intensity of diffracted light to higher orders upon diffraction by an amplitude transmission grating. The issue of optimizing the topology of a high-order diffraction grating by computer simulation methods is considered. The optimum value of the parameters of the strokes was found for the successful use of the +4 diffraction order for the analysis of the spectra of optical radiation.
Keywords: diffraction grating, optimization, spectral range, optics, transmittance function, modeling

INTRODUCTION

The diffraction grating is one of the most important optical elements in the research problems of the spectral composition of the optical radiation. Spectral devices based on diffraction gratings are used in various fields of science and technology [1-3]. Nomenclature of diffraction gratings is a wide range of different types of gratings: amplitude, phase, reflective, holographic, etc. [4]. The simplest in the making is an amplitude diffraction grating, which represents inflicted on the optical transparent and nontransparent strokes-stripes. Usually, this grating is made on the divider machine, where the non-transparent strokes are formed by "cutting" strips by diamond cutter with an equal interval. In this way, a topology of the diffraction grating is formed, which is transparent and opaque strokes of the same width.

A distinctive feature of diffraction gratings is the formation of a multiordinal diffraction pattern, which can be both a virtue and a disadvantage. On the one side, multiorder diffraction allows the formation of several spectral channels and, thus, it is possible to divide the optical beam for several channels. On the other side, multiorder diffraction means that the energy of diffracted light into a separate beam will be small, which is undesirable in spectral analysis, since it will lead to a deterioration of the signal/noise ratio in the device.

It should also be noted that in the usual amplitude grating, the intensity of diffracted light decreases with an increase in the number of the diffraction order. At the same time, in higher orders, one should expect a multiple improvement in the resolution of the instrument with such a grating [5]. Therefore, the urgent include the task of increasing the intensity of diffracted light into higher orders is relevant in order to improve the resolution of the device as a whole. This is possible by changing the topology of the diffraction grating and thus by redistributing the intensity of diffracted light between orders.

For example, in this paper [6] was used the harmonic modulation of the location of the strokes of the diffraction grating. This allows you to completely suppress the +2 diffraction order and increase the intensity of +1 order. This results in an increase in the spectral range, since the adjacent orders do not overlap. However, this topology change does not improve the spectral resolution of the instrument.

This work is devoted to optimization of the topology of the diffraction grating in order to improve the spectral resolution by working in higher orders.

MATHEMATICAL MODEL OF DIFFRACTION PATTERN FORMATION

In the paper [7] is proposed the radio-optical model of the formation of the diffraction pattern from the grating. According to this model, the spectral device with the diffraction grating is represented as the following optical scheme, as shown in Fig. 1.

According to the proposed model, radiation is modulated by space according to the function of the transmission of the diffraction grating $T(\xi)$, which for convenience of consideration can be represented in the form of decomposition into a complex Fourier series

$$T(\xi) = \sum_{-\infty}^{\infty} C_n \exp(in\frac{2\pi}{T_g}\xi), \tag{1}$$

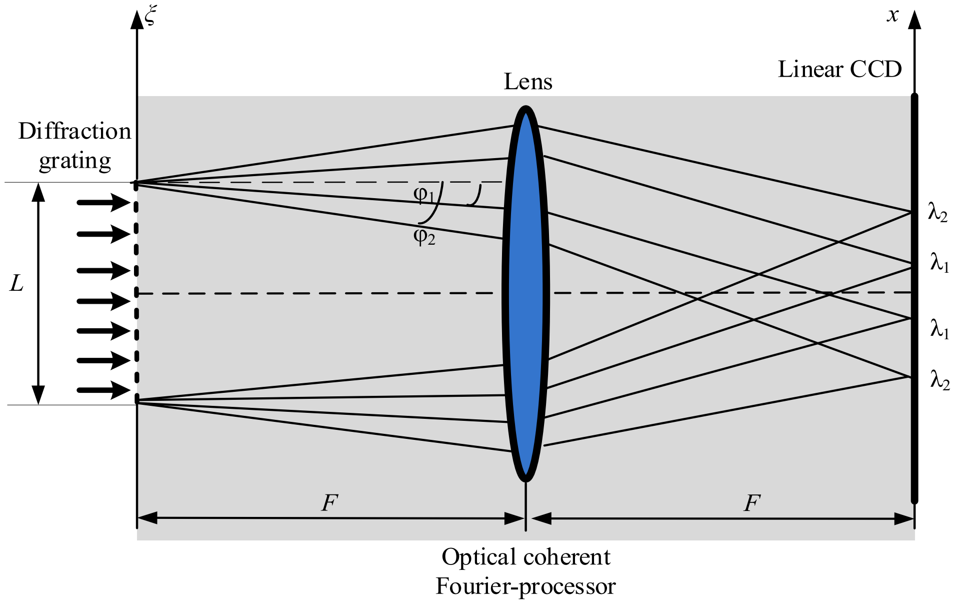

Fig. 1. Optical scheme of a spectral device with a diffraction grating

where the coefficients of decomposition C_n determine the intensity of diffracted light in the n-th order, T_g – the period of the diffraction grating.

The coefficients C_n are calculated using a known formula:

$$C_n = \frac{1}{2T_g} \int_{-\frac{T_g}{2}}^{\frac{T_g}{2}} T(\xi) e^{-in\frac{2\pi}{T_g}\xi} d\xi. \tag{2}$$

For a conventional diffraction grating with an equal width of transparent and non-transparent strokes, the distribution of the C_n coefficients is as follows (Fig. 2).

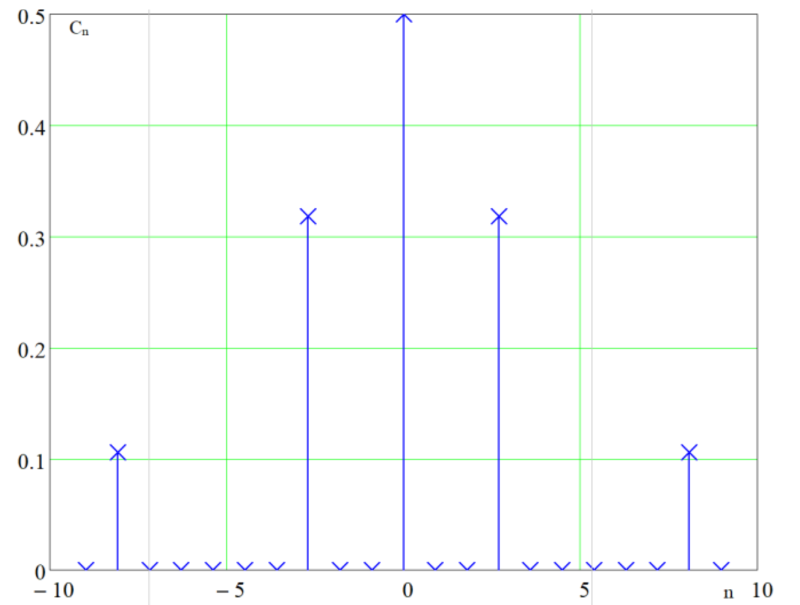

Fig. 2. The distribution of C_n coefficients for a regular grating

In the paper [8] the so-called "high-order" diffraction grating with a modified topology of the location of strokes is proposed. The topology change is that each third opaque array stroke is 2 times wider than the others. This makes it possible to obtain a diffraction of light in 3 and 4 orders much more than in 1 and 2.

The transmission function of such a diffraction grating can be recorded as:

$$T(\xi)=\begin{vmatrix}1,\xi\in[0,a]\\0,\xi\in[a,a+b]\\1,\xi\in[a+b,b+2a]\\0,\xi\in[b+2a,2(b+a)]\\1,\xi\in[2(b+a),2b+3a]\\0,\xi\in[2b+3a,2b+3a+c]\end{vmatrix}, \tag{3}$$

where a – width of transparent grating element, b и c – width of opaque strokes, while $a=b\leq c$.

On Fig. 3 shows the result of observing the diffraction pattern from such a lattice when it is illuminated by radiation from a helium-neon laser (632 nm) for strokes parameters: $a=b$, $c=2a$.

Fig. 3. Diffraction on a high-order grating

From Figure 3 it is clear that despite the increase in the intensity of diffracted light in higher orders (third and fourth), this topology requires further optimization, since higher orders interfere with each other to effectively analyze the spectrum in each of them.

OPTIMIZATION TOPOLOGY OF THE GRATING

In terms of optimization of the topology of the diffraction grating, it is necessary to define those parameters that will allow to obtain a solution for the topology of the grating, which allows to suppress diffraction in neighboring orders and leave only one, necessary, high order.

In other words, it is necessary to choose the parameters of the grating in such a way as to maximize the values of the C_n decomposition coefficient for a certain order (for example, at $n = 4$) and at the same time the C_n values for neighboring orders (n=3 и 5) should be minimal or zero. In our case, the size of the decomposition coefficients depends on the only parameter that should be changed – the width of the opaque element c.

Thus, the optimization task is reduced to finding the maximum value $C_n(c)$:

$$P=\begin{vmatrix}\max C_n(c,n)\text{ for}\\ \min C_n(c,n-1)\\ \min C_n(c,n+1)\end{vmatrix}. \tag{4}$$

The MathCad system was modeled and the following results were obtained, allowing to select the optimal parameter c for the high-order grating.

On Fig. 4 shows the result of calculating the decomposition coefficients for n=–6…6 for the stroke parameter c=2,3,4.

It should be noted that this form of presentation of results is not quite convenient for selecting the optimal parameters of the stroke c. On Fig. 5 shows the result of calculating the decomposition coefficients depending on the width of the stroke c.

This form of representation of modeling results allows to see that the value of coefficient C_4 is maximal in range c=2..4. at that the neighboring coefficients are small. The results of the accurate trace of the graph show that at c=3,2 the ideal balance between C_4 value and neighboring coefficients is observed. Thus, the value c=3,2 can be considered the optimal solution. Fig. 6 shows the results of the calculation of the decomposition coefficients for the optimal parameters of the diffraction lattice topology.

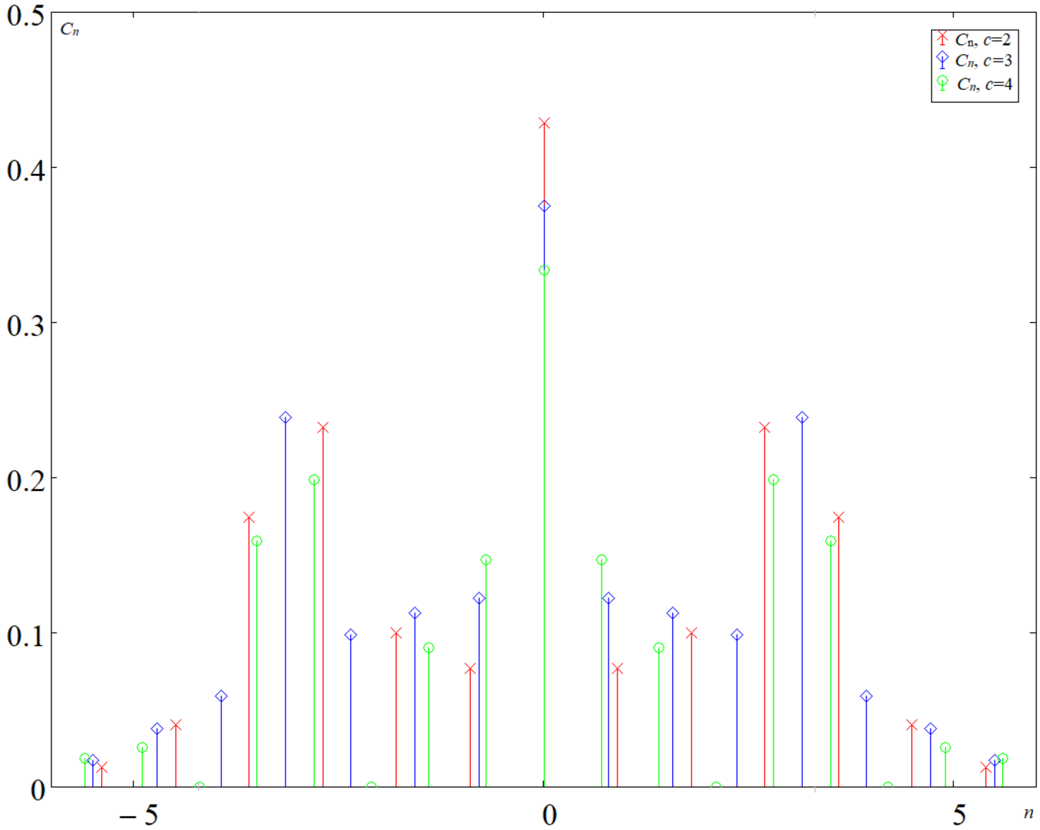

Fig. 4. Calculation of decomposition coefficients C_n

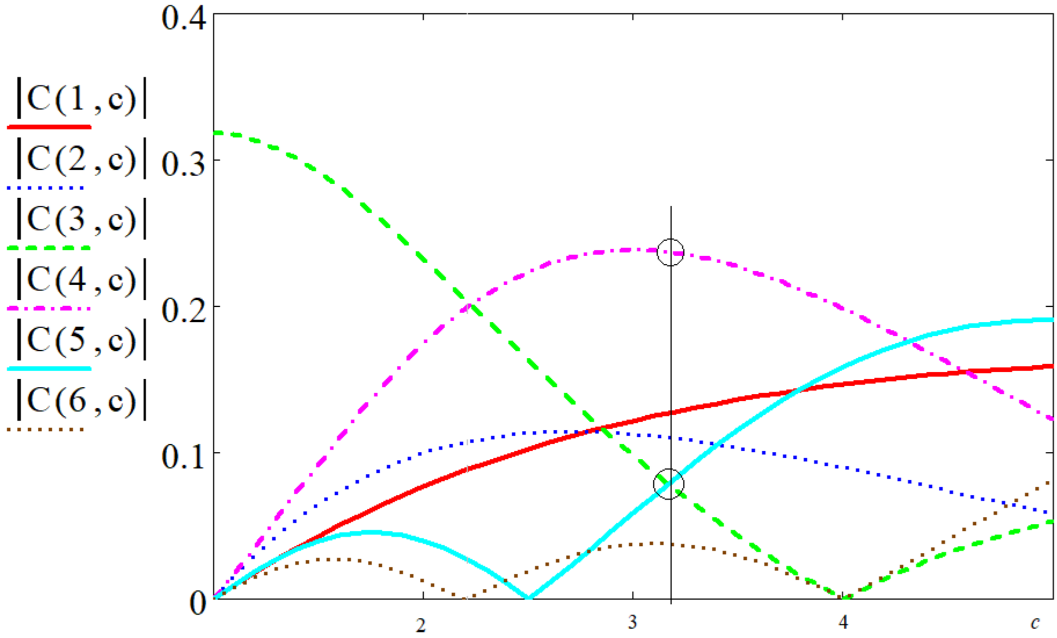

Fig. 5. Calculation of the coefficients of the decomposition of C_n depending on the width of the opaque element c (in relative units)

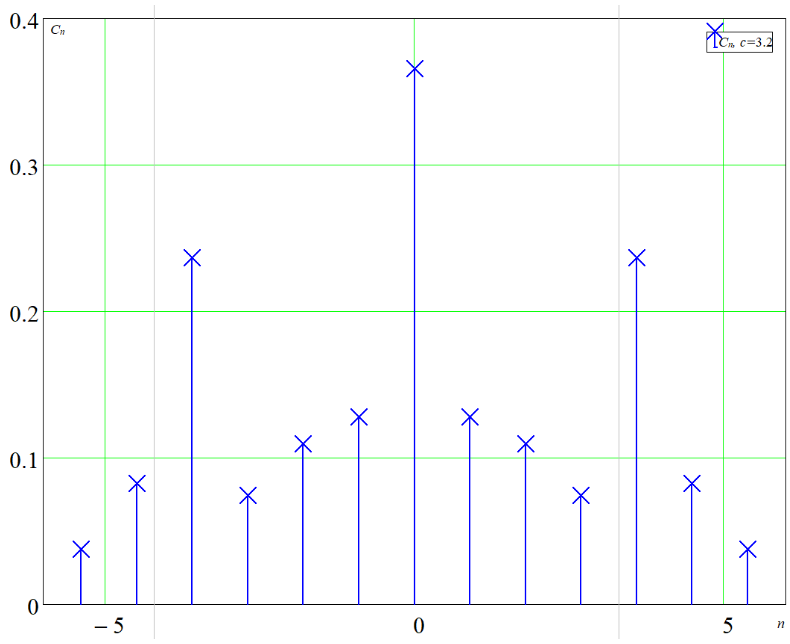

Fig. 6. The simulation result with the found optimal parameter c = 3,2 i.e.

CONCLUSION

The issue of the possibility of increasing the intensity of diffracted light to higher orders upon diffraction by an amplitude transmission grating is considered. It is shown that by changing the topology of the diffraction grating, redistribution of light between diffraction orders is possible.

A model is proposed for optimizing the topology of a high-order diffraction grating, and strokes parameters are found that can successfully use the +4 diffraction order for analyzing the spectrum of optical radiation.

ACKNOWLEDGMENT

This work was supported by Russian foundation for basic research (RFBR): projects №18-07-00636 and 20-07-00648.

REFERENCES

[1] Kazakov, V.I. Contactless optical spectroscopy methods in the tasks of monitoring physical and technological processes in extreme conditions/ V.I. Kazakov, O.D. Moskaletz, A.S. Paraskun, M.A. Vaganov// Proc. of SPIE Optical Measurement Systems for Industrial Inspection XI, Vol. 11056. – Bellingham, WA, 2019. P. 110563W.

[2] Глинкин, В. А. Автоматизированная система оптического контроля процесса электронно-лучевой зонной плавки при получении монокристаллов тугоплавких металлов / В. А. Глинкин, А. И. Любимов, С. А. Парамонов // Вестник Казанского технологического университета, 2015. №18 (5). С.137-140.

[3] Введенский, Л. Е. Методы спектрального анализа металлов / Л. Е. Введенский, С. Л. Мандельштам, С. М. Райский. Л.: ГИТТЛ, 1940. 88 с.

[4] Palmer, C. A. Diffraction grating handbook / C. A. Palmer, E. G. Loewen. N. Y.: Newport Corporation, 2005. 271 p.

[5] Казаков, В. И. Измерение оптических спектров решеточным спектральным прибором в высших дифракционных порядках / В. И. Казаков, О. Д. Москалец // Датчики и системы. 2018. №12. С. 22-27.

[6] Gao, N. High-order diffraction suppression using modulated groove position gratings / N. Gao, C. Xie // Optics Letters. 2011. Vol. 36. No. 21. P. 4251-4253.

[7] Казаков, В. И. Комплексные спектры в дифракционном решеточном спектральном приборе / В. И. Казаков, О. Д. Москалец // Радиопромышленность. 2016. №4. С. 32-37

[8] Kazakov, V. I. Grating spectral device with possibility of working in high diffraction orders / V. I. Kazakov, A. S. Paraskun // 2018 Wave Electronics and its Application in Information and Telecommunication Systems, IEEE Conference Publication Program, Conference Record №45890. 2018. P. 860441

TRAINING COMPLEX FOR MODELING NONLINEAR AUTOMATIC CONTROL SYSTEMS

Vataeva Elizaveta

Saint – Petersburg University of Aerospace Instrumentation,
Saint – Petersburg, Russia
evataevv@inbox.ru

Annotation
The paper discusses one of the possible approaches to the construction of a modern laboratory facility designed for laboratory and educational research is considered. Some characteristics of the developed training stand are given. The NI ELVIS-II(-III) platform is used as the hardware and also application package Matlab / Simulink.

Historical traditions of engineering education suggest that the learning process includes not only theoretical courses and the performance of various calculation tasks, but also a direct study of the elements, components and systems with which the future engineer will encounter in his professional life. As a rule, the experimental and practical part of training is carried out within the framework of laboratory courses of disciplines with the use of specialized stands of industrial production or developed in the educational institution itself.

The considerable quantity of the laboratory equipment operated now in engineering higher educational institutions is based still on the element base and the methodical maintenance, created and developed in 80th years of the last century, and often has essentially limited functionality connected with deterioration of the equipment. Complete replacement of such equipment is often impossible because of absence of necessary accessories if laboratory complexes are made by universities independently, or discrepancies of training sets produced by the industry to requirements. In particular, such a situation is observed in respect of laboratory equipment intended to provide disciplines related to the theory of control. The equipment produced by numerous enterprises is either oriented to the study of control theory basics or represents highly specialized engineering simulators designed to study specific industrial equipment. In addition, the equipment produced has a significant value and has some redundancy associated, in particular, with the measuring equipment. To drawbacks as it is possible to carry certain closedness of the laboratory stands which does not allow to leave beyond the limits of lists of laboratory works offered by manufacturers.

The modern level of development and availability of computer modeling programs allows to compensate to some extent the absence of physical models, but mathematical modeling does not allow to receive in full both representation and skills of work with objects of the real world.

In this regard, it seems promising to create simple modular laboratory units that not only allow trainees to get acquainted with real elements of control systems, but also allow them to conduct training and research work that expands the range of acquired competencies.

A convenient platform for creating a modern laboratory workshop can be the laboratory station ELVIS-III, produced by National Instruments [1] especially for educational institutions of different levels. This choice is supported by the composition of the station's equipment – it includes all the most frequently used measuring instruments, signal sources and power supply modules for low-power electronic circuits, excluding their repeated duplication. Since the station is controlled by a PC, it is possible to easily collect and process experiment results.

One of the least covered areas of control theory in laboratory equipment is adaptive systems, and in particular extreme seeking systems (ESS). This class includes systems that have the property of automatic maintenance of the regulatory action value, providing an extreme value of either coordinates or some process efficiency indicator (minimum material consumption, maximum efficiency factor, etc.) with uncontrolled and previously unknown changes in both the properties of the object itself and its operating conditions.

Extreme systems deserve special attention because they are often linked to life safety or resource efficiency issues. Let us consider a few examples related to energy and transport equipment.

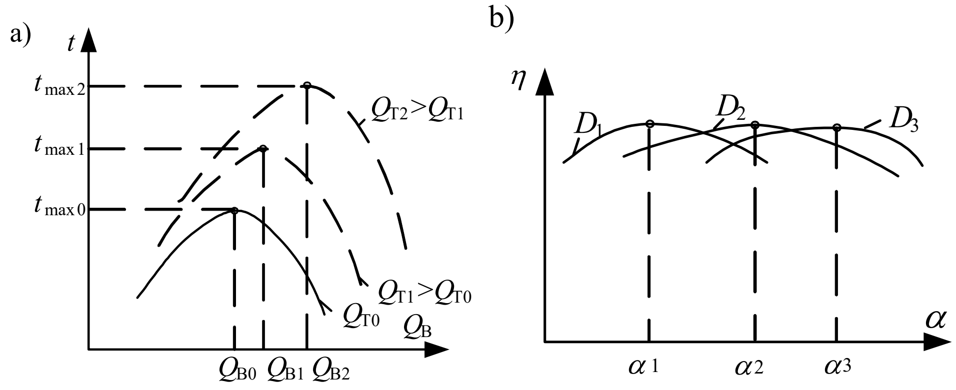

Figure 1 – Characteristics of energy devices
a) static characteristics of the furnace device; b) static characteristics of the steam boiler

Typical examples of power equipment include furnace units and steam boilers. The static characteristic of the furnace unit [2] in the channel "air flow – flue gas temperature" has a pronounced extreme character: the maximum temperature of flue gas $t°_{max}$ is obtained for a given amount of fuel Q_T at a fairly certain amount of air supplied to the furnace Q_B (Fig. 1, a). The same kind of characteristic is characteristic of a steam boiler. Here, the dependence between the efficiency of the boiler and the coefficient of excess air α, supplied to the furnace of the boiler for combustion of fuel, is of extreme character. Moreover, when the steam load *D* of the boiler changes, the value of the excess air coefficient, corresponding to the maximum value of efficiency for the given steam load, changes (Fig. 1, b).

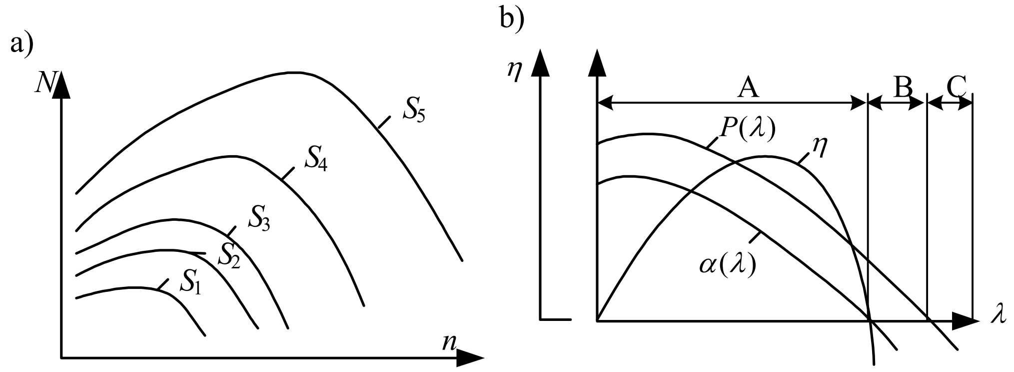

Figure 2 – Characteristics of the elements of the propeller group
a) the throttle characteristics of the internal combustion engine
b) the dependence of the efficiency factor of the propeller on the relative pitch

Air propellers are still actively used in aviation as a propeller driven by an internal combustion engine. Both main components of the propeller group have characteristics that have extreme dependencies. For an engine such a dependence is present in the throttle characteristic [3] and determines the maximum power given at the most favorable number of revolutions (Fig. 2, a). As can be seen from the figure, the characteristic strongly depends on the degree of the throttle opening *S*. For the propeller is an extreme nature of the dependence of efficiency on the relative arrival of the propeller λ (Fig. 2, b) [4]. Although the figure does not show it clearly, the position of the maximum efficiency depends on engine speed and air speed. Matching engine speed and propeller pitch at different stages of the flight is a fairly difficult task.

While developing the stand for studying the device and extremum seeking control (ESC) operation, special attention was paid to a wider coverage of variants of the control object characteristics and the possibility of extending the functionality of the workshop by using software extensions.

The hardware layout of the extreme control system is based on the classical ESC with memory of the extremum [3]. This type of ESC is chosen because, on the one hand, it is one of the easiest to understand and investigate and leaves quite a lot of space for extended experiments. In addition, the basic part of the layout – the object with the extremum itself – can be used in modeling and research of other types of ESC.

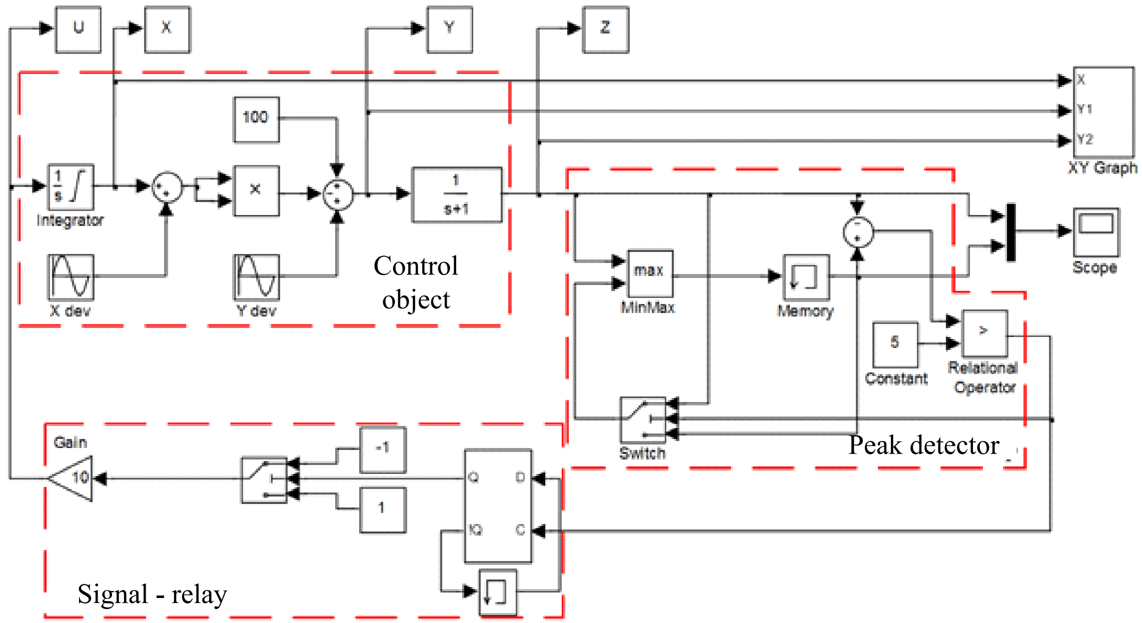

Figure 3 – Simulink model of extreme seeking control

The mathematical model of the system prototype, implemented in the MATLAB/Simulink package, is shown in the Fig. 3. The model includes three main components: a control object with an extreme characteristic, an extremum memory device (peak detector) with a comparison element, and a control signal shaper (signal-relay).

A device for storing an extremum is based on a maximum determinant with a memory element (ME). The difference between the signals from the peak detector input and ME output is fed to a comparator, where it is compared with a given trigger threshold defining the control error. The signal from the comparator output is fed to the signal relay based on the D-trigger and the control signal switch. From the switch output, the control signal of positive or negative polarity is fed to the input of the control object.

The control object consists of a simulator of an executive mechanism built on the basis of an integrator with a variable gain, a nonlinear link with an extreme characteristic and a linear part of the object – an aperiodic link with a variable time constant.

The nonlinear characteristic of the object is set as a square function of the form

$$y(x) = ax^2 + bx + c,$$

where a, b and c are the coefficients determining the type and position of a nonlinear characteristic. The choice of such a nonlinear function is conditioned by the possibility of obtaining comparable characteristics, both in the mathematical model and in the hardware implementation, without using unnecessarily complex circuit solutions. The possibility of changing the type of characteristic in the process of system operation is also taken into account.

The analysis of methods of nonlinear characteristic formation using electronic schemes shows that the most common method is piecewise linear approximation. Thus, it is possible to form characteristics of a rather complex type, but having a static character. This is explained by the difficulty of conjugation of separate segments of approximation at displacement or deformation of nonlinearity. Practically the only way to bypass this restriction relatively easily is the analytical nonlinearity task. With regard to obtaining the extreme characteristic in the form of an electronic model, the above expression can be implemented on the basis of analog signal multiplication schemes. In the considered mathematical model a simplified nonlinear characteristic is implemented, limited only by the operation of erection into a square, realized by means of the multiplication operation. To obtain the effect of non-stationarity of the characteristic, additional components are mixed to its input and output signals, which can be both regular and random.

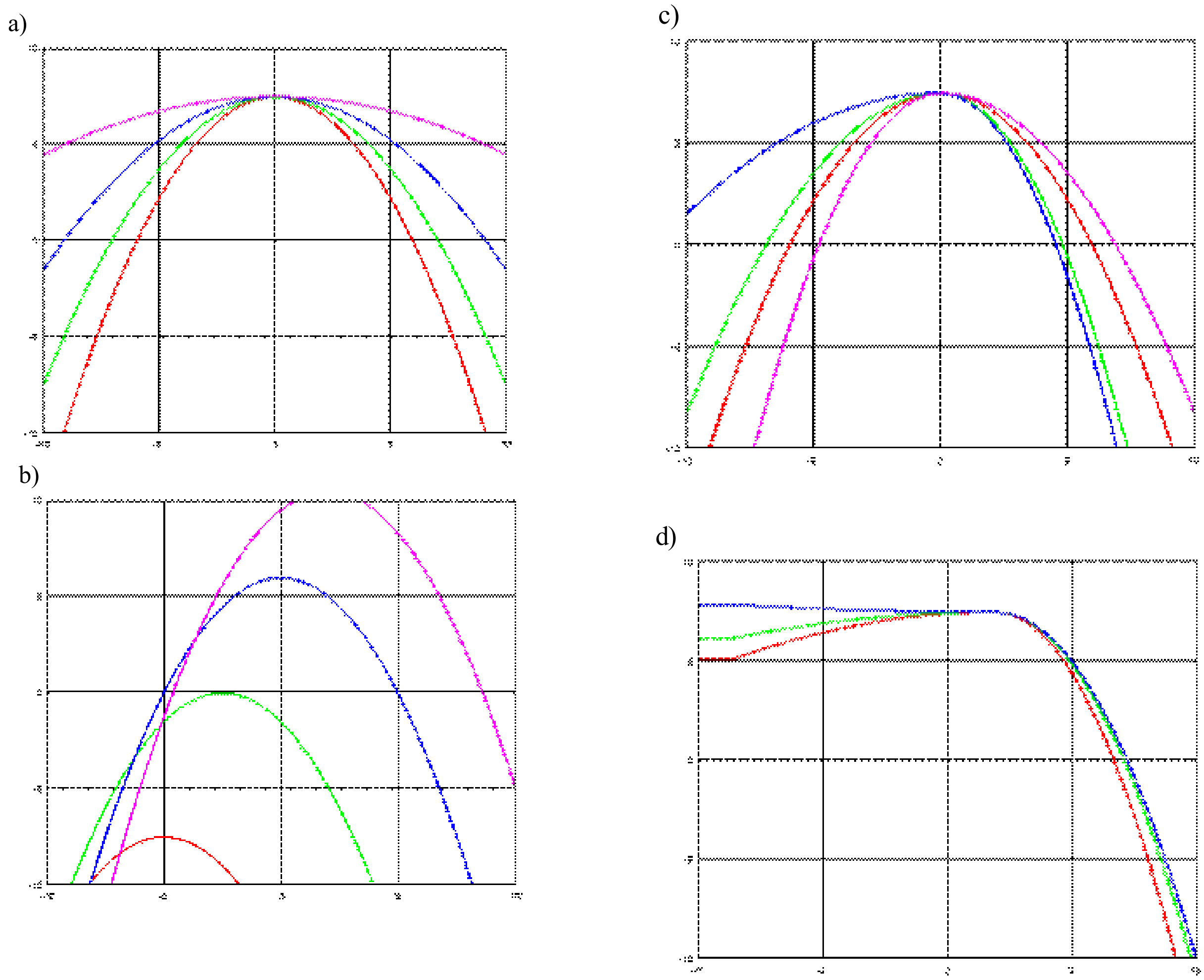

Figure 4 – Control of the form extreme characteristic
a) change in slope b) change in the extreme position c)d) – asymmetry of the characteristic

The main difference between hardware implementations of ESC is in a more complex extreme characteristic shaper. The hardware shaper allows not only deviation by input and output coordinates, but also a significant change in the shape of the characteristic. A wider range of the position of the extremum in the workspace is possible, the steepness of the characteristic and its degree of symmetry with respect to the extremum abscissa can be changed. Examples of possible changes in the shape of the extremum are shown in Fig. 4a-d. Non-linearity can be controlled either manually or by means of software or hardware-defined actions from external sources in relation to the signal model.

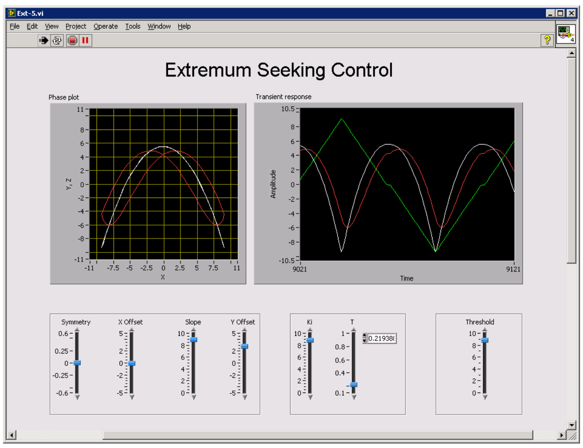

Figure 5 – Front panel of the control device

Hardware implementation of ESC is made as a replaceable module for laboratory station NI ELVIS-III. Interaction with the user is carried out with the help of the control program, implemented in the environment of development of virtual laboratory devices LabVIEW [5]. The front panel of the control device is shown in Fig. 5. In the upper part of the panel there are signal recorders, which allow not only to observe the processes in the system, but also to save the results of experiments as text files for further processing and analysis. In the lower part there are the sliders of regulators, allowing to change parameters of the control object and regulator. They are grouped according to their functional purpose:

- non-linear characteristic control – position (X Offset, Y Offset) and form (Symmetry, Slope) specifications;
- object parameter control – set the search speed of extremum (K_i) and linear part time constant (T);
- control of the regulator parameters – setting the sensitivity threshold (Threshold).

The use of the workshop assumes that work with it begins with the study of basic theoretical material and experiments with the mathematical model of the system. After obtaining initial knowledge about the structure and operation of the system of extreme control, it is possible to proceed to experiments with hardware (physical) model, followed by comparative analysis of results obtained on two types of system models. Further work with the layout includes elements of development and research of own variants of the regulator, research of more complex behavior of nonlinear link depending on external factors, thus allowing the trainee to acquire knowledge, skills and abilities of different levels of competence connected with development of control systems for complex objects.

References

1. NI Educational Laboratory Virtual
Instrumentation Suite II Series (NI ELVIS™ II Series) User Manual, Document number 374629C-01, National Instruments Corporation, June 2011
2. Pletnev G.P. Automated controlof
thermal power plants: Textbook. manual for universities. – Moscow.: Energoizdat, 1981. p.368
3. Liberzon L. M., Rodov A. B.
Extreme regulation systems. // Library for automation. Issue 154. – Leningrad: Energy, 1965.
4. Nikolaev L.F. Aerodynamics and
flight dynamics of transport aircraft: Textbook. for universities. – Moscow.: Transport, 1990. p.392
5. Travis J., Kring J. LabVIEW for all –
Moscow.: DMK Press, 2015. p. 880

REPLACING REVERSE ENGINEERING IN ADDITIVE TECHNOLOGY

Vinnichenko Alexandra

Saint-Petersburg State University of Aerospace Instrumentation,
Saint-Petersburg, Russia
E-mail: alex23rain@gmail.com

Abstract
The article sets the task to simplify the process of reverse engineering by introducing three-precision 3D scanning, which allows accelerating the technological stages of reverse engineering to the time of manufacture of the product, as well as simplify the process of detection of finished products and simplify the implementation of unification principles.

In the modern world, there is a predominance of modern, generally recognized traditional technologies for creating machine parts, products, Assembly units, and other component groups of products necessary to ensure the functionality of the complex Assembly. Such technologies include casting, surface machining processes, forming, smelting, and other commonly recognized technologies.

A promising direction for the development of the metallurgical, machine-building, electric power and robot-building industries is the creation of control models and complexes that compactly combine various processes into a single technological line. The introduction of reverse engineering based on additive technologies in the production process can significantly simplify the production line and simplify the interaction of processes such as defection and unification.

The use of 3D technologies can significantly improve the production efficiency of industrial sectors by reducing the cost of repairs and correction of defects.

The main problems of traditional technologies are long life cycles and features of technological processes that produce the planned products. A high level of defects is typical for heavy industry and the existing labor-intensive control operation not only increases the cost of production, violates the terms of contracts, but also creates prerequisites for the formation of a negative image among the supplier companies.

Reverse engineering is the study of a ready-made device or program, as well as its documentation, in order to understand how it works; for example, to discover undocumented features (including software bookmarks), to make a change or reproduce a device, program, or other object with similar functions, but without direct copying.

Copying various mechanisms and machines without actual development. Allows you to reproduce a successful design with minimal costs, for example:

– an item is urgently needed, but for certain reasons it has been discontinued, the price of the product is too high, or you will have to wait a long time for its delivery;

– project documentation does not match the device, papers are lost, difficult to obtain, or documents were not originally made;

– it is necessary to analyze the condition of the product and perform stress calculations after prolonged use to improve its quality;

– you need to analyze the details or devices of competitors.

In this issue, additive manufacturing technologies that allow manufacturing any product based on a 3D computer model can come to the rescue in the first place [1].

The reverse engineering process itself includes all stages, starting with scanning and ending with testing of the received part (fig. 1). Reverse engineering is, of course, not just getting drawings. And it's not so much getting drawings as making a specific part based on them and understanding that you have achieved your goal [2].

Cleaned parts are subjected to defects in order to assess their technical condition, identify defects and establish the possibility of further use, the need for repair or replacement. In fault detection reveal: the wear of the working surfaces in the form of changes in the size and shape of the part; the presence of vykashivaniyu, cracks, chips, holes, scratches, grooves, burrs, etc.; the residual strain in bending, torsion, warpage, the change of physico-mechanical properties result from the effects of heat or environment [3].

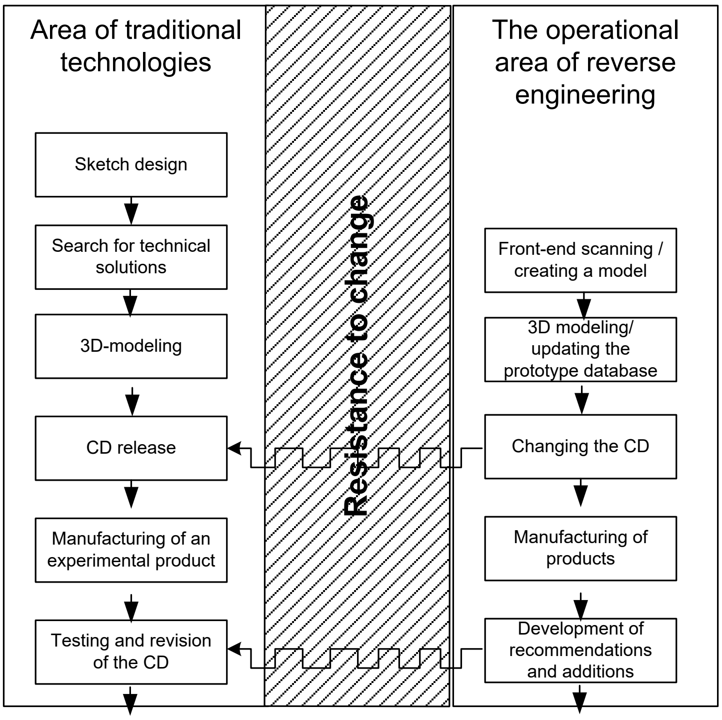

Figure 1- stages of reverse engineering

Figure 2 shows a map of the applicability of changes to the technical system. To solve the problems of restoring a technical system after serial failures caused by severe factors of the operating environment, or following the decisions to modernize structural elements at the request of the market environment and the requirements of normative and technical documents on the part of strategic factors of advanced standardization in a non-stable competitive environment, it is advisable to apply reverse engineering to reduce the cost of restoration or modernization processes.

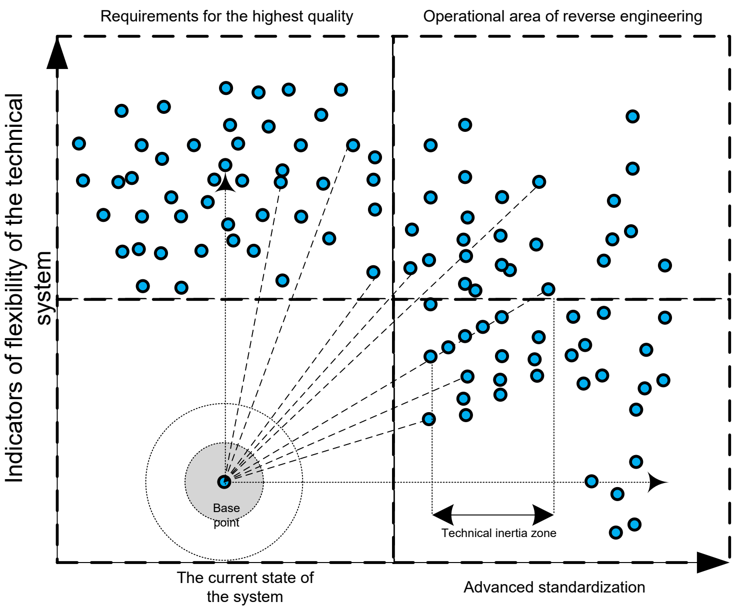

Figure 2 – map of applicability of changes to the technical system under the influence of regulatory documents and environmental requirements

As a practical addition, we will give an example of the results of a defect in the technical system of the hydraulic brake drive. In one batch, data on the types and number of defects were collected in a statistically revalent way, and a Pareto diagram was built on the basis of the data obtained (table. 1) [4].

Table 1-data on defects in the production of a hydraulic brake actuator

Types of defects	Sum of defects	The cumulative percentage of defects
Destruction of rubber cuffs	22	16,54%
Thread wear in holes	20	31,58%
Breaks on the mounting flanges	19	45,86%
Swelling of rubber cuffs	17	58,65%
Cracks on mounting flanges	15	69,92%
Failure of thread in the holes	13	79,70%
Wear of the main cylinder	11	87,97%
The wear of the wheel brake cylinder	8	93,98%
Cloggingess	8	100,00%

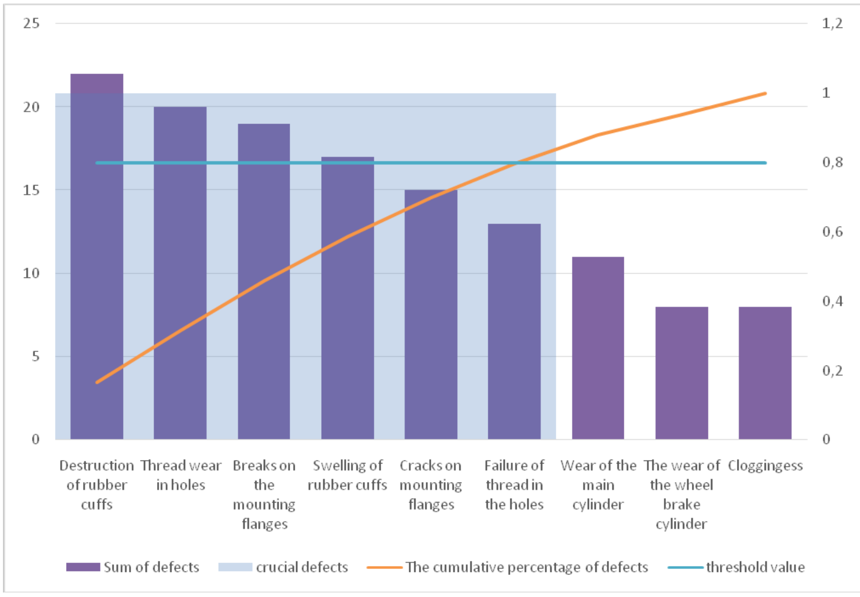

Figure 3-Pareto Diagram for analyzing defects in the production of hydraulic brake drives

After analyzing the data from the Pareto chart, you can select a group of key marriages that are separately highlighted (Fig.3). This group also needs to be paid special attention when analyzing and reducing marriage.

In cases where it is necessary to produce a limited batch of small-sized components to replace parts related to the aesthetic form of the product, design or interface element, the system that needs to establish the problem of the existing industry has a sufficiently serious research.

The result, which carries out rationalization changes in the organizational structure of those enterprises that have decided to take this difficult step of restructuring in order to achieve efficiency and preventative effectiveness of issues of integration of the ideology of synchronized production.

This can be achieved by implementing 3D scanning of individual elements in the production of hydraulic brake drives, replacing defective parts with printed 3D models.

3D printers that represent additive manufacturing are able to work not only with them, but also with engineering plastics, composite powders, various types of metals, ceramics, and sand. This simplifies the defect procedure and creates a positive social effect for the introduction of reverse engineering elements.

In the context of the scientific and technical revolution, the principles of unification should be used rationally as a complex process that covers the issues of design, technology, control and operation of machines, mechanisms, devices and devices.

Such decisions should be based on a comprehensive analysis of production capacity and achieved through the teamwork of all managers who own the main production process and make decisions at their functional locations.

References

1. Kenneth Wong. Generative Design: Advice from Algorithms [electronic resource]// Digital Engineering magazine. 2018. January 2, URL: https://www.digitalengineering247.com/article/designadvice-algorithms (дата обращения 31.01.2020).
2. Волин, Д.В. Применение технологии обратного инжиниринга в машиностроении [электронный ресурс] // Технические науки: проблемы и перспективы: материалы IV Междунар. науч. конф. (г. Санкт-Петербург, июль 2016 г.). — СПб.: Свое издательство, 2016. — С. 67-69. — URL https://moluch.ru/conf/tech/archive/166/10534/ (дата обращения: 04.02.2020).
3. Грабченко, А.И. Современное оборудование и программное обеспечение обратного инжиниринга промышленных изделий / А. И. Грабченко [электронный ресурс] // Сучасні технології в машинобудуванні Modern technologies in mechanical engineering: зб. наук. пр. – Харків: НТУ "ХПІ", 2010. – Вип. 5. – С. 138-152.
4. Леонидович, А.Б. Влияние изменения технических характеристик элементов тормозных механизмов на работу тормозного привода / Леонидович, А.Б, Кацай В.В., Шарыпов А.В. [электронный ресурс] // Вестник Курганского государственного университета. 2015. №3 (37). URL: https://cyberleninka.ru/article/n/vliyanie-izmeneniya-tehnicheskih-harakteristik-elementov-tormoznyh-mehanizmov-na-rabotu-tormoznogo-privoda (дата обращения: 04.02.2020).

CONTENTS

The scientific edition

ИЗВЕСТИЯ КАФЕДРЫ UNESCO ГУАП
«ДИСТАНЦИОННОЕ ИНЖЕНЕРНОЕ ОБРАЗОВАНИЕ»

Сборник статей

Выпуск 5

BULLETIN OF THE UNESCO DEPARTMENT
«DISTANCE EDUCATION IN ENGINEERING» OF THE SUAI

Collection of the papers

Issue 5

Computer imposition

Papers are publish in author's edition

Подписано в печать 20.04.2020. Формат 60x84 1\8.
Усл. печ. л. 15,9. Тираж 150 экз. Заказ № 133.

Редакционно-издательский центр ГУАП
190000, Санкт-Петербург, Б. Морская ул., 67
Department of operative polygraphy SUAI
190000, St. Petersburg, st. B. Morskaya, 67